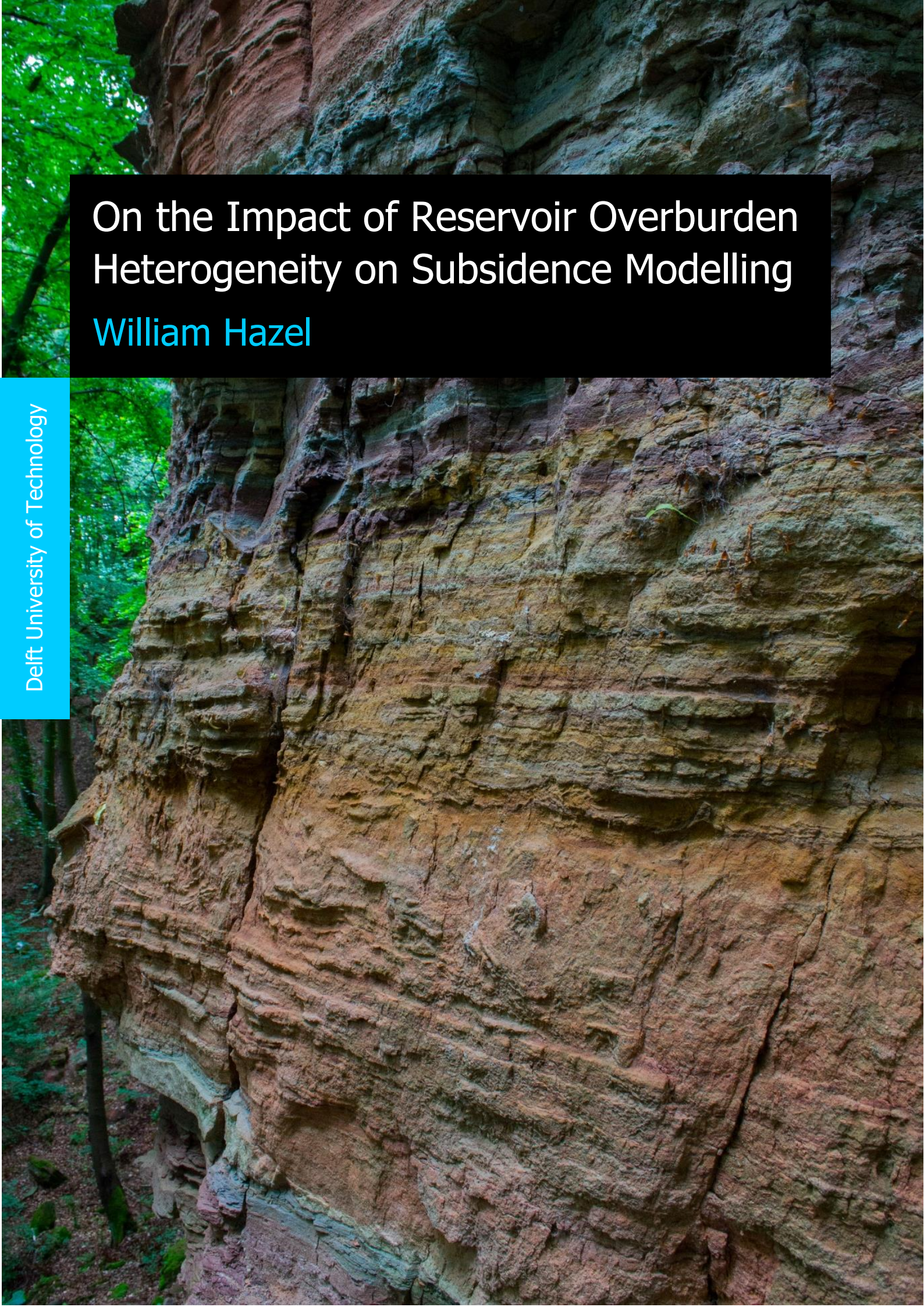

# On the Impact of Reservoir Overburden Heterogeneity on Subsidence Modelling

William Hazel

Delft University of Technology

# On the Impact of Reservoir Overburden Heterogeneity on Subsidence Modelling

by

William Hazel
Student ID: 4086813

in partial fulfilment of the requirements for the degree of

**Master of Science**
in Applied Earth Sciences

at Delft University of Technology,
Department of Geosciences and Engineering
to be defended publicly on Thursday the 21st of December, 2017 at 14:00

Supervisors & Committee

Dr. Hemmo Abels, TU Delft
Dr. Ir. Femke Vossepoel, TU Delft
Prof. Dr. Giovanni Bertotti, TU Delft

A digital version of this thesis is available at: http://repository.tudelft.nl/.

TU Delft

# Abstract

There is an increased need for modelling the Dutch overburden to improve the prediction of earthquakes and subsidence due to the extraction of hydrocarbons. Depending on the surface location, the subsidence model of the *NAM* can under or over predict the amount of subsidence by 4 to 5 cm. This is around 15 % of the current maximum subsidence of 30 cm. The underlying assumption of the *NAM* subsidence model is that the reservoir, and the overburden above it, behave the same and thus have the same elastic parameters. The purpose of this research is to obtain a better understanding of the role overburden heterogeneities play in man induced subsidence. The main research question is: *To what extent do overburden heterogeneities affect subsidence caused by reservoir depletion?* Followed by the hypothesis: *The heterogeneities of the overburden affect subsidence and should therefore be incorporated*.

The results show that modelling the overburden as multi-layered, rather than as one homogeneous layer, leads to a difference of 0.75 cm. This is greater than the measurement error of the InSAR data, which is used to determine the subsidence of the Groningen field, and is significant when compared to the current discrepancy of 4 to 5 cm. Elastic parameters have been calculated from acoustic well data for geological units around the Groningen area. The calculated values differ from the values used by the *NAM*. When the calculated values are used for the Upper North Sea and Lower North Sea groups, the difference with the reference model is up to 2 cm for a reservoir radius of 3 km and 0.87 cm for a Groningen scale reservoir. The results suggest that the heterogeneities of the overburden affect subsidence significantly enough to warrant further investigation. Due to the fact that the obtained results are for horizontal layers, there is much potential for more complex overburden geology e.g. salt structures and non-horizontal layers.

**Keywords: subsidence, overburden, Plaxis, elastic parameters.**

# Acknowledgements

First of all, I would like to thank my main supervisor Dr. Hemmo Abels for coming up with this project which has allowed me to learn about a subject that I otherwise would not have considered and is a hot topic this very moment. He gave me a lot freedom (I really like freedom) to pursue things that I personally found interesting and would help steer me back on track to ensure a certain amount of focus. I learnt a lot from our sometimes lively discussions on the subject matter, which I am sure will help me to think more critically about my future work. It was also Hemmo who pushed me to seek contact with an industry professional, thereby allowing me to obtain data that is not yet publicaly available.

Secondly, I would like to thank Dr. Ir. Femke Vossepoel with whom I had regular and fruitful meetings. Femke was a good complimentary advisor to Hemmo, due to their respective specialisations. I am positive that this combination allowed me to learn more than if I only discussed my work with one of them. She also went out of her way to help me with personal matters, which I truly appreciate. I will use this opportunity to thank Irene, Maarten, Karlijn, Hoessein and Mohammed for the discussions we had during the monthly meetings and helping each other with our problems.

Third but not least, I would like to thank Prof. Dr. Giovanni Bertotti. I did not see Giovanni as often as my other supervisors, but nonetheless his opinion is always valued due to his unique way of 'keeping it real'. His reality checks are often needed and helped me to pursue tangible goals for this project. Over the years I have considered Giovanni to be a mentor of sorts and I genuinely look up to him.

I would like to thank Ronald Brinkgreve and the *Plaxis* support team for helping me with issues and helping me to understand how *Plaxis* works.

I would like to thank Morgane Bizouray, Tom Bradley, Gerhard Diephuis and Evert van de Graaff for answering my questions on wireline logging and other petrophysics related questions. It is always nice to get a perspective from industry as well.

I would like to thank Pauline Kruiver for her advice on my project and referring me to her contact at the *NAM*. Now I would like to thank Remco Romijn and the *NAM* for giving me their well data and allowing me to publish the results in this document.

I would like to thank Adriaan van Natijne and Karlijn Beers for helping me to create the maps in this report.

I would like to thank my family for their support and interest during my studies at Delft. They have always given me advice and emotional support when I needed it. My parents also ensured that I did not have to worry about my personal finances throughout my studies.

Finally, I would like to thank Debby den Besten for supporting me and the time we have spent together during my time here at Delft. She is also responsible for motivating me to perform to the best of my abilities at University.

William Hazel
*16th of December 2017, Delft*

# Contents

# List of Figures

# List of Tables

# 1

# Introduction

This report was written as part of completing the thesis for the master's degree in Applied Earth Sciences at *Delft University of Technology*. The main research question of this report is: *To what extent do overburden heterogeneities affect subsidence caused by reservoir depletion?*

Man induced subsidence is a global problem and caused by the extraction of a resource, for instance oil or water, and then the sinking of the ground above this resource (Doornhof et al., 2006). The pressure depletion in the subsurface leads to compaction of the reservoir which in turn causes subsidence (Figure 1). Some notable examples are Groningen in the Netherlands (gas), Ekofisk in the North Sea (oil) and Venice in Italy (water and gas) (Keszthelyi et al., 2016; Gambolati et al., 2006; Gambolati et al., 1991). The maximum predicted subsidence for the Groningen field is 50 cm (NAM, 2016) which is less than the 9 m in Wilmington California (www-1). However, a large portion of the Groningen area is below sea level and protected by dikes (Nagel, 2001) which means that the subsidence poses considerable risk to the surrounding area. Production of the gas has a profound effect on the lives of inhabitants in the region. Earthquakes and subsidence cause damage to property and living quality, which cause much anger with the local population (www-2). This pressure has forced the Dutch government to reduce production to 21.6 billion cubic metres from 24 per year from the 1$^{st}$ of October 2017 (www-3). This change means that revenues to the state will be reduced by around 300 million euros on a per year basis. Due to these constraints, there has been a strong decline in gas production from the Groningen field as the new production level is less than half of the level in production year 2012-2013 which was 53 billion cubic metres (www-4).

## 1.1 Subsidence Modelling

The exact relationship between earthquakes/subsidence and damage to properties is not known. A report on the causes of damage to property will be published in the spring of 2018 (www-5) and should be used once it becomes available as it would allow a researcher to set clear benchmarks for modelling, e.g. what amount of subsidence causes damage. The negative effects of gas extraction from the Groningen field have led to an increased interest in accurately modelling the overburden to better predict earthquakes (Kruiver et al., 2017). If the report concludes that subsidence is a major contributor to damage then it needs to be modelled accurately. Appendix A shows the subsidence modelling error for the year 2013 of the Groningen field. Depending on the location, it can be seen that the model underestimates the subsidence by about 5 cm and overestimates by around 4 cm (NAM, 2016). Hence there is room for improvement as the predicted subsidence for the present day is around 30 m, meaning that the error is above 10 %. The way the overburden, material above the reservoir, is modelled could account for this.

There are currently multiple ways of determining subsidence. For the oil and gas industry the preferred methods are: using a linear approach, for instance a variant of Geertsma's (1973) solution, or coupled models that link the stresses with fluid flow. In the Netherlands the *Nederlandse Aardolie Maatschappij* or *NAM* (Dutch Oil Company) and *TNO* conduct a lot of research on subsidence (NAM, 2013; NAM, 2016; van Thienen-Visser et al., 2015). Their research is particularly aimed at predicting subsidence and seismicity for the large Groningen field. There are published models that at least incorporate more than one layer of rock material (Fokker, 2006) and (Mehrabian and Abouseleiman, 2015) as for some models it is the case that the reservoir and surrounding material are assumed to behave the same.

## 1.2 Research Objectives

The first purpose of this thesis is to study the effect of the overburden on subsidence. This effect comes on top of the effect of the depleting reservoir. Overburden heterogeneities, in the context of this thesis, are horizontal layers with varying elastic properties. The main research question is:

- *To what extent do overburden heterogeneities affect subsidence caused by reservoir depletion?*
- From a practical point of view, this is then followed by: *Can variations in elastic properties of the overburden be ignored for subsidence modelling?*
- The hypothesis is: *The heterogeneities of the overburden affect subsidence and should therefore be incorporated*.

A second purpose of this thesis is to acquire more knowledge on the Dutch subsurface in terms of elastic parameters such as the Young's modulus and Poisson's ratio. These two parameters form the foundations of linear elastic modelling, which is a popular type of modelling in finite element programs. Data of these elastic parameters appears to be limited for the Dutch overburden and the values used by the *NAM* do not give an uncertainty estimate. Considering how fundamental these parameters are in finite element subsidence modelling, it makes sense to attempt to get a hold on this issue. The public data bank *NLOG* is used to obtain wireline log data to determine these parameters and a comparison will be made to existing literature. The gamma ray and neutron porosity logs will be used to discern possible lithological trends within the elastic parameters. The two research questions for well data are then as follows:

- *How do the literature values of elastic parameters compare to those determined in this thesis?*
- *Can lithological links within the elastic parameters be discerned through the use of the gamma ray and neutron porosity logs?*

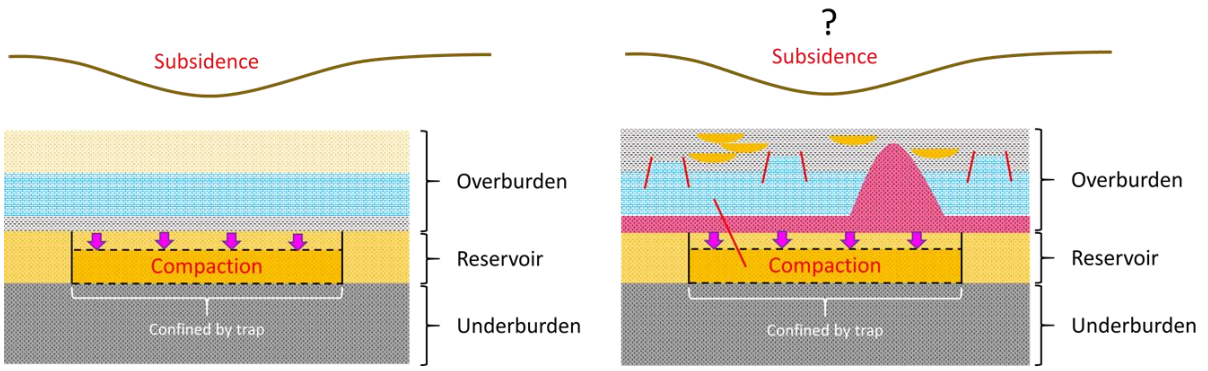


**Figure 1**: The main research issue is the relationship between subsidence and the overburden (left) in the context of horizontal layers. Ultimately one would like to know what the response of a more complicated geological scenario would be (right).

The general approach and lay out of this report can be seen in Figure 2. Chapter 2 deals with the existing theory forming the basis of this thesis. It describes basic geomechanics and the Geertsma (1973) subsidence model. It also provides information on existing literature for the Dutch subsurface. The method, results and discussion of the well analysis are shown in chapter 3. Chapter 4 has the same structure, but focusses on the finite element program *Plaxis* that has been used for subsidence modelling. This chapter is intended to show how sensitive the modelled subsidence is to variations in rock properties of the overburden. Finally, the two research approaches are brought together in chapter 5, where subsidence research questions are answered. Conclusions and recommendations are given in chapter 6.

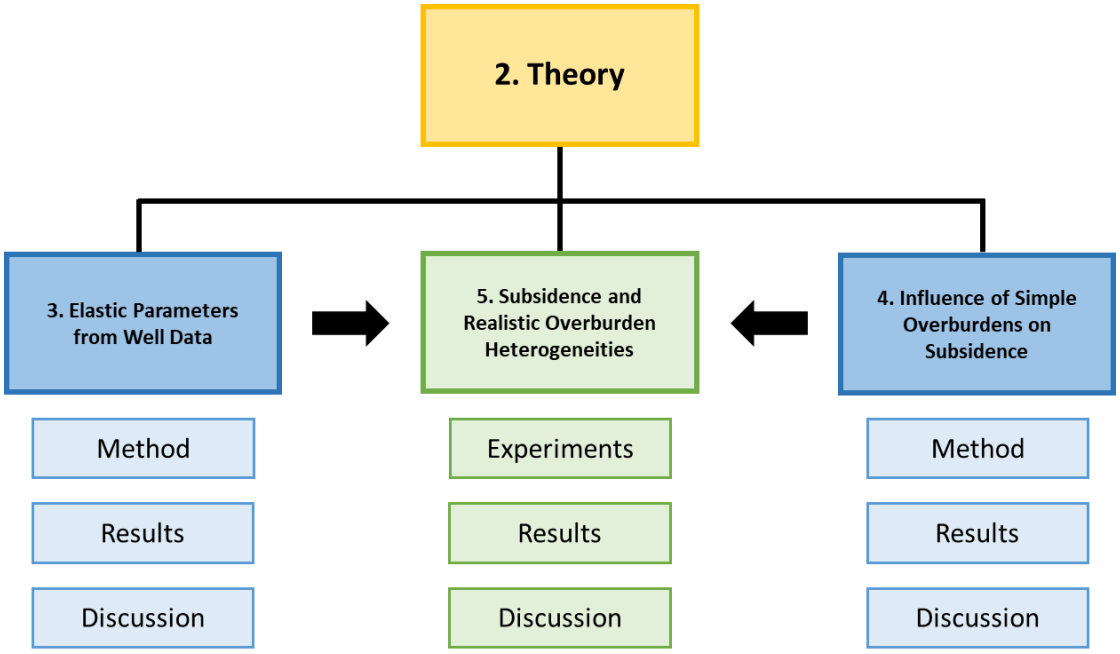


**Figure 2**: Approach of this thesis. The theory underpins the obtaining of elastic parameter from the well data (chapter 3), the subsidence modelling in *Plaxis* (chapter 4) which are then combined for more practical cases based on the Groningen geology (chapter 5).

# 2

# Theory

This chapter discusses the underlying physics of linear elasticity and subsidence whilst also addressing the publically available knowledge of the Dutch subsurface. The first part (2.1) will focus on geomechanics, particularly linear elastic and perfectly plastic behaviour that forms the basis of the experiments in this thesis. The second part (2.2) deals with subsidence models developed by Geertsma (1973) and Geertsma and van Opstal (1973) which are used as a reference. In the third part (2.3) the current knowledge of the Dutch subsurface is introduced which is compared with the obtained results in chapter 3.

## 2.1 Geomechanics

It is essential to be able to mathematically describe materials in order to model them. Rocks, whether at the surface or in the subsurface, are subjected to forces that can temporarily or permanently deformed by these. When a material such as a rock is subjected to a force, it has an ability to resist and even recover from deformation (Fjaer et al., 2008). One can imagine a person trying to crush a rock with his or her bare hands. In most cases the person in question will be left with sore skin, wounded pride and nothing else to show for. Hence showing said rock's ability to resist the implemented force. A material's capability to withstand and recover from a force is called elasticity and the foundations for the theory of elasticity are stress and strain. These concepts are discussed in this chapter. The purpose of this chapter is to help someone who has little or no experience with elasticity, to understand the concepts terminology that are discussed further in this thesis.

Section 2.1.1 discusses forces and stresses which cause elastic behaviour. The concept of strain is explained in section 2.1.2 and information on so-called elastic moduli can be found in section 2.1.3. Section 2.1.4 describes linear elastic and perfectly plastic behaviour which are two popular ways of material modelling. Finally elastic moduli can be determined from certain types of acoustic waves and this is discussed in section 2.1.5.

### 2.1.1 Forces and Stresses

An example is shown (Figure 3) to illustrate the concept of forces and stresses. A weight is laying on top of a pillar. For the purpose of this example we will neglect the mass of the pillar. This weight creates a force that acts on and through the pillar. The cross section, or area, at level $a$) is $A$ and with an acting force $F$ this leads to a following stress $\sigma$ which is defined below (Fjaer et al., 2008).

$$\sigma = \frac{F}{A} \tag{2.1}$$

It is evident from eq. (2.1) that the larger the area $A$ is, the smaller the stress is and vice versa. The stress at $a$) will be smaller than at $b$), hence different parts of the column will undergo different stresses.

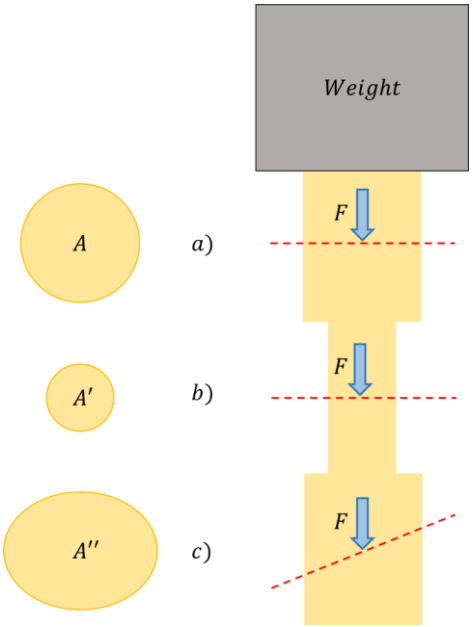


**Figure 3**: Example of a constant force and varying stresses. After Fjaer (2008).

To define the stress at a point $P$ one can divide a cross-section into small sub areas $\Delta A$. The same can be done for the force $F$ which can also be subdivided into smaller sub forces $\Delta F$. The stress on sub area $\Delta A_i$ becomes $\Delta F_i/\Delta A_i$. Point $P$ (Figure 4) can be considered to be infinitesimally small and thus the stress on this point is $\Delta F_i/\Delta A_i$ to the limit of zero, giving:

$$\sigma_P = \lim_{\Delta A_i \to 0} \frac{\Delta F_i}{\Delta A_i} \tag{2.2}$$

Eq. 2.2 defines the local stress at a point $P$ within a larger cross-section where the average stress at the cross-section is described by Eq. 2.1.

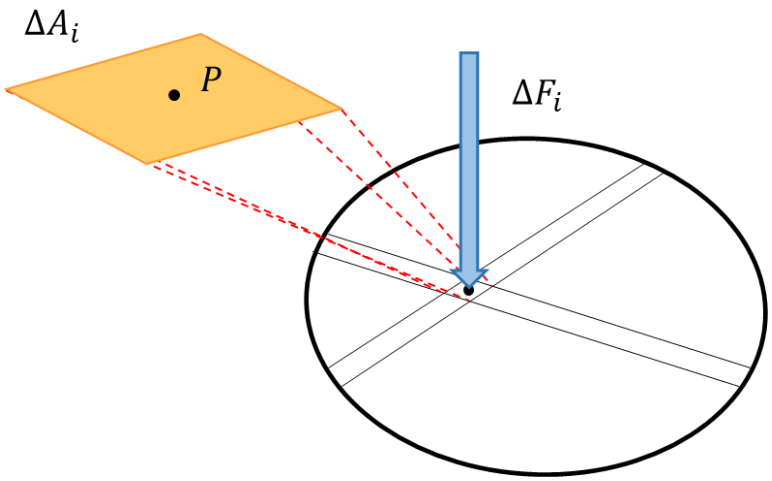


**Figure 4**: The local stress at a point P. After Fjaer (2008).

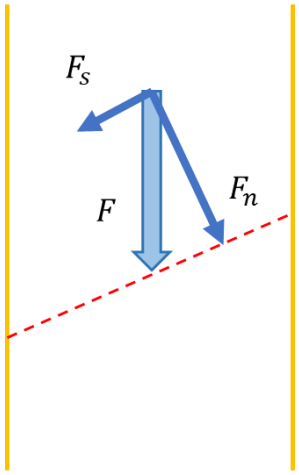


**Figure 5**: Normal and shear forces. After Fjaer (2008).

One also needs to take the orientation of the force acting on a cross-section into account. If one were to take cross-section $A''$ in Figure 3 then the acting force can be decomposed into two separate forces (Figure 5). There is one force acting normal to the cross-section $F_n$ and one acting parallel to the cross-section $F_p$. The so-called *normal stress* is given by (Fjaer et al., 2008):

$$\sigma_n = \frac{F_n}{A''} \tag{2.3}$$

and the *shear stress* by:

$$\tau = \sigma_s = \frac{F_s}{A''} \tag{2.4}$$

Both forces depend on the orientation of the plane and it is clear that if for instance the plane were to be vertical that the normal stress becomes zero. For this thesis the normal stresses are of most interest.

### 2.1.2 Strain

To give an example of strain, consider Figure 6 where an object has been deformed by a force. Due to this, a particle at point $(x, y, z)$ is moved to point $(x', y', z')$. The change in $x$-direction can be denoted by $u$, the change in $y$-direction by $v$ and change in $z$-direction by $w$. These new constants are called displacements. After this the new position of the particle can be described by the following equations:

$$x' = x - u \tag{2.5}$$

$$y' = y - v \tag{2.6}$$

$$z' = z - w \tag{2.7}$$

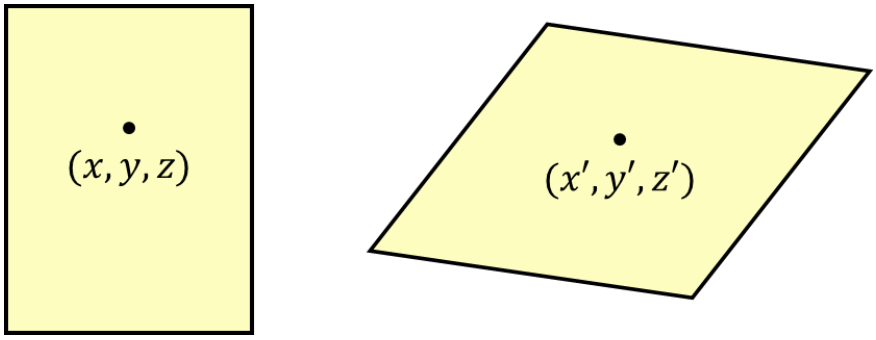


**Figure 6**: Example of a material (left) that has undergone deformation (right) and the location of a particle or point within this material. After Fjaer (2008).

In a case where the all the displacement constants are equal, the object has undergone translation. As an example where a cube is pushed across a table. The cube itself has not changed shape, it has simply moved to somewhere else. A different example is rotation where the example cube simply rotates around an axis. If a new position of a particle cannot be reconstructed from the old via rotation or translation, the particle is said to have undergone *strain* (Fjaer et al., 2008). For a more detailed explanation, an interested reader is referred to chapter 1 of Fjaer (2008) and chapter 2 of (Fossen, 2010). Figure 7 shows an example of a strained object.

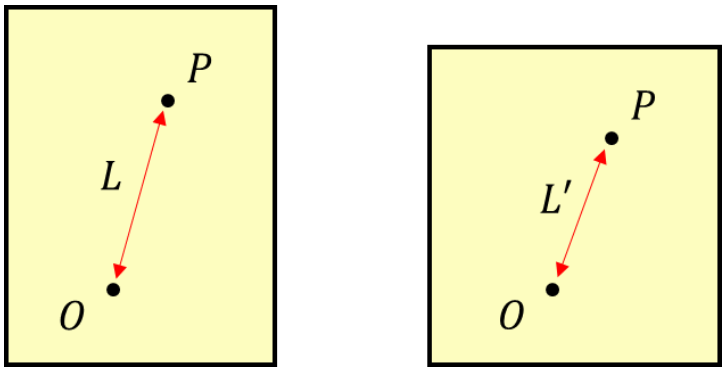


**Figure 7**: A sample undergoing deformation. With the left illustration showing the unaltered state. After Fjaer (2008).

The amount of change in length between points $O$ and $P$ is called *elongation* and is defined as:

$$e = \frac{L-L'}{L} = \frac{\Delta L}{L} \tag{2.8}$$

## 2.1.3 Elastic Moduli

The theory of linear elasticity describes the deformation behaviour of materials that show a linear relationship between applied stresses and the resulting strains. For rocks this is at best an approximation as the majority of rocks do not behave linearly (Fjaer et al., 2008). The Ekofisk field is a good example of this: when waterflooding was applied the previous subsidence was not recovered, hence the reservoir had undergone plastic deformation (Doornhof et al., 2006). In the case of linear behaviour the relationship between stress and strain can be described by Hooke's law:

$$e_z = \frac{1}{E}\sigma_z \tag{2.9}$$

Where $E$ is the Young's modulus which is one of multiple elastic moduli. The Young's modulus describes the stiffness, or ability to withstand uniaxial stress. Assuming that a stress acting on a sample is compressive (Figure 8), then for most materials the sample will expand laterally. In Eq. 2.9 and Eq. 2.10 vertical contraction of the sample is defined by a positive number, hence negative strain equates an increase of the sample size in that dimension.

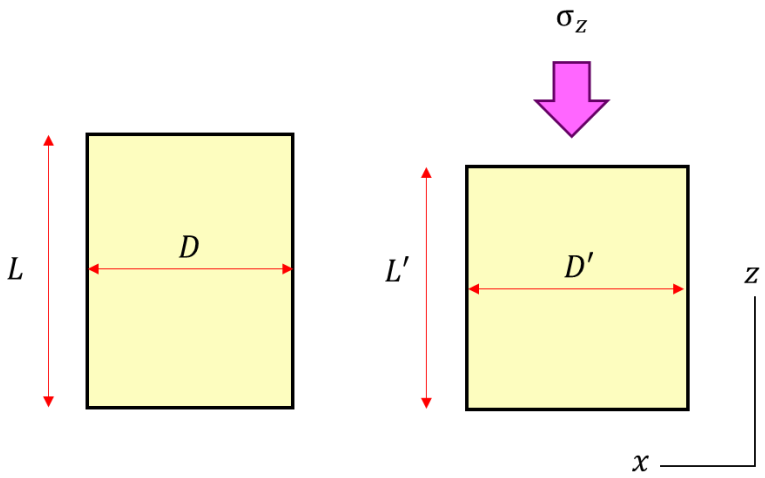


**Figure 8**: A sample undergoing deformation due to uniaxial stress. After Fjaer (2008).

The ratio with which a material expands laterally when compressed longitudinally is called the Poisson's ratio and is:

$$\nu = -\frac{e_x}{e_z} \tag{2.10}$$

Figure 9 shows an example of two materials. Cork has a Poisson's ratio of almost 0 and rubber 0.5. These two materials can be seen as two extremes, but there are some materials that can have a negative Poisson's ratio, i.e. they expand when they become more elongated (Fossen, 2010). Sandstones tend to have a value between 0.21 and 0.38 (Fossen, 2010) and rocks that are highly compressible have a low Poisson's ratio (Fjaer et al., 2008).

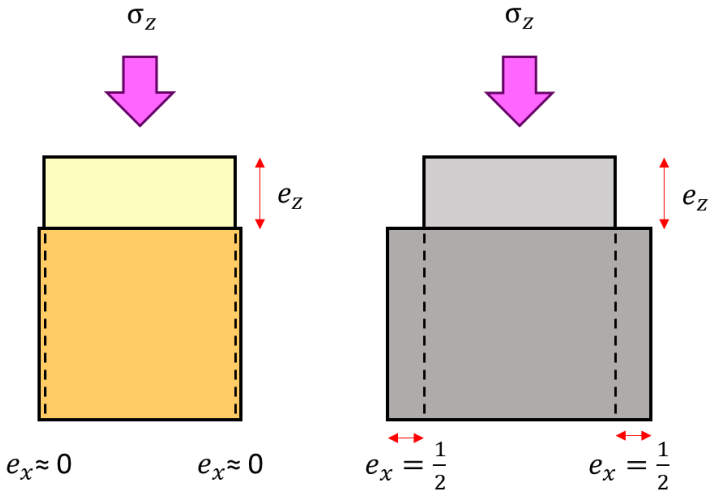


**Figure 9**: A sample of cork (left) and rubber (right) deforming due to uniaxial stress. After Fossen (2010).

Two other common elastic moduli are the shear modulus $G$ (Figure 10) and the bulk modulus $K$ (Figure 11). The shear modulus describes a material's ability to withstand a shear stress (Eq. 2.11). The bulk

modulus is the ratio between hydrostatic stress $\sigma_p$ and volumetric strain $e_{vol}$ (Fjaer et al., 2008) and states the resistance of the material to hydrostatic compression (Eq. 2.10). In a hydrostatic stress state the normal stresses are $\sigma_p = \sigma_x = \sigma_y = \sigma_z$ whilst the shear stresses are zero. Elastic moduli are all related to one another, so when two are known all the others can be determined as well. A table can be found in chapter 1 of Fjaer (2008) which includes other elastic parameters as well.

$$G = \frac{Fl}{A\Delta x} = \frac{\sigma_s l}{\Delta x} \tag{2.11}$$

$$K = \frac{\sigma_p}{e_{vol}} \tag{2.12}$$

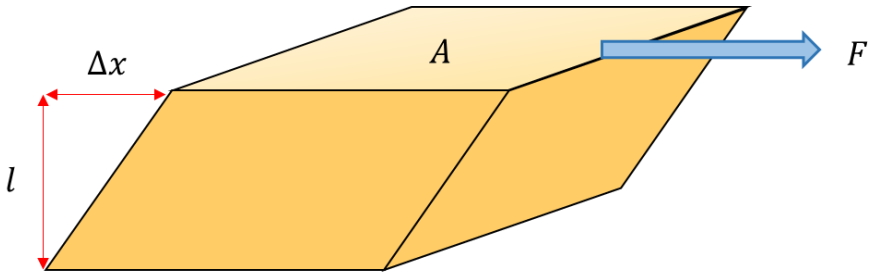


**Figure 10**: A sample undergoing shear deformation. After (www-6).

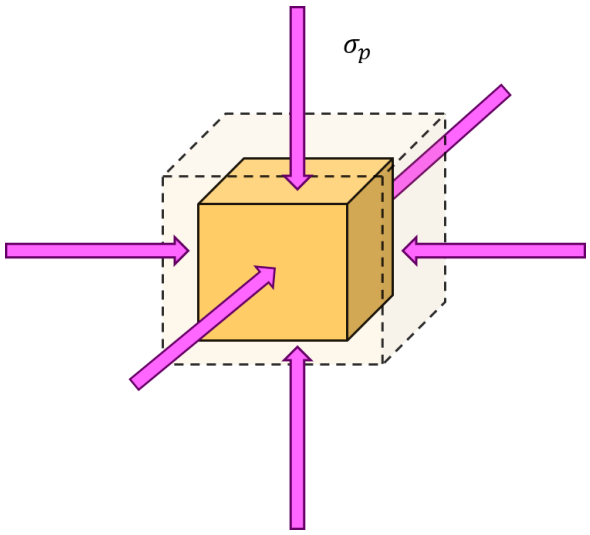


**Figure 11**: A sample undergoing hydrostatic stress. After (www-7).

Strains as function of stresses, when ignoring shear stresses, can be expressed by the following equations for Hooke's law in three dimensions (Fjaer et al., 2008):

$$e_x = \frac{1}{E}\{\sigma_x - \nu(\sigma_y + \sigma_z)\} \tag{2.13}$$

$$e_y = \frac{1}{E}\{\sigma_y - \nu(\sigma_x + \sigma_z)\} \tag{2.14}$$

$$e_z = \frac{1}{E}\{\sigma_z - \nu(\sigma_x + \sigma_y)\} \tag{2.15}$$

These can be rewritten into a more practical form when it comes to modelling subsidence (Fjaer et al., 2008):

$$e_h = \frac{1}{E}\{\Delta\sigma'_h - \nu(\Delta\sigma'_H + \Delta\sigma'_v)\} \quad (2.16)$$

$$e_H = \frac{1}{E}\{\Delta\sigma'_H - \nu(\Delta\sigma'_h + \Delta\sigma'_v)\} \quad (2.17)$$

$$e_v = \frac{1}{E}\{\Delta\sigma'_v - \nu(\Delta\sigma'_H + \Delta\sigma'_h)\} \quad (2.18)$$

Note that the driver for deformation is the change in effective stresses. An example calculation is provided in chapter 4.

### 2.1.4 Linear Elastic and Perfectly Plastic

Linear elasticity is a popular way to model rocks, but it assumes that deformations are not permanent. When a material undergoes permanent deformation this is called plastic deformation. Mohr-Coulomb is a linear elastic and perfectly plastic model and thus combines the two. Some exploratory modelling has been conducted using Mohr-Coulomb, but only results conducted with linear elastic modelling are shown in this report. A common mechanical analogy for linear elastic materials (Figure 12) is a spring which can be pulled and pushed without permanent deformation. The mechanical analogy for perfectly plastic materials is a rigid block resting on a surface that provides friction. As the block is fixed to the surface it can only elongate once the yield stress has been achieved. The force pulling the object needs to be increased to the point that it overcomes friction and can begin to deform the block.

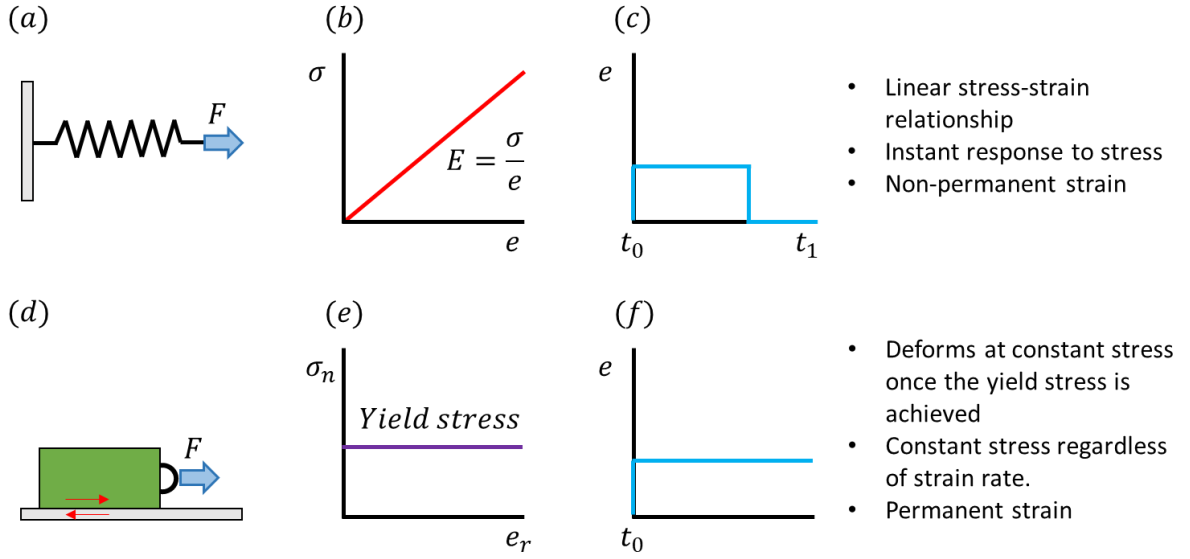


**Figure 12**: Linear elastic and perfectly plastic behaviour. After Fossen (2010). N.B. the text bulletins in the figures are direct quotes from Fossen (2010).

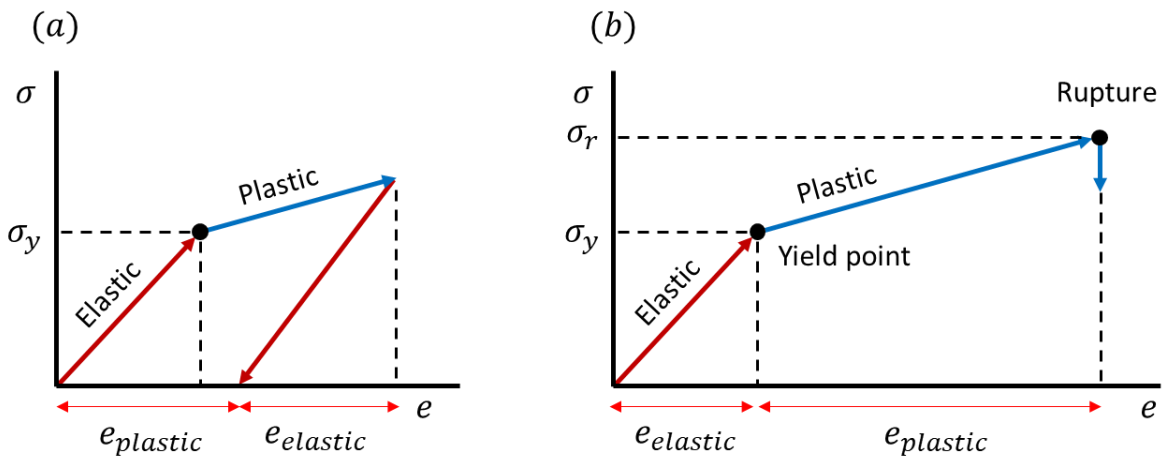


**Figure 13**: A material undergoing elastic and then plastic deformation (a). Once the stress is released the elastic strain is recovered, but the plastic strain remains. In (b) a material is loaded to breaking point. After Fossen (2010).

Figure 13 shows two different samples where both are plastically deformed, but $(b)$ is loaded to an extent that it breaks. Figure 14 shows three different types of plastic behaviour. In reality stress strains curves for material are more complex and can show (multiple) strain softening and hardening periods. A combined linear elastic and perfectly plastic model is shown in Figure 15.

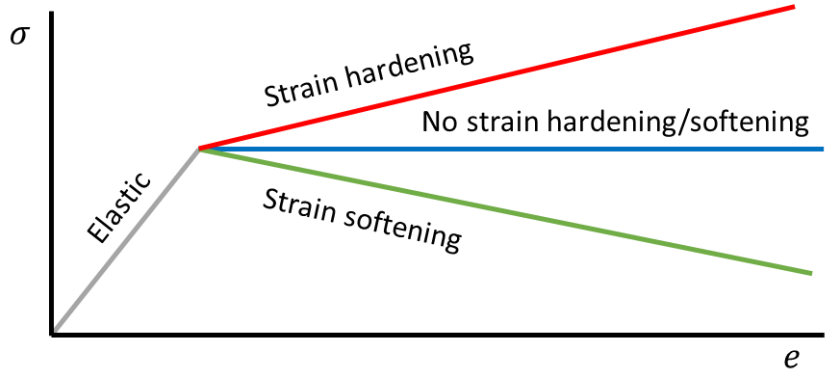


**Figure 14**: Stress-strain curves for three types of plastic behaviour. After Fossen (2010).

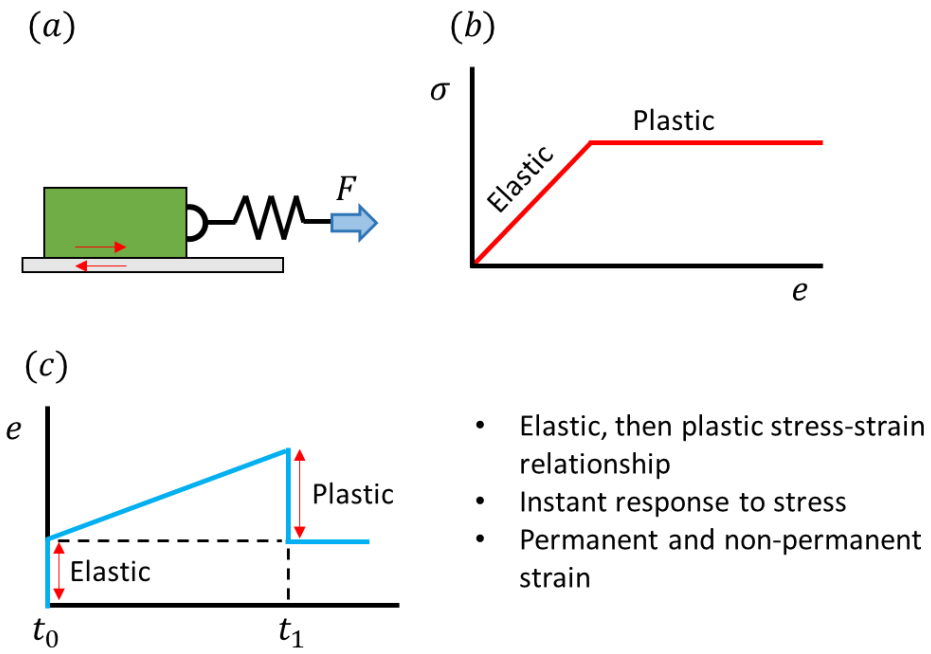


**Figure 15**: Linear elastic perfectly plastic behaviour.

### 2.1.5 Elastic Wave Theory

The Poisson's ratio can be expressed in terms of acoustic wave velocities of P-waves ($V_p$) and S-waves ($V_s$). These are compressional and shear waves respectively and are characteristics of elastic deformation. For compressional waves the deformation is parallel to the direction of wave propagation and for shear waves this is perpendicular to the wave propagation (Fossen, 2010). The Poisson's ratio can be described as follows:

$$\nu = \frac{(V_p^2 - 2V_s^2)}{2(V_p^2 - V_s^2)} \tag{2.19}$$

This allows one to use wireline log data to determine elastic properties of rock formations. It should be noted that a distinction is made between these 'dynamic' parameters and 'static' parameters that are determined through loading and crushing rock samples in a lab. This needs to be kept in mind as for the Young's modulus in particular the dynamic values are usually larger than the static values (Eissa and Kazi, 1988). When dynamic parameters are calculated the rock material is assumed to behave linear elastically, to be homogenous and isotropic. These assumptions are often the cause of the difference between dynamic and static values (McCann and Entwisle, 1992) and attempts have been made to correct for this, as can be seen in section 2.1.5.1 below. In this report the dynamic parameters are expressed as follows (Fjaer et al., 2008 and McCann and Entwisle, 1992):

$$E_{dyn} = \frac{\rho_b V_s^2 (3V_p^2 - 4V_s^2)}{(V_p^2 - V_s^2)} \tag{2.20}$$

$$\nu_{dyn} = \frac{(V_p^2 - 2V_s^2)}{2(V_p^2 - V_s^2)} \tag{2.21}$$

$$G_{dyn} = \rho_b V_s^2 \tag{2.22}$$

$$K_{dyn} = \rho_b \left(V_p^2 - \frac{4}{3} V_s^2\right) \tag{2.23}$$

### 2.1.5.1 Dynamic Young's Modulus

A number of relationships between static and dynamic Young's modulus exist in literature as can be seen below. McCann and Entwisle (1992) used a linear trend to fit their data (Eq. 2.24) and their approach was based on Eissa and Kazi (1988) who devised Eq. 2.25.

$$E_{stat} = 0.64E_{dyn} - 0.32 \quad (2.24)$$

$$E_{stat} = 0.74E_{dyn} - 0.82 \quad (2.25)$$

Research by *TNO* (van Eijs et al., 2006) states that Dutch operators use Eq. 2.18., hence this is one of the conversion techniques that is applied in this report. Eissa and Kazi (1988) state that their preferred correlation is Eq. 2.26. Which for their data set had a correlation coefficient of 0.96.

$$log_{10}E_{stat} = 0.02 + 0.77log_{10}(\rho_b E_{dyn}) \quad (2.26)$$

$$log_{10}E_{stat} = log_{10}(\rho_b E_{dyn}) - 0.55 \quad (2.27)$$

Another log-linear model (Eq. 2.27) was developed by Barree et al. (2009) which provided the best fit for their data set. The behaviour or the four models can be seen in Figure 16.

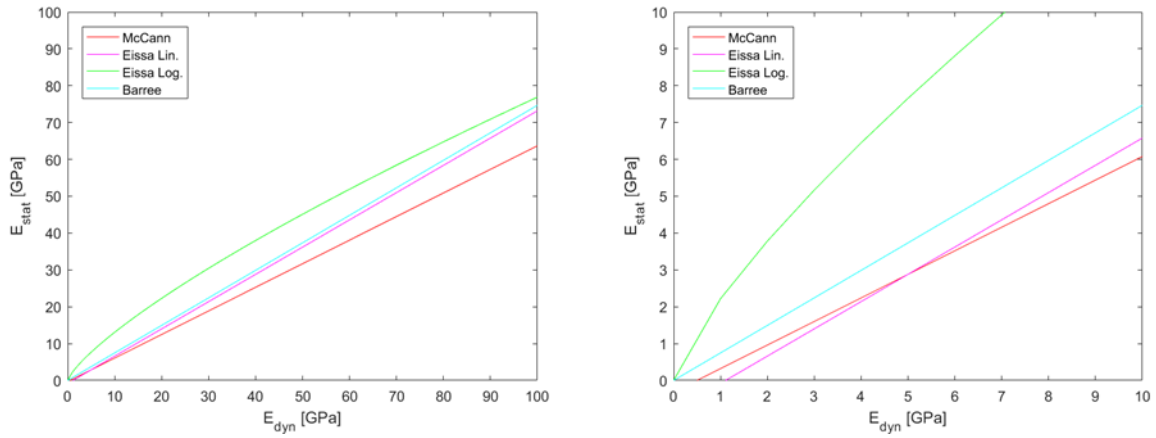


**Figure 16**: Behaviour of static Young's modulus conversion methods. Note that some models become negative for small dynamic Young's moduli. For these plots a density of 2.65 g/cc was used.

### 2.1.5.2 Dynamic Poisson's ratio

The dynamic Poisson's ratio is quite close to the static value. Depending on the imposed stress state, Barree et al. (2009) found that the static value was 93 % or 96 % of the dynamic value. However, Morales and Marcinew (1993) state: "No apparent correlation between static and dynamic Poisson's ratio was observed".

# 2.2 Subsidence

There are many types of subsidence models available and of these a number are based on the (shallow) extraction of groundwater from aquifers (Poland, 1984). They can range from extrapolating measured subsidence to coupled equations which take fluid flow and reservoir compressibility into consideration. The cause of subsidence is the compaction of the reservoir due to pressure depletion. Currently, subsidence modelling is typically conducted with either a semi-analytical model or by using coupled equations, linking fluid extraction and reservoir compaction. Most models assume that the overlying material above the reservoir is homogeneous, but some (e.g. Mehrabian and Abousleiman, 2015) incorporate multiple layers with different properties.

In section 2.2.1 a number of subsidence controlling issues are laid out. Following this the semi-analytical Geertsma (1973) model of subsidence is explained in 2.2.2. In section 2.2.3 a numerical scheme is shown which is used for subsidence calculations by the *NAM*. Multiple researchers have built upon the work by Geertsma, including Mehrabian and Abousleiman (2015). The derivation of their work assumes that the different geological layers have the same Poisson's ratio, making this unsuitable for modelling the Slochteren reservoir. The Slochteren Formation has a considerably different Poisson's ratio (≈ 0.17) from the overburden (0.20 – 0.35) but quite close to the underburden (0.20) (Lele et al., 2015) so this technique would be more suitable for different cases. A partial explanation of their model can be found in Appendix B including rewritten equations for ease of reading in Appendix C. A link between the work by Geertsma and poroelasticity is made in Appendix D as incorporating poroelasticity allows for more realistic modelling, but was not done for this study.

## 2.2.1 Controls of Subsidence

There are multiple effects and structures that influence subsidence and the most important are listed below (Gambolati et al., 2006).

- **Rock mechanical properties**: the physical properties of a rock define how it will behave in certain settings. Linear elastic, non-linear elastic, elasto-plastic, visco-elasto-plastic are some common ways of modelling rocks. Each type requires input parameters and generally more of them as models become more complex. Whilst simple, linear, models are popular they might not be representative due to the fact that rocks often do not behave linearly and are not homogeneous and isotropic (Fjaer et al., 2008).
- **Hysteresis of rock mechanics**: over hundreds of millions of years rocks will undergo a variety of processes such as burial, folding and uplift. Each affects the properties of a rock, often permanently, which is 'remembered'.
- **Geo-mechanical anisotropy**: rocks are often inherently anisotropic due to the way they are deposited. For instance laminations of different grainsizes in a fluvial sandstone or different cementation zones.
- **Preconsolidation effect**: there is a sudden increase in rock compressibility at some stage during the field development. This is very hard to determine.
- **Underconsolidation**: in over-pressurised reservoirs (e.g. Gulf of Mexico) the reservoir material can be under consolidated and hence relatively weak.

- **Lateral/bottom aquifer**: aquifer influx, or the lack thereof, will help determine the pressure system in the reservoir. For the Groningen field the aquifer influx is low (Geertsma, 1973), meaning that the large amount of pressure depletion will not be recovered for some time.
- **Faults**: their number, size orientation and (re)activation. Faults may make predictions more complicated as they often compartmentalise a reservoir, leading to uneven pressure depletion.

It is important to keep this in mind as all models are a simplification of reality. As will be seen in the coming pages, some models emphasise the effect of one particular parameter such as the rock mechanical properties and exclude everything else. Ultimately one would like to take all of these into account, however for this study the focus will be on linear elastic behaviour and the effect of the required elastic moduli for modelling this type of behaviour.

### 2.2.2 Geertsma Model

The underlying cause of subsidence is the compaction of the reservoir and thus the focus of available research and parameters is on the reservoir interval (NAM, 2016). When assuming that a reservoir is laterally extensive compared its height, then most of the deformation is in the vertical plane. Due to this the compaction in the formation can be represented by vertical strain $e_z$ (Geertsma, 1973) with a reservoir height of $h$:

$$e_z = \frac{dz}{z} = \frac{\Delta h}{h} \tag{2.28}$$

From chapter 2 it is known that the vertical strain is the change in reservoir thickness with respect to the original thickness prior to depletion. Reducing the reservoir pressure $p$ reduces the pore pressure which in turn increases the effective stress acting on the reservoir. Then a so called *uniaxial compaction coefficient* can be described which represents the reservoir compaction per unit of pore pressure reduction (Geertsma, 1973):

$$c_m = \frac{1}{z}\frac{dp}{dz}, \text{ and} \tag{2.29}$$

$$e_z = c_m dp \tag{2.30}$$

The total reduction in reservoir thickness, or height, is then expressed as:

$$\Delta h = c_m \Delta p h \tag{2.31}$$

Which is also known as compaction. Whilst strictly speaking the compaction coefficient is a function of effective stress, and thus $p$, it can be assumed to be constant throughout the pressure range of reservoir depletion. Geertsma (1973) had thus identified three different parameters that influence compaction and therefore subsidence. He concludes that, a thick and unconsolidated reservoir undergoing a large pressure drop will cause significant subsidence.

The model that worked in predicting subsidence was the so-called nucleus-of-strain concept developed by Mindlin and Cheng (1950). This resulted in the following descriptions for surface deformation (Geertsma, 1973) which can be seen below, where Eq. 2.32 is a solution for vertical displacement and Eq. 2.33 a solution for horizontal displacement.

$$u_z(r,0) = -\frac{1}{\pi} c_m (1-\nu) \frac{D}{(r^2+D^2)^{3/2}} \Delta p V \tag{2.32}$$

$$u_r(r,0) = +\frac{1}{\pi} c_m (1-\nu) \frac{r}{(r^2+D^2)^{3/2}} \Delta pV \tag{2.33}$$

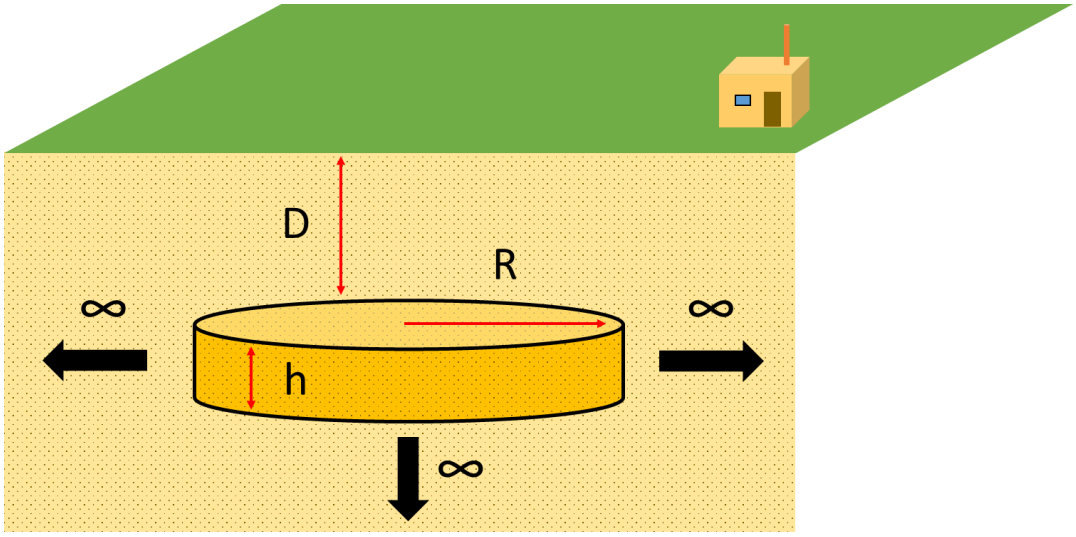


**Figure 17**: A cylindrical reservoir undergoing compaction in a semi-infinite half space.

Subsequently Geertsma (1973) integrated the nucleus-of-strain solution over the entire volume of a disc-shaped reservoir. The assumptions for this are that there is an isolated porous or non-porous elastically deforming half space (Figure 17) with a traction free surface and that the reservoir and the surrounding rock are homogeneous in their deformation behaviour (i.e. $c_m$ and $\nu$ are constant). This then leads to the following integrals:

$$u_z(r,0) = -2c_m(1-\nu)\Delta phR \int_0^\infty e^{-D\alpha} J_1(\alpha R) J_0(\alpha r) d\alpha \tag{2.34}$$

$$u_r(r,0) = +2c_m(1-\nu)\Delta phR \int_0^\infty e^{-D\alpha} J_1(\alpha R) J_1(\alpha r) d\alpha \tag{2.35}$$

These are semi-infinite integrals including Bessel functions and are known as Hankel-Lipschitz integrals (Geertsma, 1973). Numerical solutions have been tabulated by Easson et al. (1955) and when dimensionless parameters of reservoir thickness and reservoir depth are introduced then these can rewritten as:

$$\rho = \frac{r}{R} \tag{2.36}$$

$$\eta = \frac{D}{R} \tag{2.37}$$

$$u_z(r,0) = -2c_m(1-\nu)\Delta phA(\rho,\eta) \tag{2.38}$$

$$u_r(r,0) = +2c_m(1-\nu)\Delta phB(\rho,\eta) \tag{2.39}$$

The tabulated values for A and B can be found in either Geertsma (1973) or Easson et al. (1955). Finally a solution for vertical displacement above the centre of the reservoir is given by:

$$u_z(0,0) = -2c_m(1-\nu)\Delta ph\left(1 - \frac{\eta}{\sqrt{1+\eta^2}}\right) \tag{2.40}$$

Previously in this chapter compaction has been stated to be equal to $c_m \Delta ph$. When using Eq. 2.38 this means that:

$$\frac{Vertical\ surface\ displacement\ (subsidence)}{Compaction} = -2(1-\nu)A \tag{2.41}$$

$$\frac{Horizontal\ surface\ displacement}{Compaction} = +2(1-\nu)B \qquad (2.42)$$

Hence for the Geertsma solution, vertical and horizontal surface displacement depend on the location from, the depth and lateral extent of the reservoir (Figure 18). It should be noted that for the Geertsma (1973) solution the subsidence can actually exceed subsidence. For very laterally extensive reservoirs the maximum ratio is $2(1-\nu)$, where theoretically it could be twice as large as the compaction.

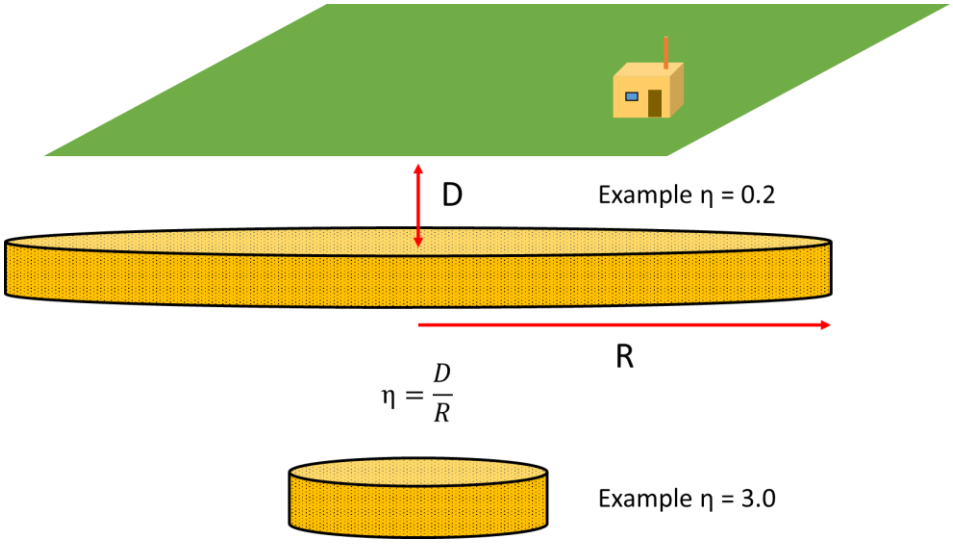


**Figure 18**: Two reservoirs that have a different dimensionless parameter and thus subsidence bowls. After Poland (1984).

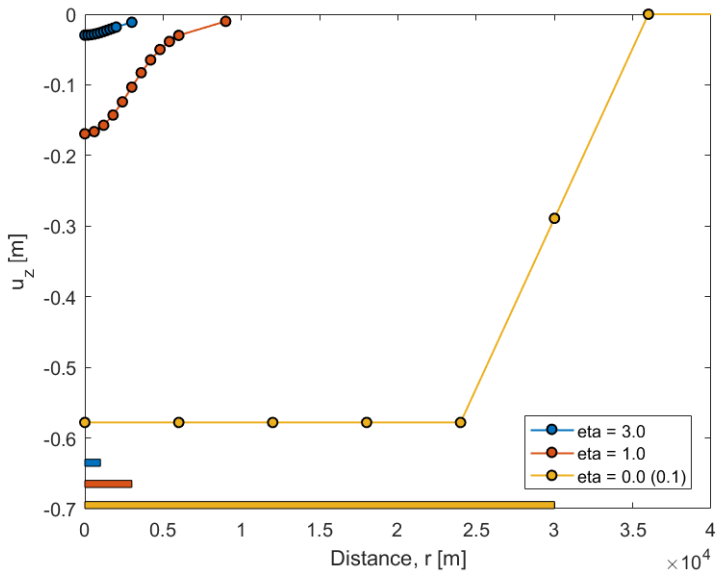


**Figure 19**: Geertsma (1973) solutions for different eta (D/R) values. The reservoirs are at a depth of 3000 m, but each has a different radius indicated by the relevant rectangle. Note that a very small eta value is represented by a D/R ratio of 0.1.

Figure 19 shows different subsidence results for three different reservoirs at a constant depth of 3000 m. For very laterally extensive reservoirs a large part of the subsidence bowl is only dependent on the amount of compaction of the reservoir rock and the Poisson's ratio. This should be kept in mind for the results part of chapter 4.

## 2.2.3 Geertsma and van Opstal Numerical Model

Geertsma and van Opstal (1973) developed a numerical formulation for subsidence above a compacting reservoir. As with the semi-analytical model, the numerical version (Figure 20) is based on the nucleus-of-strain concept and is only applicable in a homogeneous medium (Geertsma and van Opstal, 1973). A volume integral version of Eq. 3.5 over a block-sized reservoir element with dimensions $l_{xn}$, $l_{yn}$ and $l_{zn}$ becomes (Burkitov et al., 2016):

$$u_z(x,y,0) = \frac{1-\nu}{\pi}\sum_{n=1}^{N} c_{m,n}\Delta p_n \frac{L_{zn} l_{xn} l_{yn} l_{zn}}{\left[(x-L_{xn})^2+(y-L_{yn})^2+L_{zn}^2\right]^{\frac{3}{2}}} \qquad (2.43)$$

Where:

$u_z(x,y,0)$: vertical displacement or subsidence at the surface [m]
$x, y$: surface coordinates [m]
$\nu$: Poisson's ratio [-]
$c_{m,n}$: uniaxial compaction coefficient [bar$^{-1}$]
$\Delta p_n$: pressure change in each reservoir grid block [bar]
$L_{zn}$: depth of the reservoir grid block [m]
$L_{xn}, L_{yn}$: distances in the $x$ and $y$ directions respectively from the surface location to the reservoir grid block [m]
$l_{xn}, l_{yn}, l_{zn}$: dimensions of a reservoir grid block, where the product of these equals to a grid block volume [m]

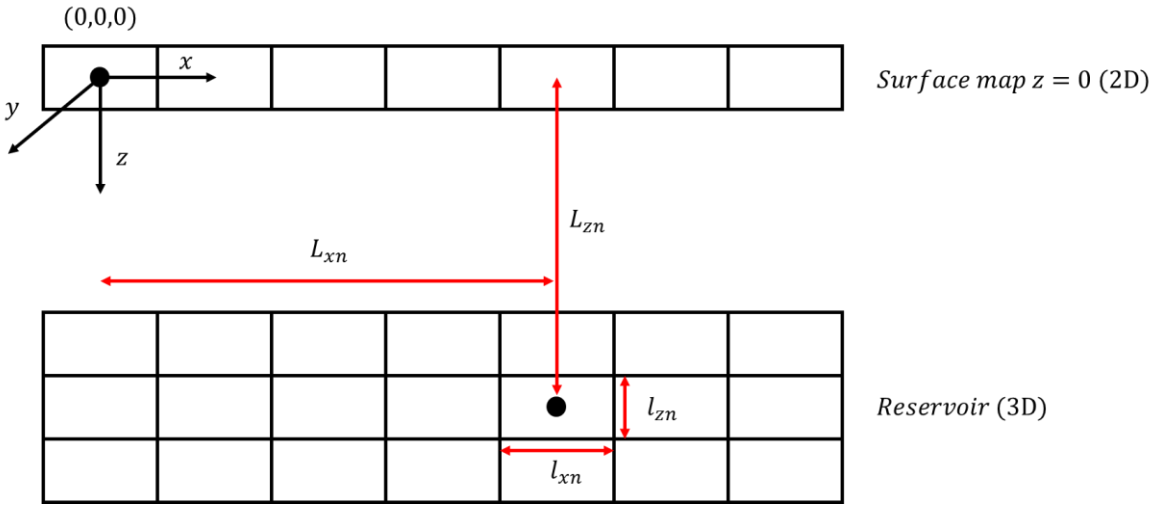


**Figure 20**: Illustration for the numerical subsidence model. After (NAM: Burkitov et al., 2016).

It can be seen from Eq. (2.43) that each reservoir grid block contributes to each surface grid block (Burkitov et al., 2016). Additionally the equations for horizontal displacement are (Geertsma and van Opstal, 1973):

$$u_x(x,y,0) = \frac{1-\nu}{\pi}\sum_{n=1}^{N} c_{m,n}\Delta p_n \frac{(x-L_{xn}) l_{xn} l_{yn} l_{zn}}{\left[(x-L_{xn})^2+(y-L_{yn})^2+L_{zn}^2\right]^{\frac{3}{2}}} \qquad (2.44)$$

$$u_y(x,y,0) = \frac{1-\nu}{\pi}\sum_{n=1}^{N} c_{m,n}\Delta p_n \frac{(y-L_{yn})l_{xn}l_{yn}l_{zn}}{\left[(x-L_{xn})^2+(y-L_{yn})^2+L_{zn}^2\right]^{\frac{3}{2}}} \qquad (2.45)$$

It should be noted that the *NAM* (Burkitov et al., 2016) uses a slightly different notation as the uniaxial compaction coefficient is not a constant, but also a unique grid cell property as with the reservoir pressure drop. Comparing Burkitov et al. (2016) to Geertsma and van Opstal (1973) it is clear that there is a typo in the original work of Geertsma and van Opstal, where for the horizontal displacement in the $x$-direction the power of the denominator in Eq. was $\frac{2}{2}$ instead of $\frac{3}{2}$.

# 2.3 The Dutch Subsurface

The Dutch subsurface is relatively well understood and an interested reader is referred to the book *Geology of the Netherlands* (Wong et al., 2007). There is a large amount of publically available data via the websites *DINOloket* (www-8) and *NLOG*. (www-9) However, most of this knowledge is concentrated on the shallow subsurface (10s of metres) and around reservoir level (2-3 kilometres), whilst interest in the Dutch overburden has increased recently (Kruiver et al., 2017). Work by Kroon et al. (2009) shows that at the very least a separation needs to be made between deep (e.g. hydrocarbon extraction) and shallow (e.g. aquifer production). This section provides a brief summary of the current knowledge of the Dutch subsurface, particularly relating to existing geological models and elastic moduli for modelling.

In section 2.3.1 the geological units of the Dutch subsurface are introduced as these nomenclatures will be used further in this report. Section 2.3.2 discusses the current knowledge of the Dutch subsurface in terms of existing subsurface models that are publically available on the *DINOloket* website. In section 2.3.3 the publically available elastic parameters are discussed. In section 2.3.4 the uniaxial compaction coefficient is discussed as it forms a fundamental part of subsidence modelling. Finally, section 2.3.5 summarises what has been discussed in the chapter and a case is made for expanding the existing knowledge through well data analysis.

## 2.3.1 Dutch Stratigraphy

In the following chapters there will be widespread use of geological units in the Dutch subsurface. The group names are of particular interest. Figure 21, on the next page, shows a graph representing a canonical stratigraphy of the Dutch subsurface form the website *DINOloket*. The nomenclature that will be used throughout this report can be found under the lithostratigraphy column. It should be noted that there is a considerable amount of variability in the subsurface as entire units were either not deposited or have eroded over time. For instance, the entire Jurassic is not present above the Groningen field.

Figure 22 shows a north-south cross section of the Groningen field. The grey layers form the Limburg Group (Carboniferous) which is the source rock that produced the gas in the Groningen field (Wong et al., 2007). The burgundy red is the Upper Rotliegend Group and it consists of the Slochteren Formation, which is the reservoir rock, and the Silverpit Formation which acts in part as a seal for the reservoir. The dark pink is the Zechstein Group which forms the main seal of the Groningen gas field. The light pink represents the Upper Germanic Triassic Group and the Lower Germanic Triassic Group. As can be seen the thickness varies throughout the area. There is a relatively thin layer of the Rijnland Group (dark green), which is overlain by the Chalk Group (light green). The red and yellow layers are the Upper North Sea Group and Lower North Sea Group respectively. These sediments were deposited during the Cenozoic and are poorly consolidated compared to the other groups.

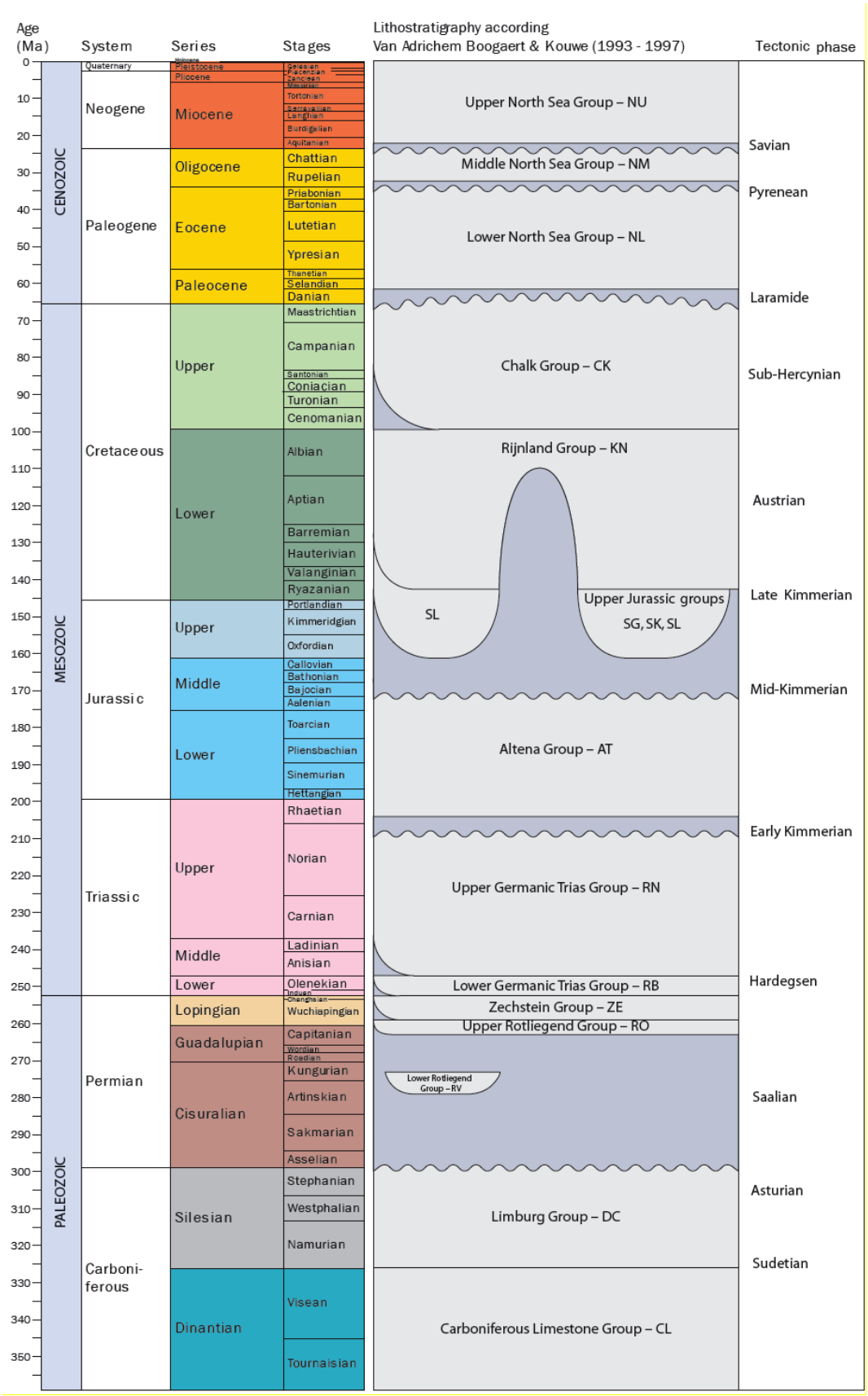


**Figure 21**: Stratigraphy of the Dutch subsurface. From DINOloket (www-10).

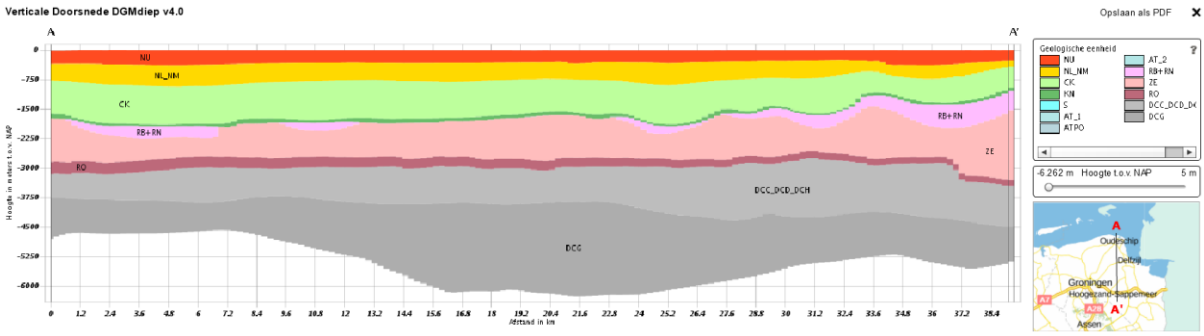


**Figure 22**: North-south cross section of the Groningen field. Note the change of thickness of the Triassic groups (RB+RN).

## 2.3.1 Geological Models

The knowledge of the Dutch subsurface is considered to be good when compared to other nations however, most of the knowledge is confined to the very near surface (10s of metres) and at reservoir depth (around 2-3 kilometres). On the *DINOloket* website there are 4 publicly available models and for this study DGM-Diep is of the greatest interest due to its (large) scale and the fact that there will not be fluid flow modelling in this Master thesis.

### 2.3.1.1 *DGM* (Digitaal Geologisch Model)

*DGM* is a regional scale layered model that goes down to a depth of around 500 m. This part of the Dutch subsurface consists mostly of unconsolidated sediments such as sand, clay and peat. The layers are subdivided, based on lithology and other characteristics, into different litho-stratigraphic units (Figure 23). The model incorporates the mainland of the Netherlands and does not extend into the Dutch part of the continental shelf (www-11). The *DINOloket* database consists of approximately 430,000 (shallow) drilling surveys of which 26,500 well described ones were used to build this model. The drilling measurements have been subdivided into the litho-stratigraphic units. The *DGM* forms the basis for another subsurface model called *REGIS II*. It should be noted that *DGM* is a regional scale model and thus it is not suitable for accurate local modelling. Another model, *GeoTOP*, would be more suitable (www-12) for this purpose and a description of it can be found at (www-12), but this model goes too shallow for the interest of this thesis.

These lithostratigraphic units are described in terms of grainsize range, mineral content (varies), colour and whether they contain other notable objects such as shells. PDF files containing this information can be downloaded from *DINOloket*. It is important to note that these PDF files do not contain geomechanical parameters of the respective layers so these will have to be determined.

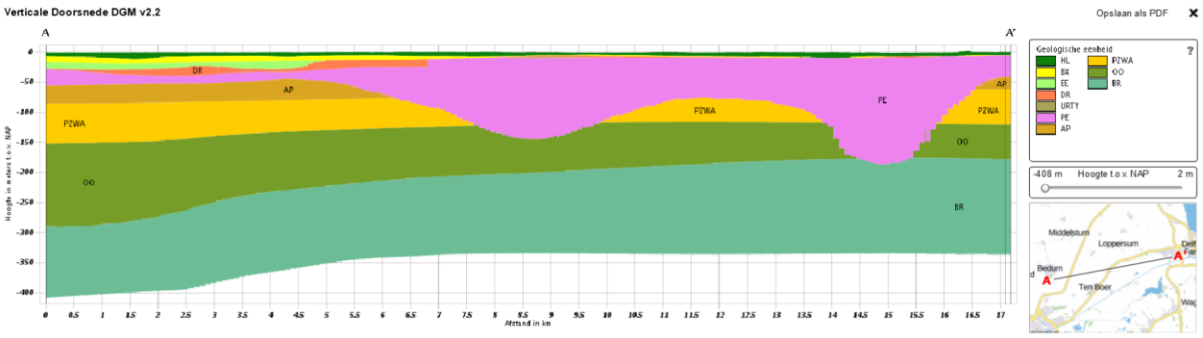


**Figure 23**: Example of DGM between Bedum and Delfzijl in the Groningen area. The different colours denote different geological units of the Dutch Cenozoic.

### 2.3.1.2 *DGM-Diep*

The *DINOloket* database consists of more than 135 3D seismic surveys which cover an area of 99,900 km$^2$ (the Netherlands is 41,543 km$^2$) and 577,000 km of 2D seismic lines. There are 5800 confidential wells. All the publicly available 3D surveys and 1305 wells were used to create the subsurface model. 2D surveys were used where 3D surveys were not available. The used wells and seismic data can be found on *NLOG* (www-13).

As with *DGM*, this model is on a regional scale and is not suitable for reservoir scale modelling. This model does cover 3 miles offshore of the Netherlands. An example is shown below (Figure 24) around the city of Utrecht.

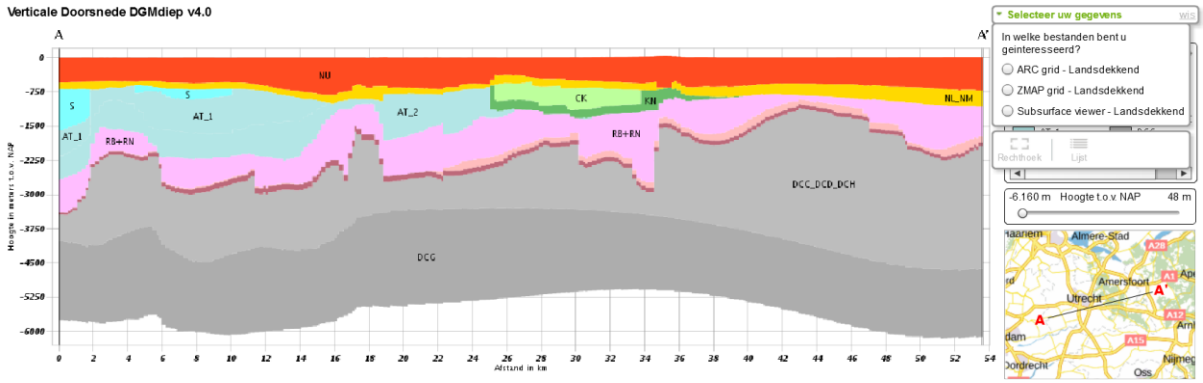


**Figure 24**: Example of DGM-Diep around the city of Utrecht. Red and orange: Tertiary. Green: Cretaceous. Blue: Jurassic. Pink: Triassic. Red-pink: Permian (Zechstein). Burgundy: Permian (Rotliegend). Grey: Carboniferous. Note the widespread erosion of the Jurassic and Cretaceous.

### 2.3.1.3 *Regis II*

*Regis II* is a hydrogeological model and consists of permeable and impermeable layers. The model contains hydrogeological layers which have more or less the same hydraulic properties. These layers are either the same or form part of the layers in *DGM*. The horizontal resolution is 100 m by 100 m. Because *Regis II* is based on *DGM*, the same size and resolution constraints are applicable to this model. This model will not be used for further research as water flow is not the topic of this thesis.

### 2.3.1.4 *GeoTOP*

*GeoTOP* is a more detailed model of the subsurface reaching to a maximum depth of 50 m (with respect to the NAP). The voxel resolution of *GeoTOP* is 100 m by 100 m by 0.5 m. Not all parts of the country are covered by this model. As an example to map the province of Zuid-Holland, 50,000 drilling measurements were used. By oil industry standards this is a very fine scale model, but for this study

is not suitable as it is constrained to the near surface. If one were to look at near surface reasons for subsidence, then this could be a useful tool for that purpose.

### 2.3.3 Elastic Parameters

At present there are a few sources that provide numbers on elastic parameters of the Dutch subsurface. A large part of this knowledge appears to be limited to research performed by the *NAM* and it is not traceable in public literature how the values of the overburden units were determined as for example Lele et al. (2015) does not elaborate on this. The values of two *NAM* reports are shown in Table 1 below. The data from the 2015 report served a different purpose than the values shown from the 2013 report, the latter was explicitly used to model subsidence and the former fault (re)activation. The values from the 2015 report will form the benchmark for this study.

**Table 1**: Geomechanical parameters for the Groningen Field formations (Lele et al., 2015; NAM, 2013). Values in brackets are from the 2013 Technical Addendum to the Winningsplan. *In the 2013 source, Rijnland and Triassic are modelled together as Lower Cretaceous/Triassic. **Judging by the parameters the Anhydrite was not modelled in the 2013 report. Differences between the two sources are marked in red.

| Unit | | E [GPa] | ν [-] | ρ [kg/m$^3$] |
|---|---|---|---|---|
| North Sea | | 2 (2) | 0.30 (0.30) | 2150 (2150) |
| Chalk | | 10 (10) | 0.25 (0.25) | 2350 (2350) |
| Rijnland* | | 16 (16) | 0.25 (0.25) | 2350 (2300) |
| Triassic* | | 16 (16) | 0.25 (0.25) | 2350 (2300) |
| Zechstein** | Halite | 30 (30) | 0.35 (0.35) | 2100 (2200) |
| | Anhydrite | 70 (n/a) | 0.25 (n/a) | 2900 (n/a) |
| Ten Boer | | 40 (40) | 0.20 (0.20) | 2300 (2300) |
| Slochteren | Heterolithic | Por. (1-40) | Por. (0.2) | Por. (2300) |
| | Reservoir | Por. (1-40) | Por. (0.2) | Por. (2300) |
| Carboniferous | | 40 (40) | 0.20 (0.20) | 2300 (2300) |

It is explicitly stated in (Lele et al., 2015) that the parameters for the Slochteren heterolithic and reservoir units were obtained via core data. The data for the Slochteren unit was estimated based on trend lines within graphs of the core data. As the exact data points were not available, four points were estimated on each trend line which were then used to create approximate trend lines. The values of the four points for each graph can be viewed in Table 2. These led to the following equations: Young's modulus Eq. 2.46, Poisson's ratio Eq. 2.47, density Eq. 2.48 and the Biot coefficient Eq.2.49 Graphs for these relationships can be found in Appendix D.

**Table 2**: Data point positions for geomechanical parameters of the Slochteren unit graphs and trendlines. Porosity is the controlling parameter.

| Porosity [-] | Young's Modulus [GPa] | Poisson's Ratio [-] | Density [kg/m$^3$] | Biot coef. [-] |
|---|---|---|---|---|
| 0.10 | 20.0 | 0.14 | 2.50 | 0.75 |
| 0.15 | 13.7 | 0.15 | 2.39 | 0.83 |
| 0.20 | 9.3 | 0.17 | 2.28 | 0.88 |
| 0.25 | 6.7 | 0.18 | 2.19 | 0.91 |

$$E = 41.27e^{-7.34\varphi} \quad (2.46)$$

$$\nu = 0.28\varphi + 0.11 \quad (2.47)$$

$$\rho = -2.08\varphi + 2.70 \quad (2.48)$$

$$\alpha = 0.67e^{1.28\varphi} \quad (2.49)$$

Table 3 and 4 show elastic moduli that were used by Orlic (2016) for geomechanical modelling of two different reservoirs in the Netherlands. As can be seen a distinction is made between the Upper and Lower North Sea Group. Table 3 is geologically more detailed as for the Rijnland Group there are parameters for specific members. Whilst Table 4 is more akin to the group scale values used by the *NAM*, there are some significant differences between the tables which allows for the studying of different values for the same geological units and the effect of this.

**Table 3**: Material properties used by Orlic (2016) for modelling the De Lier gas field. It is only stated that these parameters come from multiple sources. The Ommelanden Formation is part of the Chalk Group and is marked by (C). Units that are part of the Rijnland Group are marked by (R).

| Unit | E [GPa] | ν [-] | ρ [kg/m$^3$] |
|---|---|---|---|
| North Sea Group | 0.25 | 0.38 | 1960 |
| Ommelanden chalk (C) | 10 | 0.18 | 2300 |
| Upper Holland marl (R) | 5.5 | 0.26 | 2300 |
| Middle Holland claystone (R) | 5.5 | 0.26 | 2300 |
| Greensand (R) | 4.5 | 0.20 | 2300 |
| Lower Holland marl (R) | 5.5 | 0.24 | 2300 |
| De Lier sand (R) | 10.5 | 0.19 | 2300 |
| Vlieland claystone (R) | 5.5 | 0.23 | 2300 |
| Rijswijk sandstone (R) | 15 | 0.23 | 2300 |

**Table 4**: Material properties used by Orlic (2016) for modelling the P18-04 gas field.

| Unit | E [GPa] | ν [-] | ρ [kg/m$^3$] |
|---|---|---|---|
| Upper North Sea Group | 0.5 | 0.30 | 1960 |
| Lower North Sea Group | 5 | 0.30 | 2600 |
| Chalk | 20 | 0.17 | 2300 |
| Rijnland | 17 | 0.30 | 2650 |
| Schieland | 13 | 0.30 | 2100 |
| Altena | 15 | 0.30 | 2600 |
| Upper Germanic Trias | 26 | 0.30 | 2600 |
| Detfurth, Hardegsen | 20 | 0.20 | 2600 |
| Volpriehausen | 25 | 0.20 | 2600 |
| Lower Germanic Trias | 29 | 0.30 | 2600 |
| Zechstein | 20 | 0.35 | 2100 |
| Carboniferous | 30 | 0.25 | 2650 |

### 2.3.4 Uniaxial compaction coefficient

The *NAM* has developed a porosity based relationship, based on core data, (Eq. 2.50) for the uniaxial compaction coefficient (NAM et al., 2016):

$$c_m = 267.3\varphi^3 - 68.72\varphi^2 + 9.85\varphi + 0.21 \quad (2.50)$$

From Appendix D we know that the uniaxial compaction coefficient can be described in terms of Young's modulus and Poisson's ratio. A comparison is made between the compaction coefficient determined directly (Eq. 2.50) or indirectly via the elastic moduli of Eq. 2.46 and Eq. 2.47. The results can be seen below in Figure 25. The difference between the two is very large. Using the polynomial would lead to values roughly one order of magnitude larger than when using the Young's modulus and Poisson's ratio. Considering that for Geertsma type subsidence modelling the subsidence is linearly dependent on compaction this would result in a very large difference. The uniaxial compaction coefficient is not actually used in *Plaxis*, as this is essentially replaced by the Young's modulus.

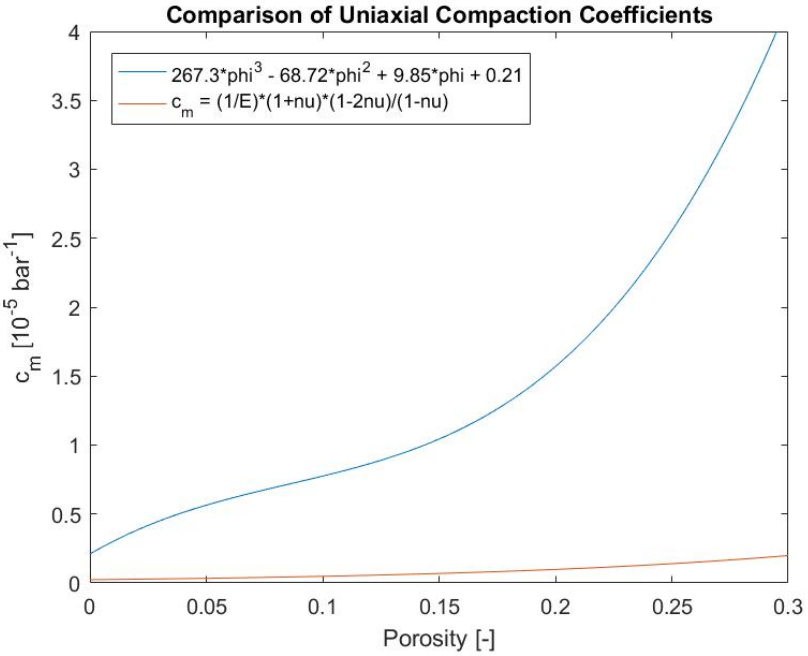


**Figure 25**: Comparison between two differently determined uniaxial compaction coefficients.

# 3

# Elastic Parameters from Well Data

To gain a better understanding of the Dutch overburden, multiple wells have been analysed and the results are displayed in this chapter. From this well data one can obtain elastic parameters such as the Poisson's ratio and Young's modulus which are then compared to existing data from chapter 2. As stated previously, current literature does not describe how the obtained values were acquired. The purpose of this well analysis is to shine a light on this issue and find potentially interesting phenomena. The two research questions are:

- *How do the literature values of elastic parameters compare to those determined in this thesis?*
- *Can lithological links within the elastic parameters be discerned through the use of the gamma ray and neutron porosity logs?*

Chapters 3, 4 and 5 are split into three parts: method, results and discussion due to the large amount of results. The first part in this chapter (3.1) gives a brief description on how the data was obtained and processed. The results can be found in the second part (3.2) and are discussed in the third and final (3.3) part of this chapter.

## 3.1 Method

In this part the methodology for obtaining the well data is explained. Section 3.1.1 briefly describes how the data is obtained and gives an overview of the publically available shear wave acoustic data. Section 3.1.2 details the workflow that was applied to find suitable wells. Some core data was also used and is described in section 3.1.3.

### 3.1.1 Data Acquisition and Processing

As of 03-10-2017 there are 6429 wells on *NLOG* of which 163 are supposed to contain shear wave acoustic data. One can simply find the available wells on *NLOG* and download the desired files. Section 3.1.2 will explain why it is not always the case that this data is usable or even present.

An underlying issue with this study is that there is simply too much data to go through for one individual in the considered time span. Only a few files per well were deemed necessary and the remaining have been ignored. The majority of wells have tens of LAS files and it would be too time consuming to go through all of them. Furthermore, only LAS files were studied as LIS files cannot be

opened in *Excel* or *Notepad*. LIS files contain much more information than LAS files in particular regarding to resolution.

There was a multitude of reasons why some wells could not be analysed. The most common have been listed below. A further issue that limits the use of data is that sometimes the density and acoustic logs were not taken at the same time, but more importantly, at different depth intervals. This further reduces the nett interval that can be analysed.

- **Zeros**. In many files the acoustic (shear wave and/or compressional) data consisted of zeros. Hence these wells could not be used.
- **No LAS file**. Whilst a well might contain acoustic wireline data it would not have bulk density data. These wells were discarded. In a few cases there was no LAS file for acoustic data.

Many wells contain potentially useful data, but need to be adjusted for further analysis. The two issues are described below:

- **Poor stacking**. In many files the data is poorly stacked for use in *Excel*. The data points were repositioned in *Matlab* and then reimported into *Excel*. An example m-file is shown in Appendix F.
- **Discrepancy in resolution**. For many wells the only log that contains bulk density values is the composite log constructed by *TNO*. The resolution of the composite log is per decimetre, which means that it cannot be used for a one to one comparison with logs that were measured with a resolution of per half foot. Usually the well measured in decimetres was decimated to ensure that the measured intervals were the same. This procedure involved rounding values, which means that the corresponding measurements linked to a certain depth were not precisely measured at that location. The discrepancy is in the centimetres. An example m-file is shown in Appendix G which was used to remove duplicate values.

Based on the data usability, logs are either kept or discarded. Figure 26 shows the overview of usable wells and the process that was undertaken to acquire usable data can be seen in Figure 27. Once a well is deemed suitable the elastic moduli were calculated using equations from section 2.5. For this report the focus is on the wells that were (immediately) usable and, due to time constraint, the rectified wells are not further discussed. Hence there is still a group of wells which probably contain useful information that can still be used in a future study.

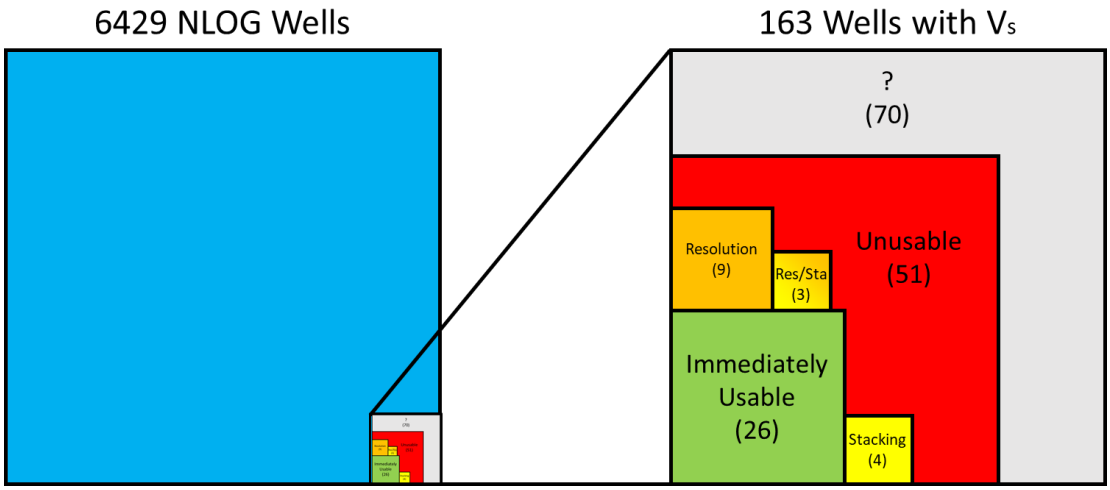


**Figure 26**: Overview of number of suitable wells on 03-10-2017. Note that there is an overlap between wells with stacking and resolution issues.

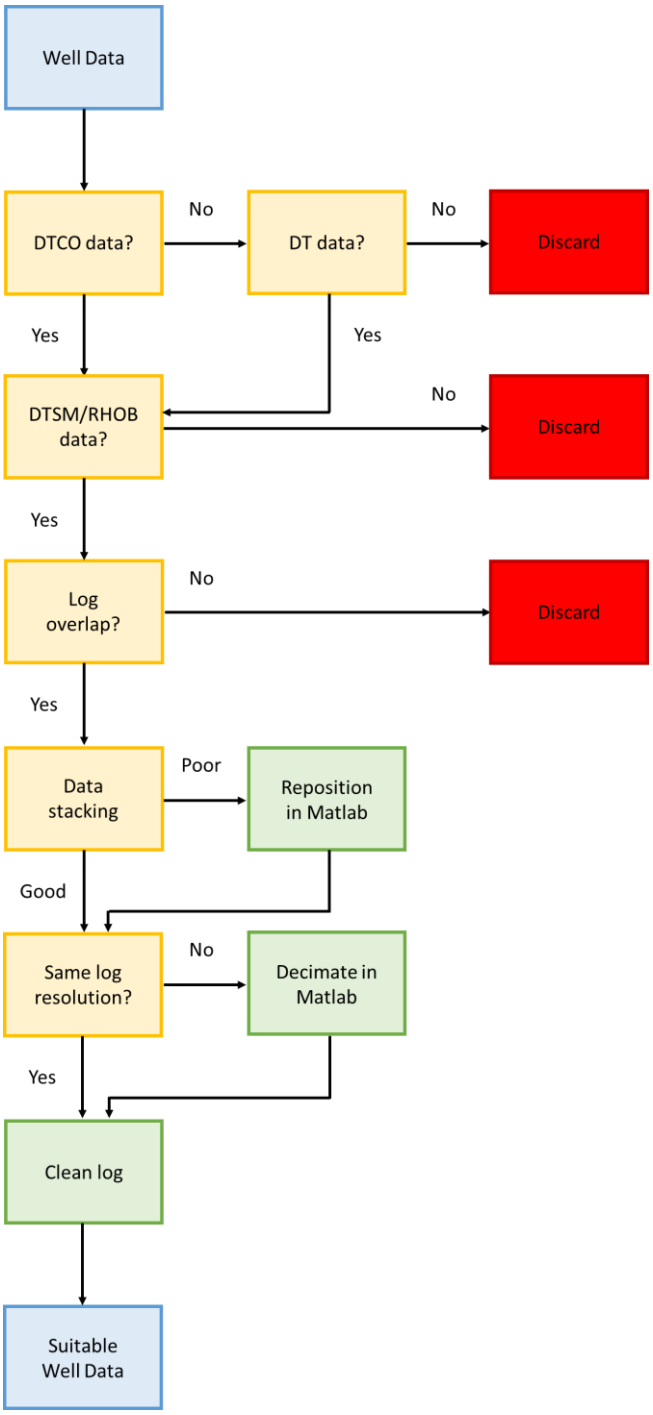


**Figure 27**: Flow chart showing the undertaken steps to acquire suitable well data. Cleaning refers to removing obvious measurement errors such as constant and negative values.

Figure 26 shows number of wells with data issues. As can be seen, from the 93 analysed wells, only 26 were immediately usable. A total of 27 wells are deemed to be the best for calculating elastic moduli. This is mainly based on the length of the logged interval. This leaves a total of 15 potential well that could still be looked at in a future study. It might be beneficial to use a program where one can determine the desired resolution of all the logs manually, rather than adjusting them through a decimation procedure.

**Table 5**: List of wells with suitable acoustic data. The wells marked in green are considered to be the most interesting for further study and are addressed in the results section. Core data marked in yellow indicates that the acoustic and core data do not overlap. The acoustic interval is the nett usable interval after cleaning the logs.

| Well | Acoustic Interval [m] | Reservoir Fill | Core data |
|---|---|---|---|
| A15-02 | 385 | Gas shows | No |
| ANN-05 | 150 | Gas | No |
| B13-04 | 588 | Dry | No |
| B16-01 | 871 | Gas | No |
| BIR-13 | 760 | Gas | Yes |
| CAP-01 | 744 | Oil shows | Yes |
| COV-40 | 269 | Gas | No |
| F02-07 | 648 | Oil shows | No |
| F10-03 | 114 | Dry | No |
| G14-02 | 57 | Dry | No |
| GRL-01 | 950 | Gas | Yes |
| J06-04 | 475 | Gas | No |
| K04-A-04 | 147 | Gas | Yes |
| K06-D-02 | 704 | Gas | No |
| K11-14 | 266 | Dry | Yes |
| K12-B-08-S1 | 328 | Gas | No |
| L03-02 | 391 | Dry | No |
| L04-06 | 194 | Gas | Yes |
| L05-06 | 427 | Dry | No |
| L06-01 | 284 | Dry | No |
| L09-06-S1 | 334 | Gas | Yes |
| P08-06 | 616 | Dry | No |
| P15-14 | 1110 | Gas | Yes |
| PRW-01 | 1050 | Oil/Gas | Yes |
| Q04-C-01 | 399 | Gas | Yes |
| Q11-03 | 538 | Dry | Yes |
| WBMS-01 | 901 | Gas | Yes |

Table 5 shows the 27 wells with the pore fill of the target and whether it is used for the results in the next part of the chapter. As can be seen from the table the majority of wells are offshore. However, the presence of natural gas reduces the bulk density, when compared to a water fill, and therefore dynamic Young's modulus. The dynamic Poisson's ratio will also be distorted by gas fill. It is also of interest to try and find lithological relationships with the elastic moduli, hence the gamma ray and neutron porosity logs were also used. With reasons similar to stated previously, a number of the 27 wells cannot be used in this manner.

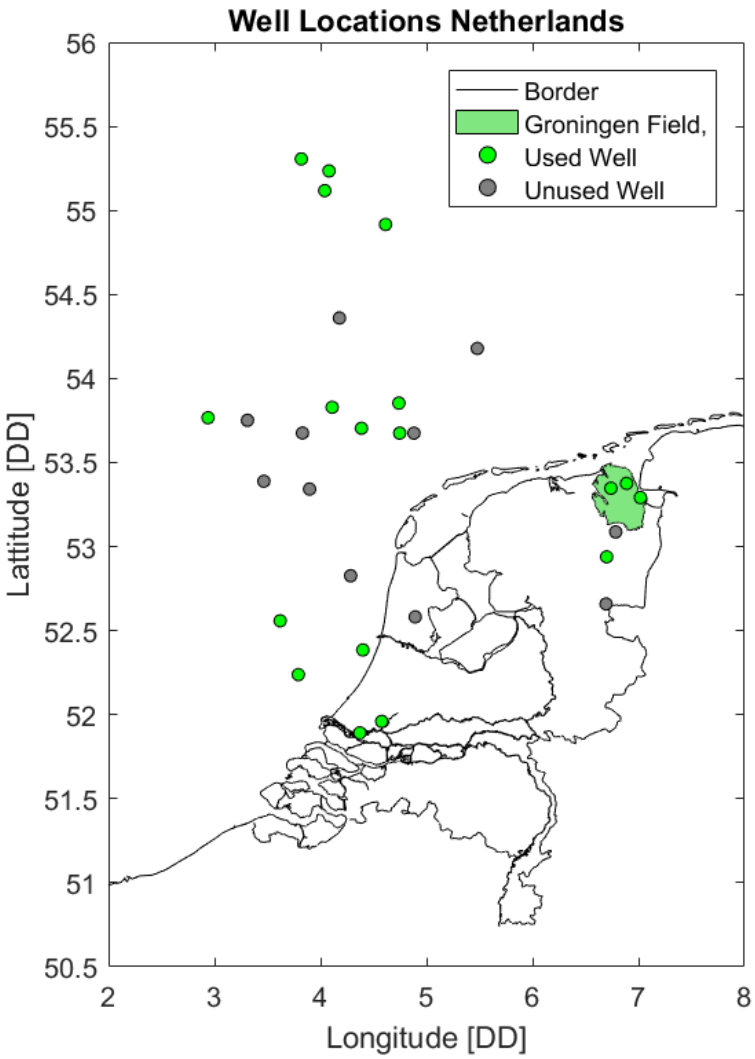


**Figure 28**: Locations of used (green) and unused (grey) wells from the data set. The Groningen field is marked in green. Note that the majority of wells are located offshore and that only 3 are part of the Groningen field.

Figure 28 shows a map of the Netherlands and the Dutch offshore containing the coordinates of the used wells in decimal degrees (DD). The Groningen field is coloured green and three of the used wells are part of it. From the figure it is clear that the majority of the wells are located offshore and that almost all the wells are far from the Groningen field and hence care needs to be taken when comparing wells with one another. In Figure 29 three wells that penetrate the Groningen field can be seen. The wells BRW-05 and ZRP-02 have been obtained via the *NAM* as the data from these wells is not yet publically available. The figure also shows the position of the Groningen field and it should be noted that the eastern part of the city lies over the field.

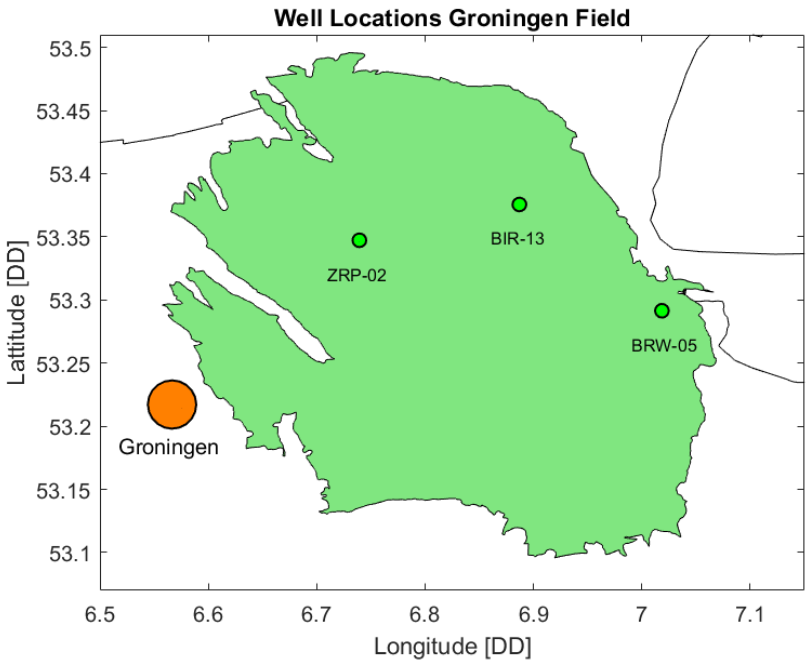


**Figure 29**: Three wells that are used to calculate elastic moduli around the Groningen field. The small satellite fields that are part of the Groningen field have been left out. The city of Groningen is marked by the orange circle. Note that in reality the eastern part of the city lies on top of the field.

### 3.1.2 Core data

Initially it was intended to use core data to reproduce similar graphs (Appendix E) that the *NAM* uses to describe the properties of the Slochteren Formation, however there is no suitable overlap between the acoustic data and the core data. Nonetheless a process has been developed to couple the nearest wireline measurement with the relevant core data point. The difference between the points ranges between nearly 0 and 8 cm which is not bad in terms of the common wireline logging interval of 15 cm. An example script is shown in Appendix H. Only the results of well BIR-13 are shown in this report.

# 3.2 Results

The results of the well data analysis can be found in this section. Results for the different stratigraphic units are discussed from young to old. A summary of the mean, median, mode and standard deviation of the Young's modulus and Poisson's ratio per well can be found in Appendix I. Finally 2 wells have been obtained from the *NAM* which, compared to the wells in the preceding sections, have a very long measured interval of acoustic data. The first research question is how the calculated values compare to those from literature. The other research questions is whether lithological links to the elastic moduli can be found. Hence, roughly half of the figures show moduli plotted against the neutron porosity combined with the gamma ray and the other half of the figures are histograms of these parameters. Additional figures are used to identify interesting findings.

## 3.2.1 Upper North Sea Group

For the Upper North Sea Group 3 wells are used: A15-02, B13-04 and B16-01. These three wells are located offshore. None of the wells that were analysed contained information on the Middle and Lower North Sea Group.

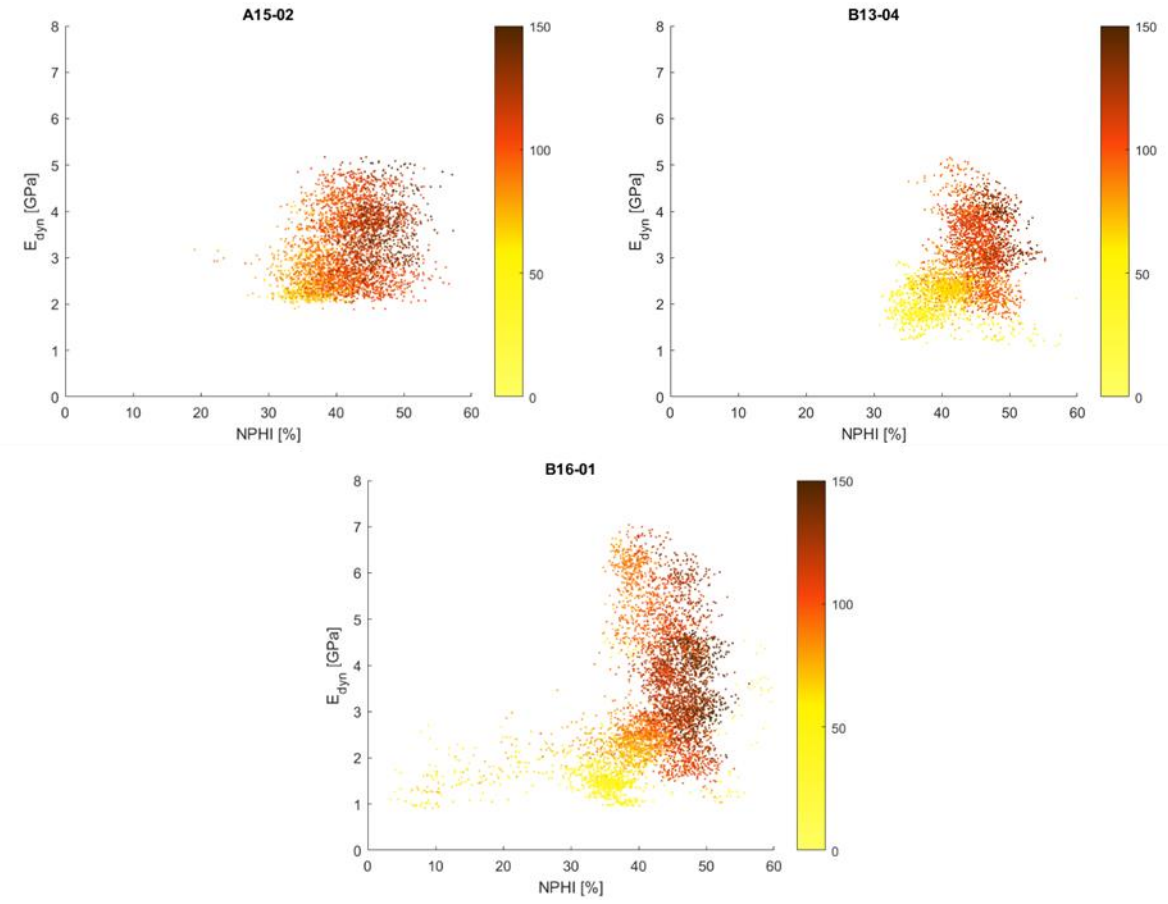


**Figure 30**: Dynamic Young's modulus vs. neutron porosity combined with the gamma ray log in [GAPI] for the Upper North Sea Group for wells A15-02, B13-04 and B16-01. All three wells show that the material with a low gamma ray response has a lower dynamic Young's modulus than the material with a high response. What is also noticeable is that well B16-01 has a

large range of values compared to the other two wells. What is also the case is that the low gamma ray material forms smaller data clusters.

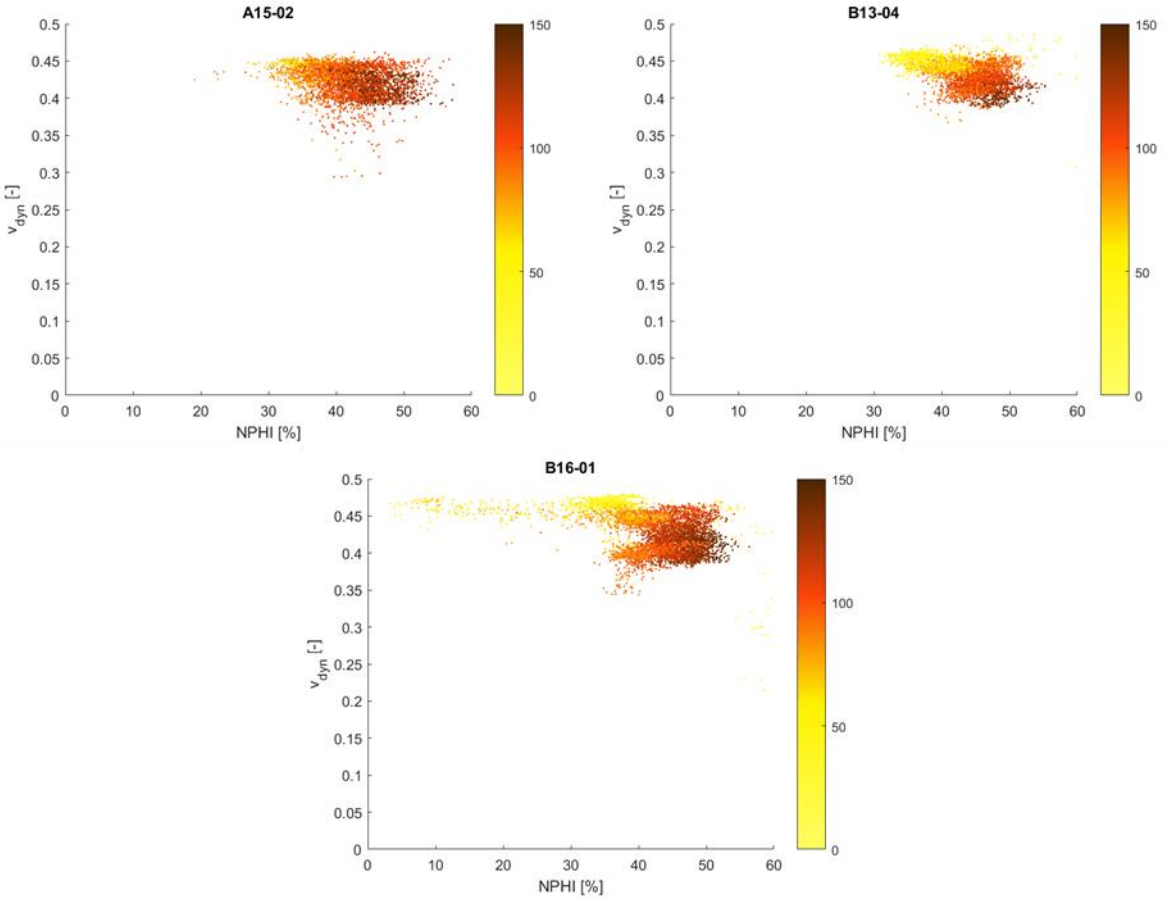


**Figure 31**: Dynamic Poisson's ratio vs. neutron porosity combined with the gamma ray log in [GAPI] for the Upper North Sea Group for wells A15-02, B13-04 and B16-01. All three wells show that the material with a low gamma ray response has a higher Poisson's ratio. There appears to be a general trend of decreasing Poisson's ratio with an increasing gamma ray response. B13-04 shows concentrated clusters, whilst B16-01 has a relatively large spread. Compared to the Young's modulus, the Poisson's ratio has a narrower range.

Figure 30 shows reasonably similar results between the three wells. B13-14 and B16-01 both have distinct clusters where there is a separation between low gamma ray material and the high gamma ray material. This distinction is less so for A15-02. In Figure 31 it can be seen that the Poisson's ratio behaves similar to that of the Young's modulus. Wells B13-14 and B16-01 show distinct clusters which is visible with the gamma ray log. Well A15-02 does not have an equally clear distinction, but there is a trend from a higher Poisson's ratio with a low gamma ray to a bit lower Poisson's ratio with a high gamma ray response. Of the three wells, B13-14 shows the narrowest band of possible values along with a clear lithological distinction based on the gamma ray and neutron porosity.

On the next page the Young's modulus vs. measured distance from the rotary table can be seen in Figure 32. It is clear that for B13-14 and B16-01 that the material with a low gamma ray response is towards the top of the of the Upper North Sea Group and that around 700 m MDRT the material has a much higher gamma ray response. There is a clear increase in Young's modulus with depth in both wells. This can be caused by an increase in the bulk density (Figure 33), but this shows a more or less constant value with a slight increase towards the bottom.

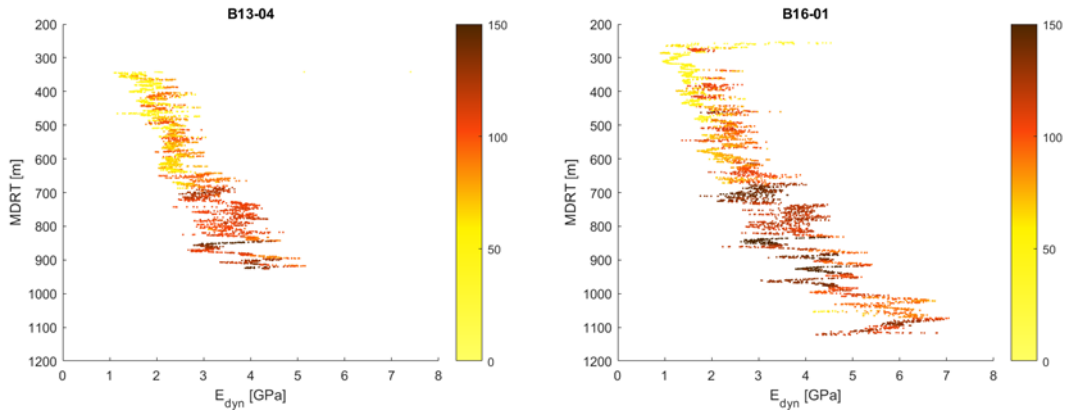


**Figure 32**: Measured distance from the rotary table vs. dynamic Young's modulus with the gamma ray log in [GAPI] for the Upper North Sea Group for wells B13-14 and B16-01. Both wells clearly show that the low gamma ray material is towards the top of the measured interval. Well A15-02 shows similar behaviour, but not as clear as these two wells.

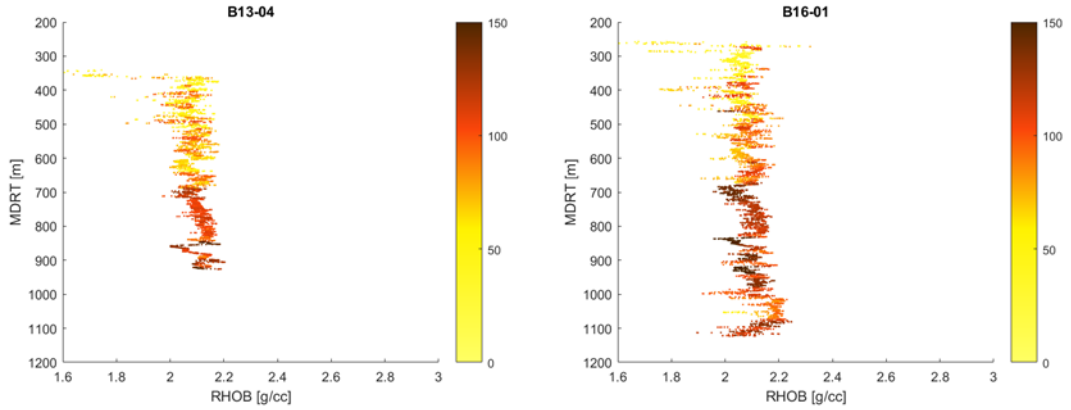


**Figure 33**: Measured distance from the rotary table vs. bulk density with the gamma ray log in [GAPI] for the Upper North Sea Group for wells B13-04 and B16-01. Note that the bulk density does not vary much with depth.

Figure 34 shows the histograms of the dynamic Young's modulus, converted static Young's modulus and Poisson's ratio for the three wells. A15-02 and B13-04 show much overlap for both elastic parameters. Well B16-01 has a much wider range of values for the Young's modulus (Figure 30) and a wider range for the Poisson's ratio. B16-01 has two peaks for the Poisson's ratio which is visible in Figure 31. When looking at the reference numbers, the Orlic (2016) value shows a poor fit with the Young's modulus data. The value used by the *NAM* is closer to the data set. Both sources use the same value for the Poisson's ratio and does not fit the data.

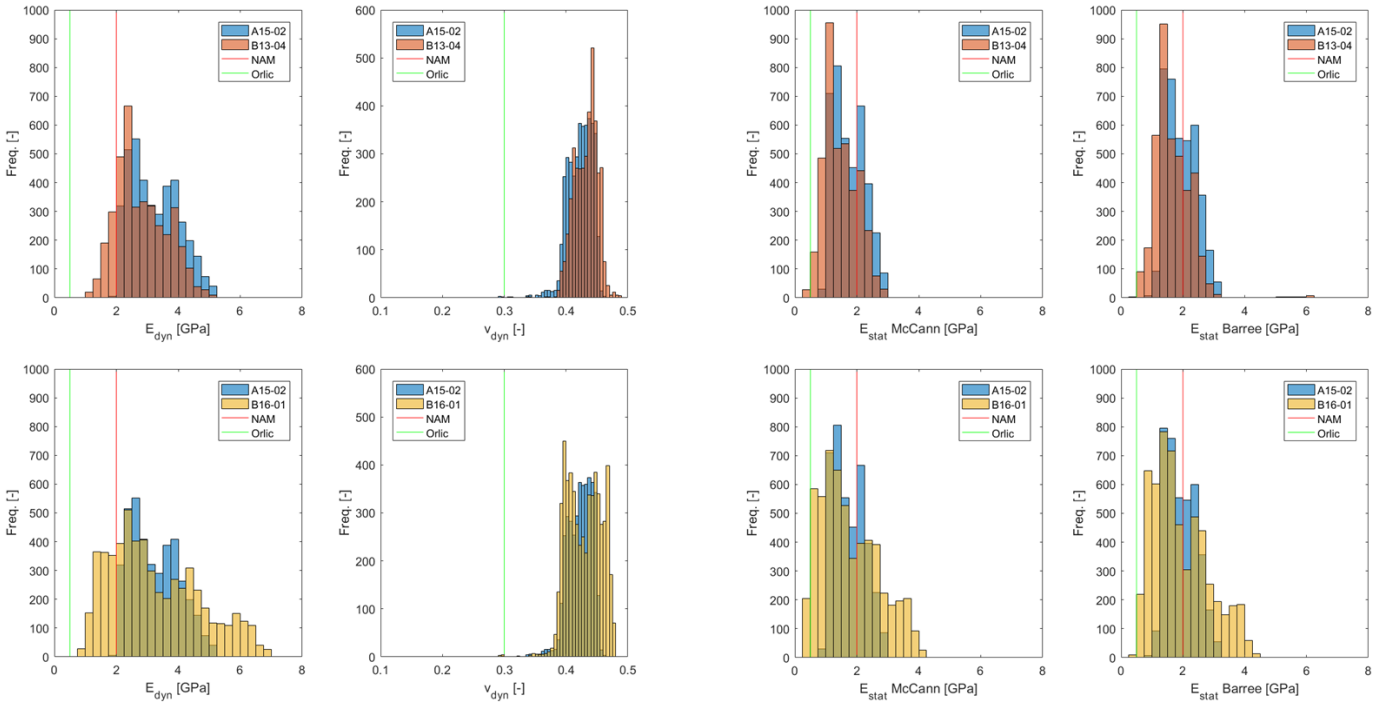


**Figure 34**: Histograms showing dynamic Young's modulus and dynamic Poisson's ratio (left) with the converted static Young's modulus (right) for the Upper North Sea Group for wells A15-02, B13-04 and B16-01. Note the quite close overlap between A15-02 and B13-04. The wider spread in values for well B16-01 in Figure 3.4 can clearly be seen in the histograms, especially the Young's modulus. The value used by Orlic (2016) has a poor match with the obtained data, regardless of dynamic or static conversion. Based on Table 3.5 the *NAM* value has a closer match with the Barree et al., (2009) conversion.

## 3.2.2 Chalk Group

For the Chalk Group 2 wells are looked at: BIR-13 and P15-14. BIR-13 consists of the Ommelanden Formation whilst P15-14 consists of the underlying Texel Formation. There is core data available for BIR-13 which has been combined with the wireline data. Well BIR-13 is part of the Groningen structure and hence suitable for comparison with the *NAM* wells BRW-05 and ZRP-02.

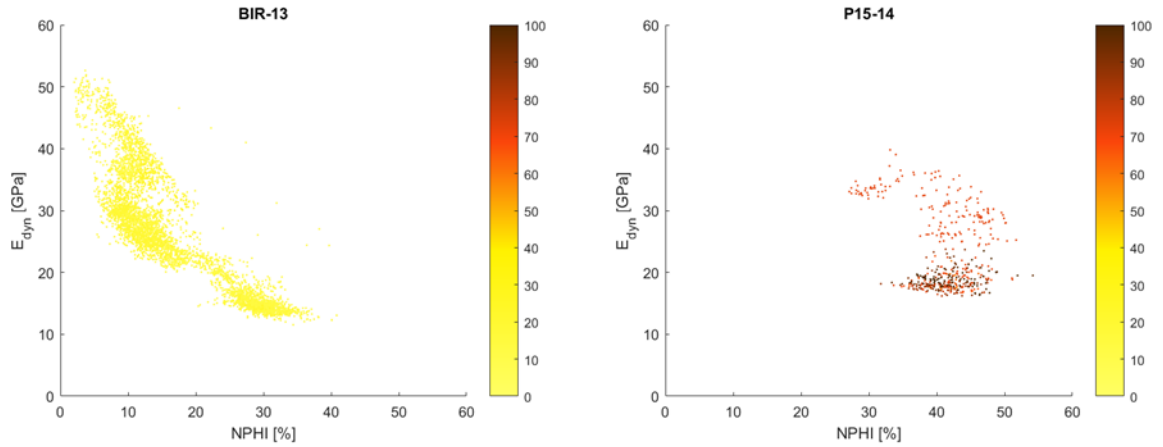


**Figure 35**: Dynamic Young's modulus vs. neutron porosity combined with the gamma ray log in [GAPI] for the Chalk Group for well BIR-13 (left) and P15-14 (right). The Texel Formation does not show a correlation between the Young's modulus and the two wireline measurements. Note that there is a clear correlation between the Young's modulus and neutron porosity for well BIR-13, but there appear to be three clusters.

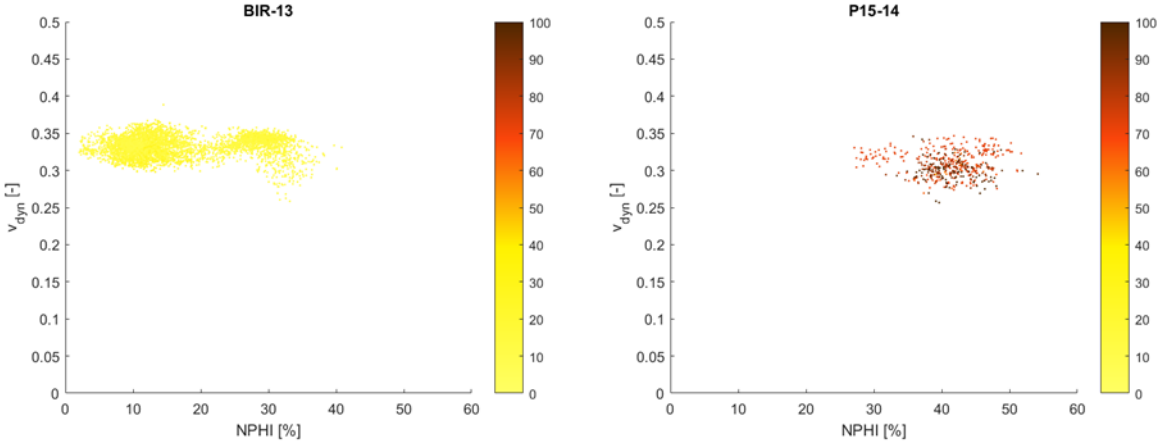


**Figure 36**: Dynamic Poisson's ratio vs. neutron porosity combined with the gamma ray log in [GAPI] for the Chalk Group for well BIR-13 (left) and P15-14 (right). Note that there is not a clear correlation between the Poisson's ratio and neutron porosity for either well, but BIR-13 has a high concentration between 0.30 and 0.35.

From Figure 35 and Figure 36 it is clear that the Ommelanden Formation (BIR-13) and Texel Formation (P15-14) are distinct from each other. Figure 35 shows that there are three clusters for the Young's modulus in well BIR-13. Well P15-14 shows a very wide scatter with a cluster at around $E_{dyn}$ = 20 GPa. The Ommelanden Chalk shows a clear relationship with the neutron porosity. Figure 36 shows that both formations have a reasonably narrow range for the Poisson's ratio. This is especially so for the Chalk in well BIR-13. What is noticeable is that the Poisson's ratio appears to be invariant to the neutron porosity.

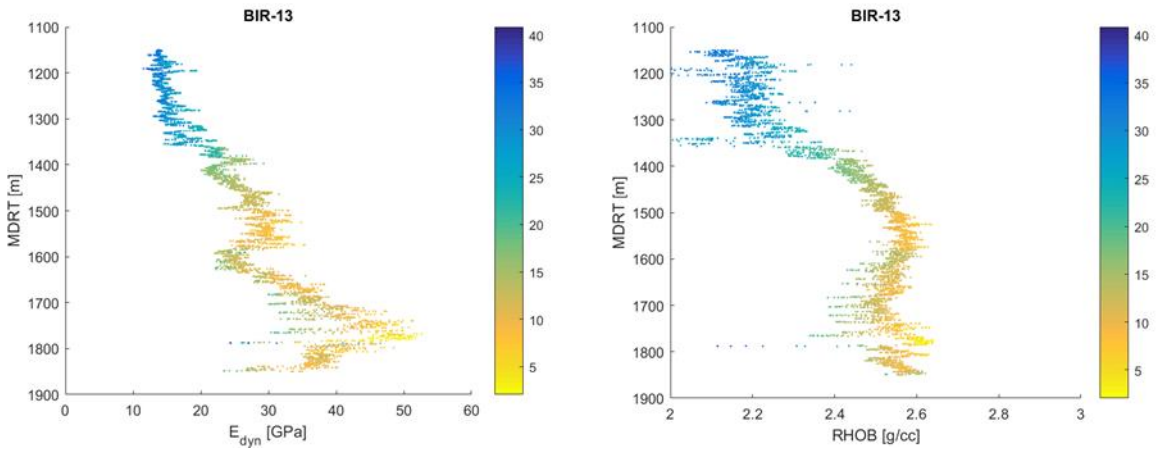


**Figure 37**: Dynamic Young's modulus vs. MDRT (left) and bulk density vs. MDRT (right) with the neutron porosity in [%] for the Chalk Group for well BIR-13. Note the strong relationship between the Young's modulus and the neutron porosity.

Figure 37 shows the dynamic Young's modulus and the bulk density versus MDRT for well BIR-13. The relationship between the Young's modulus and neutron porosity is very clear for the Ommelanden Formation with the tightest part of the formation showing the largest Young's modulus. The figure shows three zones for the Young's modulus with the top layer having a distinctly low neutron porosity. In the middle there is a layer with a noticeably higher Young's modulus and lower neutron porosity which is followed by a drop at 1600 m MDRT and then a large increase in Young's modulus. The highest Young's modulus values correspond with the lowest neutron porosity. The bulk density is clearly low for the top layer of the formation and increases suddenly after 1400 m MDRT and then remains roughly constant. It is noticeable that the very low neutron porosity zone does not have a particularly high bulk density.

The combined wireline and core data can be seen in Figure 38 and conforms to the previous results. There is a clear relationship between the Young's modulus and both porosities. The Poisson's ratio shows no relationship between either porosity. The core porosity of the formation decreases with depth and the bulk density increases with it. Note that it is not known whether the core porosity is a total or effective porosity. This knowledge resides with the operator of the well.

Both formations show a wide range of values for the Young's modulus (Figure 39). Due to this the reference values are not going to match the data well. The value used by Orlic (2016) comes closest to the determined numbers and the *NAM* value matches best with the top third of the Ommelanden Formation. The narrow band of values for the Poisson's ratio is clear in the histogram for BIR-13 and neither reference intersects the data.

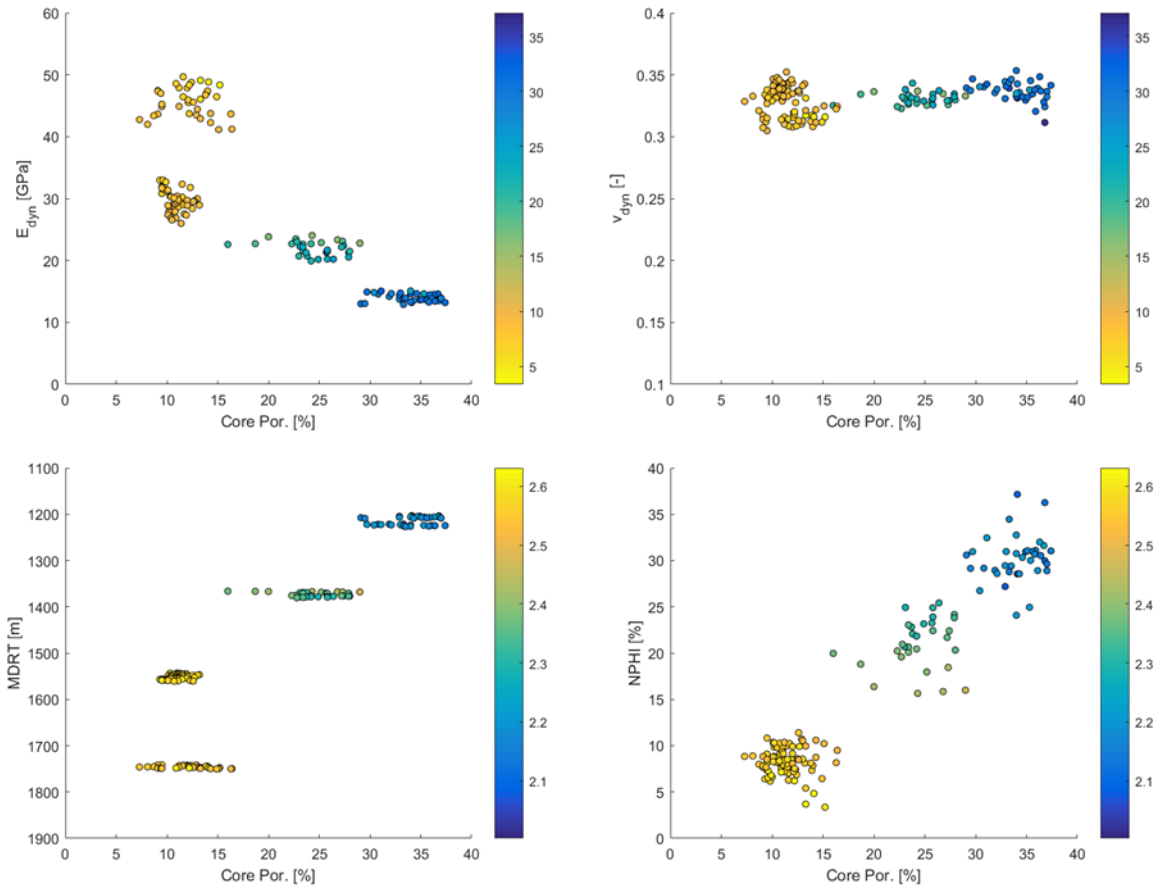


**Figure 38**: Combined core and wireline data showing the dynamic Young's modulus, the dynamic Poisson's ratio, measured distance from the rotary table and the neutron porosity for well BIR-13. For the two top plots the colour bar indicates the neutron porosity [%] and for the bottom two plots the bulk density [g/cc]. The author enquired what type of porosity the core porosity is, but this was unavailable. What is also clear is that in terms of Young's modulus there is a lot of variability within the Chalk Group. The porosity and bulk density are considerably lower towards the top of the group than at the bottom.

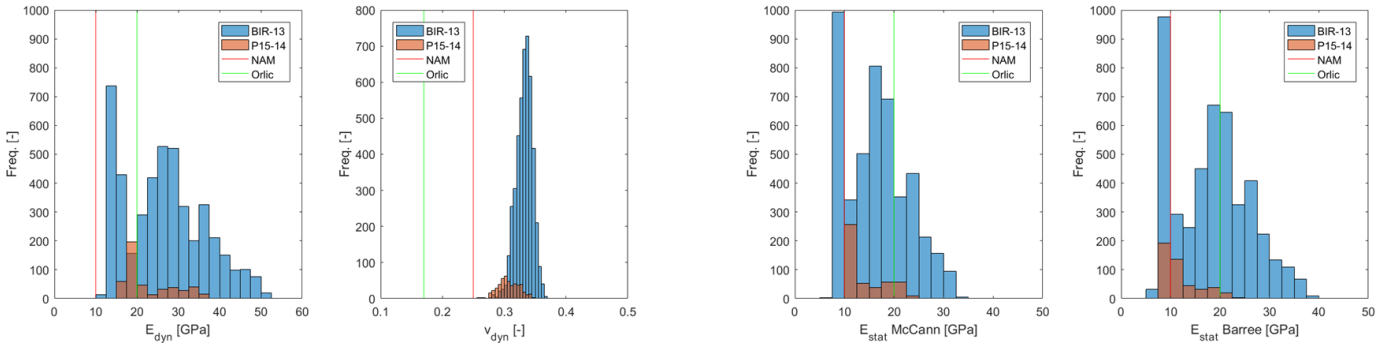


**Figure 39**: Histograms showing dynamic Young's modulus and dynamic Poisson's ratio (left) with the converted static Young's modulus (right) for the Chalk Group for wells BIR-13 and P15-14. The value used by Orlic matches the static Young's moduli quite well. The *NAM* value appears to be more suited to the upper part (not shown) of the Chalk Group and not for the lower parts with a higher Young's modulus. Note that for the Poisson's ratio the two reference values completely do not concur with the processed data.

### 3.2.3 Rijnland Group

For the Rijnland Group 2 wells are used: PRW-01 and P15-14. From Figure 40 it can be seen that the material is quite different for both wells. In well PRW-01 there are rocks with a low gamma ray response which is not the case for P15-14. The rocks in PRW-01 also show a trend between the Young's modulus and the neutron porosity. The values for P15-14 are much more scattered with a dense cloud around $E_{dyn}$ = 25 GPa.

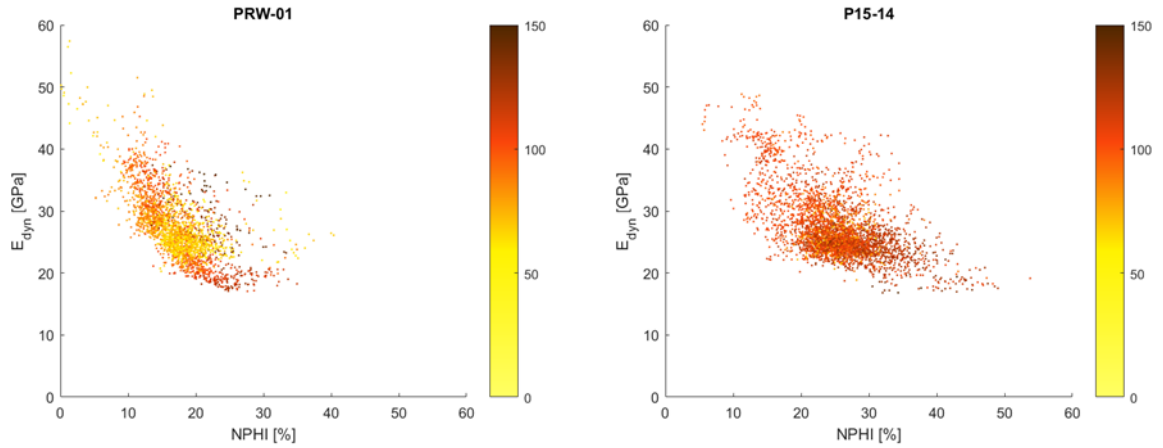


**Figure 40**: Dynamic Young's modulus vs. neutron porosity combined with the gamma ray log in [GAPI] for the Rijnland Group for well PRW-01 (left) and P15-14 (right). Note that there is a correlation between the Young's modulus and neutron porosity for well PRW-01, but this is less so for P15-14. For P15-14 there is a concentrated cluster at 25 GPa.

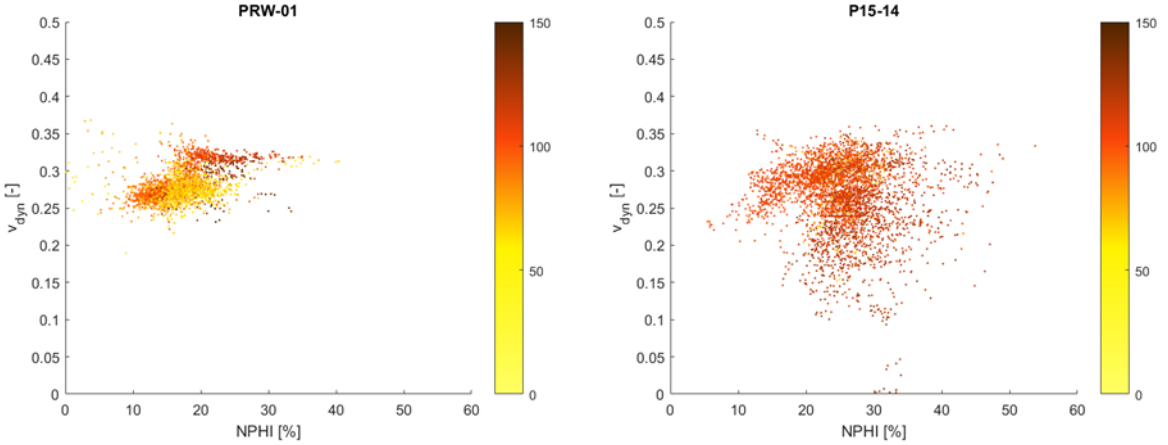


**Figure 41**: Dynamic Poisson's ratio vs. neutron porosity combined with the gamma ray log in [GAPI] for the Rijnland Group for well PRW-01 (left) and P15-14 (right). Note that there is not a clear correlation between the Poisson's ratio and neutron porosity for either well. P15-14 in particular shows a very large spread of values and no clear link can be discerned.

Figure 41 shows the Poisson's ratio for both wells and the clustering for PRW-01 is denser than for P15-14. As with the Young's modulus, P15-14 shows a very wide range of values and no clear trend. The histogram (Figure 42) clearly shows the wide range of the Poisson's ratio for well P15-14. What is noticeable is that despite the difference in gamma ray response, the range and distribution of the Young's modulus are very similar. Both literature references match well with the data for the Rijnland Group.

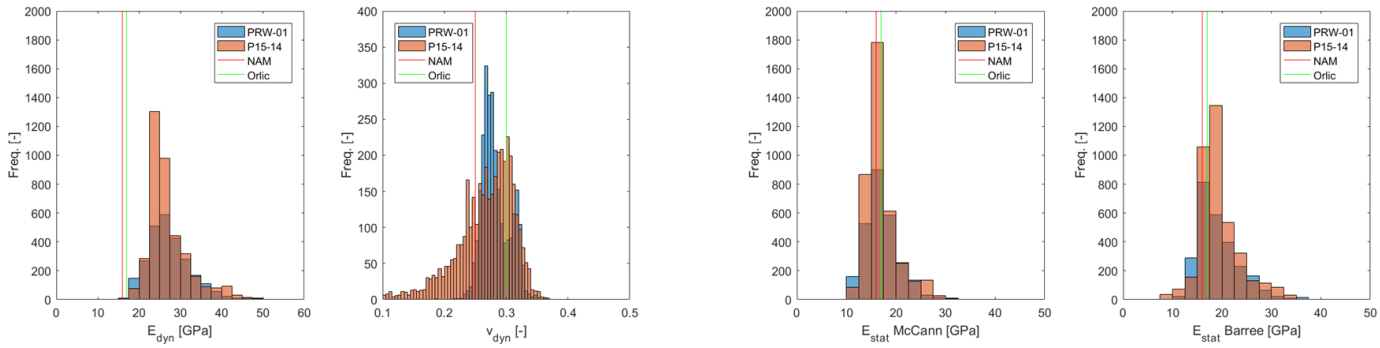


**Figure 42**: Histograms showing dynamic Young's modulus and dynamic Poisson's ratio (left) with the converted static Young's modulus (right) for the Rijnland Group for wells PRW-01 and P15-14. For both wells the Orlic reference Poisson's ratio seems to have the best match. Note that the reference values for the static Young's modulus appear to match really well.

## 3.2.4 Schieland Group

For the Schieland Group 2 wells are used: F02-07 and PRW-01. The Schieland Group rocks show a general trend (Figure 43) between the neutron porosity and the Young's modulus for well F02-07. The same can be said for PRW-01 however, there is no dense cluster for this well. Note that the trend for F02-07 appears to be exponential/bi-linear whilst PRW-01 shows a more linear trend.

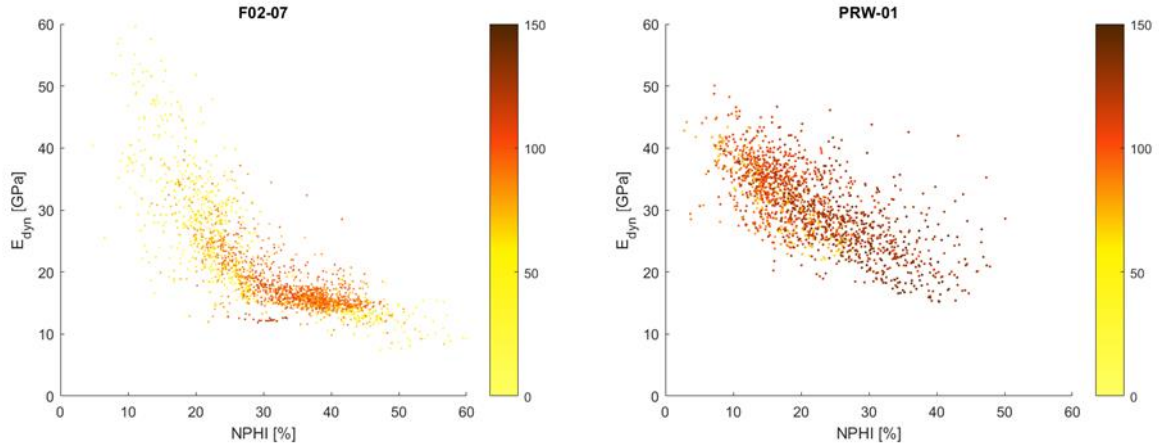


**Figure 43**: Dynamic Young's modulus vs. neutron porosity combined with the gamma ray log in [API] for the Schieland Group for well F02-07 (left) and PRW-01 (right). Note that both wells show a general trend between the Young's modulus and the neutron porosity. Well F02-07 shows a somewhat exponential relationship with the neutron porosity with a dense cluster around 15 GPa.

Figure 44 shows the dynamic Poisson's ratio for the two wells and particularly F02-07 shows a wide range in values. The values for PRW-01 stay between 0.25 and 0.35. Neither shows a link with the neutron porosity.

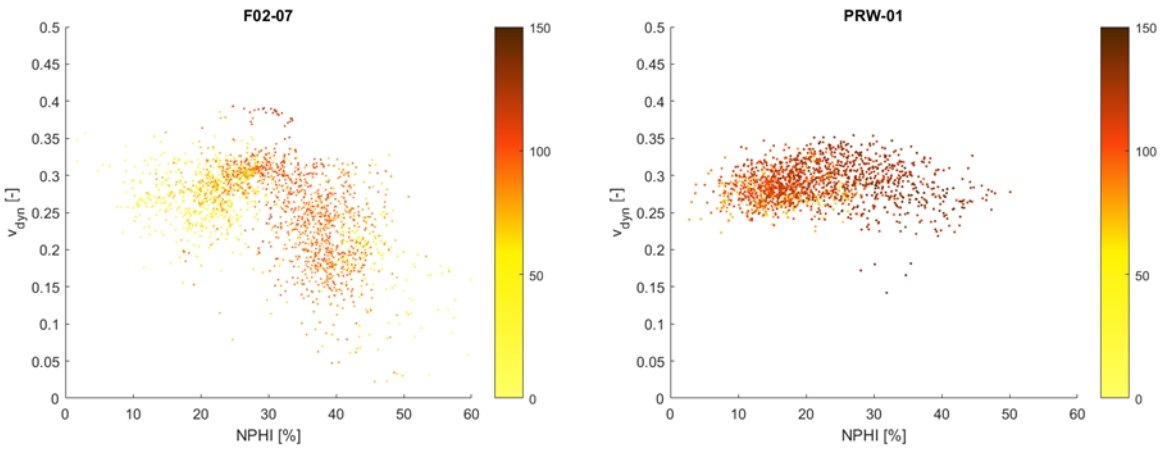


**Figure 44**: Dynamic Poisson's ratio vs. neutron porosity combined with the gamma ray log in [API] for the Schieland Group for well F02-07 (left) and PRW-01 (right). Both wells show a large scatter in values, particularly F02-07.

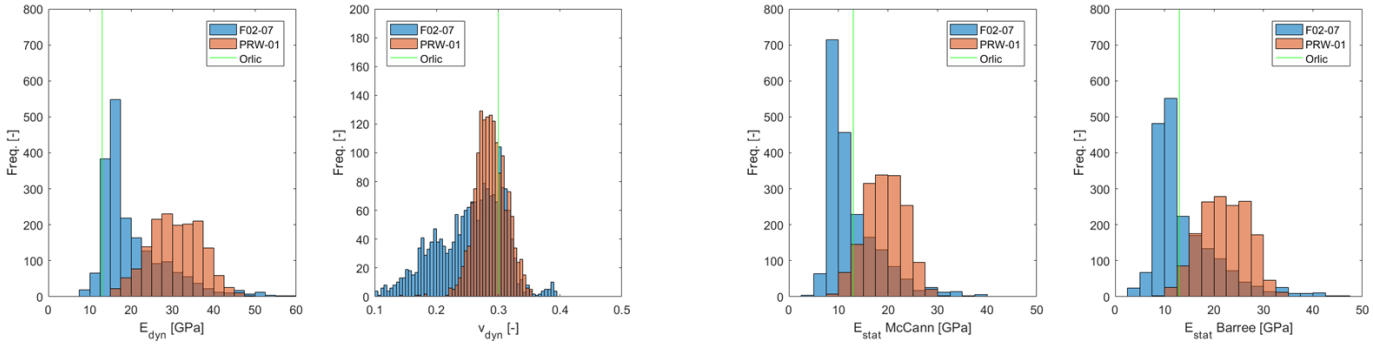


**Figure 45**: Histograms showing dynamic Young's modulus and dynamic Poisson's ratio (left) with the converted static Young's modulus (right) for the Schieland Group for wells F02-07 and PRW-01. The two wells differ a lot in rock rigidity where the rocks in F02-07 have a significantly lower Young's modulus. F02-07 clearly shows skewed behaviour whilst PRW-01 looks more like a normal distribution. Note that the reference value for the Poisson's ratio appear to match reasonably with the obtained data. The mean of the Poisson's ratio for PRW-01 is 0.29 which is very close to 0.30.

From the histograms it is clear that the Schieland Group for the two wells is quite distinct were both wells show poor overlap between one another. The range of the Poisson's ratio is relatively narrow for PRW-01 and it is wide for F02-07. There are only reference values from Orlic (2016) and the Poisson's ratio shows a very good match with the mean (0.29) of PRW-01. This is not the case for the converted static Young's moduli where the value by Orlic is much lower than that of the data. Note that the Young's modulus for PRW-01 is somewhat normally distributed, whilst F02-07 is skewed.

## 3.2.4 Scruff Group

For the Scruff Group only one well was available: F02-07. Figure 46 shows that the range of Young's modulus values is very narrow. The Young's modulus increases gently with a decreasing neutron porosity. The Poisson's ratio on the other hand, shows a relatively wide scatter.

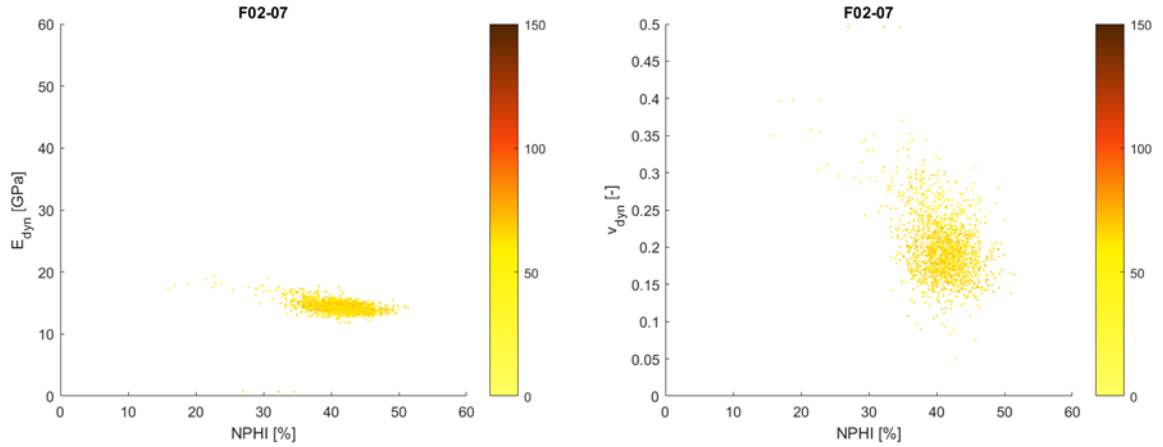


**Figure 46**: Dynamic Young's modulus (left) and dynamic Poisson's ratio (right) vs. neutron porosity combined with the gamma ray log in [API] for well F02-07. The colour bar indicates the gamma ray log in [GAPI]. The Young's modulus forms a dense cloud and there appears to be a trend with the neutron porosity. The Poisson's ratio on the other hand, shows a very scattered behaviour.

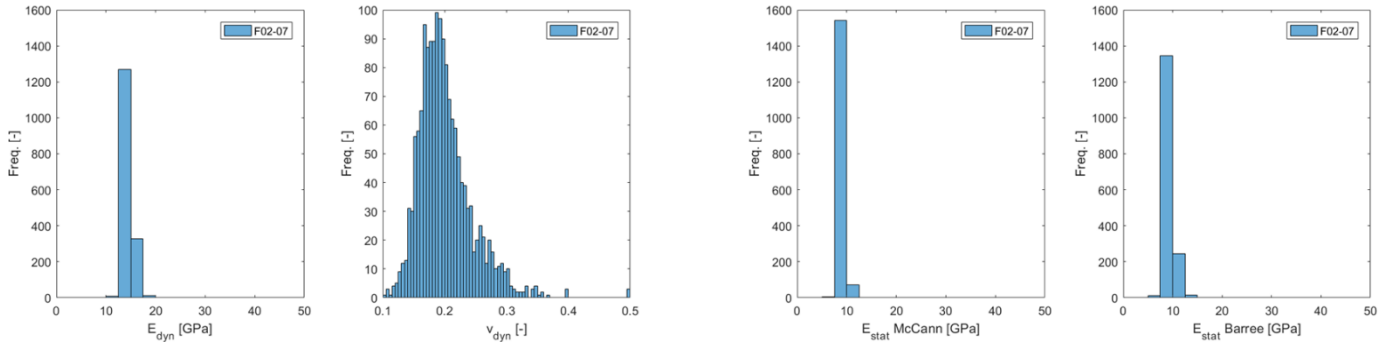


**Figure 47**: Histograms showing dynamic Young's modulus and dynamic Poisson's ratio (left) with the converted static Young's modulus (right) for the Scruff Group for well F02-07. The histograms clearly reflect the previous figure as for the Young's modulus, the vast majority of data points are within one column. The Poisson's ratio is quite spread out, but the majority of the points are around 0.20. Note there is no literature reference for the Scruff Group.

The narrow range of the Young's modulus is visible in Figure 47 as is the much wider range of the Poisson's ratio. There is no reference value for the Scruff Group.

## 3.2.5 Altena Group

As with the Scruff Group, for the Altena Group only one well was available: P15-14. Both the Young's modulus and Poisson's ratio show a wide scatter for P15-14. The Young's modulus has a dense cluster at $E_{dyn}$ = 25 GPa. The Poisson's ratio does not show an as clear concentration of values as the Young's modulus.

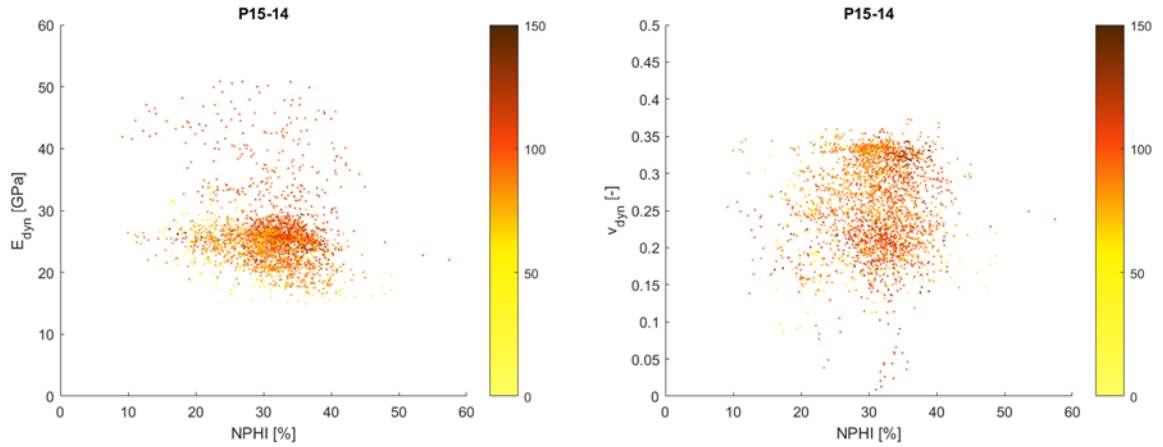


**Figure 48**: Dynamic Young's modulus (left) and dynamic Poisson's ratio (right) vs. neutron porosity combined with the gamma ray log in [API] for well P15-14. The Young's modulus forms a dense cloud at around 25 GPa, but there is a clear scatter towards higher values. The Poisson's ratio does not show an as clear concentration of values and the magnitude varies between 0.15 and 0.35.

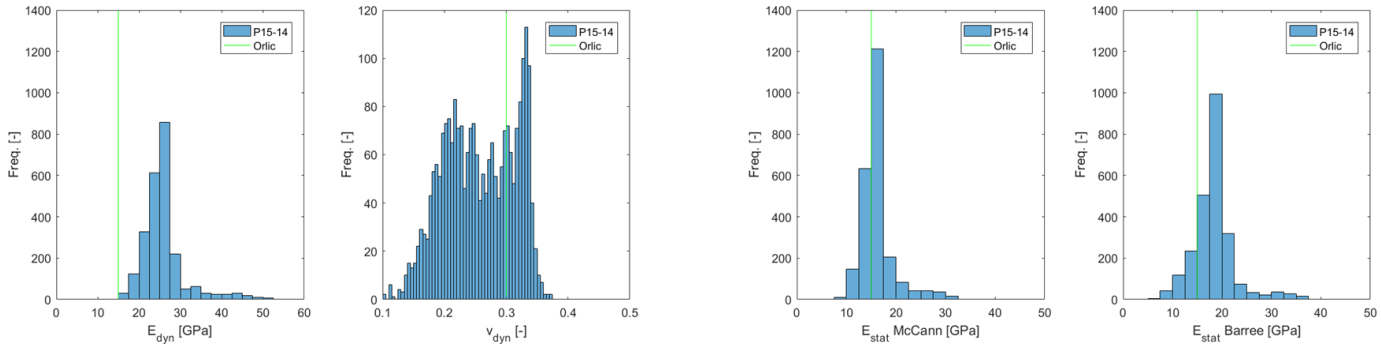


**Figure 49**: Histograms showing dynamic Young's modulus and dynamic Poisson's ratio (left) with the converted static Young's modulus (right) for the Scruff Group for well P15-14. Note that the Orlic reference value matches well with the McCann conversion for the static Young's modulus. The reference Poisson's ratio cannot match the data due to the wide spread.

The distribution of the Young's modulus shows a sudden drop at around 27 GPa with tail of higher values. The Orlic (2016) reference value shows a close match with the McCann and Entwisle (1992) conversion. The Poisson's ratio has a wide range and the reference value does not match the data.

## 3.2.6 Upper Germanic Triassic Group

For the Upper Germanic Triassic Group two wells are looked at: CAP-01 and L03-02. CAP-01 (Figure 50) shows a wide scatter and a vague increase of the Young's modulus with a lower neutron porosity. The trend is clearer for L03-02 which shows a relatively dense cluster of points.

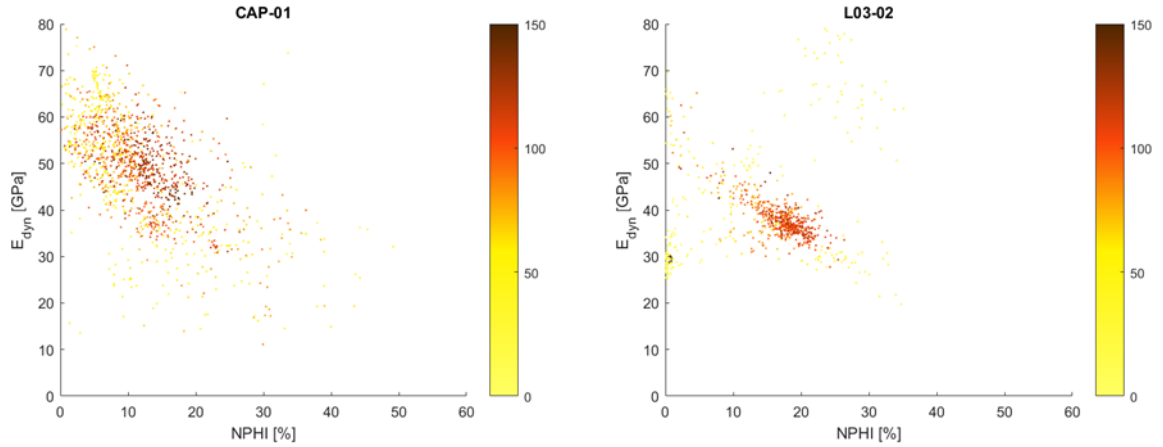


**Figure 50**: Dynamic Young's modulus vs. neutron porosity combined with the gamma ray log in [API] for the Upper Germanic Triassic Group for well F02-07 (left) and PRW-01 (right). Both show a large scatter, but a general relationship with the neutron porosity.

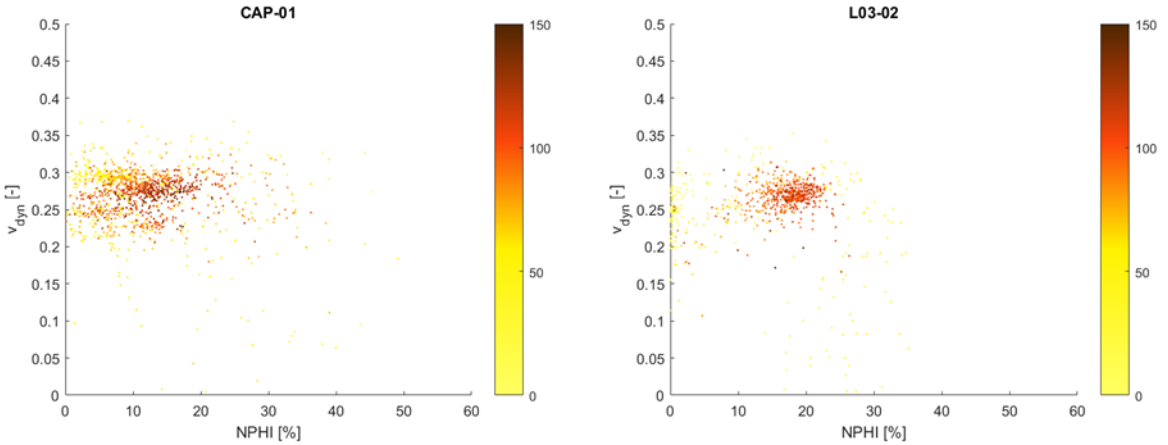


**Figure 51**: Dynamic Poisson's ratio vs. neutron porosity combined with the gamma ray log in [API] for the Upper Germanic Triassic Group for well F02-07 (left) and PRW-01 (right). As with the Young's modulus there is a wide scatter, but no particular relationship with the neutron porosity.

Figure 52 shows that the rock masses for the two well have a notably different distributions for the Young's modulus. The Poisson's ratios however, show similar behaviour. The Orlic (2016) value has a reasonable match with the static Young's moduli, but the *NAM* value does not fit either. Neither reference for the Poisson's ratio is satisfactory.

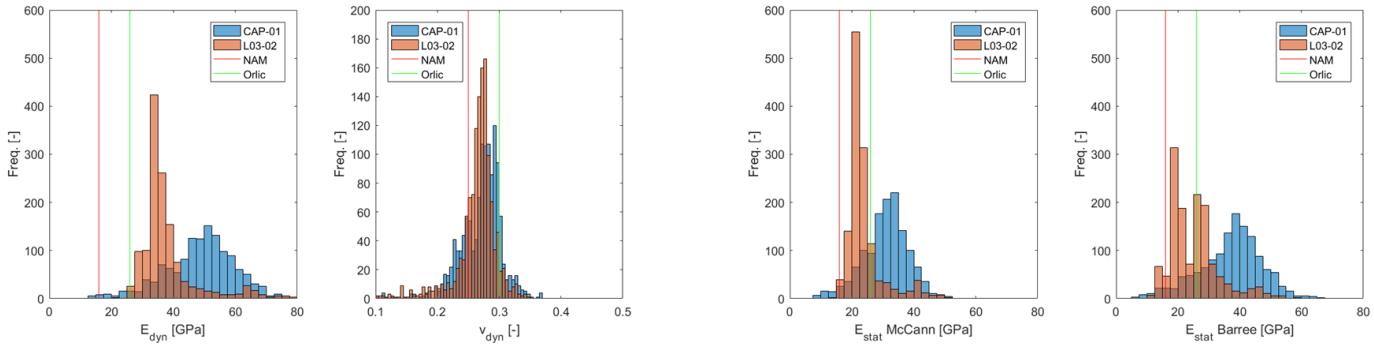


**Figure 52**: Histograms showing dynamic Young's modulus and dynamic Poisson's ratio (left) with the converted static Young's modulus (right) for the Upper Germanic Triassic Group for wells CAP-01 and L03-02. Note that whilst the Young's moduli differ substantially for the wells, the Poisson's ratio is quite similar.

### 3.2.7 Lower Germanic Triassic Group

For the Lower Germanic Triassic Group 4 wells are shown: CAP-01, L03-02, L06-01 and Q11-03. As reservoir target depth is reached, more data becomes available and can be seen with the next two geological groups as well.

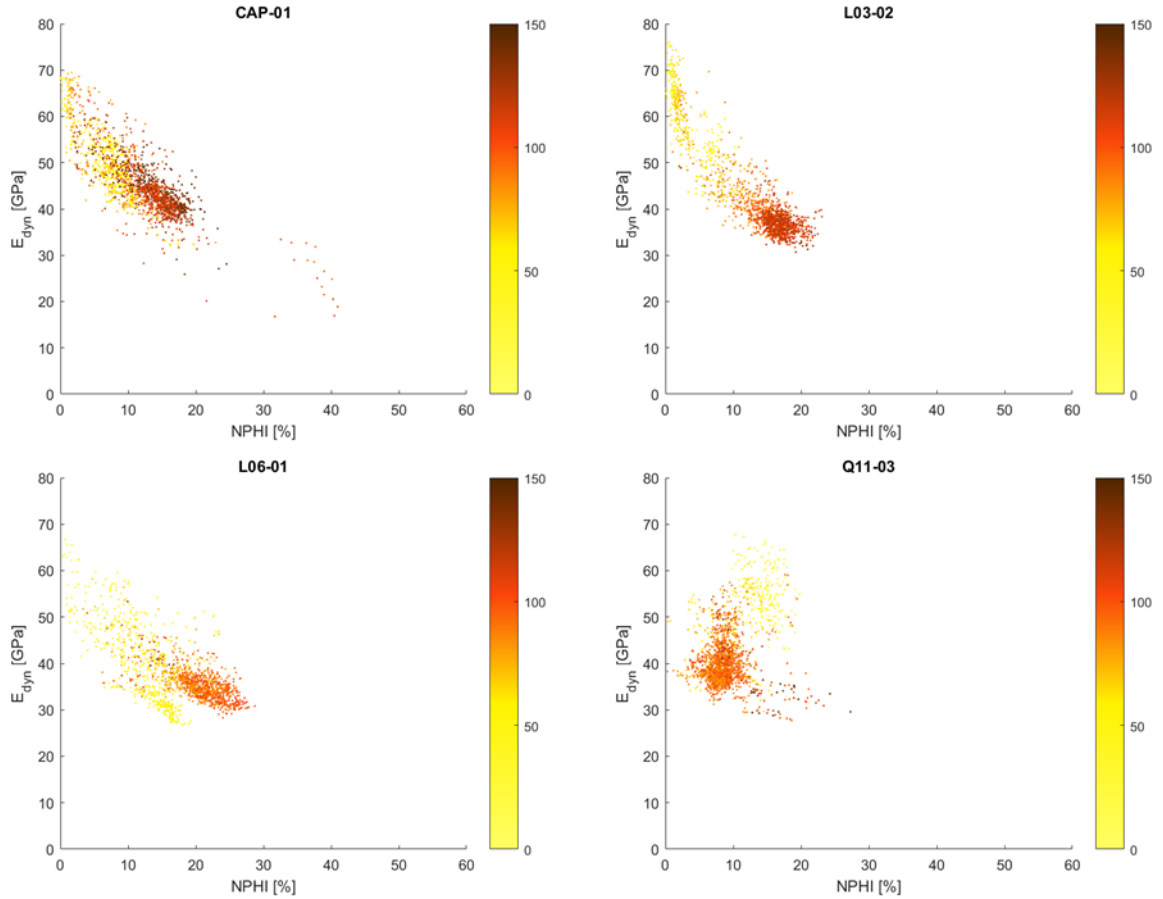


**Figure 53**: Dynamic Young's modulus vs. neutron porosity combined with the gamma ray log in [GAPI] for the Lower Germanic Triassic Group for wells CAP-01, L03-02, L06-01 and Q11-03. Wells CAP-01, L03-02 and L06-01 show a clear relationship with the neutron porosity. Notably Q11-03 does not show a clear trend, but there is a dense cluster at 40 GPa.

Figure 53 shows that there is some variability within the Lower Germanic Triassic for the Young's modulus. Wells CAP-01, L03-02 and L06-01 shows trends between it and the neutron porosity, but this is not the case for Q11-03. There is clustering based on the gamma ray, implying quite different lithologies. Well L03-02 is further looked at in Figure 54, where the Lower Volpriehausen Sandstone Member can clearly be distinguished from the surrounding rock by the neutron porosity and the gamma ray.

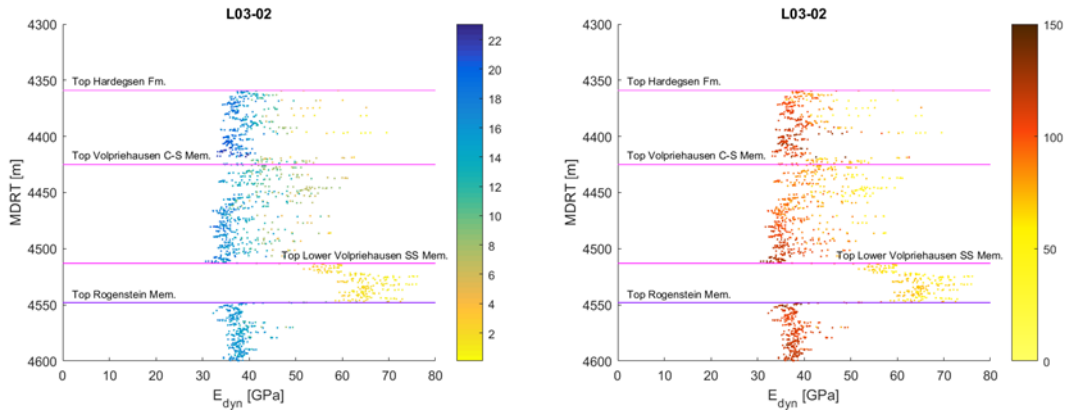


**Figure 54**: Measured distance from the rotary table vs. dynamic Young's modulus combined with the neutron porosity log in [%] (left) and the gamma ray log in [GAPI] (right) for the Lower Germanic Triassic Group for well L03-02. The Lower Volpriehausen Sandstone Member is easily distinguished by the low neutron porosity and low gamma ray response.

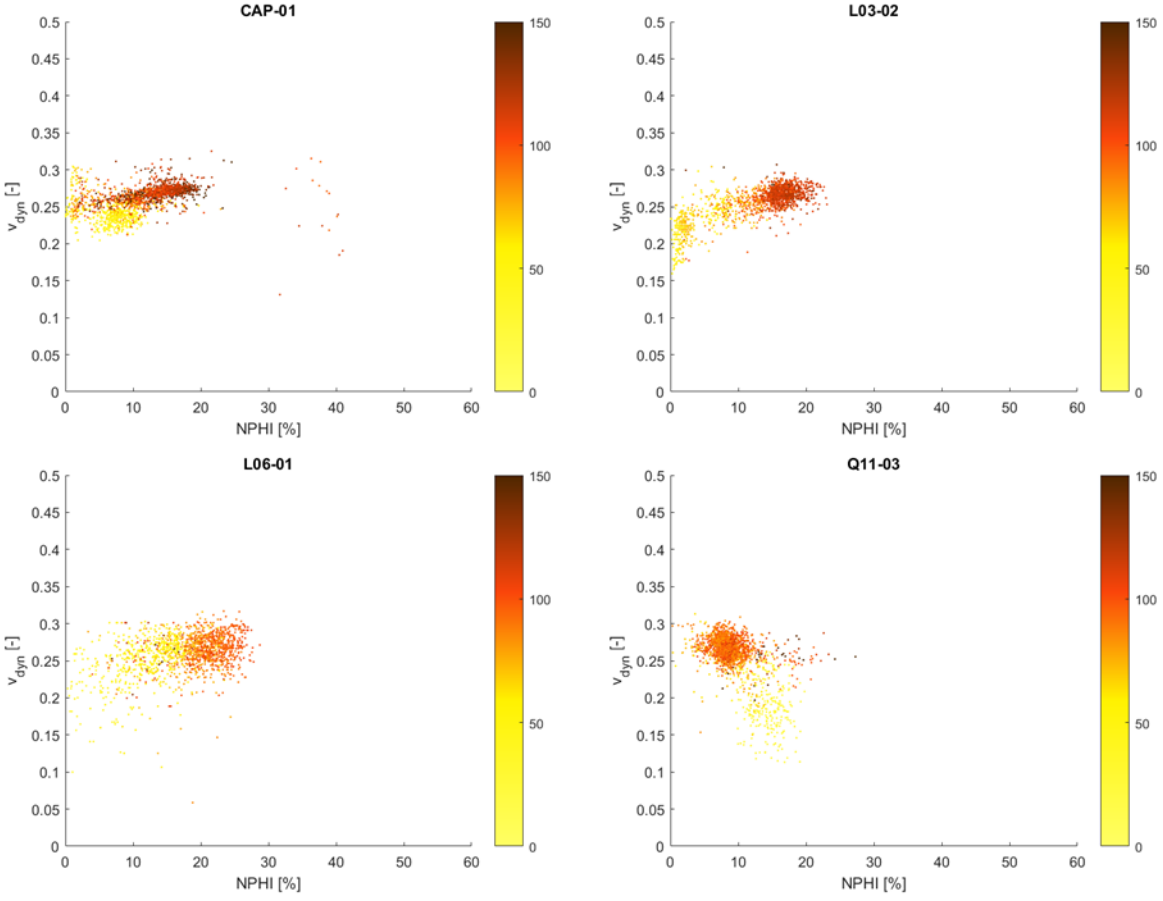


**Figure 55**: Dynamic Poisson's ratio vs. neutron porosity combined with the gamma ray log in [GAPI] for the Lower Germanic Triassic Group for wells CAP-01, L03-02, L06-01 and Q11-03. Wells CAP-01 and L03-02 show clustering based on the gamma ray log. The other two wells show this to a lesser extent. Note the very narrow ranges in well CAP-01.

The Poisson's ratio shows clear clustering for the wells CAP-01, L03-02 and Q11-03 and less so for L06-01. The rock mass with a high gamma ray response for CAP-01 seems to show a relationship with the neutron porosity, where the Poisson's ratio increases with the neutron porosity.

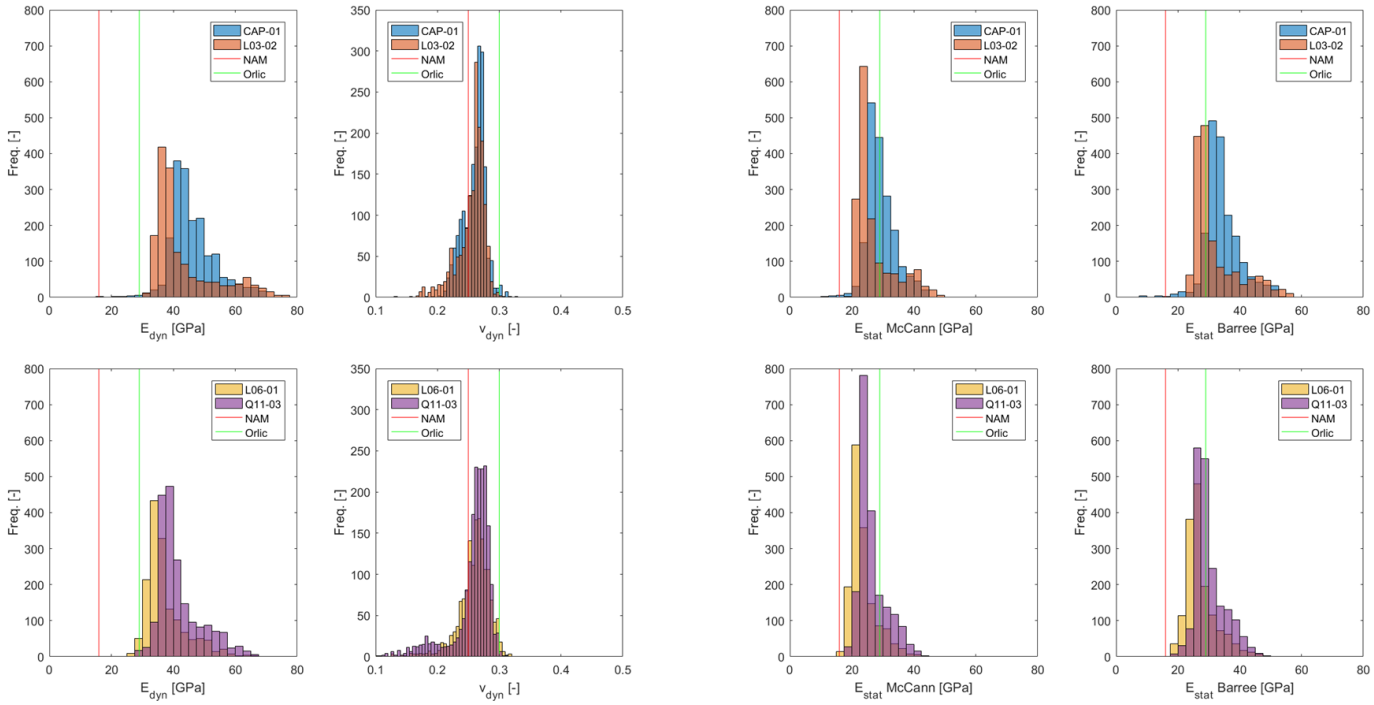


**Figure 56**: Histograms showing dynamic Young's modulus and dynamic Poisson's ratio (left) with the converted static Young's modulus (right) for the Lower Germanic Triassic Group for wells CAP-01, L03-02, L06-01 and Q11-03. For all four wells the Poisson's ratio shows a relatively narrow band, especially for CAP-01. The Orlic reference for the static Young's modulus shows a much better match than the *NAM* value.

The distribution of the Young's modulus for CAP-01 differs from the other three wells. When it comes to the reference values, the one provided by Orlic (2016) shows the best fit to the static Young's moduli. All four wells show a relatively narrow band for the Poisson's ratio and the NAM reference is nearest to the data.

## 3.2.8 Zechstein Group

For the Zechstein Group 4 wells are shown: GRL-01, J06-04, P08-06 and Q11-03. Figure 57 shows that there is considerable variability within the Zechstein Group. Wells GRL-01 and J06-04 are similar in showing clusters with a high Young's modulus and low gamma ray response caused by the anhydrite (Figure 58). In both plots there is also a wide scatter for the high gamma ray material. Well P08-06 shows two distinct clusters based on the neutron porosity and the gamma ray. There is a clear trend between the neutron porosity and the Young's modulus as well. Note that there is a group of values for well GRL-01 with a lower Young's modulus and low gamma ray values. This is deemed to be peculiar and Figure 58 shows the bulk density vs. MDRT. The figure shows that a part of the Zechstein interval contains very low bulk density values which is circumspect. These values are highly likely to be erroneous and should be ignored.

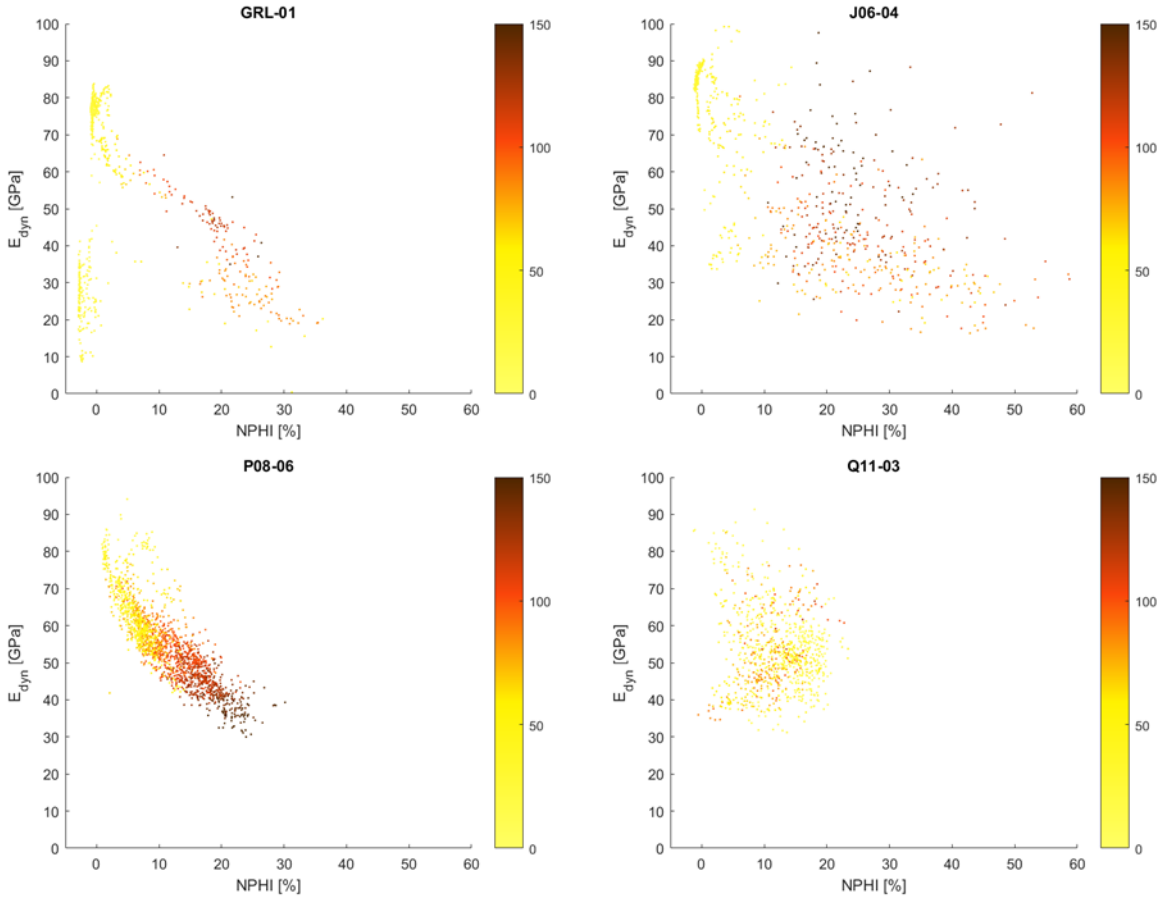


**Figure 57**: Dynamic Young's modulus vs. neutron porosity combined with the gamma ray log in [GAPI] for the Zechstein Group for wells GRL-01, J06-04, P08-06 and Q11-03. Well P08-06 shows a clear trend with the neutron porosity. What is also noticeable is the transition from high gamma ray material to low gamma ray. The other wells show a much wider scatter. GRL-01 and J06-04 show clustering at 80-90 GPa caused by anhydrite and limestone. It should be noted that GRL-01 has a very low density layer which forms the data points with a low Young's modulus and low gamma ray. This part of the data should be ignored.

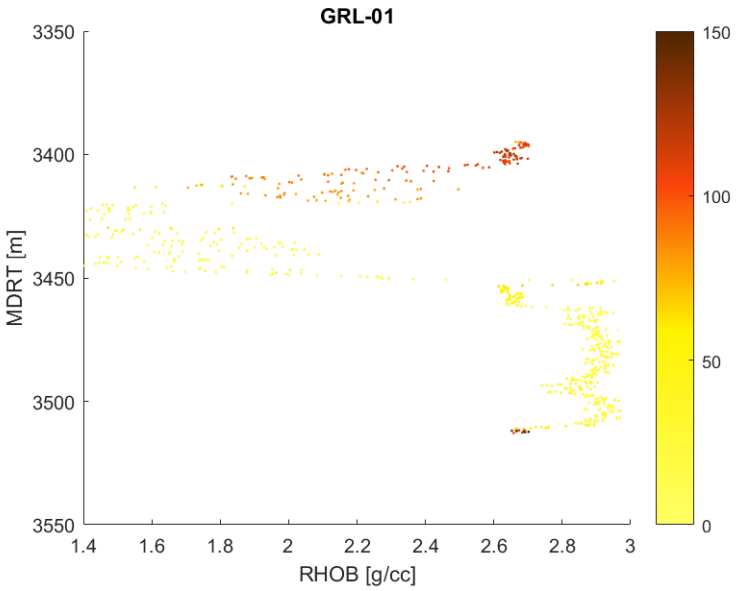


**Figure 58**: Measured distance from the rotary table vs. bulk density combined with the gamma ray log in [GAPI] for the Zechstein Group for well GRL-01. Note the very low bulk density values between 3400-3450 m which are circumspect and the very high bulk density values that are of anhydrite.

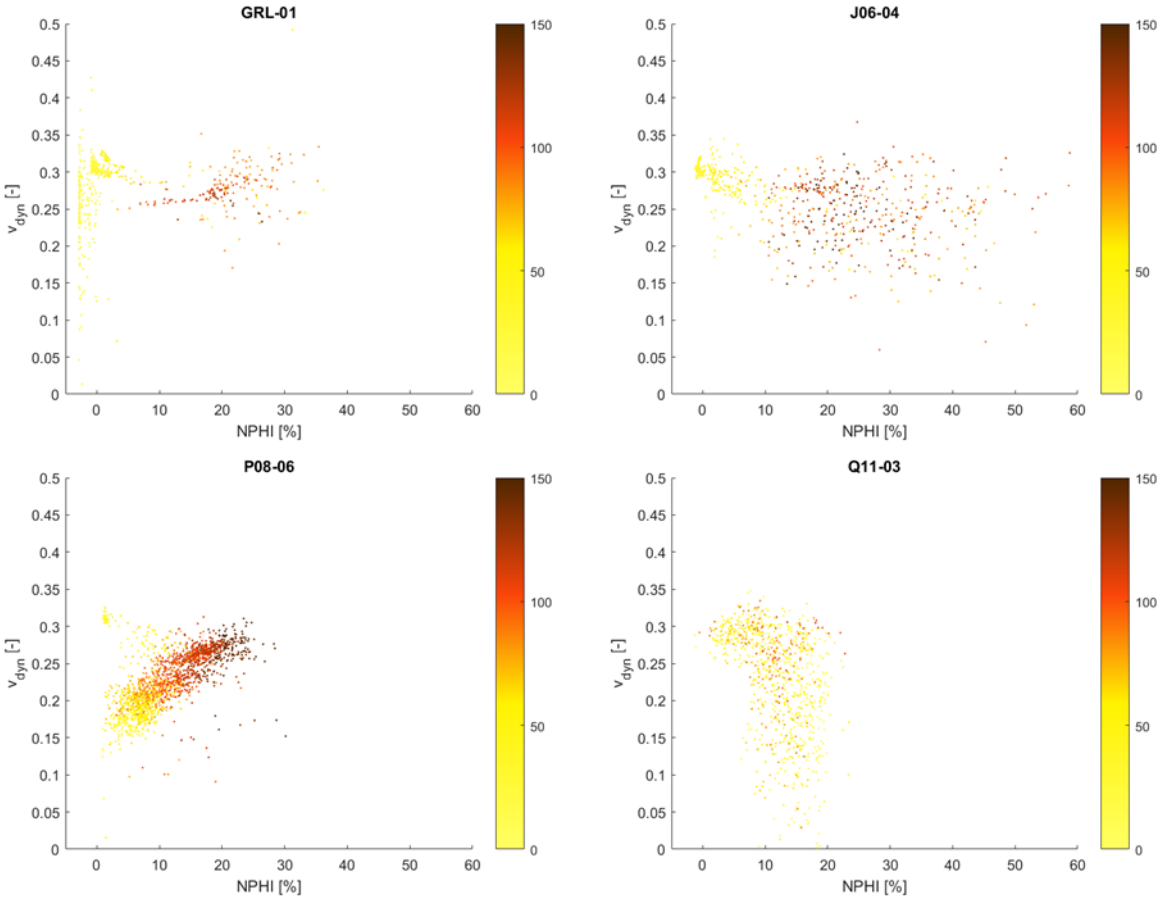


**Figure 59**: Dynamic Poisson's ratio vs. neutron porosity combined with the gamma ray log in [GAPI] for the Lower Germanic Triassic Group for wells GRL-01, J06-04, P08-06 and Q11-03. The clustering for the Poisson's ratio is somewhat similar in behaviour to the Young's modulus, with P08-06 showing a clear lithological trend and GRL-01 and J06-04 in part.

The Poisson's ratio in Figure 59 shows a similar behaviour to the Young's modulus as distinct clusters can be discerned in all wells but Q11-03. Well P08-06 shows that the Poisson's ratio decreases with decreasing neutron porosity. The anhydrite in wells GRL-01 and J06-04 shows a narrow band of values around $v_{dyn}$ = 0.30. Note that the vertical values with a low gamma ray for GRL-01 should be ignored.

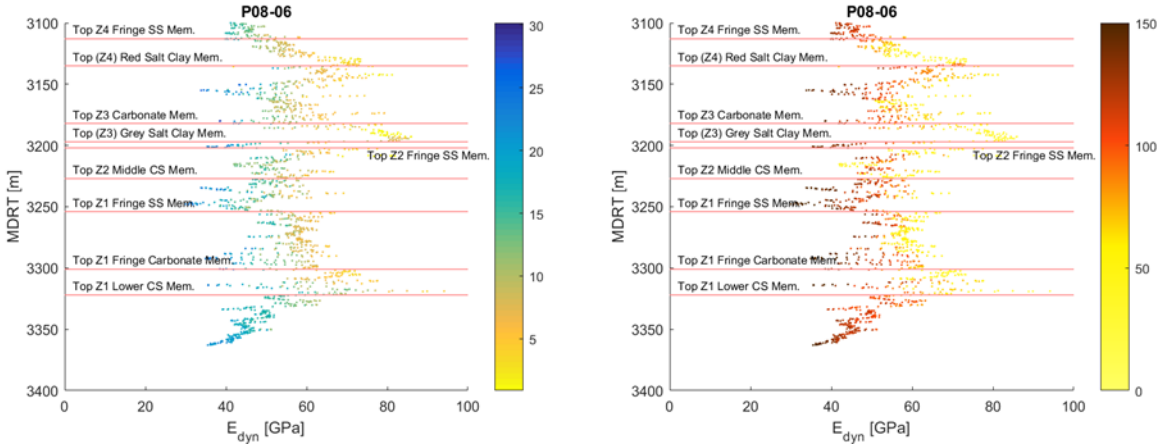


**Figure 60**: Measured distance from the rotary table vs. dynamic Young's modulus combined with the neutron porosity log in [%] (left) and the gamma ray log in [GAPI] (right) for the Zechstein Group for well P08-06. The Z3 Carbonate Member is easily distinguished by the low neutron porosity and low gamma ray response.

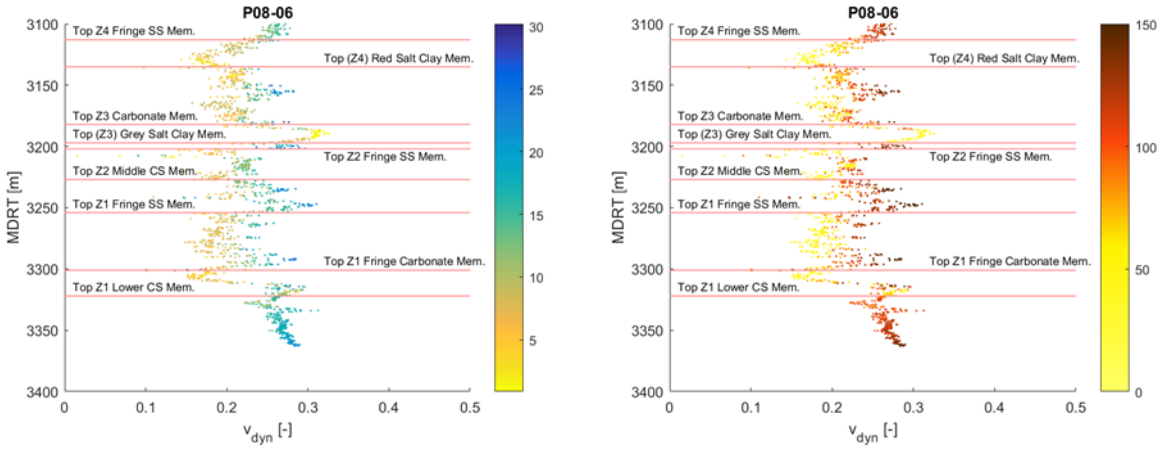


**Figure 61**: Measured distance from the rotary table vs. dynamic Poisson's ratio combined with the neutron porosity log in [%] (left) and the gamma ray log in [GAPI] (right) for the Zechstein Group for well P08-06. Note that the (Z3) Grey Salt Clay Member is particularly distinguishable.

Figure 57 and Figure 59 show that there is a separation in lithologies for rocks in well P08-06. This can be seen in Figure 60 and Figure 61 above. Rocks with a higher neutron porosity also have a higher gamma ray response and the opposite is the case for rocks with a low neutron porosity. What is noticeable is that rocks with a low gamma ray have a higher Young's modulus combined with a lower Poisson's ratio.

Wells GRL-01 and J06-04 show the widest range of Young's modulus values (Figure 62), whilst P08-06 and Q11-03 have a narrower range. The reference value of the *NAM* appears to have a good match with the data when using the McCann and Entwisle (1992) conversion. The value for the anhydrite only has a good match with the anhydrite in well J06-04. The Poisson's ratio from Orlic (2016) has a poor match as does the *NAM* value for anhydrite (0.35) as the mean for the data is around 0.30. All four wells show quite a large range of possible values for the Poisson's ratio.

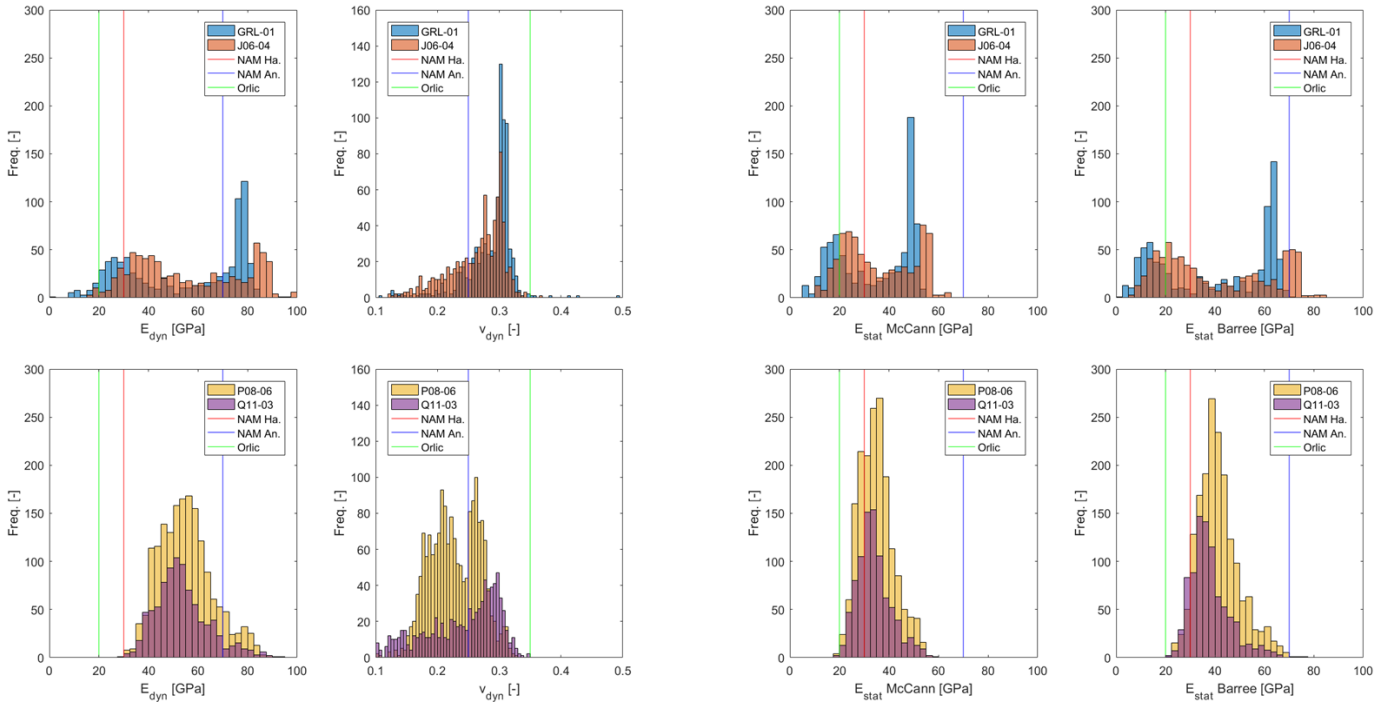


**Figure 62**: Histograms showing dynamic Young's modulus and dynamic Poisson's ratio (left) with the converted static Young's modulus (right) for the Zechstein Group for wells GRL-01, J06-04, P08-06 and Q11-03. Wells GRL-01 and J06-04 show a wide range of Young's moduli, but a more narrow distribution of Poisson's ratios. The opposite is the case for P08-06 and Q11-03.

## 3.2.9 Upper Rotliegend Group

For the Upper Rotliegend Group 3 wells are shown: L05-06, P08-06 and Q11-03. The data from well L05-06 is split into two graphs (Figure 63) where the left subplot includes the Silverpit Formation and the right one without. The other two wells did not contain the Silverpit Formation. From all three wells it is clear that there is a relationship between the neutron porosity and the Young's modulus.

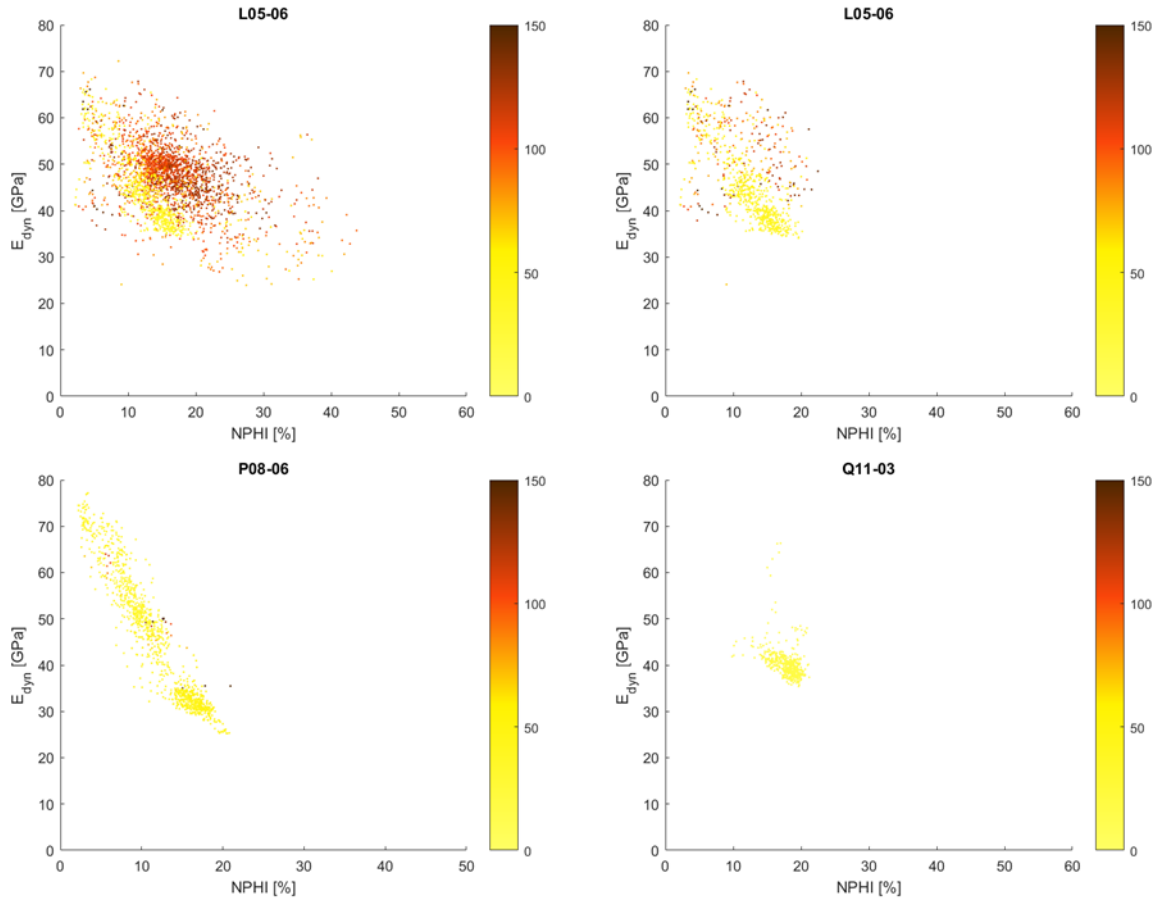


**Figure 63**: Dynamic Young's modulus vs. neutron porosity combined with the gamma ray log in [GAPI] for the Upper Rotliegend Group for wells L05-06, P08-06 and Q11-03. The top two subplots show the Silverpit Formation and Slochteren Formation together (left) and the Slochteren Formation by itself (right). Note that for the Slochteren Formation well P08-06 shows a very clear trend with the neutron porosity, which is less so for L05-06 and Q11-03.

Figure 64 shows that there are two distinct zones within the Slochteren Formation in well P08-06 which can be seen in both the Young's modulus and Poisson's ratio. These two zones are represented by the two clusters in Figure 63. The lower part of the formation has a considerably lower neutron porosity than the upper part. Figure 65 shows that the gamma ray response is constant throughout the interval and that the cause is probably not due to clay content.

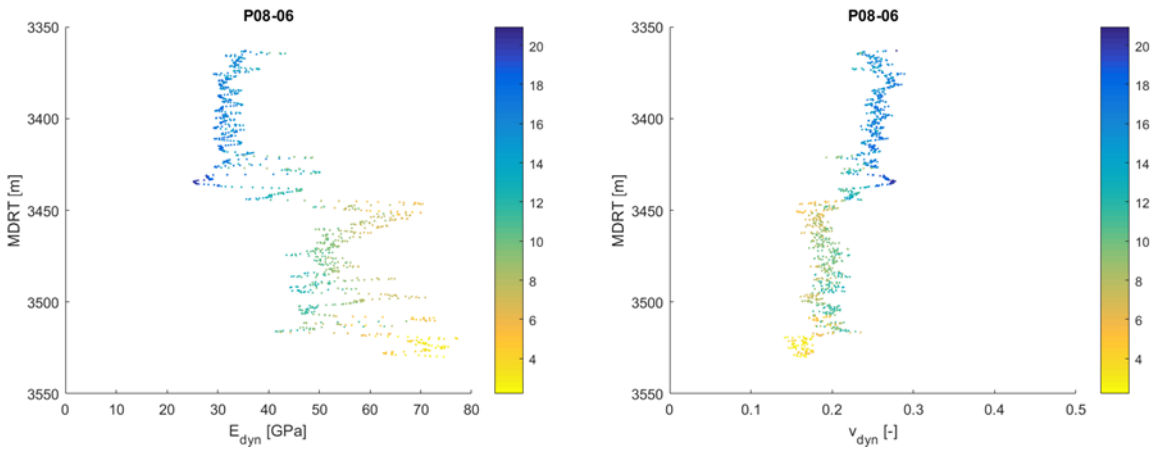


**Figure 64**: Dynamic Young's modulus (left) and. dynamic Poisson's ratio (right) vs. MDRT combined with the neutron porosity log in [%] for the Upper Rotliegend Group, in this case the Slochteren Formation, for well P08-06. Note that even within the Slochteren Formation there two distinct zones which can be seen in the by the two clusters in Figure 3.35 and Figure 3.37.

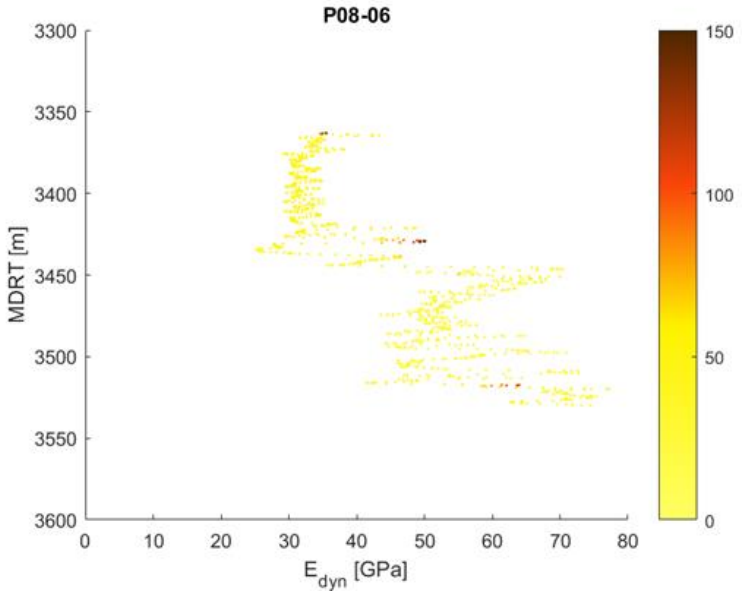


**Figure 65**: Dynamic Young's modulus vs. MDRT combined with the gamma ray log in [GAPI] for the Slochteren Formation for well P08-06. Note that the entire Slochteren interval has low gamma ray response.

Figure 66 shows the dynamic Poisson's ratio for the three wells and the behaviour between them is clearly different and does not show the similarities seen for the Young's modulus. Again the Upper Rotliegend for L05-06 is split into a subplot showing the entire interval (left) and only the Slochteren Formation (right). Note the two clusters for well P08-06.

The contrast between the Silverpit Formation and Slochteren Formation (Lower Slochteren Member) can be seen in Figure 67 by using the gamma ray log. Both formations show a wide range in values, but differences can be seen. The Young's modulus is a bit lower for the Slochteren rock (Figure 63) and the Poisson's ratio is a bit lower as well (Figure 66).

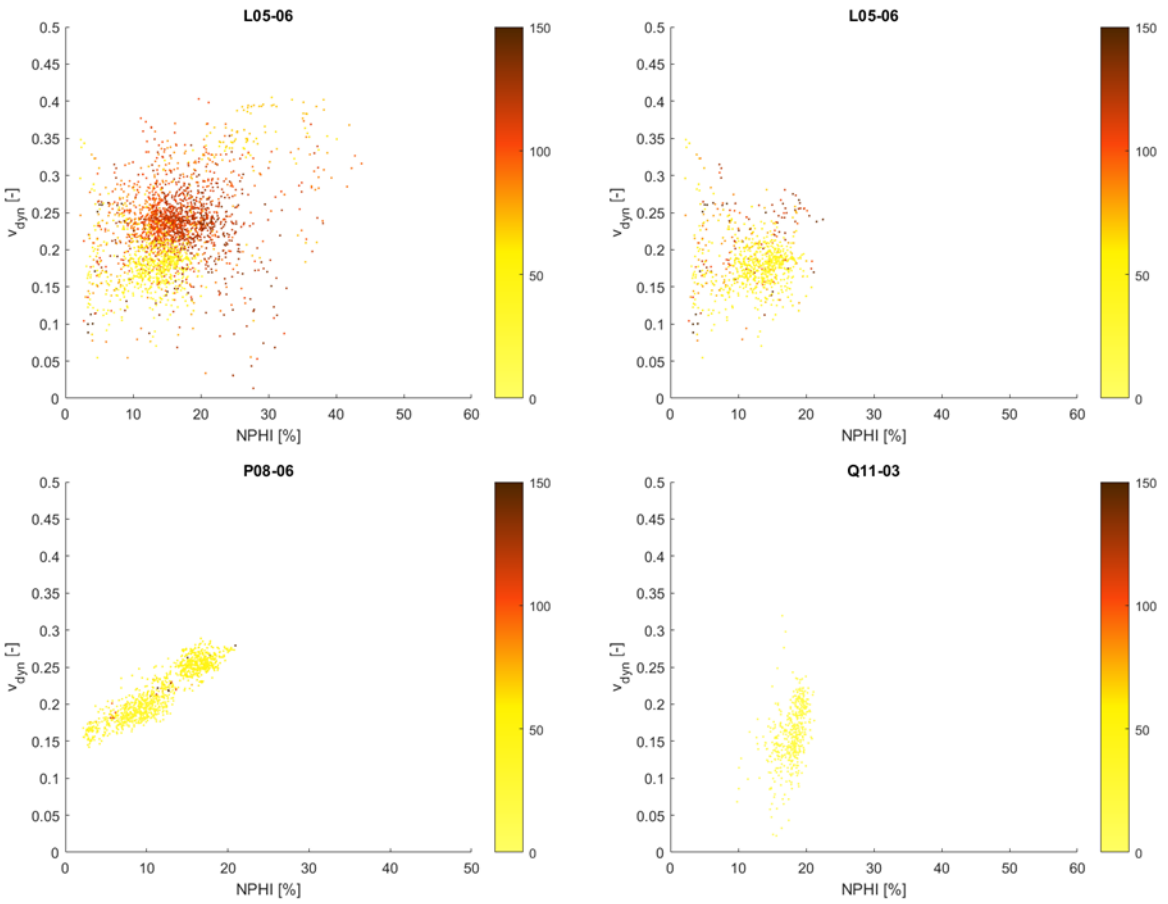


**Figure 66**: Dynamic Poisson's ratio vs. neutron porosity combined with the gamma ray log in [GAPI] for the Upper Rotliegend Group for wells L05-06, P08-06 and Q11-03. The top two subplots show the Silverpit Formation and Slochteren Formation together (left) and the Slochteren Formation by itself (right). Note that for the Slochteren Formation well P08-06 shows a very clear trend with the neutron porosity, which is less so for L05-06 and Q11-03.

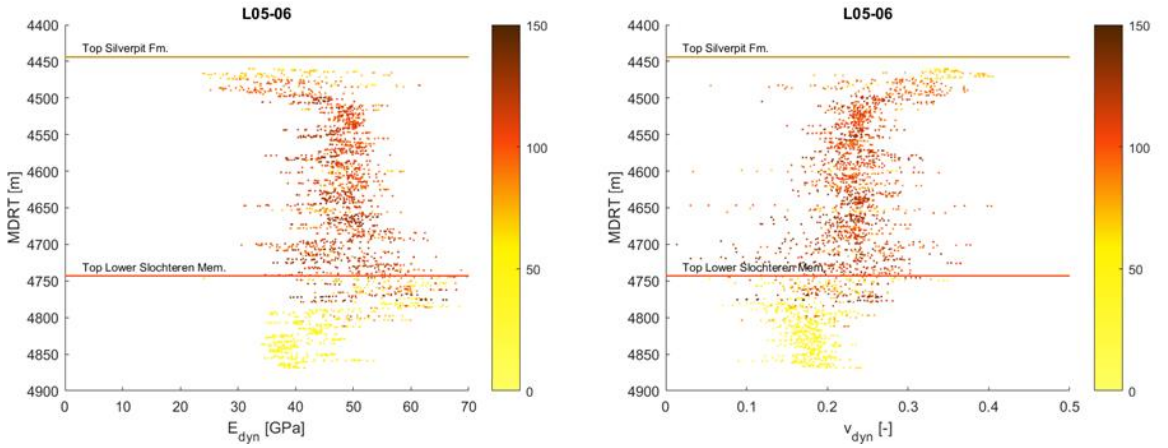


**Figure 67**: Dynamic Young's modulus (left) vs. dynamic Poisson's ratio (right) combined with the gamma ray log in [GAPI] for the Upper Rotliegend Group for well P08-06. The two formations are not easily distinguished without the aid of the gamma ray log. Note that the Poisson's shows two vertical columns, thus indicating the difference between the two rock types.

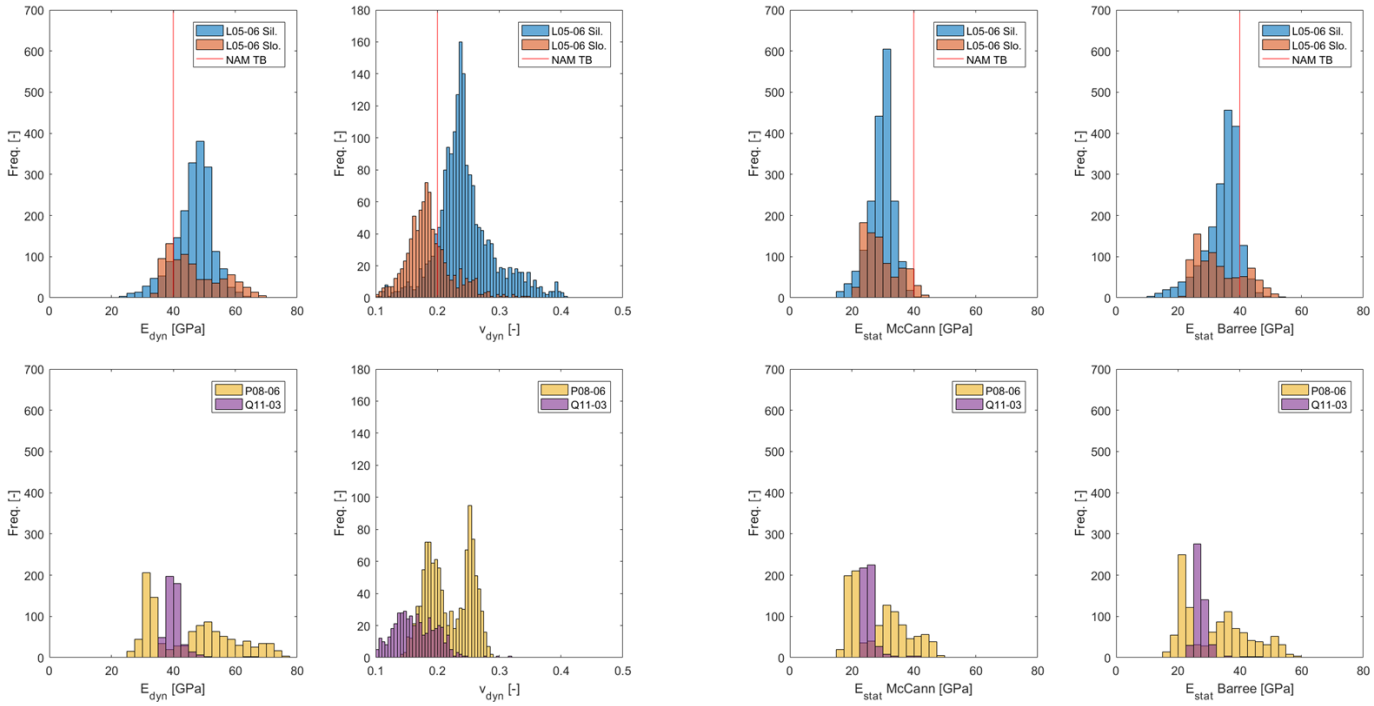


**Figure 68**: Histograms showing dynamic Young's modulus and dynamic Poisson's ratio (left) with the converted static Young's modulus (right) for the Upper Rotliegend Group for wells L05-06, P08-06 and Q11-03. All four wells shows a wide range for the Poisson's ratio. The Young's moduli show a narrower range, particularly Q11-03. The NAM range for Young's modulus for the Slochteren reservoir is 1-40 GPa.

Figure 68 shows the distributions for the elastic parameters for the three wells. The characteristics of the Slochteren rock is based on porosity distributions which can be found in Appendix E. The Young's modulus ranges between 1 and 40 GPa (Table 1). When looking at the McCann conversion, wells L05-06 and P08-06 fall within this range. Most of P08-06 also falls into this range, but a small amount of values exceeds it. It is clear that the rock in well Q11-03 has a very narrow range of values for the Young's modulus. For the Poisson's ratio wells L05-06 and Q11-03 have a similar range and P08-06 has two clear peaks. Note the clear difference between the Silverpit and the Slochteren for the Poisson's ratio and the poor match of the value used by the *NAM*.

Four tables have been constructed that contain the mean, median and standard deviation for the dynamic Poisson's ratio, dynamic Young's modulus, converted static Young's modulus using McCann and Entwisle (1992) and converted static Young's modulus using Barree et al. (2009) can be found in Appendix I.

## 3.2.10 NAM Wells

Data has been obtained from two wells of which the LIS and LAS files are not publically available yet. For this reason these two wells have been separated from the others. The same approach has been undertaken with these wells as previously. Note that the logged interval for these two is considerably longer than for any other well. Effectively the entire well is covered by shear wave acoustic data giving a complete overview of the differences of the varying geological units. Both wells have a short interval covered by the neutron porosity around reservoir level, but not for the rest of the well. Therefore there are no scatter plots for the overburden units.

### 3.2.10.1 Well BRW-05

Figure 69 shows the dynamic Young's modulus for well BRW-05 versus measured distance from the rotary table. The complete overview shows the striking differences between certain geological units. There is a large increase in the Young's modulus starting at the Chalk. The Chalk group shows a large variability which is also seen in well BIR-13 (Figure 37). There is a general increase in the Young's modulus with depth until the top of the Rijnland Group. The halite in the Zechstein is clearly visible by the constant interval.

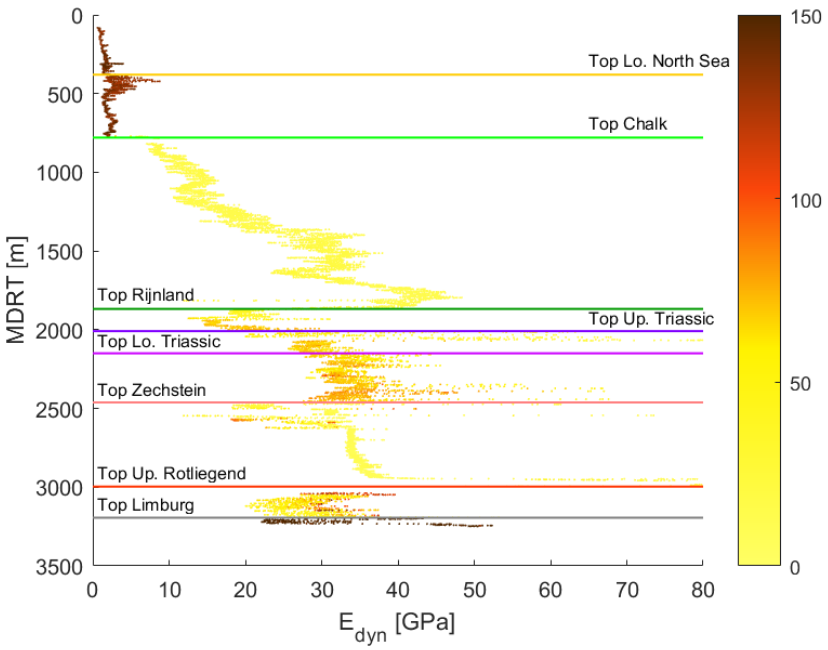


**Figure 69**: Dynamic Young's modulus vs. MDRT for well BRW-05. The well tops for the different geological groups have been added. The colour bar indicates the gamma ray response in [GAPI]. Note the general increase in Young's modulus with depth until the Rijnland Group. Within the Zechstein Group there is a noticeable constant interval from 2650 m. One can clearly distinguish the North Sea groups from the others by their high gamma ray response.

The dynamic Poisson's ratio shows a steady decrease with depth (Figure 70) until the top of the Rijnland Group is reached. As with the Young's modulus there is a clear jump ounce the Chalk Group is reached. Both Germanic Triassic groups show a relatively wide range of values, as does the Limburg Group. Note the vertical interval in the Zechstein Group. The bulk density (Figure 71) is a useful log to distinguish the different units. The halite, for instance, is clearly visible due to the low and constant value.

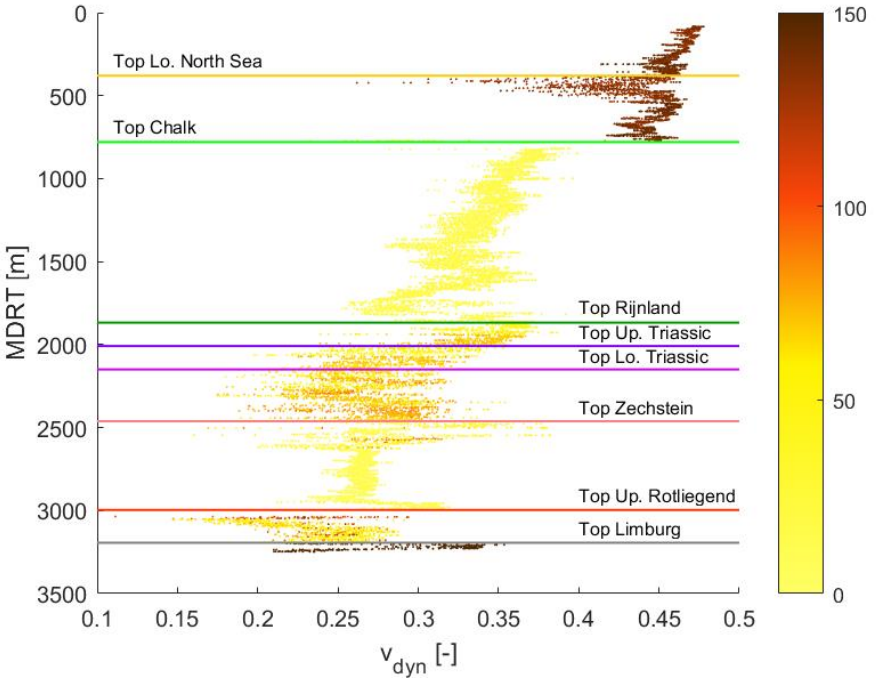


**Figure 70**: Dynamic Poisson's ratio vs. MDRT for well BRW-05. The well tops for the different geological groups have been added. The colour bar indicates the gamma ray response in [GAPI]. Note the decrease in value with depth until around 2000 m MDRT. After this it tends to vary between 0.2 and 0.3.

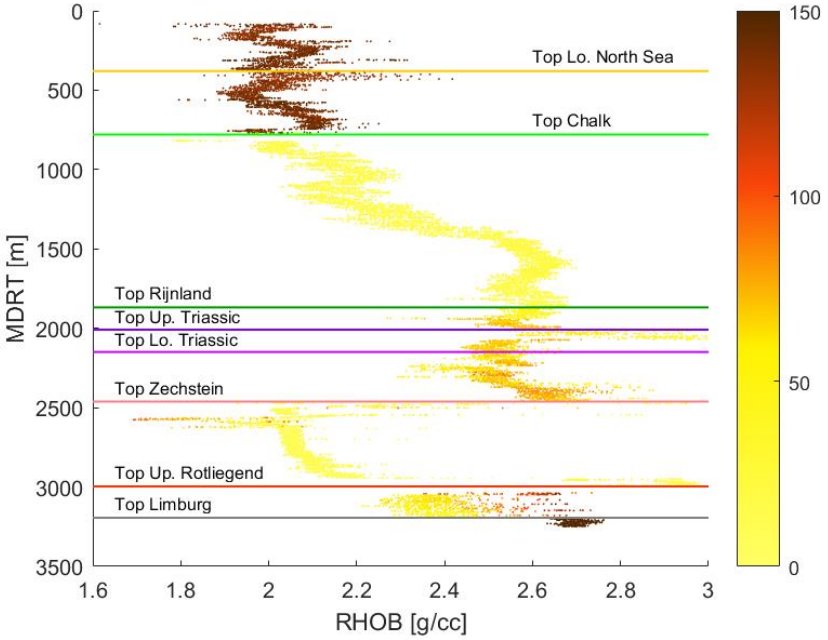


**Figure 71**: Bulk density vs. MDRT for well BRW-05. The well tops for the different geological groups have been added. The colour bar indicates the gamma ray response in [GAPI]. The Chalk Group and the Zechstein Group both show an increase with depth. For the Zechstein group there is a noticeable constant interval in the middle.

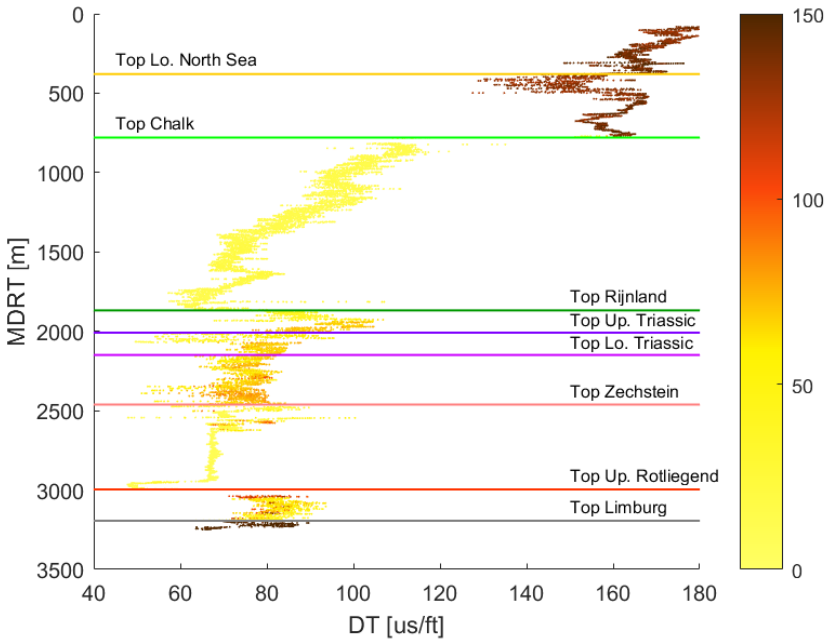


**Figure 72**: Acoustic travel time vs. MDRT for well BRW-05. The well tops for the different geological groups have been added. The colour bar indicates the gamma ray response in [GAPI]. Note the constant behaviour for the Zechstein Group. And the clear increase with depth for the North Sea and Chalk.

Figure 72 shows the acoustic slowness for the compression wave. Note the very large jump between the Chalk Group and the Lower North Sea Group which explains the changes in the Young's modulus and Poisson's ratio. The halite in the Zechstein shows a very constant behaviour.

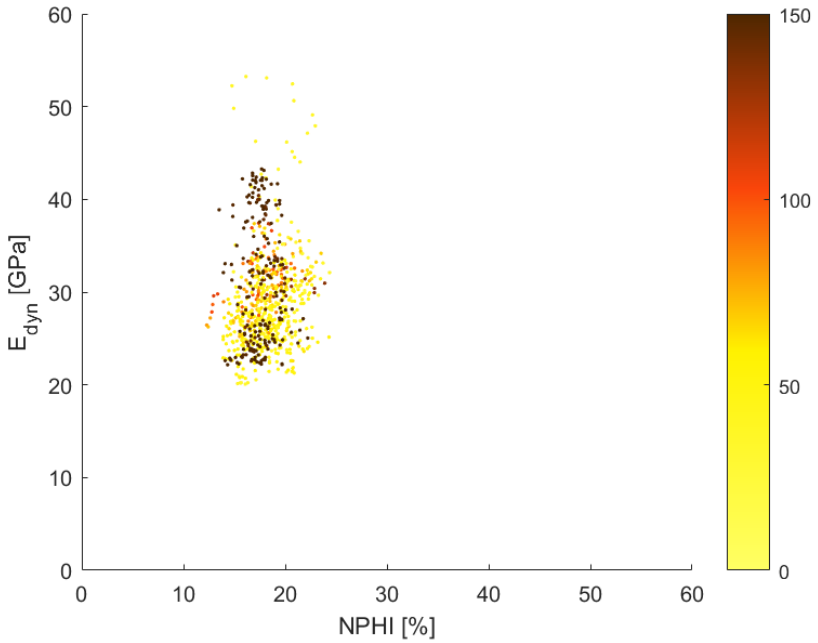


**Figure 73**: Dynamic Young's modulus vs. neutron porosity for the Rotliegend, specifically the Slochteren Formation, for well BRW-05. The colour bar indicates the gamma ray response in [GAPI]. Note the relatively large amount of high gamma ray response material.

Interestingly there is no discernible trend in the Young's modulus when combined with the neutron porosity for the Slochteren Formation (Figure 73), but the range of values is quite narrow. The figure shows that there is high gamma ray material in the reservoir unit.

### 3.2.10.2 Well ZRP-02

Well ZRP-02 is the second well obtained from the *NAM*. Figure 74 shows the dynamic Young's modulus for well ZRP-02 versus measured distance from the rotary table. The results are similar to BRW-05 and the complete overview shows the striking differences between certain geological units. There is a large increase in the Young's modulus starting at the Chalk. The Chalk group shows a large variability which is also seen in well BIR-13 (Figure 37). There is a general increase in the Young's modulus with depth until the top of the Rijnland Group. The halite in the Zechstein is clearly visible by the constant interval which is longer for ZRP-02 than BRW-05. Note that the Upper Germanic Triassic is absent in this well.

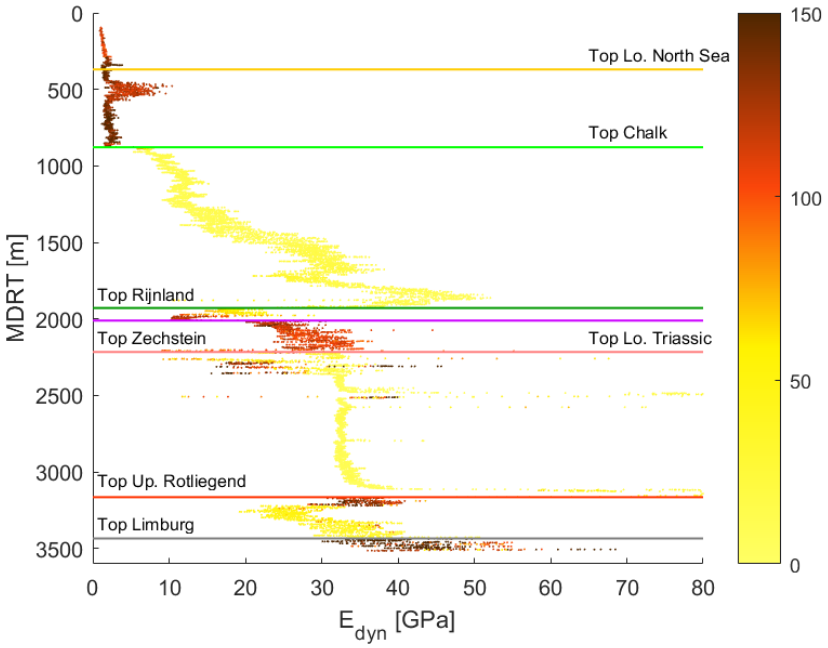


**Figure 74**: Dynamic Young's modulus vs. MDRT for well ZRP-02. The well tops for the different geological groups have been added. The colour bar indicates the gamma ray response in [GAPI]. Note the general increase in Young's modulus with depth until the Rijnland Group. The Chalk Group clearly shows a large amount of variability.

The dynamic Poisson's ratio shows a steady decrease with depth (Figure 75) until the top of the Rijnland Group is reached. As with the Young's modulus there is a clear jump ounce the Chalk Group is reached. Both Germanic Triassic groups show a relatively wide range of values, as does the Limburg Group. Note the vertical interval in the Zechstein Group. The bulk density (Figure 76) is a useful log to distinguish the different units. The halite, for instance, is clearly visible due to the low and constant value.

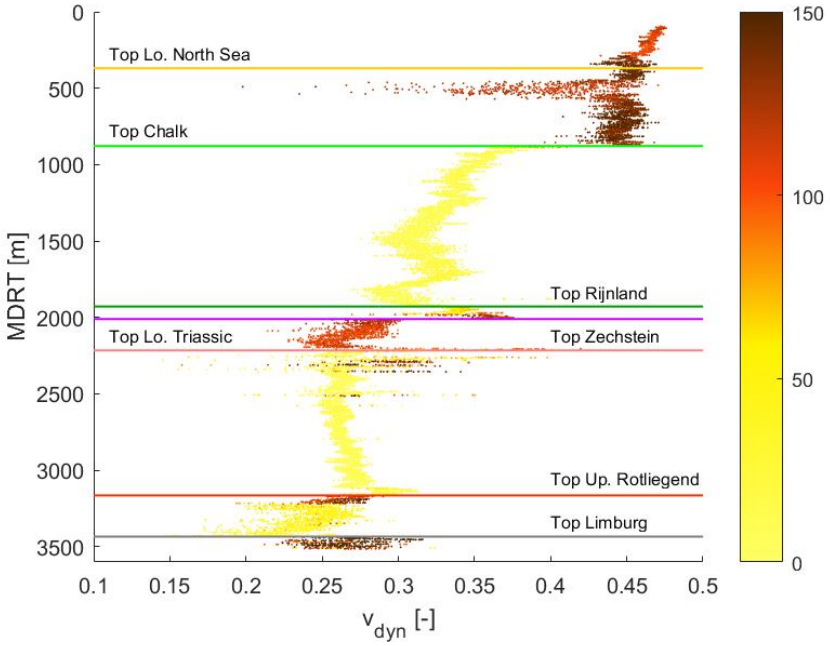


**Figure 75**: Dynamic Poisson's ratio vs. MDRT for well ZRP-02. The well tops for the different geological groups have been added. The colour bar indicates the gamma ray response in [GAPI]. Note the decrease in value with depth until around 2000 m MDRT. After this it tends to vary between 0.2 and 0.3.

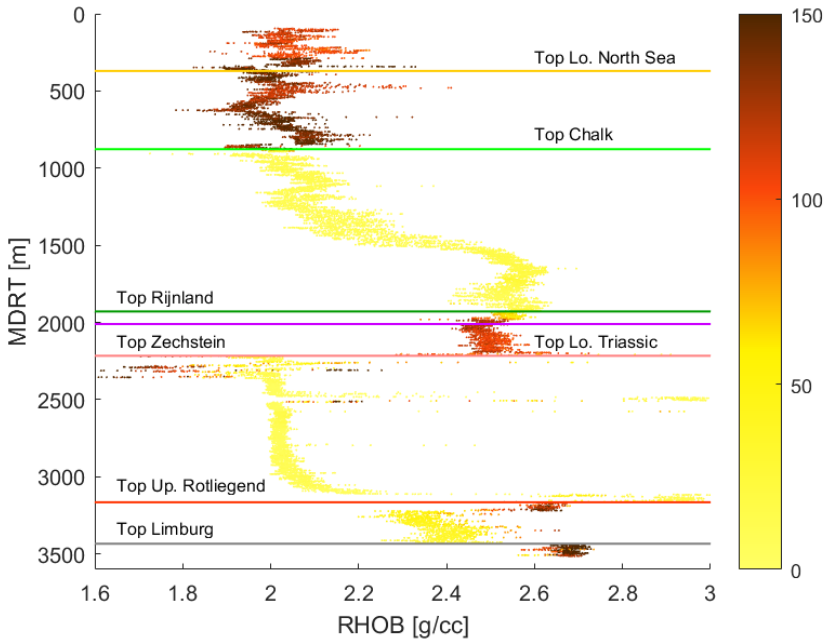


**Figure 76**: Bulk density vs. MDRT for well ZRP-02. The well tops for the different geological groups have been added. The colour bar indicates the gamma ray response in [GAPI]. The Chalk Group shows a general increase with depth. The Zechstein Group also shows an increase with depth after a long constant interval.

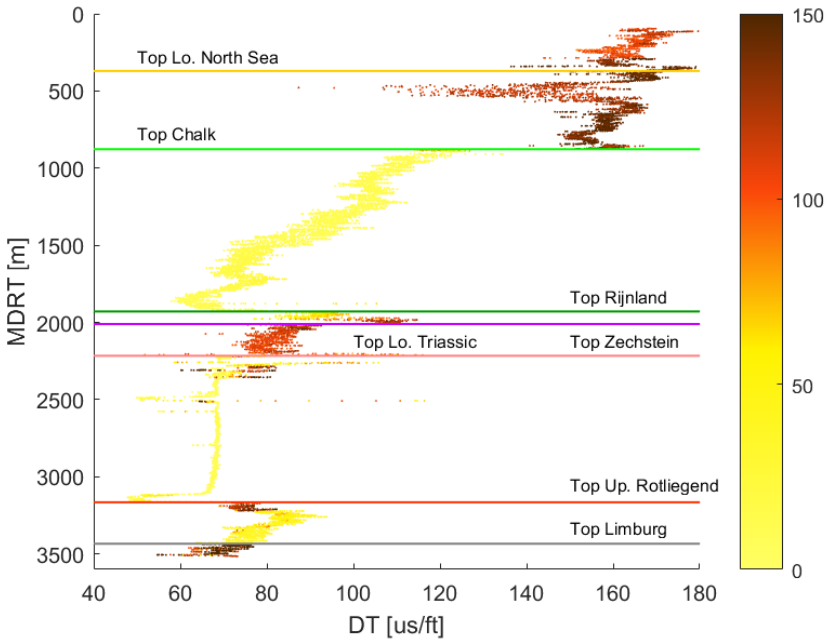


**Figure 77**: Acoustic travel time vs. MDRT for well ZRP-02. The well tops for the different geological groups have been added. The colour bar indicates the gamma ray response in [GAPI]. Note the constant behaviour for the Zechstein Group.

Figure 77 shows the acoustic slowness for the compression wave. Note the very large jump between the Chalk Group and the Lower North Sea Group which explains the changes in the Young's modulus and Poisson's ratio. The halite in the Zechstein shows a very constant behaviour and has a longer interval than BRW-05.

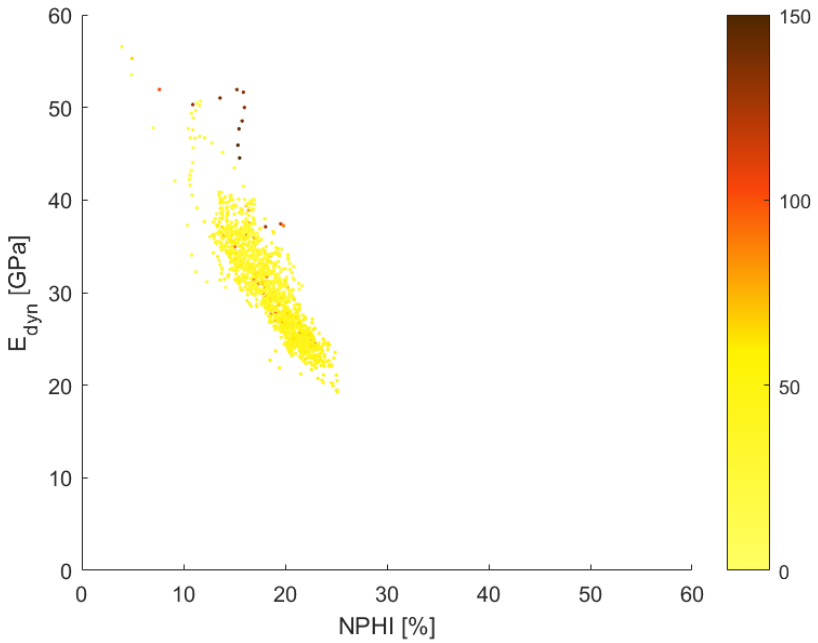


**Figure 78**: Dynamic Young's modulus vs. neutron porosity for the Rotliegend, specifically the Slochteren Formation, for well ZRP-02. The colour bar indicates the gamma ray response in [GAPI]. Note the clear linear trend of the data cloud.

Figure 78 shows that the Slochteren rock in ZRP-02 does show a trend between the neutron porosity and the dynamic Young's modulus. Note that there is gas in the well, which reduces the neutron porosity and also the dynamic Young's modulus by lowering the bulk density.

### 3.2.11.2 Histograms of the Elastic Parameters

Figure 79 shows the distributions of the two *NAM* wells for the Upper North Sea Group and Lower North Sea Group. Both groups show very narrow distriubtions for both the Young's modulus and the Poisson's ratio. The material of the Lower North Sea is more rigid and has a lager spread of values. The reference values do not match well with the data and extremely poorly for the Poisson's ratio.

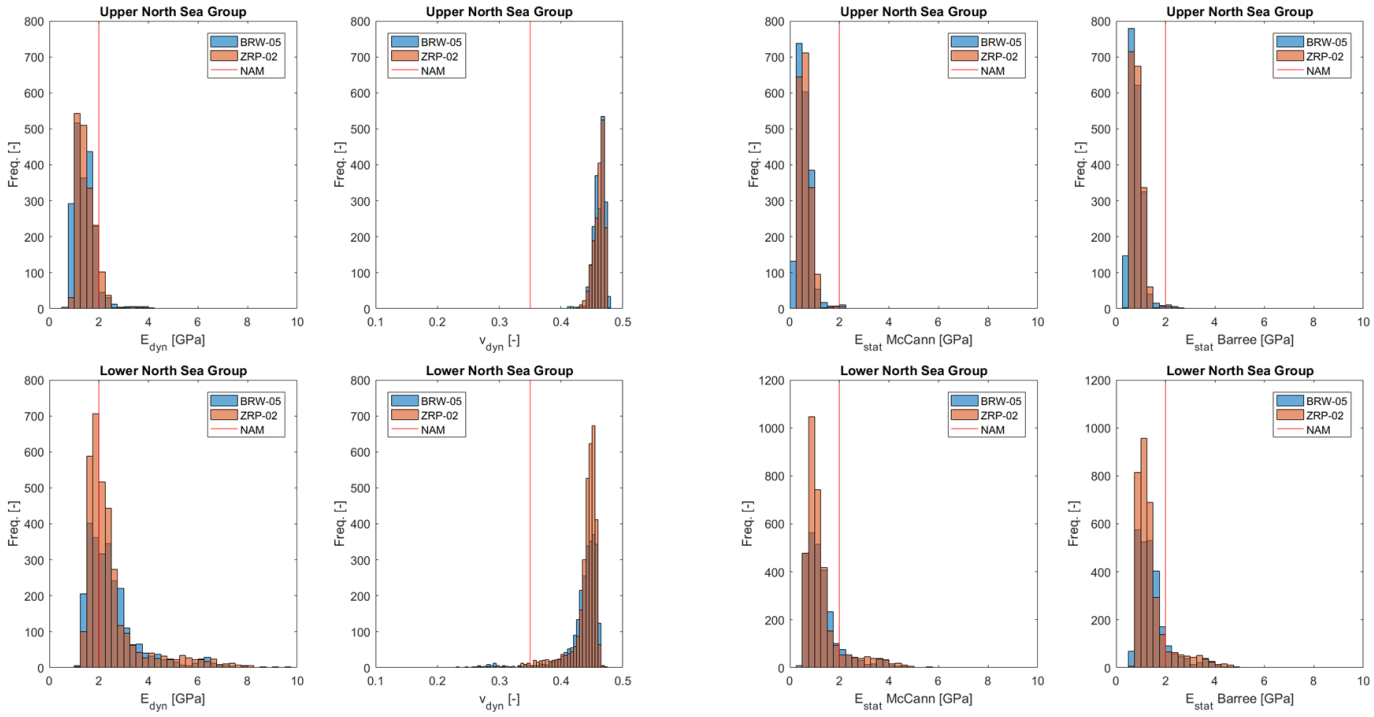


**Figure 79**: Histograms showing dynamic Young's modulus and dynamic Poisson's ratio (left) with the converted static Young's modulus (right) for the Upper North Sea Group and Lower North Sea Group for wells BRW-05 and ZRP-02. Neither the reference Poisson's ratio nor the Young's modulus fit the respective plots well. Both elastic moduli show a narrow range of values. Note that the reference Young's modulus does fit the dynamic Young's modulus.

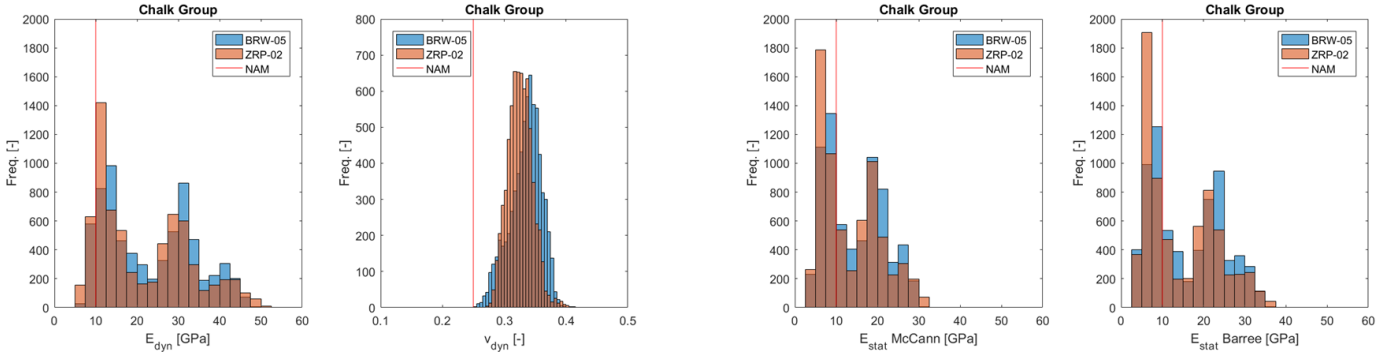


**Figure 80**: Histograms showing dynamic Young's modulus and dynamic Poisson's ratio (left) with the converted static Young's modulus (right) for the Chalk Group for wells BRW-05 and ZRP-02. The reference Poisson's ratio does not fit the data. The dynamic Young's modulus for the Chalk group has a wide spread with the dynamic values showing three distinct groups.

The Chalk Group (Figure 80) has a similarly wide distribution for BRW-05 and ZRP-02 as with well BIR-13. The distribution cannot be captured by the reference value of the *NAM* and whilst it is a good fit for the less rigid top part of the group, it does not fit well with the more rigid parts that are deeper in the subsurface. The Poisson's ratio does not match at all with the data. For the Rijnland Group (Figure 81) the reference value for the static Young's modulus shows a poor match. The distriubtion of the Young's modulus is noteceably narrower than for the Chalk Group. Just as with the Chalk, the Poisson's ratio does not overlap with the data.

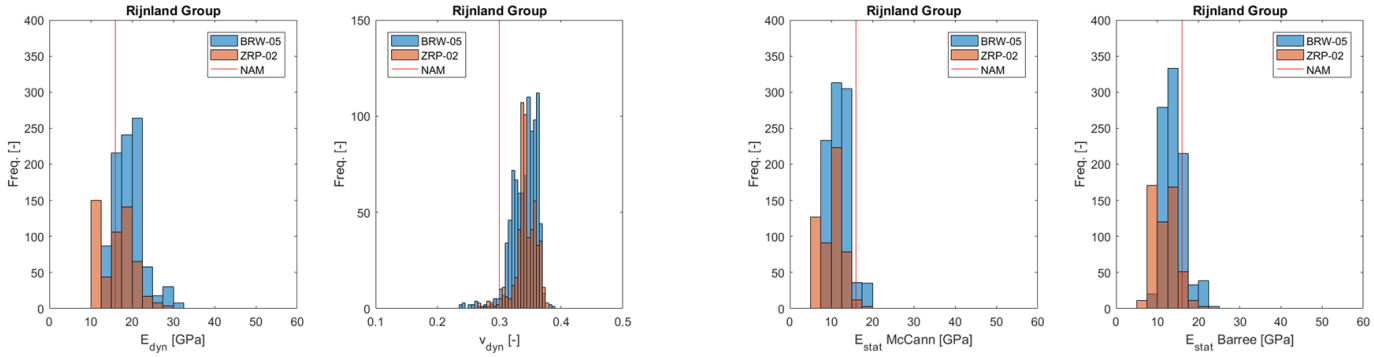


**Figure 81**: Histograms showing dynamic Young's modulus and dynamic Poisson's ratio (left) with the converted static Young's modulus (right) for the Chalk Group for wells BRW-05 and ZRP-02. The reference Poisson's ratio does not fit the data. The Rijnland shows a greater concentration with the Barree et al. (2009) conversion showing the better fit.

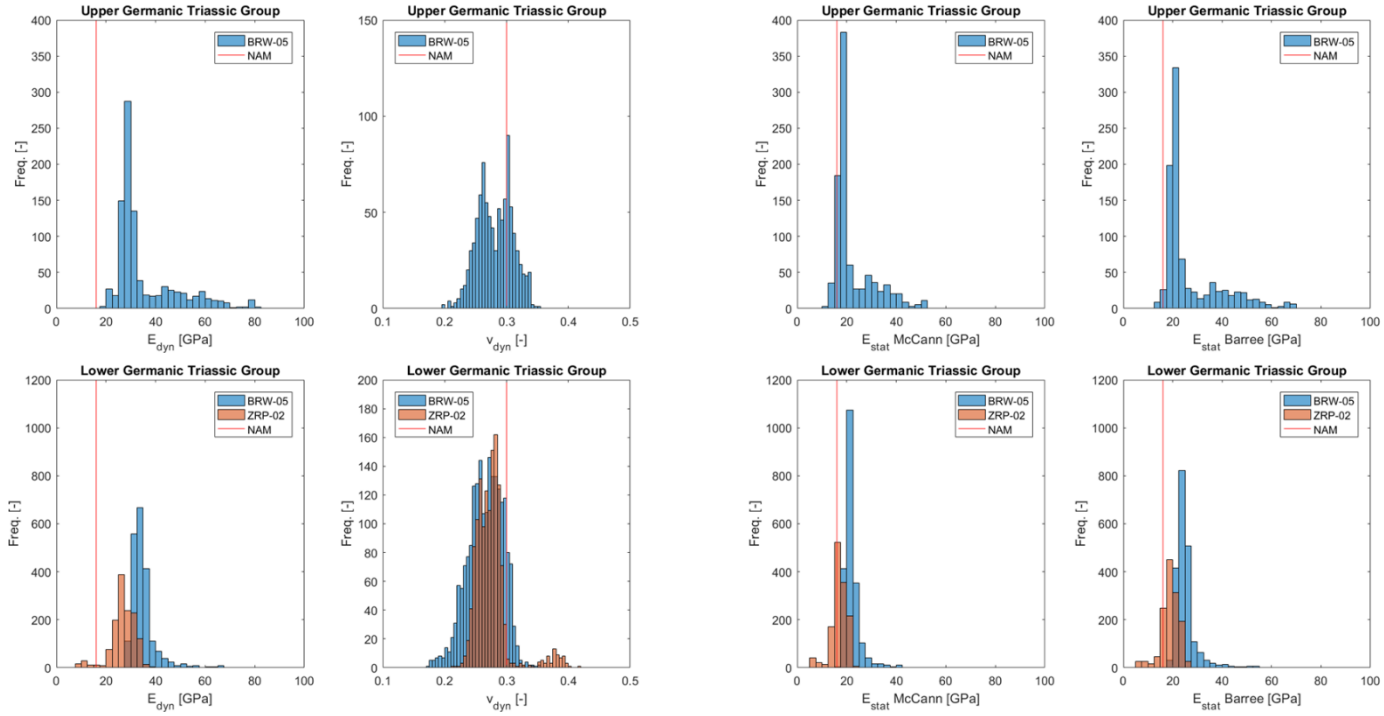


**Figure 82**: Histograms showing dynamic Young's modulus and dynamic Poisson's ratio (left) with the converted static Young's modulus (right) for the Upper Germanic Triassic Group and Lower Germanic Triassic Group for wells BRW-05 and ZRP-02. The reference value for the Poisson's ratio for the Upper Triassic shows a good fit for one of the data clouds. The number for the Lower Triassic has a poor match with both wells. The McCann and Entwistle (1992) conversion shows a good fit for ZRP-02 and comes quite close to the data for the Upper Triassic.

Figure 82 shows the distributions for the Upper Germanic Triassic and Lower Germanic Triassic Group. There is a clear concentration of values within the Upper Germanic Triassic, but also a wide range of values for the Young's modulus. The *NAM* reference value comes quite close to the peak for the McCann and Entwisle conversion. The reference Poisson's ratio matches well with one of the clusters, but not with the other. When looking at the Lower Germanic Triassic it is clear that this group also has a concentration of values, but a narrower range for the Young's modulus. The *NAM* reference matches well with ZRP-02 but not with BRW-05. The Poisson's ratio does not fit either well for the Lower Germanic Triassic. Note the difference in distribution for the two wells, where ZRP-02 has a narrower band for most of the values, but also a small cluster of higher values.

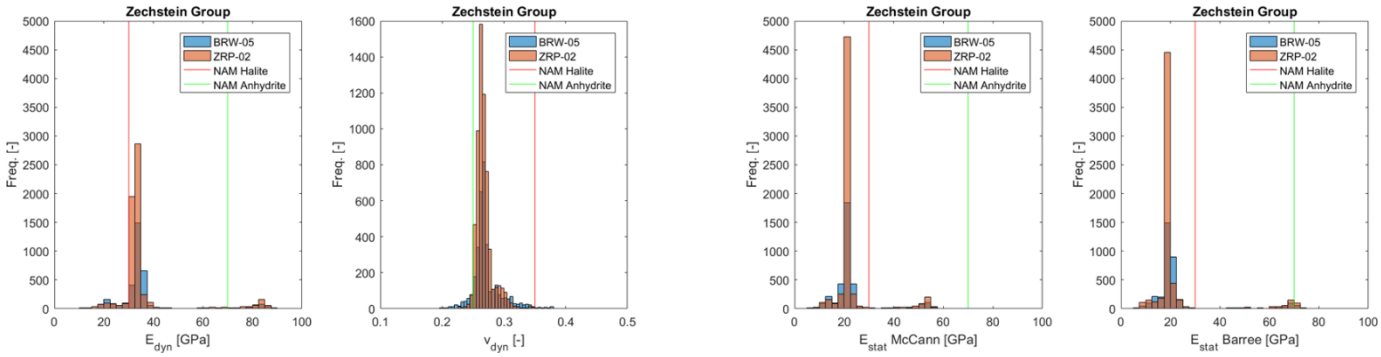


**Figure 83**: Histograms showing dynamic Young's modulus and dynamic Poisson's ratio (left) with the converted static Young's modulus (right) for the Zechstein Group for wells BRW-05 and ZRP-02.

Figure 83 shows that, for Zechstein Group, the vast majority of values fall in a narrow range. Note the small cluster of much higher Young's modulus values. For the Barree et al. (2009) conversion the cluster matches well with the *NAM* value for anhydrite. The Poisson's ratio also has a narrow range, especially well ZRP-02. The reference value for Halite does not match the data by a wide margin. The differences in Young's modulus between the halite and anhydrite can be clearly seen in these histograms. Note that due to the relative purity of evaporates it is interesting to compare the data for the Zechstein to other, more general, literature values. Markov et al. (1998) show that halite has a Poisson's ratio of 0.25 which is very different from the *NAM* value, but would fit the data much better. When using parameters from Markov et al. the Young's modulus for halite is around 36 GPa so in this case the dynamic Young's modulus is closer to 'real' value than the converted static values. This is probably due to the very low porosity of salts. According to the same source, anhydrite has a value of around 0.28 which is a bit different from the *NAM* value. The two reference values from Markov et al. (1998) give a Young's modulus of 75 and 85 GPa. The latter is close to the dynamic values of the basal anhydrite in the Zechstein Group (Figure 83).

No histograms have been made for the Upper Rotliegend Slochteren rocks as these are assumed to be filled with gas that distorts the dynamic elastic parameters. If these are to be looked at then correction should be applied to compensate for the gas saturation.

### 3.2.11.3 Tabulated values

The tables below show the dynamic Poisson's ratio (Table 6), dynamic Young's modulus (Table 7), converted static Young's modulus using McCann and Entwissle (1992) (Table 8) and converted static Young's modulus using Barree et al. (2009) (Table 9) for wells BRW-05 and ZRP-02.

**Table 6**: Dynamic Poisson's ratio values for the wells BRW-05 and ZRP-02. *In the provided data there was no specified top for the Upper North Sea Group, however it is assumed to be the first encountered unit. **The Upper North Sea Group for well ZRP-02 also contains around 30 metres of Middle North Sea Group

| Unit | Well | Mean $v_{dyn}$ [-] | Median $v_{dyn}$ [-] | Std. $v_{dyn}$ [-] |
|---|---|---|---|---|
| Up. North Sea* | BRW-05 | 0.463 | 0.461 | 0.010 |
| Up. North Sea** | ZRP-02 | 0.463 | 0.426 | 0.009 |
| Lo. North Sea | BRW-05 | 0.434 | 0.443 | 0.032 |
| Lo. North Sea | ZRP-02 | 0.438 | 0.446 | 0.029 |
| Chalk | BRW-05 | 0.334 | 0.338 | 0.026 |
| Chalk | ZRP-02 | 0.326 | 0.325 | 0.020 |
| Rijnland | BRW-05 | 0.341 | 0.345 | 0.021 |
| Rijnland | ZRP-02 | 0.343 | 0.342 | 0.018 |
| Up. Germanic Triassic | BRW-05 | 0.282 | 0.283 | 0.028 |
| Up. Germanic Triassic | ZRP-02 | n/a | n/a | n/a |
| Lo. Germanic Triassic | BRW-05 | 0.266 | 0.268 | 0.028 |
| Lo. Germanic Triassic | ZRP-02 | 0.275 | 0.273 | 0.028 |
| Zechstein | BRW-05 | 0.271 | 0.267 | 0.024 |
| Zechstein | ZRP-02 | 0.267 | 0.264 | 0.017 |

**Table 7**: Dynamic Young's modulus values for the wells BRW-05 and ZRP-02. *In the provided data there was no specified top for the Upper North Sea Group, however it is assumed to be the first encountered unit. **The Upper North Sea Group for well ZRP-02 also contains around 30 metres of Middle North Sea Group.

| Unit | Well | Mean $E_{dyn}$ [-] | Median $E_{dyn}$ [-] | Std. $E_{dyn}$ [-] |
|---|---|---|---|---|
| Up. North Sea* | BRW-05 | 1.42 | 1.37 | 0.44 |
| Up. North Sea** | ZRP-02 | 1.48 | 1.43 | 0.38 |
| Lo. North Sea | BRW-05 | 2.54 | 2.27 | 1.14 |
| Lo. North Sea | ZRP-02 | 2.52 | 2.13 | 1.24 |
| Chalk | BRW-05 | 23.16 | 21.66 | 10.77 |
| Chalk | ZRP-02 | 21.52 | 17.49 | 11.12 |
| Rijnland | BRW-05 | 19.26 | 19.25 | 3.52 |
| Rijnland | ZRP-02 | 16.44 | 17.06 | 3.94 |
| Up. Germanic Triassic | BRW-05 | 35.42 | 29.87 | 12.56 |
| Up. Germanic Triassic | ZRP-02 | n/a | n/a | n/a |
| Lo. Germanic Triassic | BRW-05 | 34.79 | 33.74 | 4.50 |
| Lo. Germanic Triassic | ZRP-02 | 26.97 | 27.02 | 5.03 |
| Zechstein | BRW-05 | 36.94 | 34.02 | 14.46 |
| Zechstein | ZRP-02 | 35.91 | 32.67 | 13.17 |

T**able 8**: Converted static Young's modulus using McCann (1992) for the wells BRW-05 and ZRP-02. *In the provided data there was no specified top for the Upper North Sea Group, however it is assumed to be the first encountered unit. **The Upper North Sea Group for well ZRP-02 also contains around 30 metres of Middle North Sea Group.

| Unit | Well | Mean $E_{stat}$ [GPa] | Median $E_{stat}$ [GPa] | Std. $E_{stat}$ [GPa] |
|---|---|---|---|---|
| Up. North Sea* | BRW-05 | 0.59 | 0.56 | 0.28 |
| Up. North Sea** | ZRP-02 | 0.63 | 0.59 | 0.24 |
| Lo. North Sea | BRW-05 | 1.31 | 1.13 | 0.73 |
| Lo. North Sea | ZRP-02 | 1.29 | 1.04 | 0.80 |
| Chalk | BRW-05 | 14.51 | 13.54 | 6.89 |
| Chalk | ZRP-02 | 13.46 | 10.87 | 7.12 |
| Rijnland | BRW-05 | 12.00 | 12.00 | 2.25 |
| Rijnland | ZRP-02 | 10.21 | 10.60 | 2.53 |
| Up. Germanic Triassic | BRW-05 | 22.35 | 18.80 | 8.04 |
| Up. Germanic Triassic | ZRP-02 | n/a | n/a | n/a |
| Lo. Germanic Triassic | BRW-05 | 21.94 | 21.28 | 3.20 |
| Lo. Germanic Triassic | ZRP-02 | 16.94 | 16.98 | 3.22 |
| Zechstein | BRW-05 | 23.32 | 21.44 | 9.25 |
| Zechstein | ZRP-02 | 22.66 | 20.59 | 8.43 |

**Table 9**: Converted static Young's modulus using Barree (2009) for the wells BRW-05 and ZRP-02. *In the provided data there was no specified top for the Upper North Sea Group, however it is assumed to be the first encountered unit. **The Upper North Sea Group for well ZRP-02 also contains around 30 metres of Middle North Sea Group.

| Unit | Well | Mean $E_{stat}$ [GPa] | Median $E_{stat}$ [GPA] | Std. $E_{stat}$ [GPa] |
|---|---|---|---|---|
| Up. North Sea* | BRW-05 | 0.81 | 0.77 | 0.28 |
| Up. North Sea** | ZRP-02 | 0.81 | 0.50 | 0.23 |
| Lo. North Sea | BRW-05 | 1.47 | 1.32 | 0.69 |
| Lo. North Sea | ZRP-02 | 1.44 | 1.21 | 0.72 |
| Chalk | BRW-05 | 16.01 | 14.11 | 8.52 |
| Chalk | ZRP-02 | 14.51 | 10.89 | 8.63 |
| Rijnland | BRW-05 | 13.97 | 14.02 | 2.73 |
| Rijnland | ZRP-02 | 11.71 | 12.20 | 2.90 |
| Up. Germanic Triassic | BRW-05 | 27.03 | 21.46 | 11.62 |
| Up. Germanic Triassic | ZRP-02 | n/a | n/a | n/a |
| Lo. Germanic Triassic | BRW-05 | 25.08 | 24.21 | 4.32 |
| Lo. Germanic Triassic | ZRP-02 | 18.97 | 18.97 | 3.66 |
| Zechstein | BRW-05 | 23.40 | 19.76 | 13.68 |
| Zechstein | ZRP-02 | 22.08 | 18.61 | 12.72 |

## 3.3 Discussion

The well results show a lot of variability. For some units, such as the Altena (Figure 48) and Upper Germanic Triassic (Figure 51) groups, it can be hard to distinguish clear lithological trends for the given wells. On the other hand, the Chalk Group (Figure 35) and Upper Rotliegend Group (Figure 63) do show clear trends between the dynamic Young's modulus and the neutron porosity. The two wells provided by the *NAM* give a complete overview of the variability of the different units and how they compare to one another. Figure 69 and Figure 74 show an increase of the dynamic Young's modulus with depth until the Rijnland Group. For the Chalk Group this is probably in part due to the increase in the bulk density (Figure 71 and Figure 76), but considering that the bulk density for the North Sea groups does not steadily increase there must be another reason that explains the increase. Lithification and cementation might play a more important role for the Young's modulus rather than bulk density in general.

The Poisson's ratio can show a very narrow range (Figure 79) or a very broad range (Figure 62), often in line with the Young's modulus (Figure 79). However, the Poisson's ratio seems to be invariant towards (neutron) porosity (Figure 36 and Figure 38) for most wells except for P08-06 (Figure 66). The Poisson's ratio might be more dependent on the mineral type and cementation than the amount of compaction as the figures 70 and 75 show that the Poisson's ratio changes without a constant increase in bulk density. The Poisson's ratio steadily decreases with depth up and till the top of the Rijnland Group (Figure 70 and Figure 75). Once the Rijnland Group is reached, there is no discernible trend with depth. In both wells the halite is easily identifiable due to the constant acoustic slowness (Figure 72 and Figure 77), which in turn leads to a constant Poisson's ratio. This is particularly noticeable for well ZRP-02.

The use of the gamma ray and neutron porosity certainly have added benefit as differences within geological units become clear. In the Lower Germanic Triassic the Volpriehausen Sandstone Member (Figure 54) can be clearly distinguished by using both logs. Even though it is the same (Slochteren) formation within well P08-06, Figure 64 shows that there are two distinct layers within the geological layer. Another example is the Upper North Sea Group (Figure 32) where the change from probably more sandy material to more clayey can be seen by using the gamma ray log. The dynamic Young's modulus increases steadily with MDRT, but this does not seem to be caused by the bulk density as this remains constant throughout the interval (Figure 33). The increase in Young's modulus might be explained by increased cementation or better connectivity between the grains, but not to the extent that the bulk density increased.

The reference values (Table 1 and Table 4) by the Lele et al. (2015) and Orlic (2016), which are shown in the histograms, often do not conform to the obtained data. For instance, an underlying issue with this study is that there is considerable variability between the literature values and the obtained results. This study would be greatly improved by static measurement for the studied geological intervals. Then one could check the existing conversion methods or even create a new one. It is the case that many wells and geological units show potential due to strong lithological relationships. Thus if the right conversion method or reference can be found, then the results of this study can be applied into practice. There is also the potential for much more detailed research as this report mostly looks at group scale and not formation and member scale.

# 4

# Influence of Simple Overburdens on Subsidence

This chapter shows the undertaken processes and results for subsidence modelling in *Plaxis*. The modelling runs in this chapter are not so much designed to be realistic from a geological point of view, but more for testing the behaviour of the program and looking at extreme limits. Another important objective is to find trends that can be applied to geological units that are representable for the geology around Groningen. These learning points can then be applied to more realistic cases in chapter 5. Part 4.1 will outline the methodology and explain the used software and modelling type. In the second part, 4.2, the result of the modelling runs can be found. Finally, part 4.3 provides a discussion of the results.

## 4.1 Method

The model builds in this chapter are relatively simple, often consisting of a homogeneous overburden. As has been stated the purpose of this chapter is to look at the behaviour of the program and the relative influence of the elastic parameters. In the next chapter though, the overburden will not be homogeneous. A program is needed that can account for the overburden by building multiple geological layers above the reservoir. One way to do this is via a finite element program. For this thesis the program *Plaxis* is used, specifically the version *PLAXIS 2D Input 2016* and its associated output program. This program will be further referred to as *Plaxis*. Whilst it is more commonly used for civil engineering purposes, it does allow for modelling rock type behaviour. Examples of previous work involving rock modelling and *Plaxis* are: Lawless et al. (2003) and Cuisiat et al. (2010). The advantage of using a finite element program is that complex structures such as salt domes can be built and studied, but this would need to be done in a 3D program as *Plaxis 2D* would not model these in a structurally realistic way.

Section 4.1.1 provides an introduction to *Plaxis* and the available modelling types. In section 4.1.2 the properties of the modelled materials are described in further detail. Hereafter in section 4.1.3 an example of a model structure and mesh are shown. Section 4.1.4 provides information on the model pore pressures which drive the deformation in the models.

### 4.1.1 Plaxis Modelling Types

There are 12 modelling types (Figure 84) readily available in Plaxis and of these, four models are stated to be suitable for modelling rock-type behaviour (Plaxis, 2017). Increasingly sophisticated models do require more input parameters, leading to a cost-benefit situation where one might be limited due to existing data. For instance, the jointed rock model requires multiple Young's moduli and Poisson's ratios to model a material's anisotropic behaviour. For the Dutch subsurface such data does not appear to exist and hence this model is not suitable. The Hoek-Brown model is stated as being unsuitable for stratified layers and hence can be disregarded for this study. Furthermore this model requires additional parameters that are not available to the writer of this report. The Mohr-Coulomb model requires few parameter inputs and is thus easier to use. However, even this modelling type requires input parameters that are not readily available for the Dutch subsurface. Hence the choice is made to use linear elastic modelling which is essentially dependent on two parameters: the Young's modulus and the Poisson's ratio.

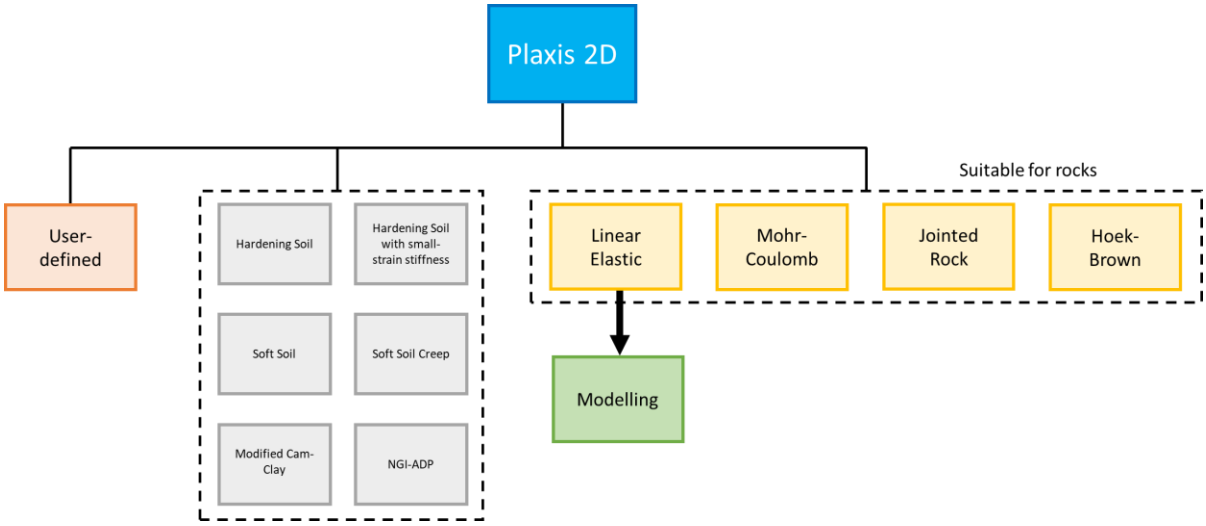


**Figure 84**: Illustration showing the available options in Plaxis 2D. The models in yellow are suitable for modelling rocks. For this thesis linear elastic modelling was chosen.

In the past the *NAM* (2013) has used a finite element model, as one of multiple techniques, to model the subsidence above the Groningen field, but concluded that the Geertsma and van Opstal (1973) method is sufficiently accurate (NAM, 2013). No mention of a finite element model for subsidence prediction is made in the latest *Winningsplan* (NAM, 2016). The used *Plaxis* model has been tailored towards the 2013 *Winningsplan* model and it is stated that the bottom boundary of the finite element model is set to 7000 metres and that the model boundary extends to one extra reservoir diameter in all x-y directions (NAM, 2013). For the *Plaxis* model the bottom boundary will also be set 7000 metres. The thickness of the reservoir is 100 metres. The reservoir radius and model extent are varied depending on the research. These two are further specified under the results part of the Chapter.

### 4.1.2 Model Materials

As has been stated, the choice is made to use linear elastic modelling of the model materials. A variety of input parameters exist for the material modelling. Ranging from grain size, flow characteristics and temperature behaviour. One of these characteristics is drainage. Model drainage is an important issue

for modelling in Plaxis as drainage determines how pore pressures influence the soil response (Plaxis, 2017). There are multiple options within the program, however for the present study the interest lies at looking at the long-term (i.e. drained) behaviour of the model and therefore the materials are modelled as such. If one needs to take into account the effect of excess pore pressures that are created due to stress changes, then an undrained model is more suitable.

The program *Plaxis* uses certain parameters which require calculating from those values which are already obtained through literature. The unit weight in Table 10 was calculated using Eq. 4.1 and the void ratio with Eq. 4.2. *Plaxis* allows for a saturated and unsaturated unit weight, but for during this study both values are set to be the same and the material is assumed to be saturated with fresh water $\rho = 1000\ kg/m^3$. During preliminary modelling using Mohr-Coulomb (and not linear elastic), the unit weight did not affect the displacement results. Nevertheless the given densities are converted to their unit weight values. The porosity or void ratio has no effect on the model output hence all material have the same porosity of 0.15 or a void ratio of 0.176 except for the Zechstein units.

$$\gamma = \rho g \tag{4.1}$$

$$e_{void} = \frac{\varphi}{1-\varphi} \tag{4.2}$$

**Table 10**: Densities and corresponding unit weights per geological unit, based on values from the *NAM* (Lele et al., 2015).

| Unit | | Density, ρ [kg/m$^3$] | Unit weight γ [N/m$^3$] |
|---|---|---|---|
| North Sea | | 2150 | 21.09 * 10$^3$ |
| Chalk | | 2350 | 23.05 * 10$^3$ |
| Rijnland | | 2350 | 23.05 * 10$^3$ |
| Triassic | | 2350 | 23.05 * 10$^3$ |
| Zechstein | Halite | 2100 | 20.60 * 10$^3$ |
| | Anhydrite | 2900 | 28.45 * 10$^3$ |
| Ten Boer | | 2300 | 22.56 * 10$^3$ |
| Slochteren | Heterolithic | 2390 | 23.45 * 10$^3$ |
| | Reservoir | 2390 | 23.45 * 10$^3$ |
| Carboniferous | | 2300 | 22.56 * 10$^3$ |

**Table 11**: Parameters from Lele et al. (2015) used in Plaxis.

| Unit | | E [GPa] | ν [-] | γ [N/m$^3$] | $e_{void}$ |
|---|---|---|---|---|---|
| North Sea | | 2 | 0.30 | 21.09 * 10$^3$ | 0.176 |
| Chalk | | 10 | 0.25 | 23.05 * 10$^3$ | 0.176 |
| Rijnland* | | 16 | 0.25 | 23.05 * 10$^3$ | 0.176 |
| Triassic* | | 16 | 0.25 | 23.05 * 10$^3$ | 0.176 |
| Zechstein** | Halite | 30 | 0.35 | 20.60 * 10$^3$ | 0.000 |
| | Anhydrite | 70 | 0.25 | 28.45 * 10$^3$ | 0.000 |
| Ten Boer | | 40 | 0.20 | 22.56 * 10$^3$ | 0.176 |
| Slochteren | Heterolithic | 14 | 0.15 | 23.45 * 10$^3$ | 0.176 |
| | Reservoir | 14 | 0.15 | 23.45 * 10$^3$ | 0.176 |
| Carboniferous | | 40 | 0.20 | 22.56 * 10$^3$ | 0.176 |

Table 11 shows the elastic parameters of the geological units around the Groningen area and form the basis for the calculations which are performed using Hooke's law in three dimensions (Plaxis, 2016):

$$e_h = \frac{1}{E}\{\Delta\sigma'_h - \nu(\Delta\sigma'_H + \Delta\sigma'_v)\} \quad (4.3)$$

$$e_H = \frac{1}{E}\{\Delta\sigma'_H - \nu(\Delta\sigma'_h + \Delta\sigma'_v)\} \quad (4.4)$$

$$e_v = \frac{1}{E}\{\Delta\sigma'_v - \nu(\Delta\sigma'_H + \Delta\sigma'_h)\} \quad (4.5)$$

Due to axial symmetry of the 2D model the horizontal stresses are equal to each other. Therefore only the last two equations are needed and $\Delta\sigma'_h = \Delta\sigma'_H$. An example calculation is shown in the results part of the chapter.

### 4.1.3 Model Structures and Mesh

The upcoming figures will show example 2D images of the models. It should be noted that all the models are modelled to be axial symmetric, hence in a 3D context the model represents a layered cylinder. Structures have to be drawn which are the objects that undergo the modelling. The material properties are assigned to the relevant structure. For all the created models the structures consist of rectangular polygons. An example can be seen in Figure 85 where geological layers of varying thickness are modelled. The bottom boundary of the model is fixed and there cannot be any vertical or horizontal movement. Elements on the flanks are free to move vertically, but not horizontally and the top boundary is completely free.


**Figure 85**: Model showing multiple geological units with varying material properties. The reservoir is the smaller red rectangle to the left. Note the pattern of different thicknesses which facilitate certain modelling runs and are not meant to represent real life geology.

When the structures are complete the model needs to be meshed. Plaxis allows for different settings that create a certain number of elements based on the desired fineness of the model. It is not possible to seed a structure line in Plaxis, hence the inbuilt refinement needs to be used. A 'medium' basis mesh is chosen and certain thin layers (e.g. Figure 86) are set to a refinement of 0.5 to: 1) ensure a larger amount of nodes at the top surface of the model and 2) a constant spacing between the nodes. The bottom half of the model is considered to be of less interest and hence is not refined. This

significantly reduces the amount of nodes and hence computational time. Figure 87 shows the mesh in multiple geological units. For the smaller elements a triangle side is between 50 and 100 metres long.

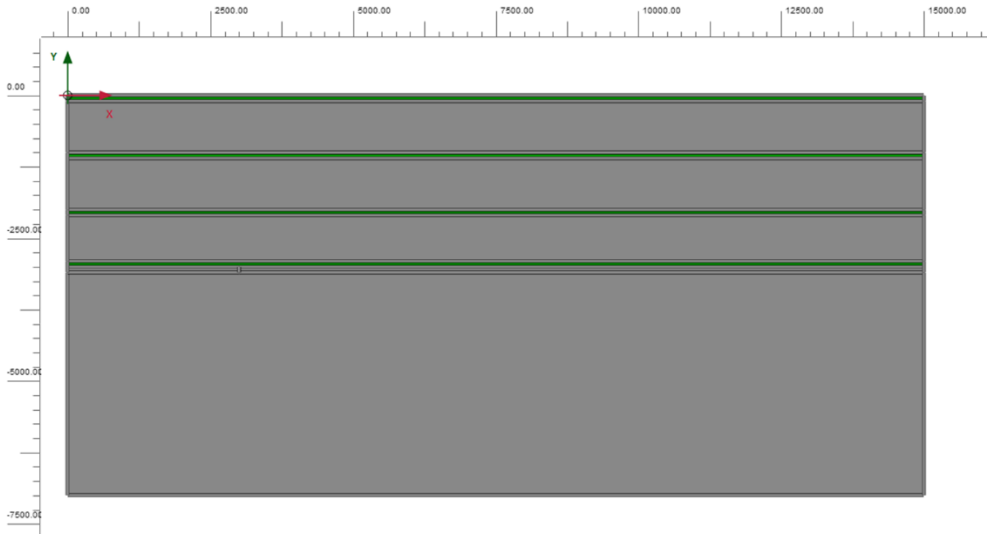


**Figure 86**: Model showing mesh refinement in certain polygons (dark green). Whilst this is not the case in this figure, the brighter the green the smaller (i.e. more elements) the mesh refinement.

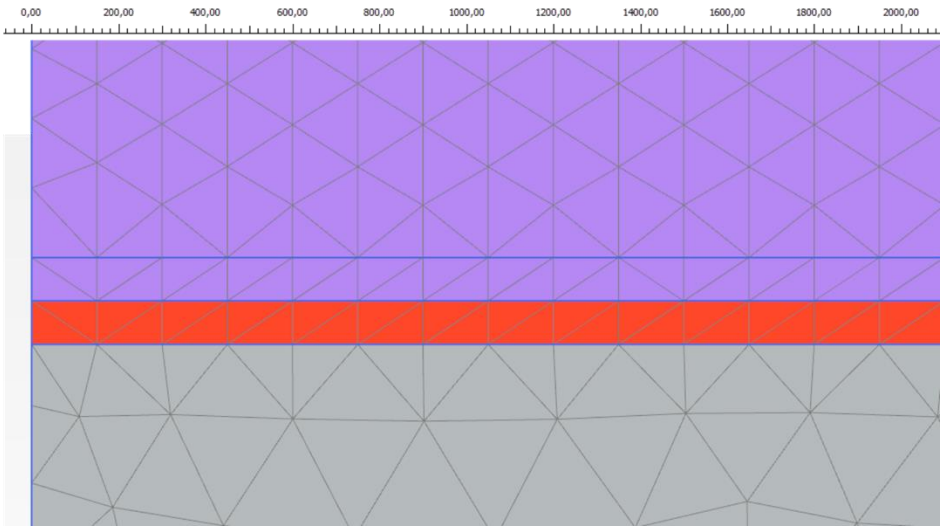


**Figure 87**: Zoomed-in image of the mesh at reservoir (red) level. One can impose a desired element interval by using mesh refinement.

The user can choose between 6-node and 15-node elements. All the models in this report were made using 15-node elements as these allow for greater accuracy. An example of the 15-node elements is given in Figure 88.

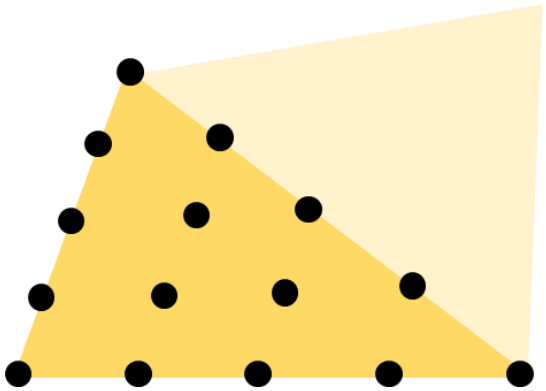

**Figure 88**: Two 15-node elements with nodes in *Plaxis*. After (Plaxis, 2017). Note the presence of nodes within the element.

### 4.1.4 Model Pore Pressures and Stresses

The vast majority of the model is assumed to be hydrostatic where the pore pressure increases linearly with depth. Only the green rectangle, representing the reservoir, (Figure 89) has a different pore pressure which is reduced on a per step basis. An example of the resulting pore pressures are shown in Appendix J. It is assumed that in the scope of this research there is no aquifer influx to recover the pore pressure. For the Groningen field this is a realistic assumption as there is slow aquifer influx.

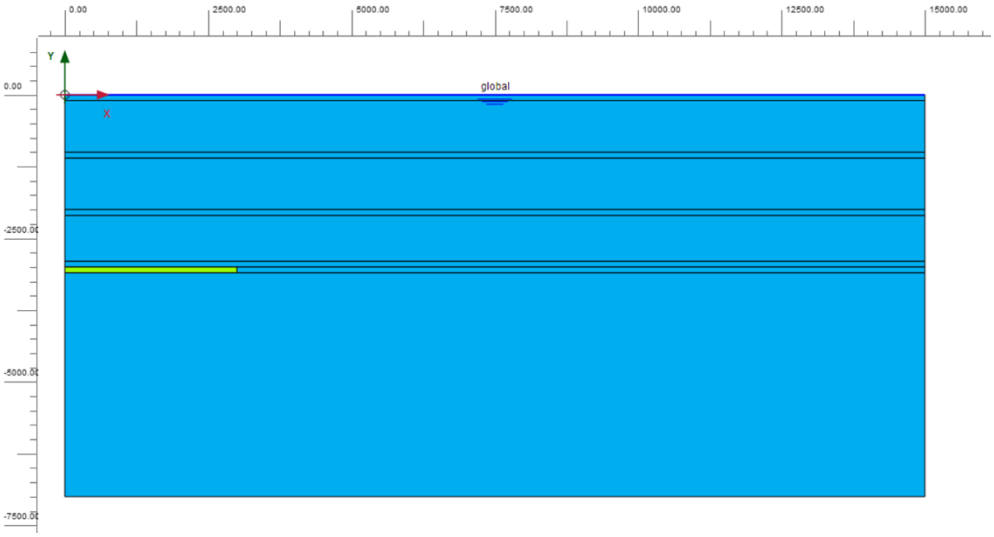


**Figure 89**: Model showing the so-called *flow conditions* in *Plaxis*. Blue areas are subject to hydrostatic pore pressures whilst the green area is user defined and represents the reservoir pore pressure.

The horizontal stress can be determined in multiple ways in *Plaxis* and all are based on the vertical effective stress, which is determined by gravity. The horizontal stress can be a simple ratio, but the choice is made to use so called *gravity loading* which generates the horizontal effective stress based on the following relationship (Plaxis, 2017):

$$\sigma_h' = \frac{\nu}{1-\nu}\sigma_v' \qquad (4.6)$$

# 4.2 Results 2D

Multiple modelling scenarios have been developed to study the effect of the elastic moduli on subsidence. There are three main geological units: reservoir (section 4.2.2), underburden (4.2.3), and overburden (4.2.4). Each component will be studied individually in the sections below. Hereafter there will be a section (4.2.5) that looks at the relative shape of the reservoir by studying the ratio between reservoir depth and reservoir radius. Only the vertical displacement is considered in detail. As a rule of thumb the horizontal displacement is greatest at the edge of the reservoir cylinder and the maximum horizontal displacement is around half of the maximum vertical displacement. Figure 90 provides a sketch of the displacement of an object and examples from *Plaxis* can be found in Appendix K. For all results, the displacements become linearly larger with the reservoir pressure drop. The chosen pressure drop for the vast majority of modelling runs is 34 MPa as this is the expected pressure drop at abandonment for the Groningen field (NAM, 2013) unless stated otherwise.

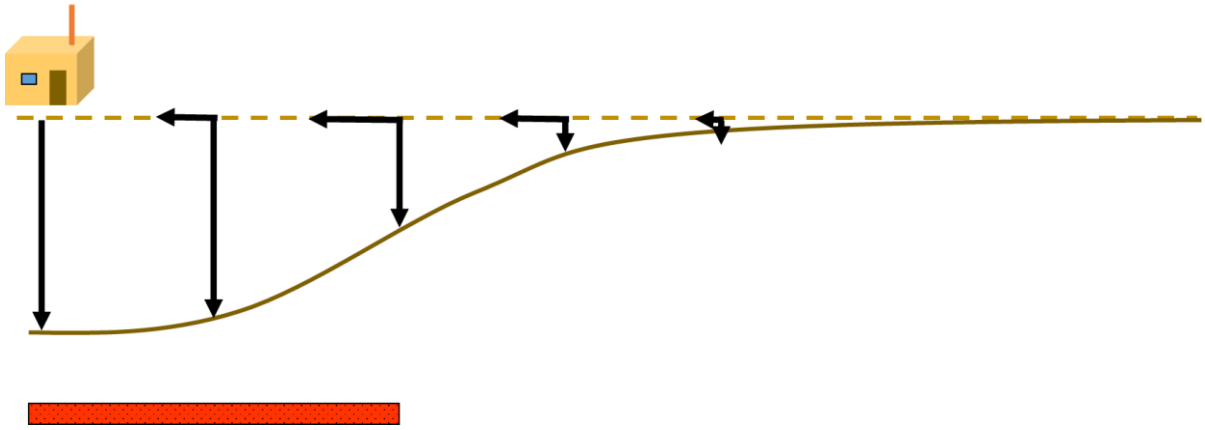

**Figure 90**: Schematic illustration of the displacements an object at the surface will undergo due to reservoir depletion. The red rectangle represents the compacting reservoir. Note that the maximum vertical displacement is at the centre of the reservoir. The maximum horizontal displacement is on the reservoir edge.

## 4.2.1 Compaction

As a program validity check, a *Plaxis* model is created where the reservoir extends from one side of the model to the other, i.e. the surface area of the top of the reservoir equals to that of the top of the surface of the *Plaxis* model. When the reservoir compacts, it is expected that the vertical surface displacement will be equal to that in the reservoir. A schematic illustration of the model can be seen in Figure 91 and the results can be seen in Figure 92. Two different scenarios were tested where in the first one the reservoir material is kept constant, but the overburden as a whole changes. In the second scenario there is a single overburden type and the reservoir material is varied.

The reservoir material throughout this report is modelled as a Slochteren rock material with a porosity of 15 % leading to a Young's modulus of 14 GPa and a Poisson's ratio of 0.15 (Appendix E).

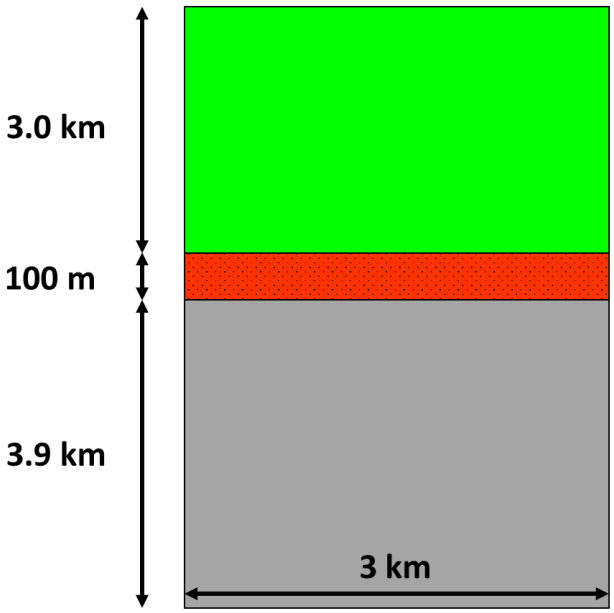


**Figure 91**: Schematic illustration of the *Plaxis* model used for the compaction modelling. The colour green indicates a Chalk Group material and grey a Carboniferous material (Table 11). The red layer is the reservoir. Note that the figure is not to scale.

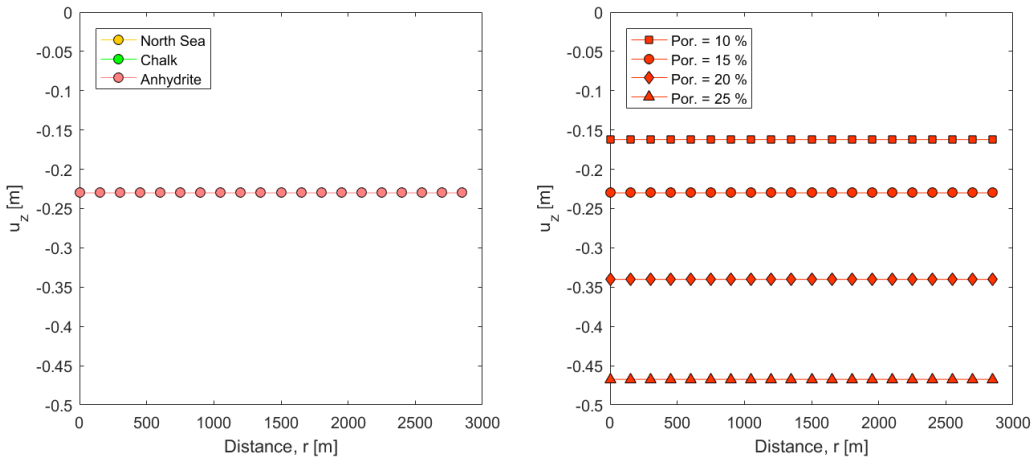


**Figure 92**: Vertical displacement of the surface for varying overburden types (left) and varying reservoir types (right). Note that only the reservoir influences the displacement. For the overburden results a reservoir with 15 % porosity was used.

The left subplot of Figure 92 shows that for different overburden types the vertical displacement at the surface is the same. The right subplot shows that when the reservoir material is varied, that there are unique surface responses, hence for this type of scenario the overburden has no effect on the vertical displacement. A simple check can be done to test the physics of the model. The stresses are taken from the *Plaxis* output program. The vertical strain of the reservoir is calculated as follows:

$$e_v = \frac{1}{E}\{\Delta\sigma'_v - \nu(\Delta\sigma'_H + \Delta\sigma'_h)\} \qquad (4.5)$$

$$e_v = \frac{1}{14\cdot10^9}\{34\cdot10^6 - 0.15\cdot(6\cdot10^6 + 6\cdot10^6)\}$$

$$e_v = \frac{1}{14\cdot10^9}\{34\cdot10^6 - 1.8\cdot10^6\}$$

$$e_v = 2.3\cdot10^{-3}$$

The strain is 0.0023 and the reservoir height is 100 metres. The reservoir compacts by 0.23 % which is equal to 23 cm and can be seen in Figure 92. For linear elasticity to be valid, strains need to be small. Some rocks show linear elastic behaviour of up to a couple of percent (Fossen, 2010), thus the model is within the margin.

In the compaction model there is no heave of the overburden due to the pressure drop. This is not the case in the other models that have a different structural set up. In these models the base of the reservoir is raised by a few centimetres. This is substantially less than the downward displacement at the top of the reservoir.

### 4.2.2 Reservoir

Figure 93 shows a schematic illustration representing the *Plaxis* model of some of the modelling runs. In the coming results the entire unit is varied, but assumed to be homogeneous. The model is 15 km wide and the reservoir radius is 3 km. The reservoir is 100 m thick and at a depth of 3000 m. The underburden is assumed to be fixed at a depth of 7000 m.

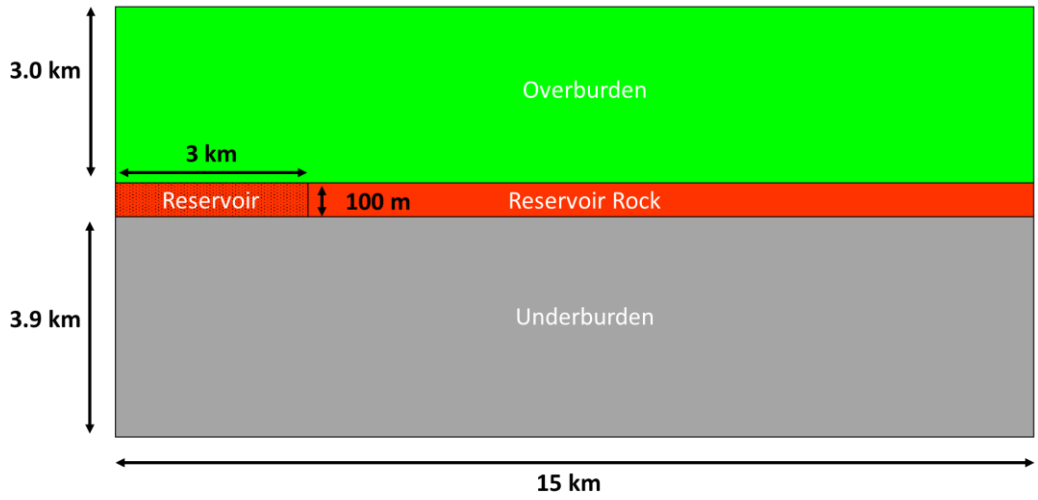


**Figure 93**: Schematic illustration showing the three modelling zones where each is assumed to be homogeneous.

The emphasis of this study is on the overburden and not the reservoir. However, to get an impression of its effect, a modelling run has been performed to gain an insight in its influence. A range of values are used for the two elastic moduli. The Young's modulus varies from 5 to 35 GPa in steps of 5 GPa and the Poisson's ratio from 0.10 to 0.30 in steps of 0.05. The overburden is modelled as Chalk material which the *NAM* models as a weak rock (E = 10 GPa) and the underburden as Carboniferous, which is much stiffer than the reservoir and overburden (E = 40 GPa). The results can be found in Figure 95 and show that for relatively high Young's modulus values the variability in vertical displacement is quite small. However, when the Young's modulus becomes less than 15 GPa the displacement becomes much larger. The Poisson's ratio also has a greater influence for relatively weak rocks and shows nonlinear behaviour in the blue part of the mesh. Note that, unless explicitly stated, most plots show the vertical displacement at (0,0) which is above the centre of the reservoir. At this location there is maximum vertical displacement.

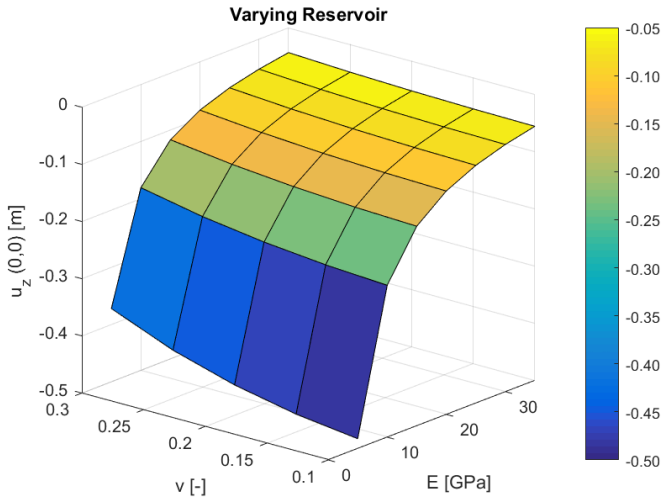


**Figure 94**: The vertical displacement at (0,0) for a varying reservoir material. Note that when the Young's modulus becomes less than 15 GPa the displacement becomes much larger and the Poisson's ratio plays a greater and nonlinear role.

## 4.2.3 Underburden

In this case the overburden is kept constant and a number of different underburdens are modelled. The results can be seen in Figure 95. The overburden consists of Chalk material from Lele et al. (2015) and the reservoir is assumed to have the material properties of Slochteren reservoir rock with 15 % porosity (i.e. E = 14 GPa and v = 0.15). The Young's modulus varies from 10 to 80 GPa in steps of 5 GPa and the Poisson's ratio from 0.10 to 0.40 in steps of 0.05.

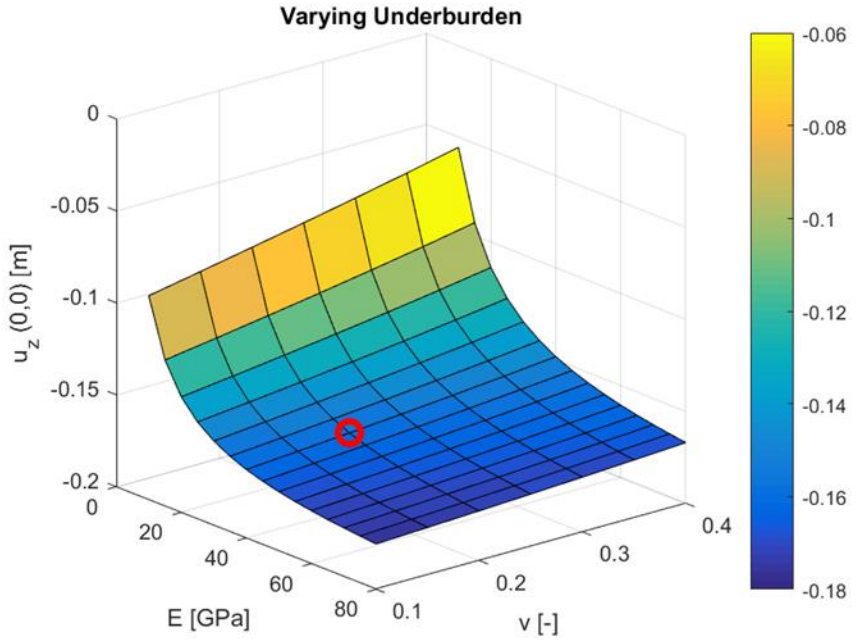


**Figure 95**: Absolute vertical displacement (left) and relative displacement with respect to the minimum absolute displacement (right) at (0,0) for varying Young's moduli and Poisson's ratios for the underburden. Note that for decreasing Young's modulus the Poisson's ratio becomes increasingly influential. The red circle indicates the elastic properties of the Carboniferous (Lele et al., 2015).

From Figure 95 it is evident that the Young's modulus has the most influence on the vertical displacement at point (0,0), as for a constant Poisson's ratio the displacement can vary by 8 to 10 centimetres. However, for lower values of the Young's modulus the Poisson's ratio becomes increasingly important. This is particularly clear for E = 10 GPa as the maximum change between the Poisson's ratio leads to a difference of 5 cm for the vertical displacement. The factor plot shows that a very large part of the varied materials there is not much difference. From a Young's modulus of around 35 GPa the vertical displacement is 3 times as much as for an underburden consisting of E = 10 GPa and v = 0.4.

## 4.2.4 Overburden

To study the effect of varying overburdens the underburden is kept constant and assumed to be same as the Carboniferous. The reservoir rock is assumed to have the properties of a 15 % (E = 14 GPa and v = 0.15) porosity rock. As the main interest of this thesis lies with the overburden, multiple scenarios have been devised to study different factors starting with a homogeneous overburden below. Unless it is a specific example, in general it would be unrealistic to model an entire overburden with a Young's modulus of 2.5 GPa. The purpose of these modelling runs is to gain a better understanding of not only the range of possible values, but also the extremities of a *Plaxis* model.

### 4.2.3.1 Homogeneous Overburden

In this scenario there is a homogeneous overburden of which the elastic properties are varied. The Young's modulus ranges from 2.5 to 80 GPa in steps of 5 GPa (and one step of 2.5) and the Poisson's ratio from 0.10 to 0.40 in steps of 0.05.

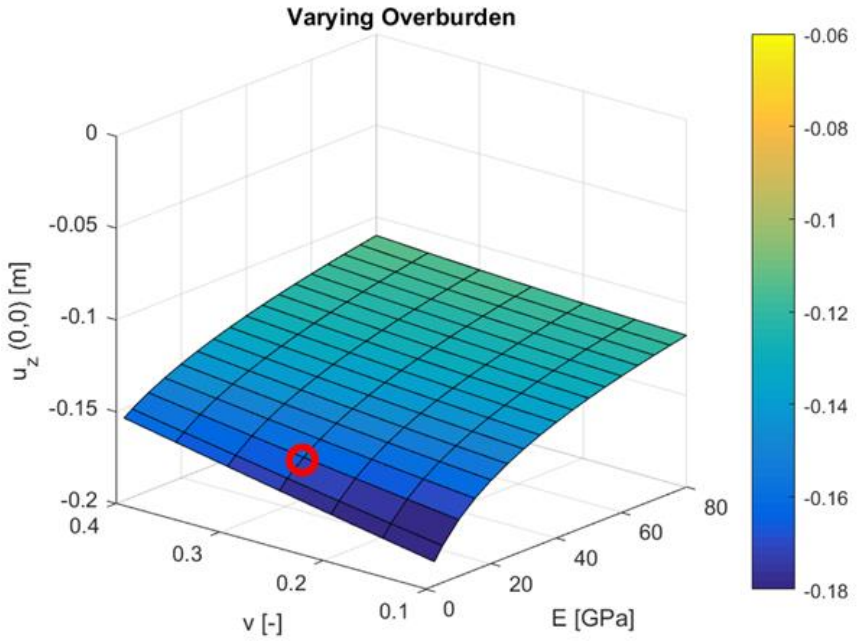


**Figure 96**: Absolute vertical displacement (left) and relative displacement with respect to the minimum absolute displacement (right) at (0,0) for varying Young's moduli and Poisson's ratios for the overburden. As with the underburden, for decreasing Young's modulus the Poisson's ratio becomes increasingly influential. The red circle indicates the elastic properties of the Chalk Group (Lele et al., 2015).

Figure 96 shows that once the Young's modulus becomes less than around E = 40 GPa, the vertical displacement becomes more sensitive to this parameter and drops more quickly per increment. The Poisson's ratio becomes more influential for lower Young's moduli. For instance, the difference between ν = 0.10 and ν = 0.40 for E = 2.5 GPa is about 3 cm. Note that the colour bar in the figure shows that there is less variability in the vertical displacement for the overburden than the underburden. Nevertheless the difference in displacement between the maximum and minimum displacement is around 7 cm.

### 4.2.3.2 Thin Layer

Now the research is made more interesting by adding another layer of material in the overburden. The material properties of a thin, 100 metre thick (Figure 97), layer are varied with the same range of values as in section 4.2.3.1. The rest of the overburden is modelled as Chalk. A layer of this thickness can be considered to be of formation scale (e.g. the Slochteren Formation) or a small group scale, e.g. the Rijnland Group above the Groningen field. Three different depth intervals were studied: one at the surface, one with the top at 1000 m depth and one right above the reservoir with the top at 2900 m depth.

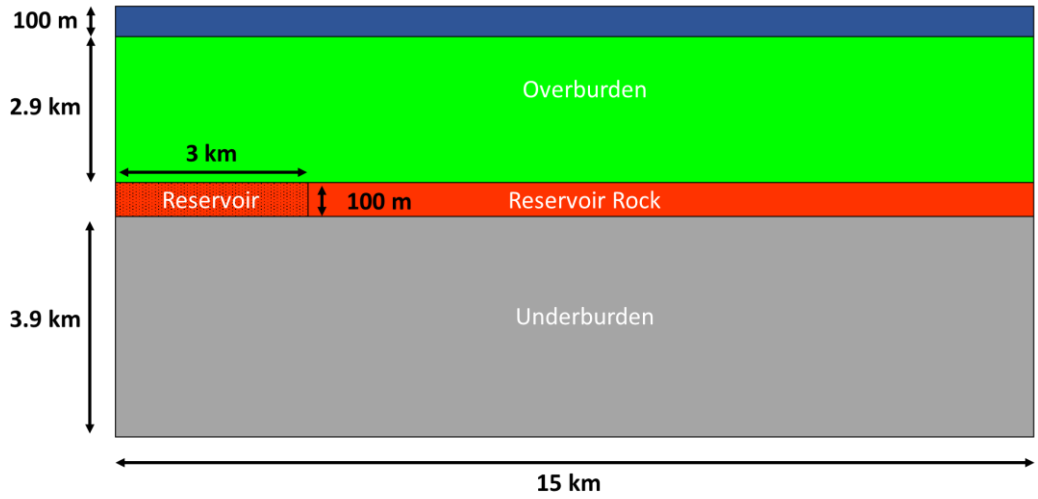


**Figure 97**: Schematic illustration showing the four modelling zones where each is assumed to be homogeneous. A 100 m thick layer has been placed on at the surface and then placed at a depth 1000 m and 2900 m. The remaining overburden and the other two zones are kept constant.

In the case of the varied layer at the surface, a larger Young's modulus leads to less displacement (Figure 99) and a larger Poisson's ratio leads to less subsidence. What is noticeable is that when the layer is not at the surface then a larger Poisson's ratio, at low Young's modulus, leads to more displacement which is the reverse of the surface case. This is probably caused by a much higher effective horizontal stress for this material combination (Appendix L). The larger effective horizontal stress causes a reduction in vertical elongation of the material in the overburden, which is visible (Figure L5 and L6) and fits the behaviour of Hooke's law. This then in turn causes a larger total downward surface displacement.

A larger Young's modulus in the subsurface layers also leads to less subsidence which is reverse behaviour. When a layer is stiff it undergoes less vertical elongation than if it were flexible (Appendix L), this also seems to cause the overburden above the rigid layer to undergo less elongation as well. In total there is a reduction in elongation in the overburden, hence the vertical displacement at the surface is larger. Note that the absolute amount of displacement for the two latter results is small, meaning that thin layers in even weak overburden material do not have large effect on the subsidence at the surface.

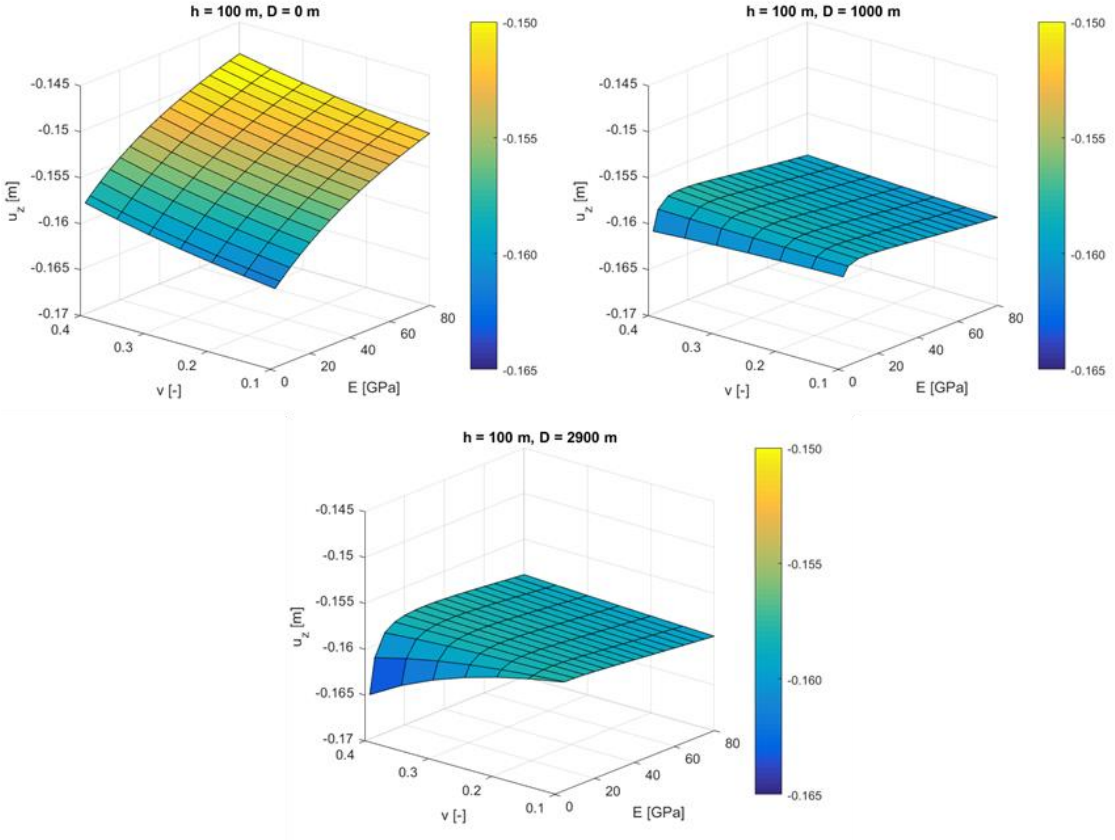


**Figure 98**: Absolute vertical displacements for a varied 100 m thick layer at three different depths. The layer at the surface sees the greatest difference in absolute displacement. Note the inverse behaviour of the other two layers where a greater Young's modulus leads to a larger displacement.

### 4.2.3.2 Thick Layer

A natural progression from experimenting with a thin layer is to make it thicker. The material properties of a thick, 1000 metre thick (Figure 99), layer are varied with the same range of values as in section 4.2.3.1. A layer of this thickness can be considered to be of a large group scale, e.g. both North Sea groups or the Chalk Group above the Groningen field. Three different depth intervals were studied: one at the surface, one with the top at 1000 m depth and one, in contact with and, above the reservoir with the top at 2000 m depth.

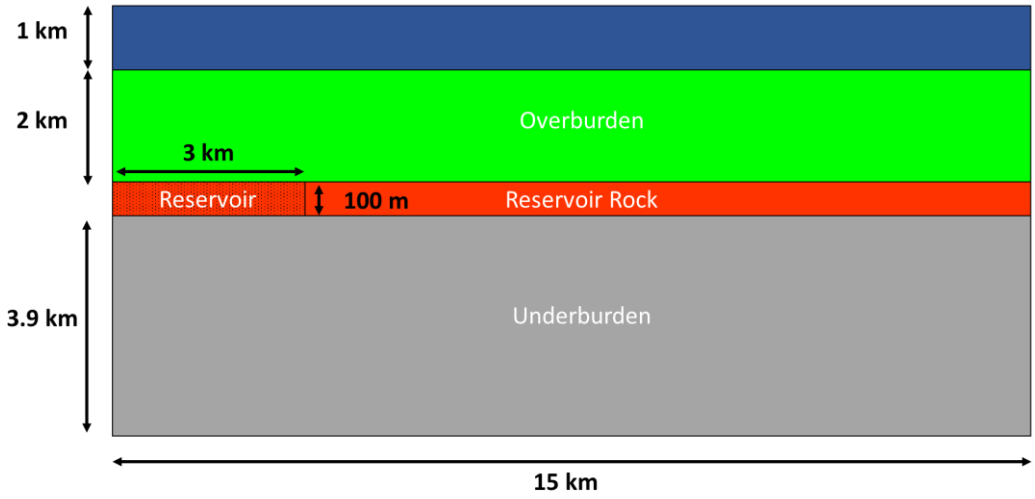


**Figure 99**: Schematic illustration showing the four modelling zones where each is assumed to be homogeneous. A 1000 m thick layer has been placed on at the surface the depth of which is varied, whilst the other three zones are kept constant.

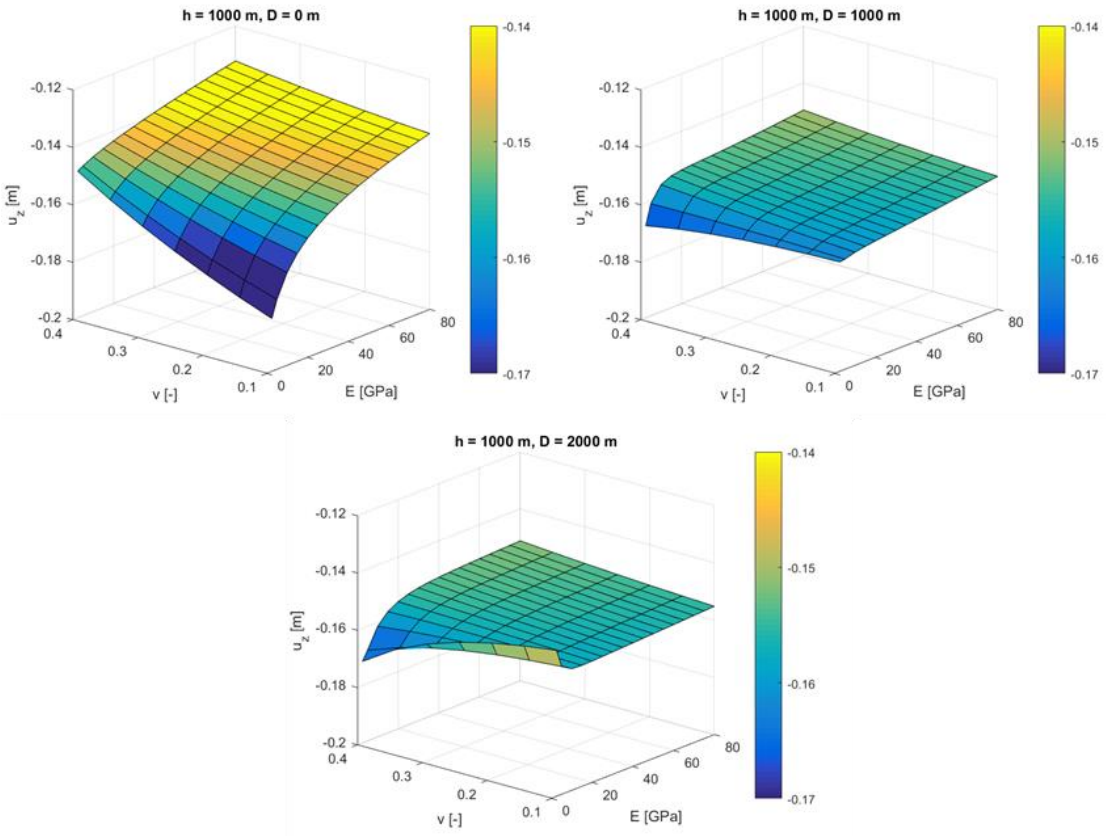


**Figure 100**: Absolute vertical displacements for a varied 1000 m thick layer at three different depths. The layer at the surface sees the greatest difference in absolute displacement.

Figure 100 shows that when the varied layers is at the surface the range of vertical displacements is greatest. This is the same as with a 100 m thick layer. The inverse behaviour, where increasing Young's modulus leads to greater displacement, is not present for the other cases. The Poisson's ratio behaves somewhat similar for low Young's moduli (D = 1000 m). Notice the remarkable switch for a Young's modulus of 2 GPa for a layer at 2000 m depth. The absolute difference for the two confined layers is not very large at around 1 cm. This is for almost all of the elastic parameter combinations. The range of absolute difference for the layer at the surface is around 5 cm.

#### 4.2.3.4 Rigid overburden

From the previous results it is clear that the greater the Young's modulus, the smaller the vertical displacements. Thus the question arises how much less it becomes when the rest of the overburden is more rigid than the relatively weak Chalk. In this case the model set up is similar to that of Figure 100, but the Young's modulus of the rest of the overburden is increased and the Poisson's ratio is kept constant to that of the Chalk (v = 0.25).

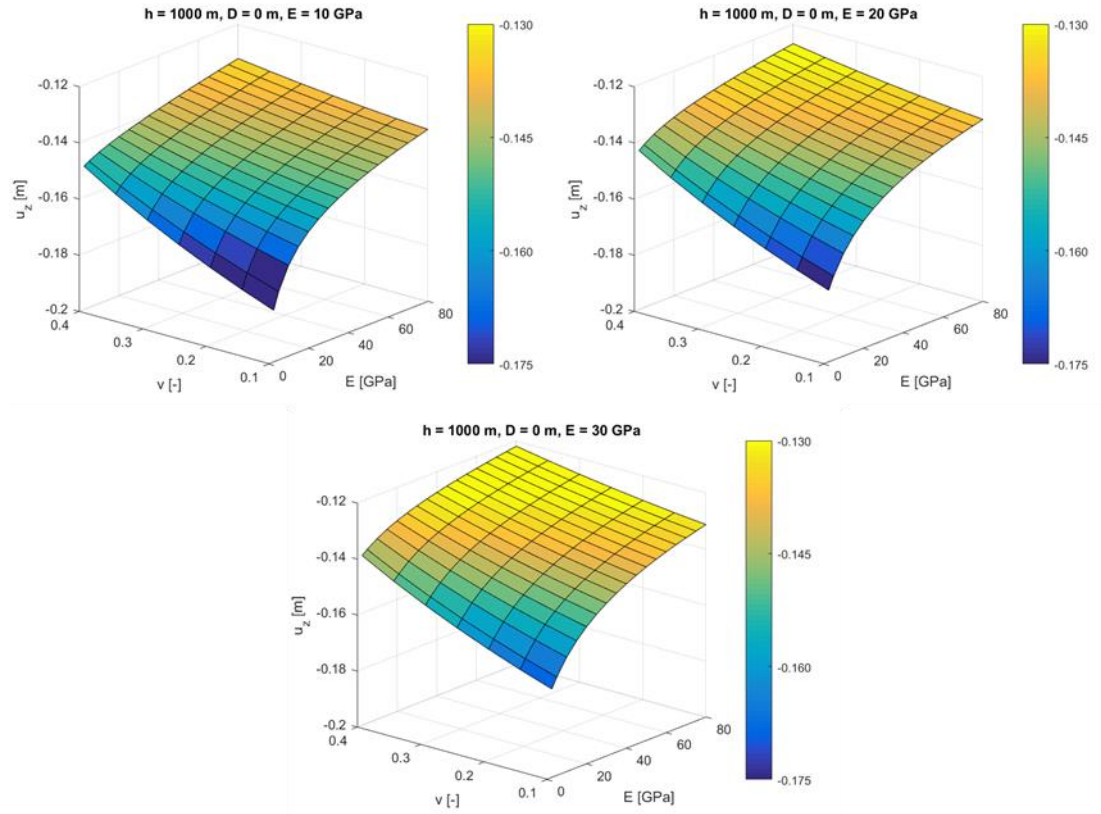


**Figure 101**: Absolute vertical displacements for a varied 1000 m thick layer the surface. The rest of the underlying overburden is changed to 20 GPa (top right) and 30 GPa (bottom). Note the reduced amount of vertical displacement, but still a wide range of displacements.

Figure 101 shows that there is less vertical displacement when the remaining overburden has a larger Young's modulus. When the underlying overburden is modelled as Chalk then the maximum difference between the smallest and largest displacement is 4.93 cm. What is noticeable is that the range of values is still large at around 4.74 cm for 20 GPa and 4.64 cm for 30 GPa. Despite the relatively large increase in Young's modulus the effect of it is quite small.

## 4.2.5 Reservoir Radius and Depth

The Geertsma (1973) subsidence solution is partly dependent on the ratio between the reservoir radius and the reservoir depth. This implies that subsidence is in part 'reservoir shape' dependent, hence *Plaxis* versions have been created to study its effect (Figure 102).

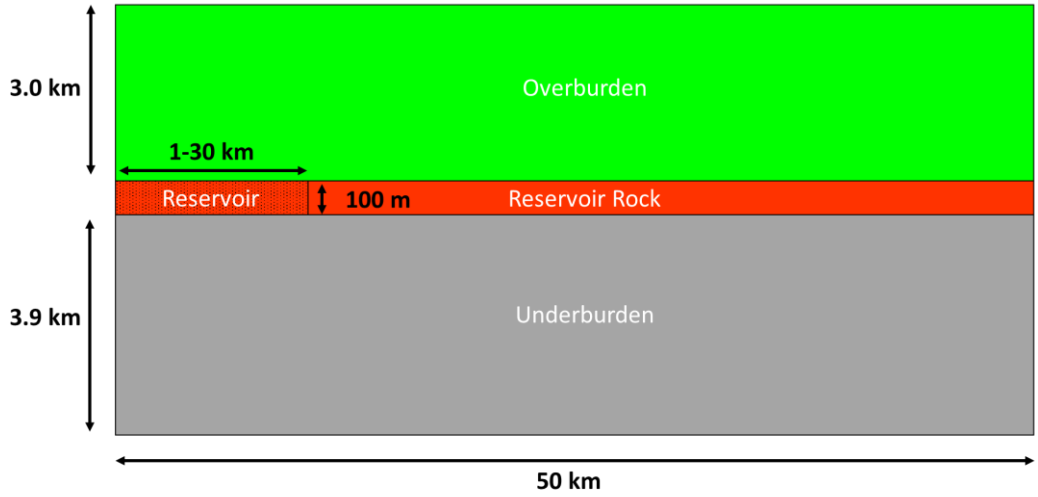


**Figure 102**: Schematic illustration showing the three modelling zones where each is assumed to be homogeneous. The model is much larger with a total extent of 50 km. The reservoir radius is varied between 1 and 30 km.

### 4.2.5.1 Vertical Displacement

The absolute vertical displacement as a function of the dimensionless parameter $\eta = \frac{D}{R}$ are shown in Figure 103. The results show that when the reservoir tends to very large or very small the overburden plays a smaller role or none at all when at the surface above the centre of the reservoir (0,0). The maximum amount of vertical displacement is around 23 cm which equals to the compaction of the reservoir (section 4.2.1). Subsidence in a Plaxis model cannot become greater than the amount of compaction in the reservoir. This is different from the Geertsma (1973) model which allows large reservoirs to have a subsidence which is greater than the amount of compaction! Hence there is a fundamental difference between using the Geertsma (1973) method and the finite element program *Plaxis*. There appears to be a maximum amount of variability in vertical displacement when $\eta = 0.8$ and $\eta = 1.0$. The overburden has the largest amount of effect for these two reservoir scales.

The reader is reminded that these results, are only at the point (0,0) which leaves over 300 others across the rest of the subsidence bowl. To take these into account the maximum difference in displacement for each of these points is determined and shown in Figure 104 and Figure 105. These two figure show that for $\eta > 0.6$ the greatest amount of difference is at (0,0) and decreases with distance. This then changes as the reservoir becomes more extensive. For $\eta = 0.1$ around 10 km of the surface subsides by the amount of compaction. Note that a 'dead zone' appears where the variability drops starkly above the edge of the reservoir (Figure 104). This is due to the fact that, at some location, displacement solutions intersect at single point. For smaller reservoirs this point is further away from the reservoir and for laterally extensive reservoir the displacements intersect above the edge of the reservoir. Figures 117, 119 and 121 show this in chapter 5.

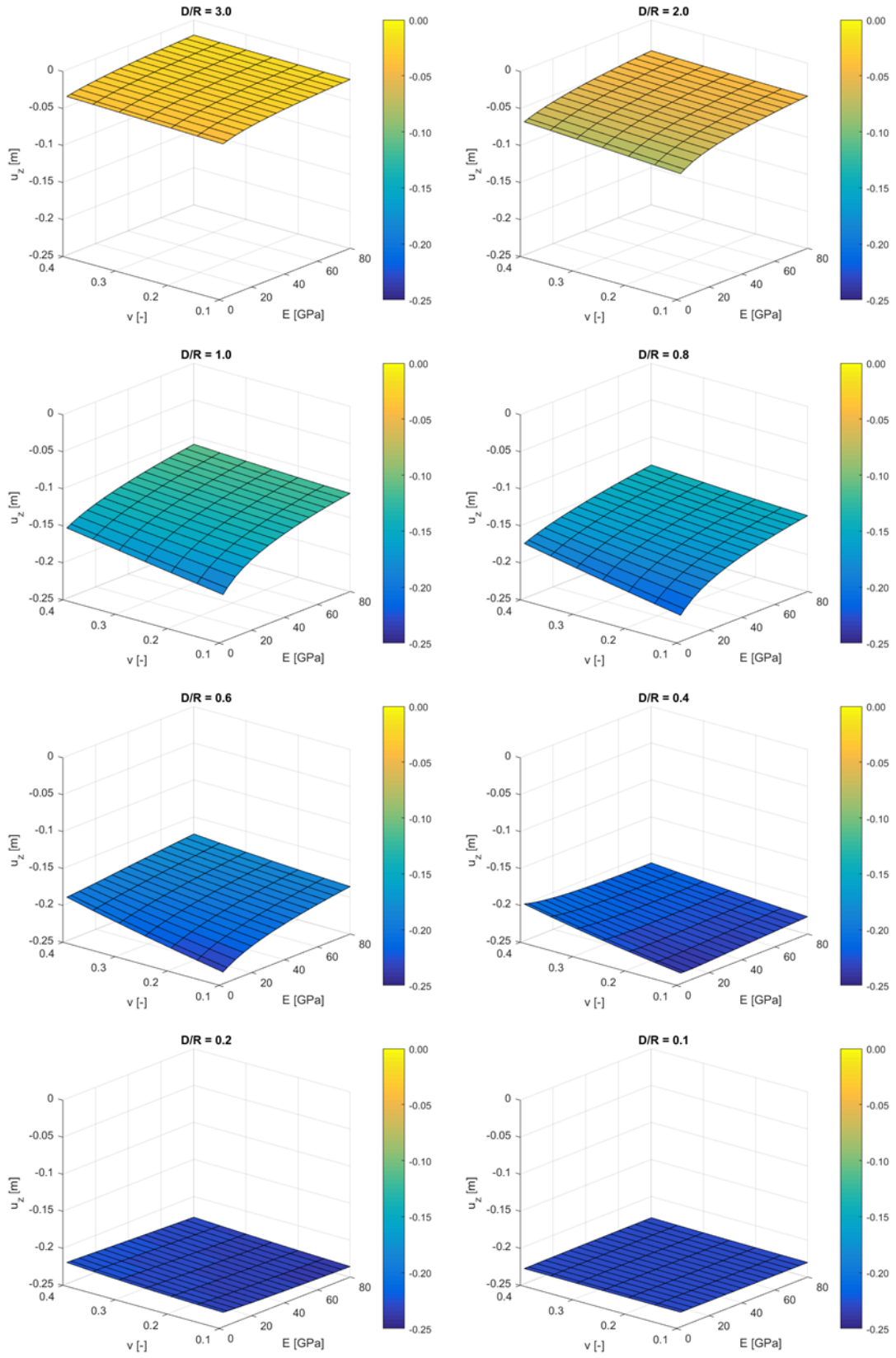


**Figure 103**: Absolute vertical displacements at (0,0) for different eta ratios. Note that for a very large reservoir radius the displacement at (0,0) becomes zero and for small reservoirs this trend is also visible. The overburden material properties become irrelevant at the centre of the reservoir disk.

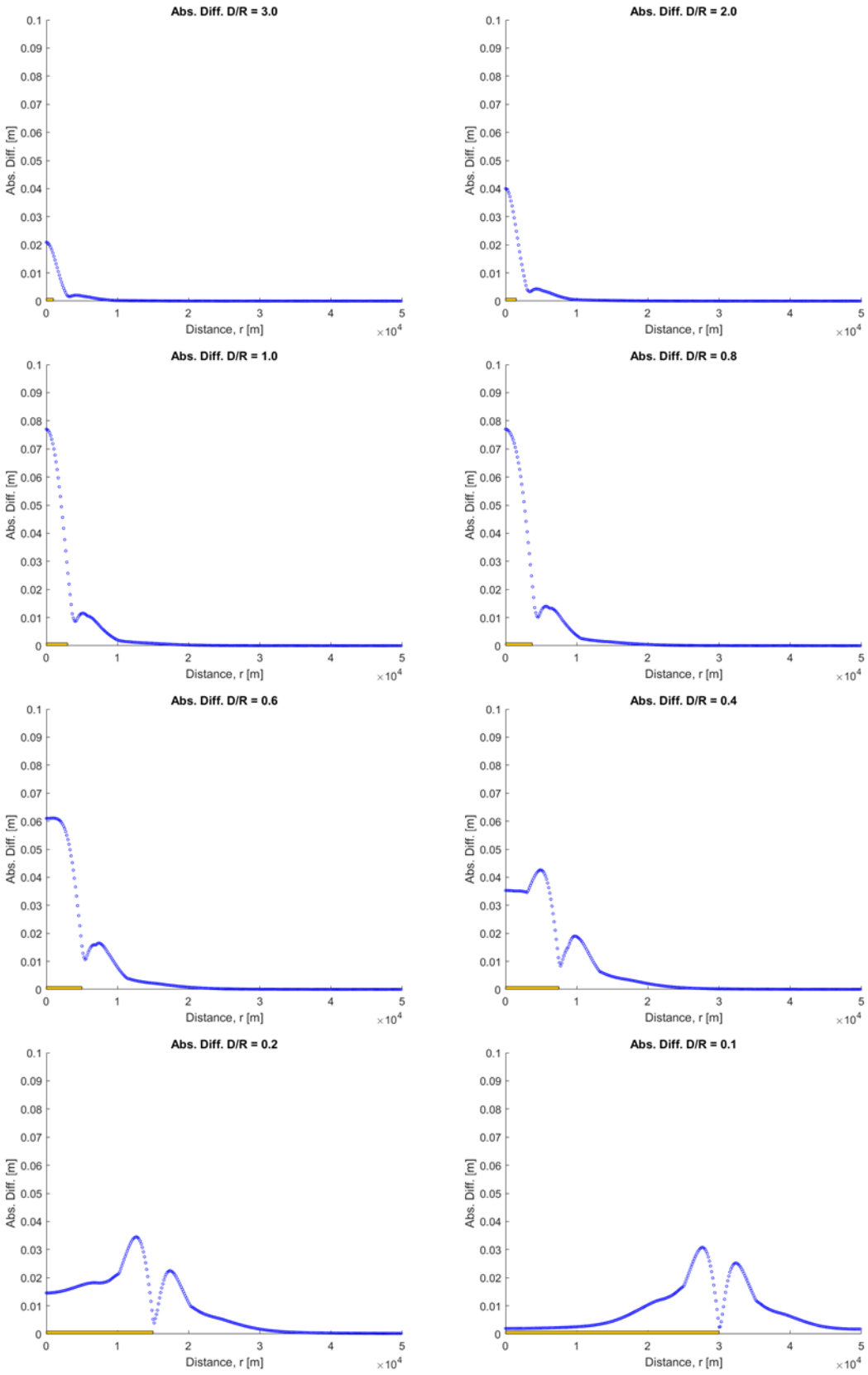


**Figure 104**: The maximum absolute difference at each subsidence bowl point. The reservoir radius is represented by the yellow rectangle. The largest difference is for R/D = 0.8 and R/D = 1.0. Note the dips for most of the models at the reservoir edge.

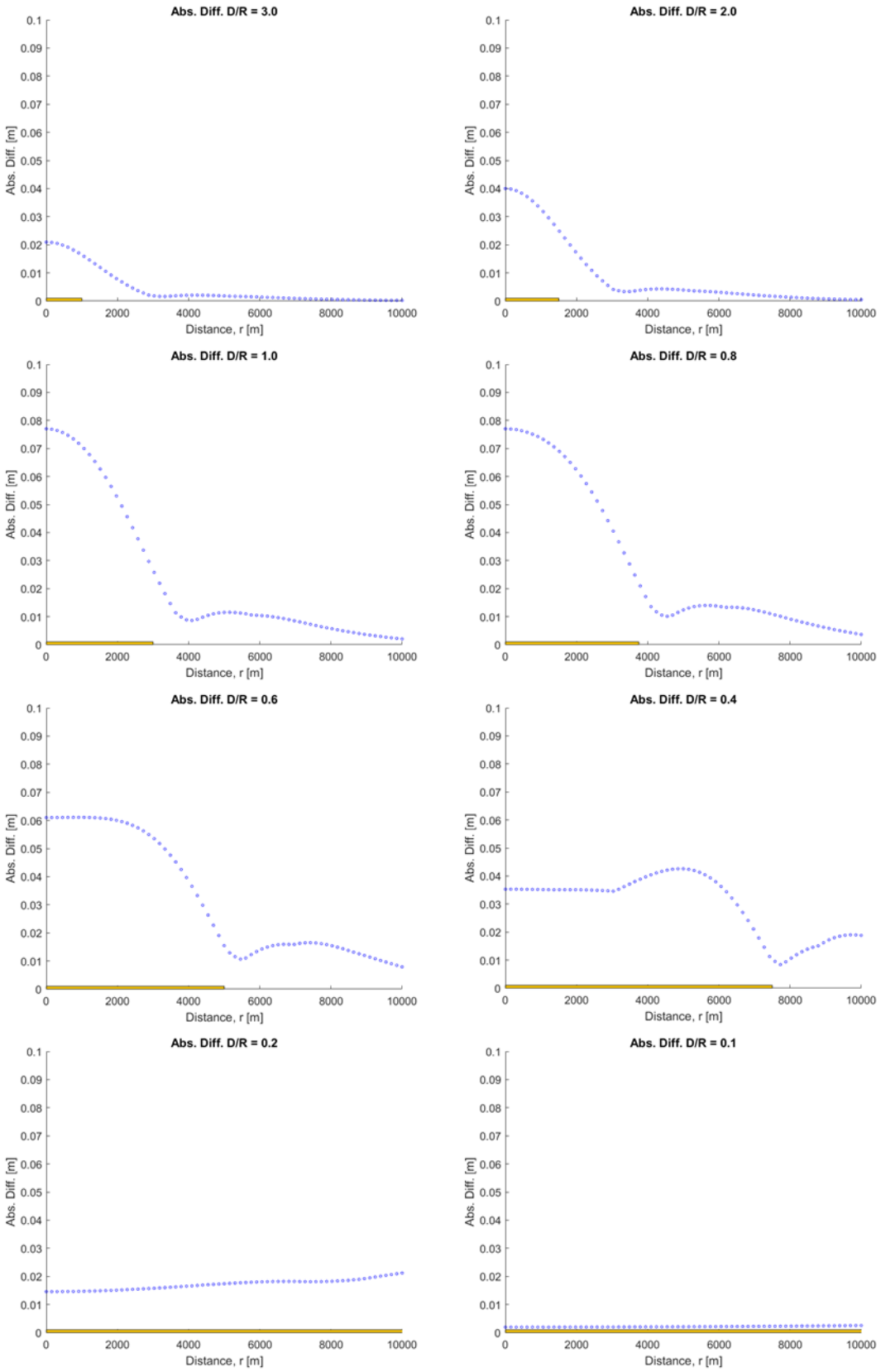


**Figure 105**: The maximum absolute difference at each subsidence bowl point. The reservoir radius is represented by the yellow rectangle. The extent of the x-axis is smaller than the previous figure. Note the dips for most of the models at the reservoir edge.

### 4.2.5.2 Zone of Influence

The absolute amount of subsidence is not the only parameter of interest, but also the area that is affected by the sinking ground. In this report it is called the zone of influence (Figure 106). Another potentially interesting feature is the extent of the ramp of the subsidence bowl as, for larger reservoirs (Figure 104) the ramp is where there is the greatest amount of sensitivity to changes in the overburden. Perhaps making this area more susceptible to damage than the surface that sinks the same amount as the reservoir compaction. For smaller reservoirs the ramp and zone of influence are essentially the same. The zone of influence is defined as any node that has a greater negative (downward) vertical displacement than 1 mm. For the ramp the criterion is that the difference between two nodes needs to be greater than 0.1 mm. The distance between the nodes is approximately 150 m.

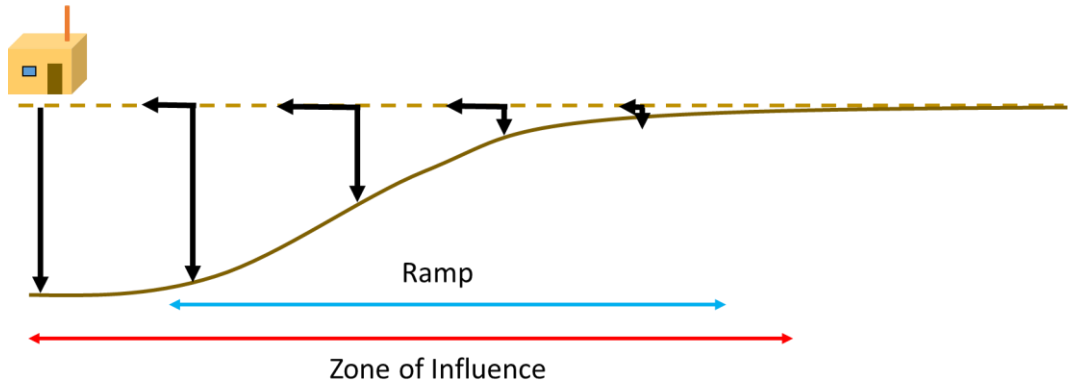


**Figure 106**: Schematic illustration showing the definitions of: zone of influence and ramp

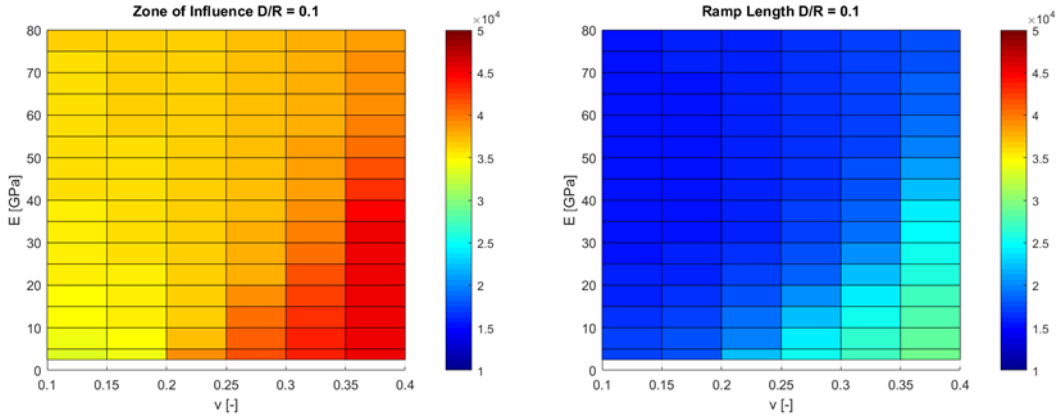


**Figure 107**: Zone of influence (left) and ramp length (right) for D/R = 0.1 (bottom). Note that the colour bar is different for the two reservoir types.

Figure 107 shows the zone of influence and the ramp length for $\eta = 0.1$. The ramp is clearly 'shorter' than the zone of influence for both models, which is to be expected as very extensive reservoirs show that a large part of the surface undergoes the same amount of subsidence (Figure 105). Figure 109 shows the zone of influence for the other eta values and Figure 110 shows the ramp length. Most of the reservoirs show that the zone of influence is largest for a combination of a large Poisson's ratio and low Young's modulus. This is not the case where the reservoir radius is less than the depth.

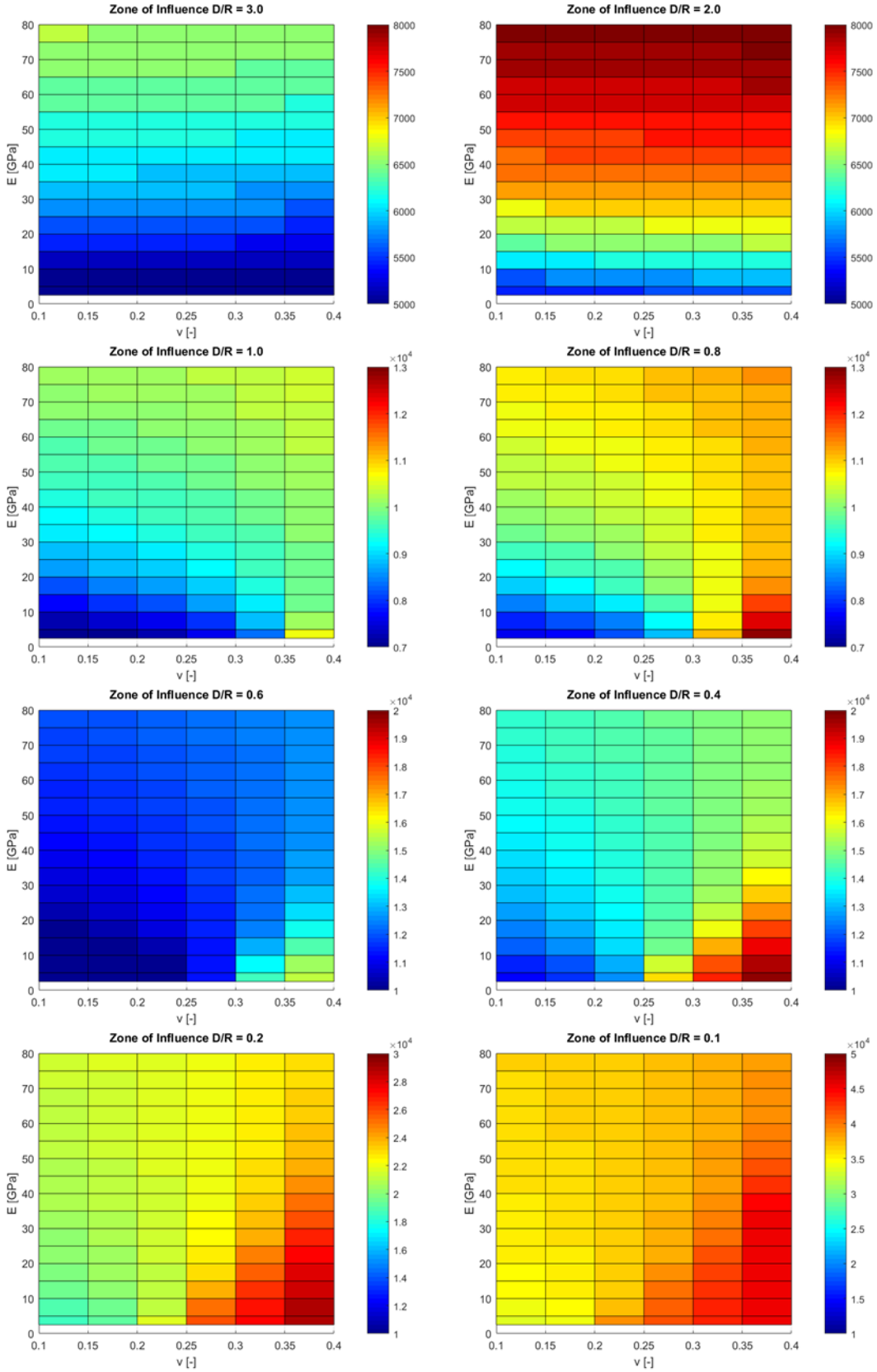


**Figure 108**: Zone of influence for the different reservoir scenarios. Note that the colour bar differs per model. Note that for the models where D/R > 1.0 the subsidence extends greatest when the overburden has a large Young's modulus. For the other models the extent is greatest for small Young's moduli and large Poisson's ratios.

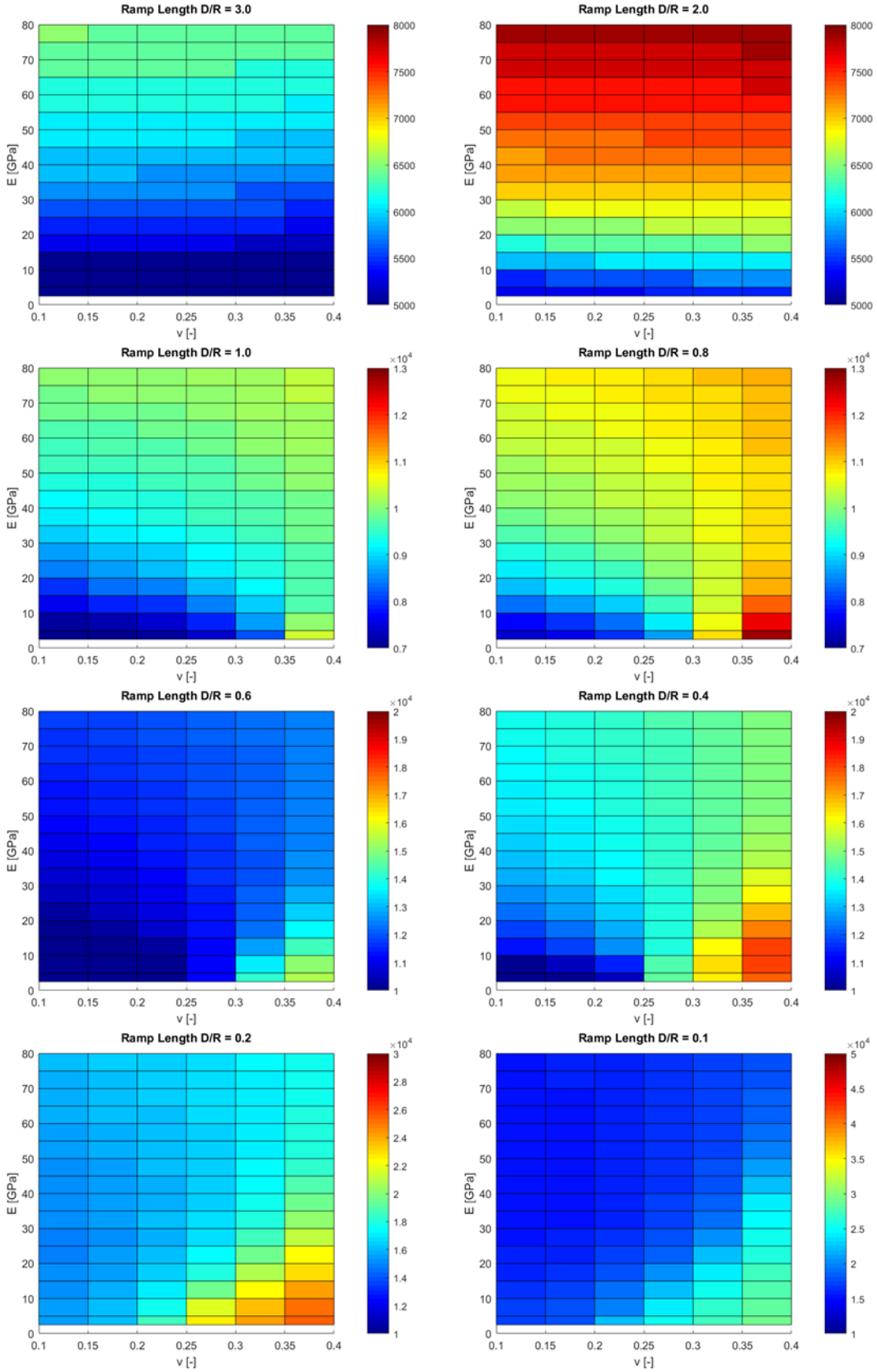


**Figure 109**: Ramp length for the different reservoir scenarios. Note that the colour bar differs per model. Note that for the models where D/R > 1.0 the subsidence extends greatest when the overburden has a large Young's modulus. For the other models the extent is greatest for small Young's moduli and large Poisson's ratios. The pattern is essentially the same as for the zone of influence.

# 4.3 Discussion

In general the results show that the Young's modulus has the greatest influence of the two elastic parameters, but note that for small Young's moduli the Poisson's ratio starts to play a greater role (Figure 100). This is to be expected as the Young's modulus specifically is the driver for the amount of deformation a material undergoes due to a change in the stress state. An overburden layer has the greatest effect on subsidence when it is at the surface and this effect increases with layer thickness (Figure 98 and Figure 100). A higher accuracy of the North Sea groups rock properties in subsidence models is important for subsidence prediction as this would be the geological unit most susceptible to change in elastic parameters. Especially as for lower Young's moduli the variability in vertical displacement becomes larger (Figure 100 and Figure 101). For deeper geological units this is less the case (Figure 100).

The results are fundamentally different from the possible outcomes of using Geertsma's (1973) method, due to the fact that in Plaxis the absolute amount of subsidence is limited by the amount of reservoir compaction. This is not the case for Geertsma as when using a Poisson's ratio of 0.15 and eta = 0.2 the maximum amount of subsidence becomes 1.36 times the compaction. An increase of 36 percent is substantial.

For the zone of influence of the subsidence bowl, both the elastic parameters and the relative shape of the reservoir are important for predicting the vertical displacement. There is a reversal in behaviour where for $\eta < 1$, a smaller Young's modulus and larger Poisson's ratio lead to a larger zone of influence (Figure 108). When the radius is smaller than the depth, the opposite is the case and a higher Young's modulus leads to a greater zone of influence. This makes sense for larger Poisson's ratios as the material is more prone to lateral expansion/compression due to changes in stress. It might be the case that due to the combination of a high Poisson's ratio and less rigidity, the overburden is more prone to deformation in the form of subsidence.

Note that all the results are in the context of horizontal layers in the program *Plaxis*. Based on the results of this chapter, an overburden can influence the vertical displacement by multiple centimetres. This is significant enough, as the mismatch between the *NAM* model and observations is also of this scale. The results in this chapter are based on models that show extreme ranges and not typically found in nature. It is thus interesting to look at narrower and more applied values for the elastic parameters. This is dealt with in chapter 5 and will answer the research questions and hypothesis.

# 5

# Subsidence and Realistic Overburden Heterogeneities

The purpose of this chapter is to combine findings from the previous three chapters and to look at more realistic geological scenarios based on the geology around the Groningen field. The desire is to look at overburden modelling from a more practical point of view than the previous chapter by incorporating specific overburden heterogeneities. This chapter is about the main and sub-research questions related to subsidence modelling and also to answer the hypothesis:

- *To what extent do the overburden heterogeneities affect subsidence caused by reservoir depletion?*
- *Can specific variations in elastic properties of the overburden be ignored for subsidence modelling?*
- Hypothesis: *The heterogeneities of the overburden affect subsidence and should therefore be incorporated*.

For the second question, the point is that the *NAM* does not give an uncertainty range for the elastic parameters. In this chapter values obtained from the well analysis will be used as input due to the fact that, for certain geological units, the results differ considerably from the *NAM* reference values. The *NAM* states that the noise level of the subsidence measurements is around 5 mm (NAM, 2016). For a change, or 'overburden effect', to be meaningful it would have to be larger than this in order to overcome the noise. The first part discusses the methodology on what different scenarios are of interest. The results can be found in the second part and are discussed in part three.

## 5.1 Experiments

*Plaxis 2D* is used, but now more realistic geological cases are created (Figure 110). Section 5.1.1 presents the two different geological models that are used for obtaining results. In section, 5.1.2, the thickness of the Triassic groups is looked at as the thickness varies above the Groningen field. Finally some new lithological layers are created using the obtained well data from chapter 3 in section 5.1.3 and replace the reference layers.

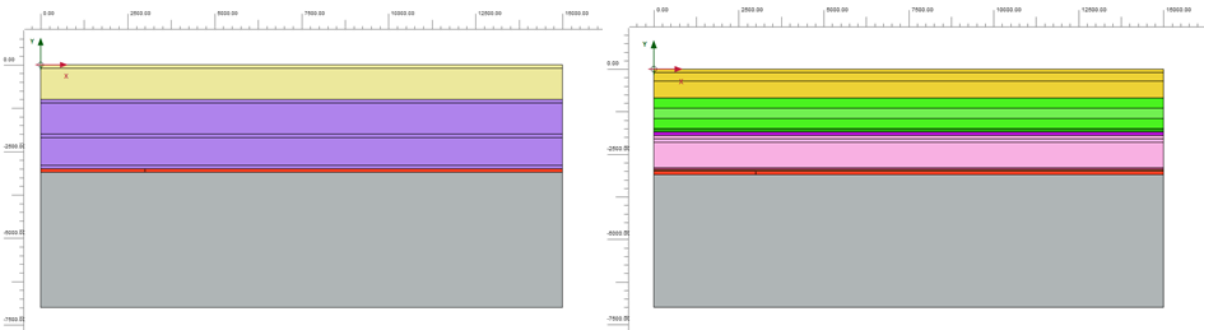

**Figure 110**: The left model shows an overburden consisting of two layers where the top layer (1000 m) is varied (chapter 4). The right model shows the increased overburden complexity based on geology around the Groningen field.

### 5.1.1 Geological Models

Two geological models have been created: one model represents the Groningen field and is approximated as a disc with a radius of 20 km (Figure 111). A smaller model (Figure 112) has been made where the reservoir radius equals the depth of 3000 m. In both models the overburden is the same, however the maximum extent of the of the 20 km reservoir model is 40 km and that of the smaller 3 km is 15 km. Throughout the chapter the two models are referred to a as 'large' and 'small'. Table 12 shows the thicknesses of the different geological units. These were determined mainly by using the *DGM-Diep* model in *DINOloket* (Appendix N) but also by using composite logs from wells and literature. It is important to note that the *Plaxis* model is a coarse approximation of the actual Groningen field as the thickness of various units changes considerably throughout the area of interest. Also all the layers in these two model are horizontal and more complex structures are not modelled.

**Table 12**: Thicknesses and depth tops of the geological units in the *Plaxis* models. Note that these numbers should be seen as rough averages. *This represents both the Upper Germanic Triassic Group and the Lower Germanic Triassic Group.

| Unit | Thickness [m] | Unit Top [m] |
|---|---|---|
| Upper North Sea Group | 350 | 0 |
| Lower North Sea Group | 500 | 350 |
| Chalk Group | 900 | 850 |
| Rijnland Group | 100 | 1750 |
| Germanic Triassic Group* | 100 | 1850 |
| Zechstein Halite | 950 | 1950 |
| Zechstein Anhydrite | 50 | 2900 |
| Ten Boer Member | 50 | 2950 |
| Slochteren Formation | 100 | 3000 |
| Carboniferous | 3900 | 3100 |

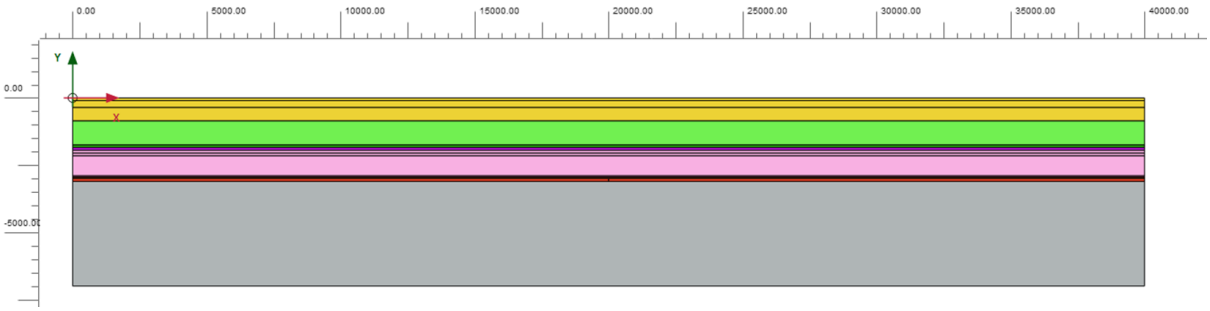


**Figure 111**: *Plaxis* model representing the Groningen field. Note the small vertical notch at 20,000 m denoting the reservoir boundary. Note a model was also made that divides the chalk (light green) into three layers.

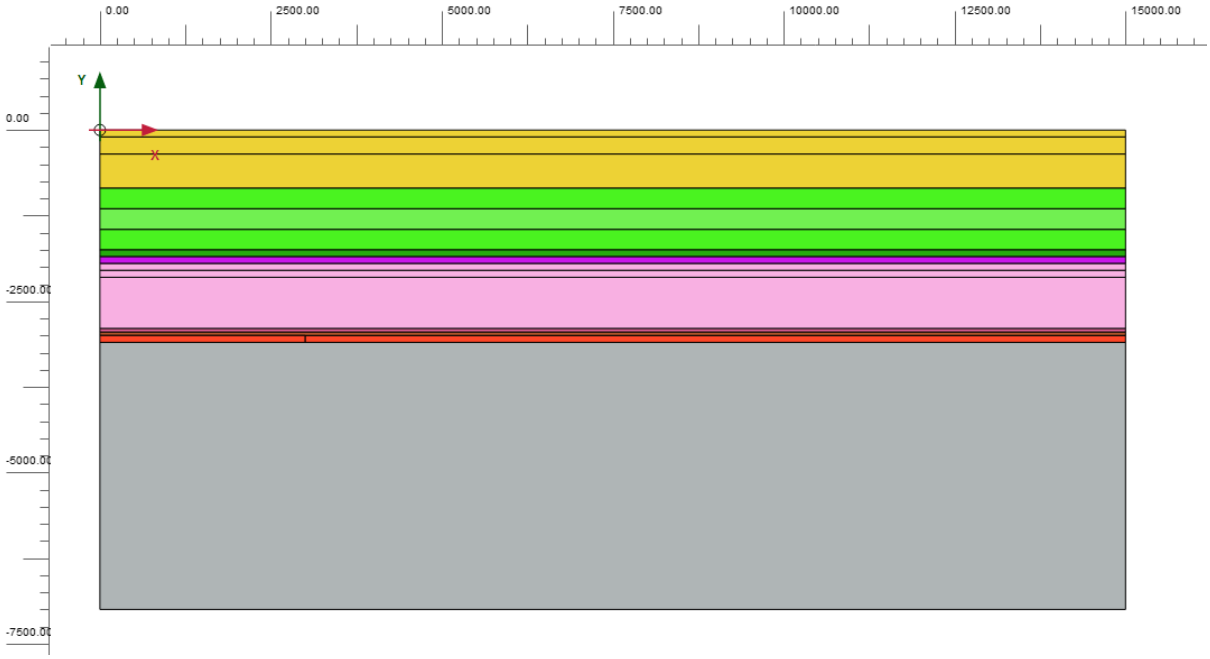


**Figure 112**: The *Plaxis* model representing the 'small' Groningen model. The colours represent the major geological units: Upper and Lower North Sea groups (yellow), Chalk Group (light green), Rijnland Group (dark green), Upper and Lower Triassic groups (purple), Zechstein halite (pink), Zechstein anhydrite (dark pink), Ten Boer Member (brown), Slochteren Formation (red) and the Carboniferous (grey).

### 5.1.1 Homogeneous Overburden

A homogeneous overburden is compared to the multi-layered Groningen models (Figure 113). The overburden is modelled exactly like the Slochteren reservoir with a porosity of 15 % (i.e. E = 14 GPa and v =0.15). This is the greatest simplification that can be made when modelling an overburden and if the difference between the two models is insignificant then there is no point in creating a complicated overburden model. This result is in the context of horizontal layers and not, for instance, complicated salt structures. This goes for all the models in this chapter.

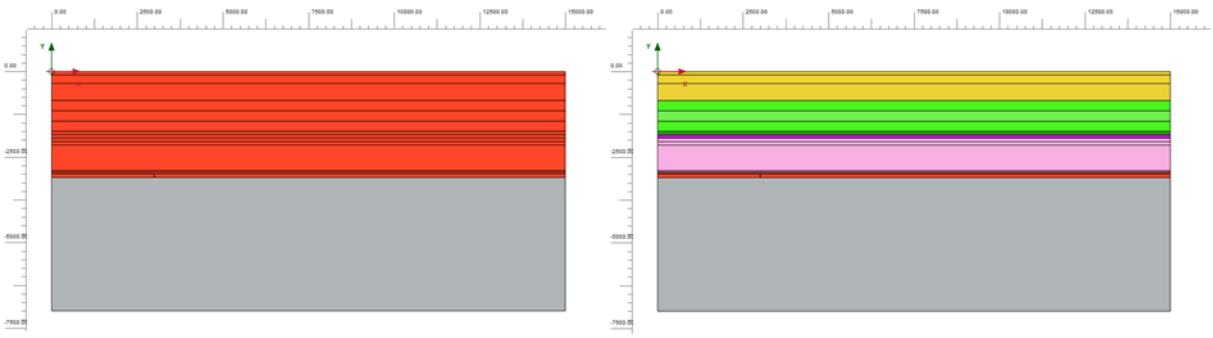

**Figure 113**: Model with a homogeneous overburden (left) consisting only of Slochteren reservoir material and a mulit-layered Groningen geology (right).

### 5.1.2 Triassic Thickness

The thickness of the Upper and Lower Germanic Triassic varies above the Groningen field (Appendix N). It is of interest to know how important it is to take this into account when performing subsidence modelling. The thickness of the Triassic groups varies between 0 and 300 metres (Figure 114). The Triassic material is replaced by the Zechstein halite for this modelling round. All units are modelled using *NAM* values.

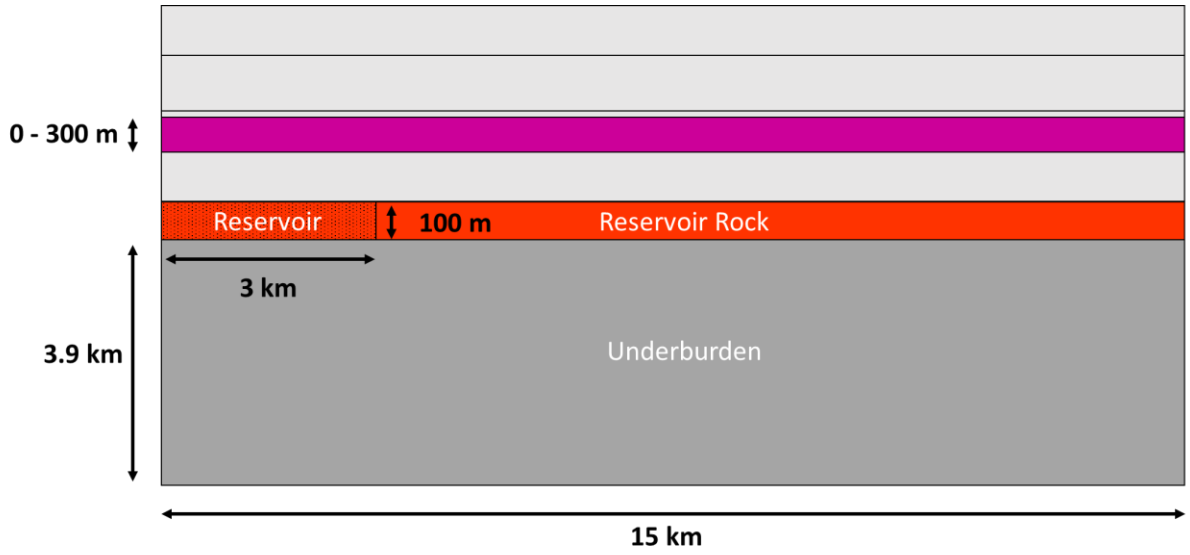


**Figure 114**: Schematic illustration showing the modelling runs for the varying Triassic thickness. The thickness is varied between 0 and 300 metres. Note that some geological units are ignored and the illustration is not to scale.

### 5.1.3 Well Data

After obtaining a large amount of well data it would be interesting to use this as input for the subsidence models. For some units the differences between the results and the *NAM* values are very large and might make for significant findings. The results from chapter 4 show that the overburden at the surface has the greatest influence on vertical displacement, hence the North Sea and Chalk units will be looked at in further detail.

The *NAM* models the Upper North Sea Group and Lower North Sea Group as the same. In this section each group is assigned unique values for the elastic parameters (Figure 115). The values are based on the dynamic Young's modulus and dynamic Poisson's ratio from Table 6 and Table 7. Dynamic Young's modulus values are chosen as the conversion techniques for static values are probably not suited for weak rocks as the converted value can become negative when the dynamic values are small.

The acquired well data differs significantly from the values used by the *NAM*. For the Chalk group the converted static Young's modulus is used (Table 8) and also Figure 80 as the Chalk Group shows three different, but roughly equally thick (300 m) intervals which are represented in Figure 116. The current *NAM* values do not properly represent the variability within the Chalk Group, regardless if the final results are similar or negligible. Table 13 shows the used values from the well data. Both North Sea groups are combined into one modelling round as are the three Chalk Group layers.

**Table 13**: Parameters used from the well data for modelling in *Plaxis*.

| Unit | E [GPa] | ν [-] | γ [N/m$^3$] | $e_{void}$ |
|---|---|---|---|---|
| Upper North Sea Group | 1.42 | 0.46 | 21.09 * 10$^3$ | 0.176 |
| Lower North Sea Group | 2.52 | 0.43 | 21.09 * 10$^3$ | 0.176 |
| Chalk Group | 7.0 | 0.35 | 23.05 * 10$^3$ | 0.176 |
| Chalk Group | 20.0 | 0.33 | 23.05 * 10$^3$ | 0.176 |
| Chalk Group | 25.0 | 0.31 | 23.05 * 10$^3$ | 0.176 |

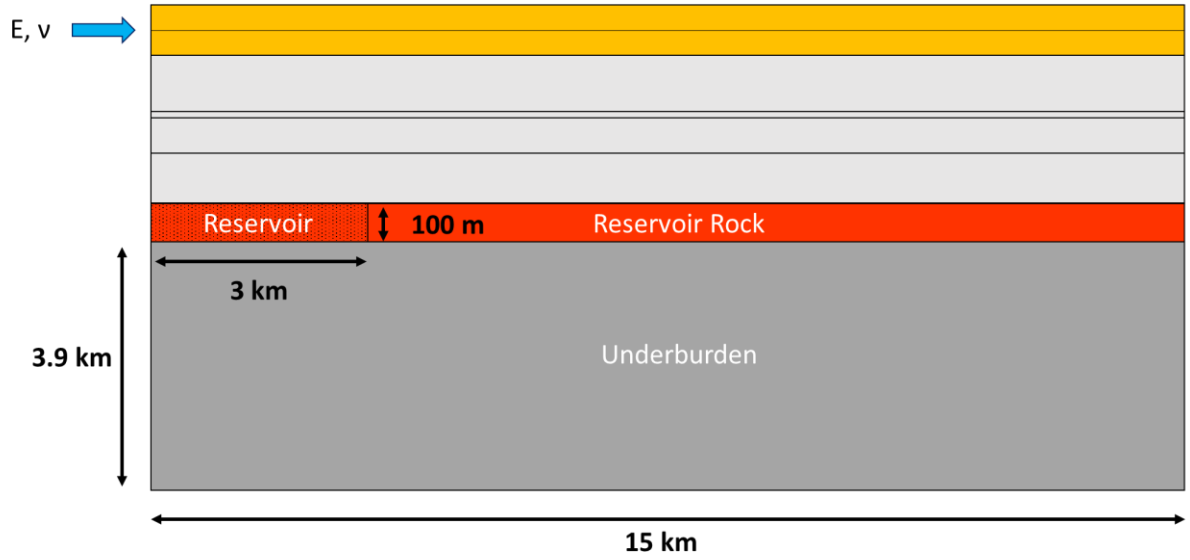


**Figure 115**: Schematic illustration showing the modelling run for the North Sea groups. The Upper North Sea and Lower North Sea are each assigned unique elastic parameters instead of being modelled as the same. Note that some geological units are ignored and the illustration is not to scale.

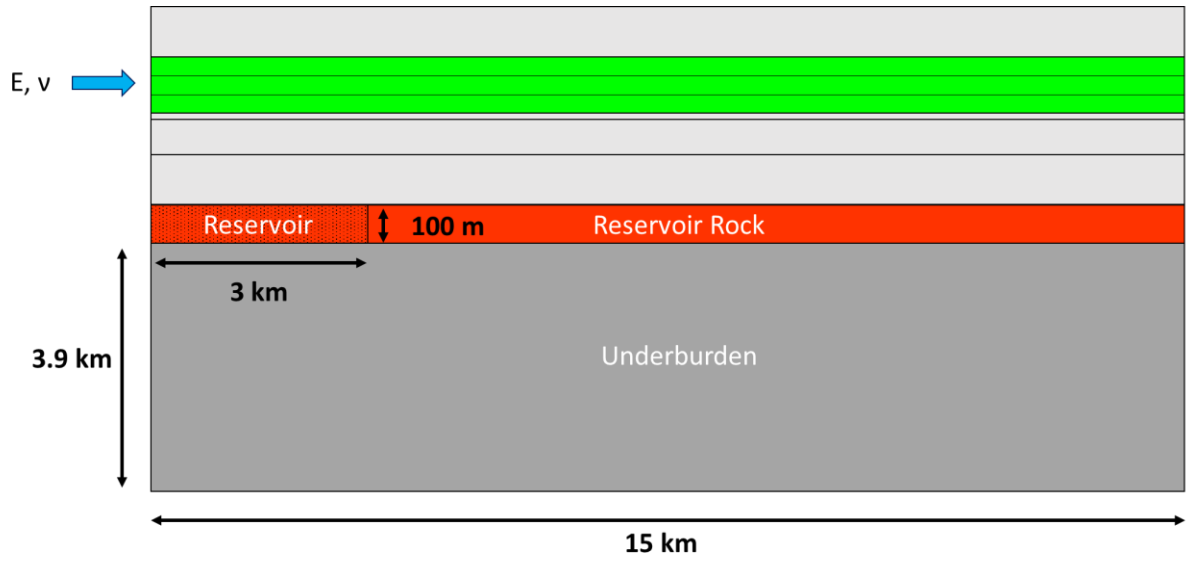


**Figure 116**: Schematic illustration showing the modelling run for the Chalk Group. The Chalk Group is divided into three 300 m thick layers and each is assigned unique elastic parameters instead of being modelled as the same. Note that some geological units are ignored and the illustration is not to scale.

# 5.2 Results

The first section (5.2.1) shows the results of comparing a homogeneous overburden with the multi-layered overburden. The results of the varying Triassic are presented in section 5.2.2 and the results for implementing the well data can be found in section 5.2.3.

## 5.2.1 Homogeneous Overburden

Figure 117 shows the vertical displacement for both the homogeneous overburden and the multi-layered model (base model). For the 20 km reservoir model, the difference between the two models is largest at a distance between 10 and 15 km which is the same behaviour in Figure 104. The absolute difference of the large model is also greater than that of the small (R = 3km) model. The behaviour of the smaller reservoir is also conform to the results from Figure 104 as the greatest difference is above the centre of the reservoir.

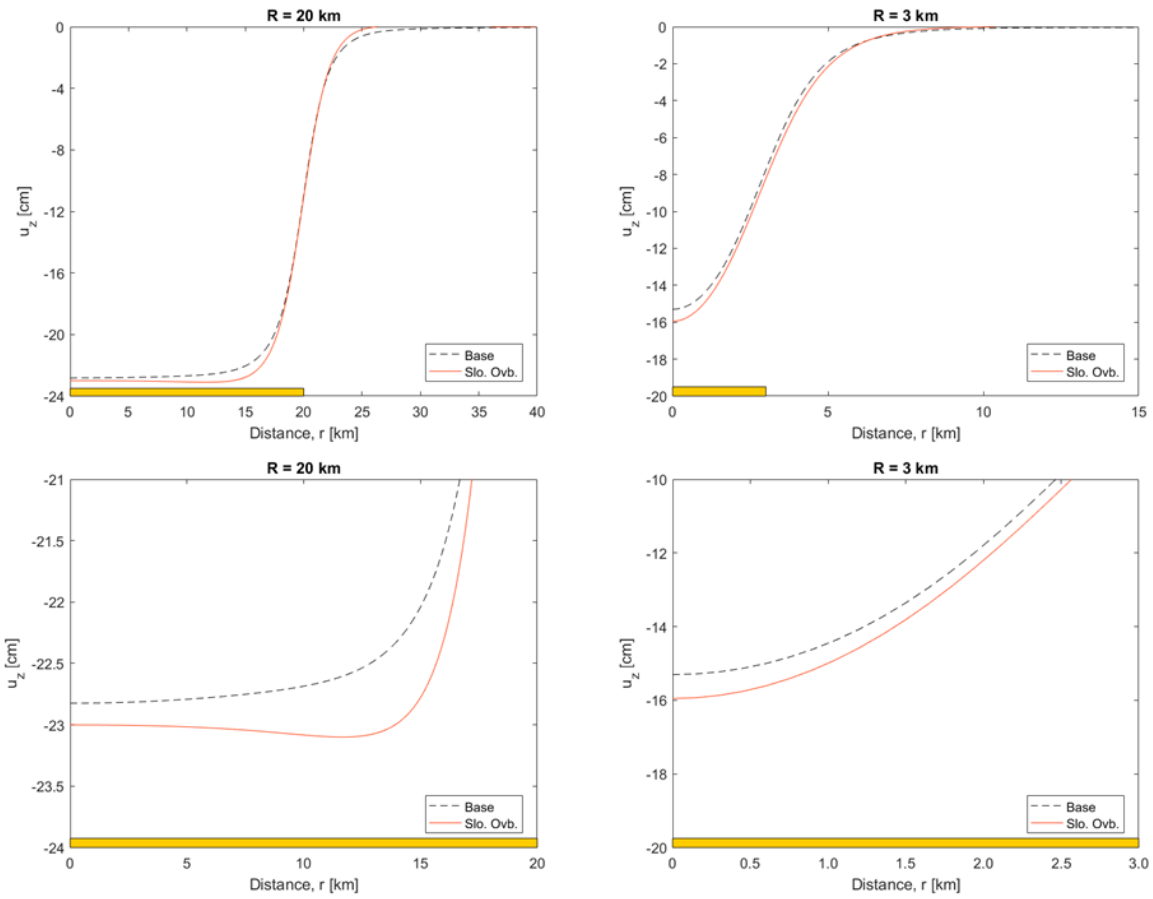


**Figure 117**: Vertical displacements for a homogeneous overburden and multi-layered overburden (base) for two different reservoir scales. Note that the large model shows the greatest difference in vertical displacement.

Figure 118 shows the difference between the overburden model and the base model. For the results to be significant the absolute difference needs to be larger than the InSAR measurement error, which is around 5 mm. As can be seen, both models do overcome this limit for parts of the distance, r. The area seems small, but it should be noted that the x-axis is in kilometres.

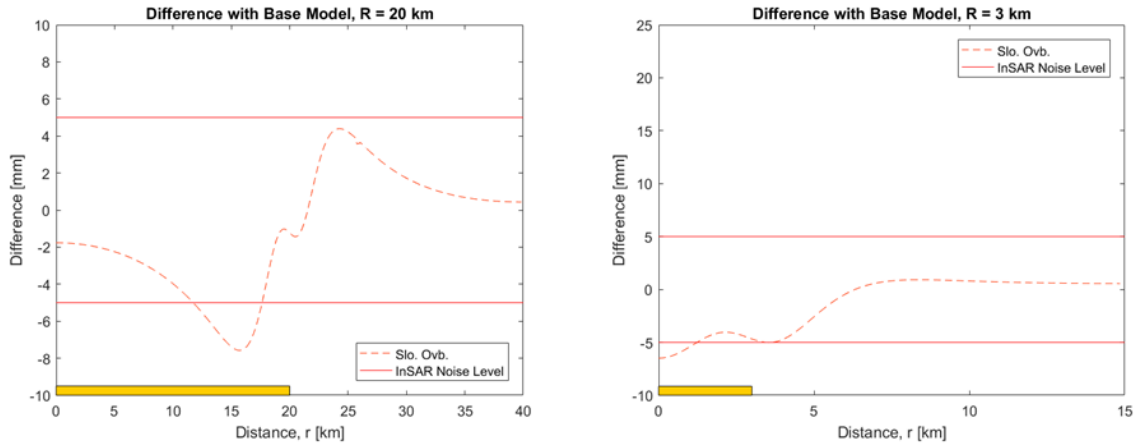


**Figure 118**: Absolute difference between the homogeneous overburden and the base multi-layered model. Note that the for both reservoir scales the difference exceeds the InSAR measurement error.

## 5.2.2 Triassic Thickness

Figure 119 shows the vertical displacements when varying the thickness of the combined Germanic Triassic groups and replacing that material with Zechstein halite. The subsidence bowls are virtually indistinguishable for both reservoir sizes. This conforms to the results in the previous chapter where, almost regardless of the thickness, a layer surrounded by overburden has relatively little influence on the displacement (Figure 98 and Figure 100).

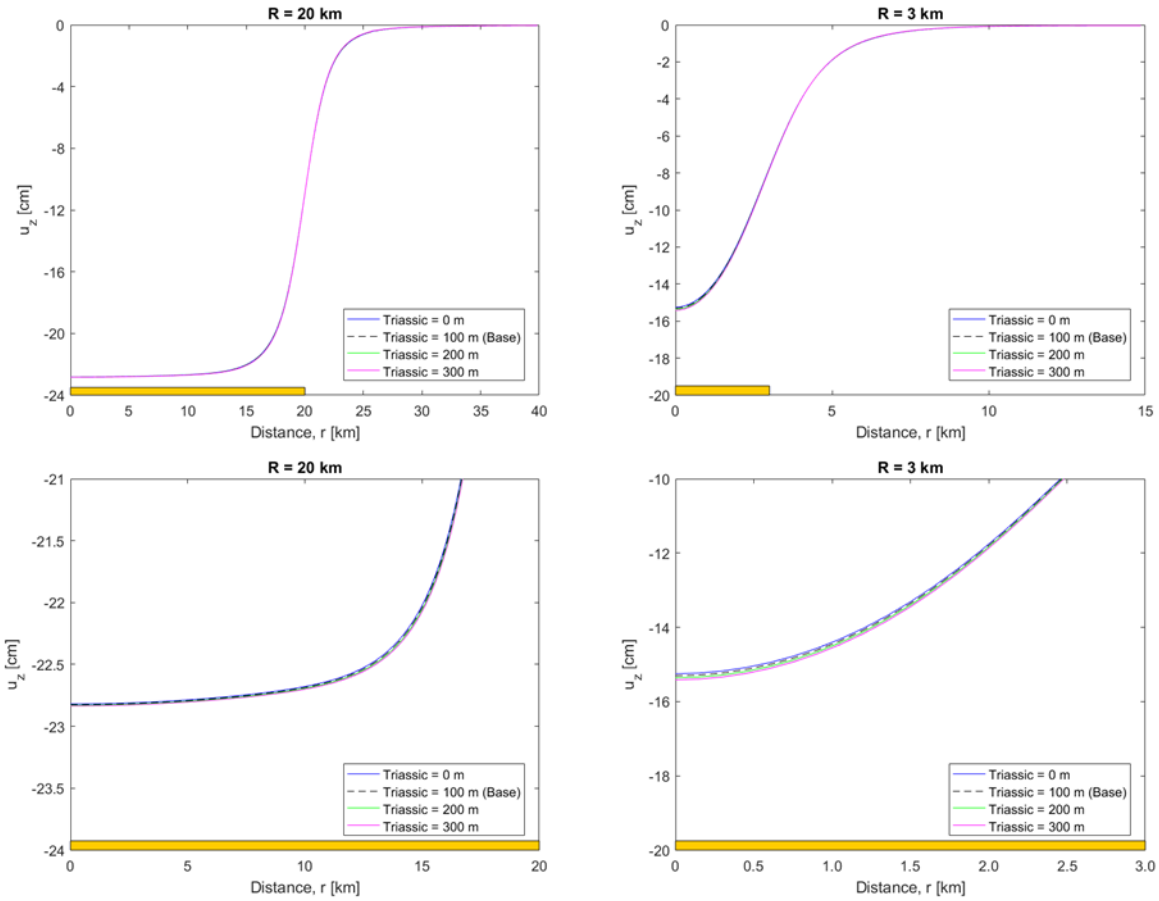


**Figure 119**: Vertical displacement for the varying Triassic thickness in the Large/Groningen (left) and small (right) model. The yellow rectangle represents the reservoir radius. Note that the subsidence bowls are virtually indistinguishable for the Groningen scale model and almost so for 3 km radius model.

Figure 120 shows the difference between the Triassic models and the base model. For the results to be significant the absolute difference needs to be larger than the InSAR measurement error, which is around 5 mm. As can be seen, both models do not overcome this limit for any distance, r.

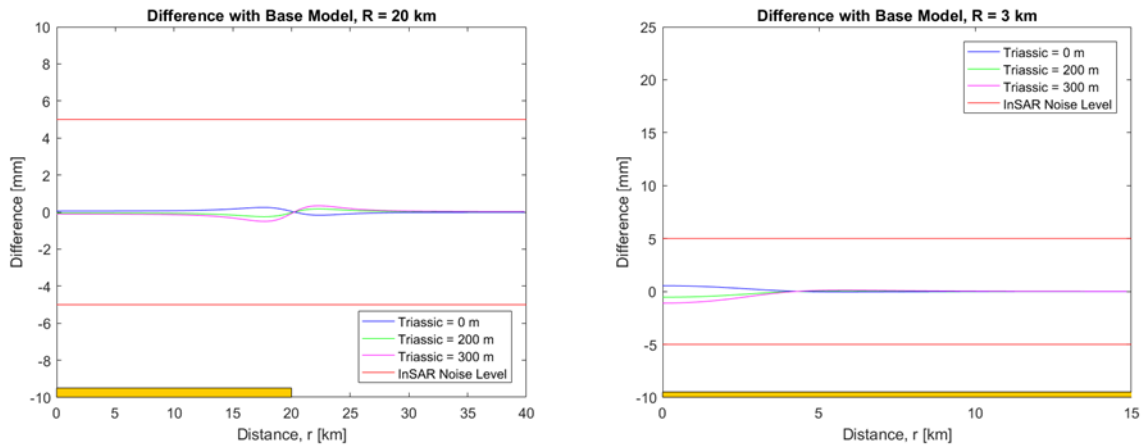


**Figure 120**: Absolute difference between the base multi-layered model and the different Triassic thicknesses. Note that the for both reservoir scales the difference stays within the InSAR measurement error.

## 5.2.3 Well Data

Figure 121 shows the vertical displacements when the Upper North Sea Group, Lower North Sea Group and Chalk Group are modelled based on the obtained well data. When the relevant group is modelled, all the other geological units are modelled based on the *NAM* reference values.

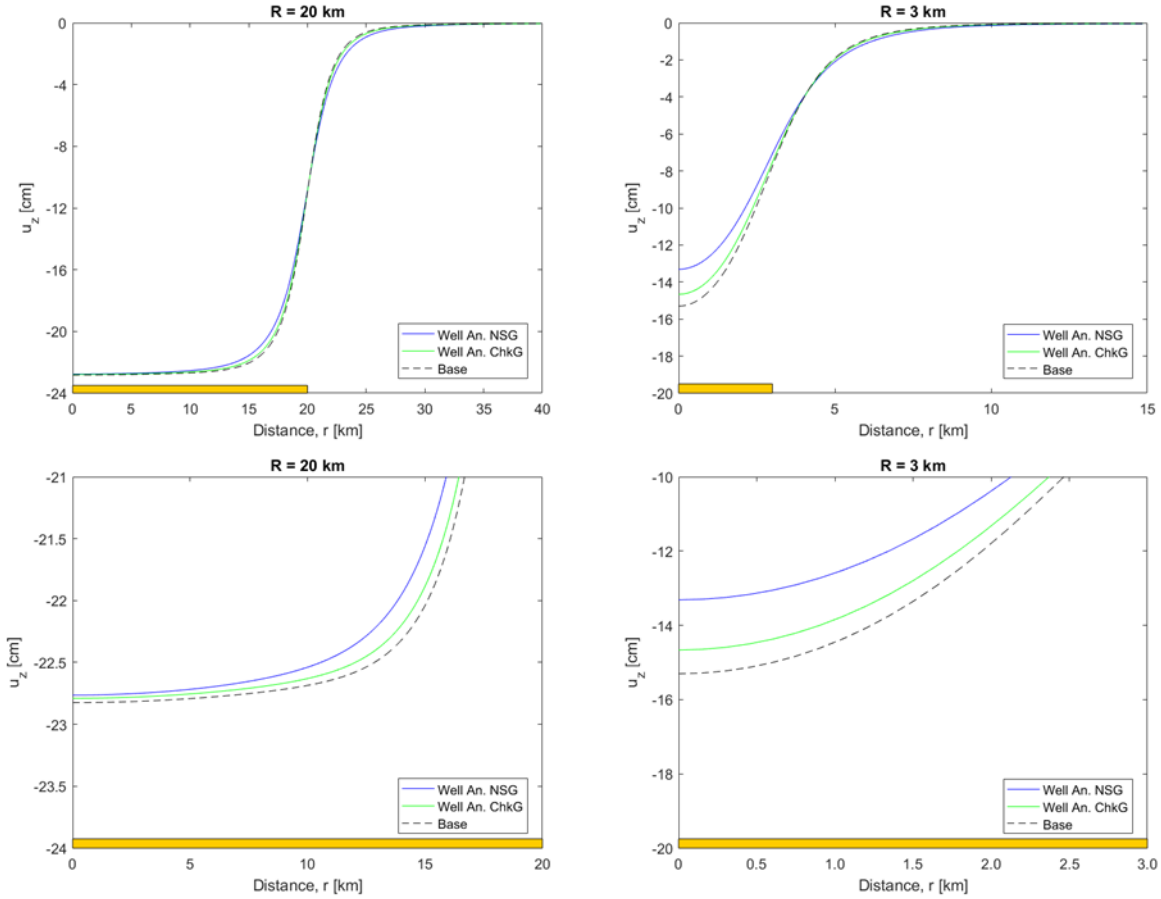


**Figure 121**: Vertical displacement for using well data for the North Sea groups and Chalk Group. The yellow rectangle represents the reservoir radius. Note that the subsidence bowls are quite distinguishable, especially for R = 3 km.

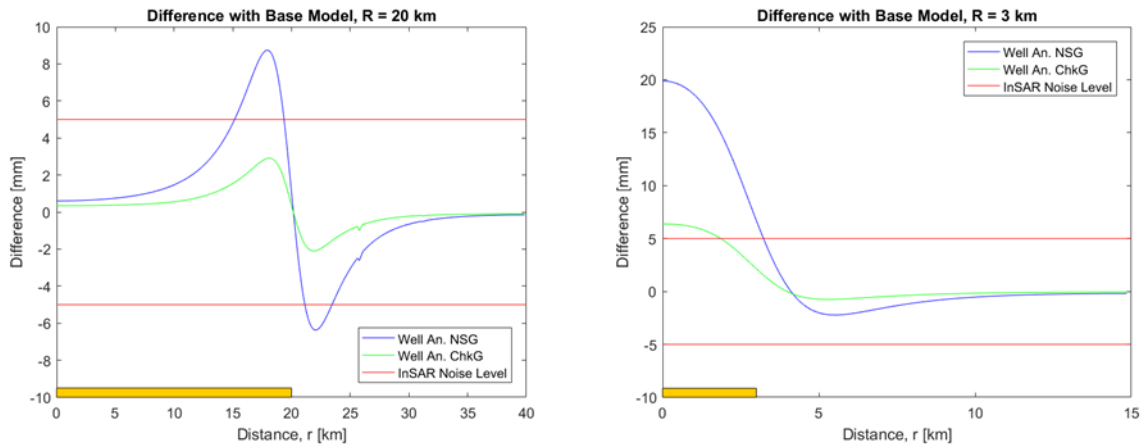


**Figure 122**: Absolute difference between the base multi-layered model and the well data models. Note that the for both reservoir scales the difference of the North Sea run is larger than the InSAR measurement error. For the Chalk Group the effect is only noticeable for a small scale reservoir.

Figure 122 shows the difference between the well data models and the base model. For the results to be significant the absolute difference needs to be larger than the InSAR measurement error, which is around 5 mm. For the large scale model, the adjusted North Sea groups results in a difference that overcomes the InSAR error. This is not the case for the Chalk Group. The results are quite different for the small scale model, because both adjusted units result in a difference that is larger than the InSAR error. The difference of 20 mm is noticeably large and these results conform to the findings in Figure 104 where reservoirs with a D/R ratio of 1 are the most susceptible to changes in the overburden.

# 5.3 Discussion

The discussion of this chapter also incorporates points from the previous two chapters. Note that all the subsidence results are in the context of horizontal layers. The research questions for subsidence and the hypothesis are given below:

- *To what extent do overburden heterogeneities affect subsidence caused by reservoir depletion?*
- From a practical point of view, this is then followed by: *Can variations in elastic properties of the overburden be ignored for subsidence modelling?*
- Hypothesis: *The heterogeneities of the overburden affect subsidence and should therefore be incorporated*.

The results of chapter 4 show that for variations in overburden properties the range of values is in multiple centimetres. This is the relevant scale considering that the *NAM* subsidence model over or under predicts the observed subsidence by multiple centimetres, depending on the location (Appendix A). Figure 117 and Figure 118 show that there is a case for adding complexity to the overburden by trying to accurately model the different geological units. The difference between the multi-layered model and the homogeneous model is greater than the InSAR error and can therefore be seen. The extent of the effect of the overburden heterogeneities is in this case around 0.75 cm. In an absolute sense this is not large, but significant when compared to current modelling discrepancies (Appendix A) on the order of 4-5 cm by the *NAM*. The answer to the hypothesis is yes.

Figure 100 shows that a thick layer at the surface can have a large influence on the vertical displacement even when the underlying overburden is more rigid (Figure 101). When the Young's modulus is low, the vertical displacement becomes very sensitive to changes in the elastic parameters. These characteristics make the North Sea Group a prime candidate for further study, especially as the well data does not match the values used by the *NAM*. When the North Sea Group is modelled on the basis of the well data, the difference between the new model and the reference model is stark (Figure 122). For the small scale model (R = 3 km) the maximum difference is 2 cm. The large scale model shows a difference of around 1 cm, which in the context of 4-5 centimetres (Appendix A) is large. These particular results answer the hypothesis with a more resounding yes than the previous comparison between a homogeneous and the base multi-layered model. The uncertainty in the North Sea elastic parameters should be narrowed down, as the two groups have a large effect on the subsidence. Based on these results it would be beneficial to acquire static values for the elastic parameters of the Upper North Sea Group and the Lower North Sea Group. The results suggest that these large variations in parameter values should not be ignored when it comes to subsidence modelling. Further research is warranted.

The variability within the Chalk Group is poorly described by the assigned values of the *NAM* (Figure 80), hence it is also studied. For a Groningen scale model (Figure 122) the difference caused by the well data Chalk Group is below the InSAR error, making it unimportant for this reservoir scale. However, when the new layers are applied to the small scale model then the difference caused by the Chalk is above the InSAR error and should therefore be incorporated. The influence is significantly less than when changing the North Sea groups.

For horizontal layers the thickness of the Triassic groups is practically irrelevant. None of the differences come near the InSAR error level and would not be visible when measured (Figure 120).

These results can be seen as a practical example of Figure 98 and Figure 100 where the thickness of a layer in the overburden does not influence the vertical displacement by a large amount.

It needs to be stated that the geological units are modelled as horizontal layers and therefore the geology is simple. The geology around the Groningen area is more complex than this (Appendix N) as there are salt pillows in the region and varying amounts of erosion for units such as the Upper and Lower Germanic Triassic. Subsidence results might be significantly different in a more accurate 3D setting. Added levels of complexity can be:

- Adding large structures such as salt pillows and study their effect in a 3D setting. Due to the way the 2D modelling works, this is not suitable in *Plaxis* 2D. The key interest is the effect of non-horizontal layering.
- The Groningen reservoir is heavily faulted (NAM, 2013) and reservoir faults have not been taken into account. If faults are (partially) sealing they will influence the pressure drop around the reservoir, which is the driver for compaction and therefore subsidence.
- Reservoir sedimentology. Currently the elastic properties are based on the porosity and are thus influenced by porosity trends caused by differences in sedimentary facies. This is probably automatically incorporated in the *NAM* subsidence model as this is in turn based on the dynamic reservoir model. Nevertheless it would be interesting to compare this effect to that of the overburden. Keeping in mind that the elastic parameters of the reservoir have more influence on subsidence than those of the overburden (Figure 94 and Figure 100).

# 6

# Conclusions

There is an increasing interest in modelling the Dutch overburden and the purpose of this research is to find links between the overburden and surface subsidence. The main research question is whether overburden heterogeneity needs to be incorporated or not. Based on these findings the overburden does have a significant enough effect on the subsidence and a number of conclusions can be drawn:

- For a direct comparison between a homogeneous overburden modelled as Slochteren rocks and a multi-layered (i.e. heterogeneous) overburden there is a difference of 0.7 cm which is larger than the InSAR measurement error (NAM, 2013) and therefore significant. It is also relatively large when compared to the current maximum error (4-5 cm) of the *NAM* subsidence model (Appendix A).
- A thick layer at the surface has the greatest influence on the 'overburden effect' on subsidence. This is especially the case for low Young's modulus values. This makes the North Sea groups particularly influential in determining the subsidence. For a reservoir at 3000 m depth and a 3000 m radius the difference is 2 cm which is substantial. For a Groningen scale model the difference is almost 1 cm or around 25 % of the current modelling error.
- Layers that are not at the surface a have considerably less influence but when thick enough, and if their internal heterogeneities are large (e.g. the Chalk Group), they can still cause a significant enough effect and should therefore be incorporated in subsidence modelling.

The second purpose of this thesis is to compare calculated elastic parameters to those in literature, particularly the values used by the *NAM*. An attempt was also made to find lithological links within the elastic parameters by using the gamma ray and neutron porosity logs. The conclusions for the well data are as follows:

- The calculated values often do not match either the *NAM* reference values or those from Orlic (2016), indicating uncertainty of the elastic parameters.
- It is clear from the two *NAM* wells that there are very stark differences within certain geological units with the Upper North Sea Group, Lower North Sea Group and Chalk Group showing clear trends with depth.
- The Chalk Group and Slochteren Formation show that, when a rock has a pure lithology, there is a clear relationship between the Young's modulus and the porosity. The Poisson's ratio on the other hand, rarely shows a relationship with porosity. If a suitable relationship between the (neutron) porosity is available, then the well data can be used to calculate the Young's modulus instead of using acoustic data. This allows for more possibilities than being reliant on core data.

A number of recommendations can be made for future studies:

## Well Data

- The well data would be greatly improved if there were static values for comparison. If possible static Young's moduli and Poisson's ratios should be determined for each geological unit from each well. A study like this would allow one to use, or even discard, the data from this study. It might be less relevant for the overburden units below the Chalk Group, but considering that the elastic parameters of the reservoir are the dominating factor for subsidence modelling, there are still gains to be made in this regard.
- A large amount of well data has not been looked at. There is possibly a large amount of interesting data left that could further conform to results that have already be found. This is more relevant for the geological units that have the most influence, i.e. the Upper North Sea Group, Lower North Sea Group, Chalk Group and the Slochteren Formation.
- One should try to overcome discrepancies in log resolution by trying to use the LIS files and export a desired resolution. This would make calculations more accurate by avoiding having to shift and link data points.

## Subsidence Modelling

- The overburden has been modelled as horizontal layers. The Dutch subsurface is considerably more complex (Appendix N) as there are entire fault networks and salt domes which might have considerable influence. These types of structures would need to be modelled in the *Plaxis 3D* program.
- Considering the dominant role of the reservoir it would be interesting to add heterogeneity to it in further *Plaxis* studies. The porosity within the reservoir could be varied and by extension the elastic parameters as they are now fixed and constant. Reservoir compartments could be modelled by varying the pressure distribution in the reservoir. In reality the Groningen reservoir has a porosity distribution and contains extensive fault networks. The 2D program is not suitable for this type of modelling and *Plaxis 3D* would have to be used.
- As a general recommendation, future studies should be performed using *Python* input scripts to build the *Plaxis* models. Due to logistical issues the modelling runs had to be done by hand, as were adjustments to the data. This is very time consuming which is better spent doing more research.

# Appendices

# Appendix A

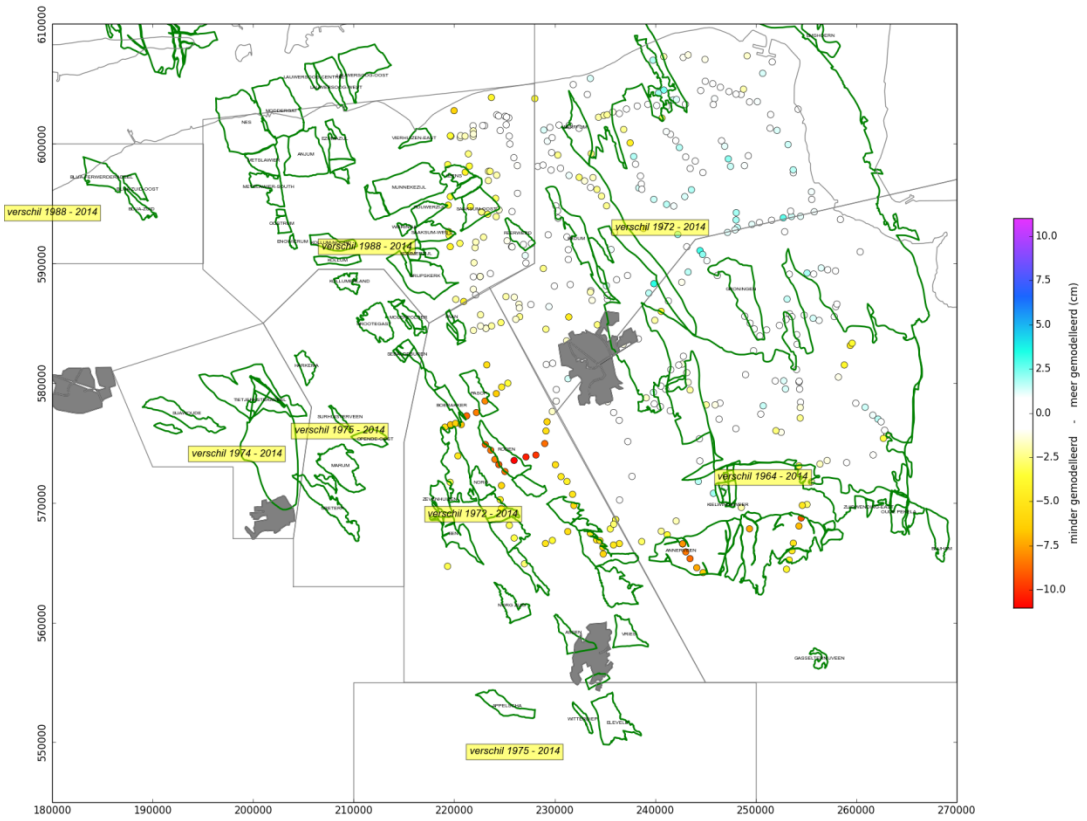


**Figure A1**: Difference between the measured and estimated subsidence until the year 2013 using the RTCiM compaction model of the *NAM*. Note that for some locations the actual subsidence for the Groningen field is around 4 cm less (blue) than the modelled subsidence and around 5 cm more (yellow). Copyright (NAM: *NAM* et al., 2016).

# Appendix B

## Mehrabian and Abousleiman Solution

The Geertsma solution has been built on by a number of researchers. For instance van Opstal (1974) and later Tempone et al. (2010) added a rigid basement to the Geertsma solution, whilst Fokker and Orlic (2006) created a model with multiple visco-elastic layers (Tempone et al., 2010). Mehrabain and Abousleiman (2015) have extended the Geertsma solution to a layered stratigraphic model. In this model (Figure A1) the reservoir rock is assumed to have the same Poisson's ratio as the overburden and underburden rock $\nu_o = \nu_{res} = \nu_u$, however the shear moduli are different $G_{res} \neq G_o = G_u$ allowing for two different rock materials albeit with the same Poisson's ratio. The Hankel-Lipschitz integrals for surface deformation derived by Mehrabian and Abousleiman are as follows:

$$u_r(r,0) = -\frac{c_m \Delta p h R}{\mu} \int_0^\infty [2(1-\nu) + (\mu - 1)\xi] J_1(R\xi) J_0(r\xi) e^{-\xi} d\xi \qquad \text{(A.1)}$$

$$u_z(r,0) = +\frac{c_m \Delta p h R}{\mu} \int_0^\infty [(\mu - 1)\xi + (\mu + 1) - 2\nu] J_1(R\xi) J_0(r\xi) e^{-\xi} d\xi \qquad \text{(A.2)}$$

For more information on deriving these equations, an interested reader is referred to Mehrabian and Abousleiman (2015). At the centre of the subsidence bowl the solution for vertical displacement is:

$$\frac{u_z(0,0)}{c_m \Delta p h} = -\left(\frac{1+\mu-2\nu}{\mu}\right)\left(\frac{1}{\sqrt{1+\rho^2}} - 1\right) + \left(\frac{\mu-1}{\mu}\right)\left[\frac{\rho^2}{\sqrt{1+\rho^2}}\right] \qquad \text{(A.3)}$$

$$\text{Where: } \rho = \frac{R}{D} \qquad \text{(A.4)}$$

Note that Mehrabian and Abousleiman use a different dimensionless symbol. In Appendix B the equations for subsidence at (0,0) are rewritten for consistency in parameters.

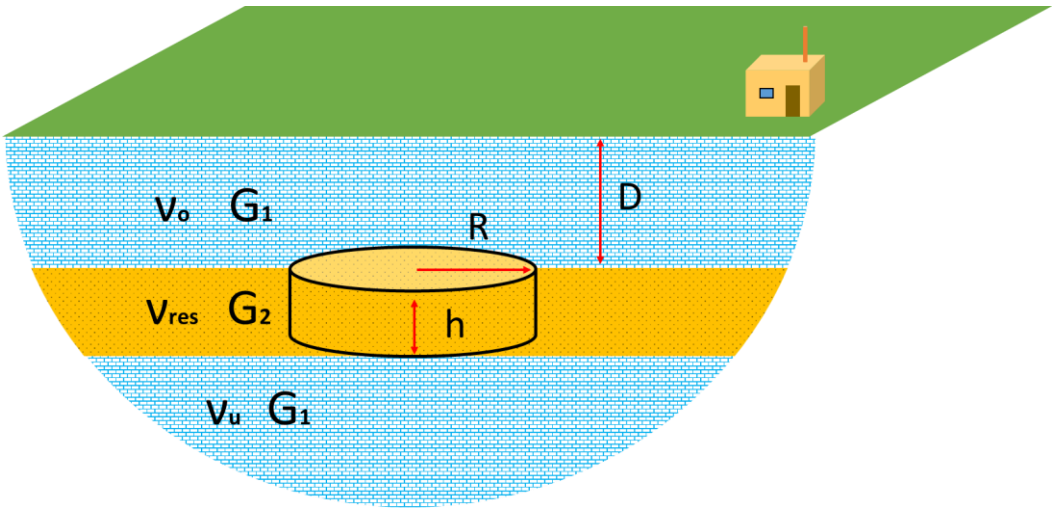


**Figure B1**. Geological situation of the Mehrabian and Abousleiman (2015) solution. Note that the Poisson's ratios of all three layers are assumed to be the same and that the overburden and underburden have the same shear modulus. After Mehrabian and Abousleiman (2015).

# Appendix C

Comparison of Formulae

The two semi-analytical solutions of Geertsma (1973) and Mehrabian and Abousleiman (2015) presented in this Chapter use different notations for, in some cases, the same thing. This section rewrites all three equations to ease the understanding for the reader. Both solutions are for the centre of the subsidence bowl at (r,z) coordinate (0,0). Geertsma's solution for subsidence:

$$\frac{u_{z1}(0,0)}{c_m \Delta p h} = -2(1-\nu)\left(1 - \frac{\eta}{\sqrt{1+\eta^2}}\right) \tag{B.1}$$

Where: $\eta = \frac{D}{R}$

$$\frac{u_{z1}(0,0)}{c_m \Delta p h} = -2(1-\nu)\left(1 - \frac{\frac{D}{R}}{\sqrt{1+\left(\frac{D}{R}\right)^2}}\right) \tag{B.2}$$

Mehrabian and Abousleiman write their subsidence solutions as follows:

$$\frac{u_{z1}(0,0)}{c_m \Delta p h} = -\left(\frac{1+\mu-2\nu}{\mu}\right)\left(\frac{1}{\sqrt{1+\rho^2}} - 1\right) + \left(\frac{\mu-1}{\mu}\right)\left[\frac{\rho^2}{\sqrt{1+\rho^2}}\right] \tag{B.3}$$

Where: $\rho = \frac{R}{D}$ and $\mu = \frac{G_1}{G_2}$. When $\rho$ is replaced in Eq. (B.3) this leads to:

$$\frac{u_{z1}(0,0)}{c_m \Delta p h} = -\left(\frac{1+\mu-2\nu}{\mu}\right)\left(\frac{1}{\sqrt{1+\left(\frac{R}{D}\right)^2}} - 1\right) + \left(\frac{\mu-1}{\mu}\right)\left[\frac{\left(\frac{R}{D}\right)^2}{\sqrt{1+\left(\frac{R}{D}\right)^2}}\right] \tag{B.4}$$

When $\mu = 1$ Eq. B.4 can be simplified to:

$$\frac{u_{z1}(0,0)}{c_m \Delta p h} = -2(1-\nu)\left(\frac{1}{\sqrt{1+\left(\frac{R}{D}\right)^2}} - 1\right) \tag{B.5}$$

This is equivalent to the Geertsma solution (Eq. B.2).

# Appendix D

## Incorporating Poroelasticity

In the previous sections of chapter 2 and 3 it has been assumed that rocks are solid (i.e. non-porous) materials. Hydrocarbons could not be located in the subsurface if all rocks were non-porous, hence the theory of poroelasticity was developed to take porosity into account. The reservoir is still assumed to be homogeneous and isotropic. The following derivation is very close to the Geertsma (1973) solution where the main difference is the incorporation of the Biot coefficient. Deformation of a reservoir can be described by Hooke's laws in terms of changes in the effective stresses in the subsurface (Fjaer et al., 2008). When using the using the initial stress state, prior to production, the stress strain relations become:

$$E_{fr}e_h = \Delta\sigma'_h - \nu_{fr}(\Delta\sigma'_H - \Delta\sigma'_v) \quad \text{(C.1)}$$

$$E_{fr}e_H = \Delta\sigma'_H - \nu_{fr}(\Delta\sigma'_h - \Delta\sigma'_v) \quad \text{(C.2)}$$

$$E_{fr}e_v = \Delta\sigma'_v - \nu_{fr}(\Delta\sigma'_H - \Delta\sigma'_h) \quad \text{(C.3)}$$

It is assumed that there are *drained* conditions, meaning that the pore fluid in the material can escaped during compression and hence the load is borne by the solid *framework* of the material. As with the previous section the change is reservoir height is represented by the vertical strain $e_z = e_v$ (Eq. 3.1) and the horizontal strain is neglected $e_h = e_H = 0$. In the theory of uniaxial compaction the horizontal stresses increase when the object is shortened. Along with the previous assumption of zero horizontal strain the following is obtained (Fjaer et al., 2008):

$$\Delta\sigma'_h = \Delta\sigma'_H = \frac{\nu_{fr}}{1-\nu_{fr}}\Delta\sigma'_v \quad \text{(C.4)}$$

What is also assumed is that the vertical stress remains constant which means that the full force of the overburden acts on the reservoir at all times. The change in vertical stress is thus zero (Fjaer et al., 2008). In reality there is so-called *stress arching* where the overburden not directly above the reservoir reduces the load on the reservoir (Wang et al., 2015). This leads to:

$$\Delta\sigma'_v = \Delta\sigma_v - \alpha\Delta p_f = -\alpha\Delta p_f \quad \text{(C.5)}$$

Eq. C.4 and Eq. C.5 can be substituted into Eq. C.3 which gives:

$$e_z = \frac{\Delta h}{h} = \frac{1}{E_{fr}}\frac{(1+\nu_{fr})(1-2\nu_{fr})}{1-\nu_{fr}}\alpha\Delta p_f \quad \text{(C.6)}$$

The uniaxial compaction coefficient then becomes:

$$\frac{\Delta h}{h} = c_m\alpha\Delta p_f \text{ or } \Delta h = c_m\alpha\Delta p_f h \quad \text{(C.7)}$$

Which is same that Geertsma (1973) derived, but including the Biot coefficient. Eq. C.5 and C.6 can be rewritten in terms of the uniaxial compaction coefficient.

$$c_m = \frac{1}{E_{fr}}\frac{(1+\nu_{fr})(1-2\nu_{fr})}{1-\nu_{fr}} \quad \text{(C.8)}$$

The finite element program *Plaxis* does not allow for the use of the Biot coefficient in the way that the author would like it to. To simulate the effect of the parameter the pressure drops are adjusted by multiplying the Biot coefficient by the pressure drop and this new value is entered into *Plaxis* (Eq. C.9).

$$\Delta p_{f,\alpha} = \alpha \Delta p_f \tag{C.9}$$

# Appendix E

Core Data for the Slochteren Formation

The figures below are from Lele et al. (2015) and modified to show the locations of the four points that were used to derive the trend lines in section 2.3.3.

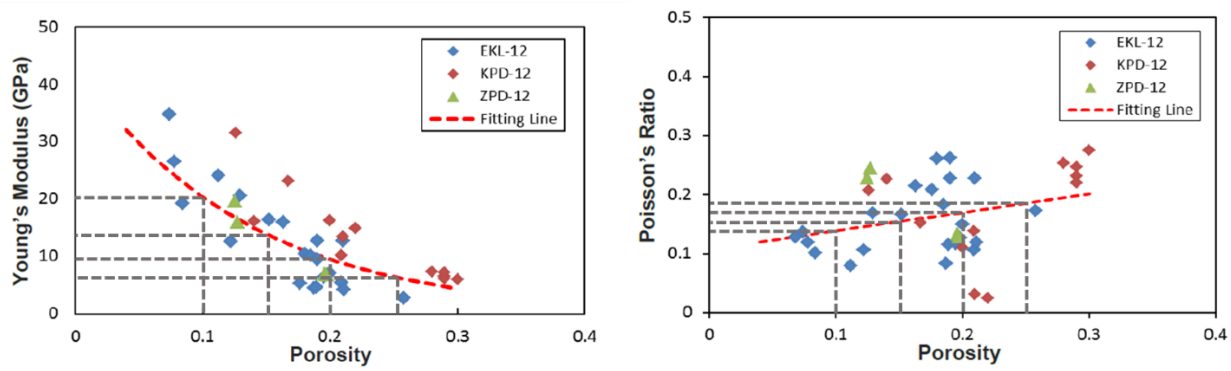


**Figure E1**: Porosity relationship graphs for the Young's modulus and Poisson's ratio of the Slochteren reservoir. Modified from Lele et al. (2015).

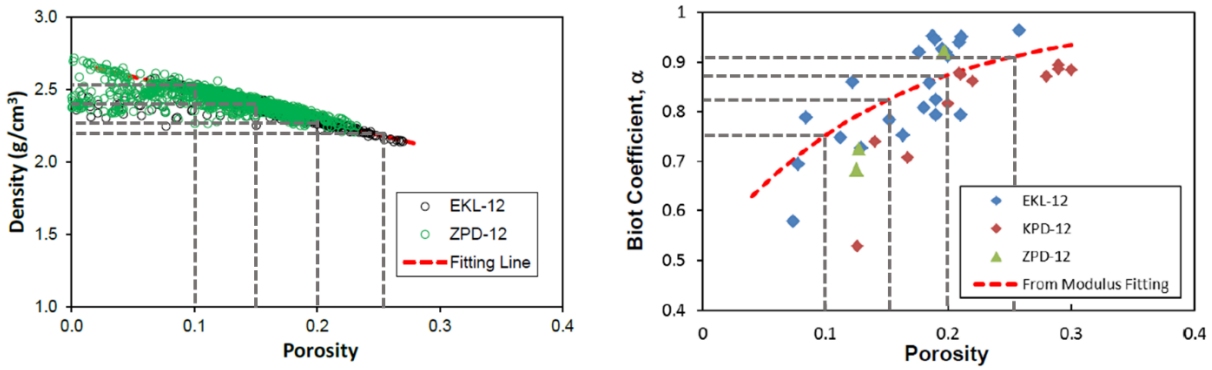


**Figure E2**: Porosity relationship graphs for the density and Biot coefficient of the Slochteren reservoir. Modified from Lele et al. (2015).

# Appendix F

*Matlab* Correction File for Poor Log Stacking

```
% Well A15-03
% Contains 156 measurements per depth interval.
A1503 = dlmread('MSc_RedoStack_Well_A15-03.txt');
A1503_sort1 = A1503';                          % Transpose data
A1503_sort2 = A1503_sort1(:);                  % Create 1 vector
mes = 156;                                     % No. of measurement types
int = length(A1503_sort2)/mes;                 % No. of depth measurements
A1503_sort3 = reshape(A1503_sort2,mes,int);    % Sort to depth
A1503_sort3 = A1503_sort3';                    % Transpose data

% Well A15-04
% Contains 30 measurements per depth interval.
A1504 = dlmread('MSc_RedoStack_Well_A15-04.txt');
A1504_sort1 = A1504';                          % Transpose data
A1504_sort2 = A1504_sort1(:);                  % Create 1 vector
mes = 30;                                      % No. of measurement types
int = length(A1504_sort2)/mes;                 % No. of depth measurements
A1504_sort3 = reshape(A1504_sort2,mes,int);    % Sort to depth
A1504_sort3 = A1504_sort3';                    % Transpose data
```

**Figure F1**: Part of the script used for correcting poorly stacked data. Note that each LAS file contains a different amount of measurement types.

# Appendix G

*Matlab* Correction File for Discrepancy in Log Resolution

```
% Well A15-03
% One file needs to be adjusted. 5th column
A1503 = dlmread('MSc_RedoRes_Well_A15-03.txt');
[~,idx] = unique(A1503(:,5));
A1503_sort = A1503(idx,:);

% Well A15-04
% Two files need to be adjusted. 2nd column.
A1504rho = dlmread('MSc_RedoRes_Well_A15-04RHOB.txt');
[~,idx] = unique(A1504rho(:,2));
A1504rho_sort = A1504rho(idx,:);

A1504dtco = dlmread('MSc_RedoRes_Well_A15-04DTCO.txt');
[~,idx] = unique(A1504dtco(:,2));
A1504dtco_sort = A1504dtco(idx,:);

% Well BHM-06
% One file needs to be adjusted. 5th column. RHOB and DRHO resorted
BHM06 = dlmread('MSc_RedoRes_Well_BHM-06.txt');
[~,idx] = unique(BHM06(:,5));
BHM06_sort = BHM06(idx,:);
```

**Figure G1**: Part of the script used for correcting the discrepancy in log resolution. The *Matlab* script is used to remove duplicates.

# Appendix H

Matlab File for Combining Core and Wireline Data

```
data = zeros(length(mdrt),13);
b = zeros(length(ChkG_WellBIR13_mdrt),1);
c = zeros(length(mdrt),1);
z = zeros(length(ChkG_WellBIR13_mdrt),length(mdrt));
for i = 1:length(mdrt)
    for j = 1:(length(ChkG_WellBIR13_mdrt))
        b(j) = abs(mdrt(i)-ChkG_WellBIR13_mdrt(j));
        z(j,i) = abs(mdrt(i)-ChkG_WellBIR13_mdrt(j));
    end
        c(i) = min(b);                              % Nearest depth
        r = find(b==min(b));                        % Index nearest depth
        data((i),1) = mdrt(i);
        data((i),2) = por_core(i);
        data((i),3) = rho_grain(i);
        data((i),4) = ChkG_WellBIR13_rhob(r);
        data((i),5) = ChkG_WellBIR13_vp(r);
        data((i),6) = ChkG_WellBIR13_vs(r);
        data((i),7) = ChkG_WellBIR13_nu(r);
        data((i),8) = ChkG_WellBIR13_edyngpa(r);
        data((i),9) = ChkG_WellBIR13_estat_mccann(r);
        data((i),10) = ChkG_WellBIR13_estat_eissa1(r);
        data((i),11) = ChkG_WellBIR13_estat_eissa2(r);
        data((i),12) = ChkG_WellBIR13_gr(r);
        data((i),13) = ChkG_WellBIR13_nphi(r);
end
```

**Figure H1**: Part 1 of an example script combining core and wireline data of the Chalk Group for well BIR-13.

```
[C, ia, ic] = unique(data(:,4:11),'rows','stable');  % Remove poor approxim
data_sorted = data(ia,:);
data_sorted(1,:) = [];                      % Remove first row
data_sorted(length(data_sorted),:) = [];    % Remove last row

co_mdrt = data_sorted(:,1);                 % Ease of readability
co_por_core = data_sorted(:,2);
co_rho_grain = data_sorted(:,3);
co_rhob = data_sorted(:,4);
co_vp = data_sorted(:,5);
co_vs = data_sorted(:,6);
co_nu = data_sorted(:,7);
co_edyngpa = data_sorted(:,8);
co_estat_mccann = data_sorted(:,9);
co_estat_eissa1 = data_sorted(:,10);
co_estat_eissa2 = data_sorted(:,11);
co_gr = data_sorted(:,12);
co_nphi = data_sorted(:,13);
```

**Figure H2**: Part 2 of an example script combining core and wireline data of the Chalk Group for well BIR-13.

# Appendix I

Calculated Elastic Parameters from *NLOG* Wells

**Table I1**: Mean, median and standard deviation for the dynamic Poisson's ratio for a number of wells from *NLOG*. The geological division is on a group basis. *Values are for the Slochteren Formation.

| Unit | Well | Mean $\nu_{dyn}$ [-] | Median $\nu_{dyn}$ [-] | Std. $\nu_{dyn}$ [-] |
|---|---|---|---|---|
| Up. North Sea | A15-02 | 0.423 | 0.424 | 0.023 |
| Up. North Sea | B13-14 | 0.432 | 0.435 | 0.020 |
| Up. North Sea | B16-01 | 0.429 | 0.429 | 0.030 |
| Chalk | BIR-13 | 0.332 | 0.333 | 0.013 |
| Chalk | P15-14 | 0.307 | 0.306 | 0.017 |
| Rijnland | P15-14 | 0.264 | 0.274 | 0.057 |
| Rijnland | PRW-01 | 0.283 | 0.277 | 0.023 |
| Schieland | F02-07 | 0.248 | 0.261 | 0.071 |
| Schieland | PRW-01 | 0.288 | 0.287 | 0.025 |
| Scruff | F02-07 | 0.200 | 0.193 | 0.044 |
| Altena | P15-14 | 0.255 | 0.254 | 0.061 |
| Up. Germanic Triassic | CAP-01 | 0.267 | 0.276 | 0.063 |
| Up. Germanic Triassic | L03-02 | 0.258 | 0.269 | 0.053 |
| Lo. Germanic Triassic | CAP-01 | 0.260 | 0.264 | 0.018 |
| Lo. Germanic Triassic | L03-02 | 0.255 | 0.262 | 0.023 |
| Lo. Germanic Triassic | L06-01 | 0.260 | 0.263 | 0.026 |
| Lo. Germanic Triassic | Q11-03 | 0.257 | 0.266 | 0.113 |
| Zechstein | GRL-01 | 0.285 | 0.301 | 0.044 |
| Zechstein | J06-04 | 0.264 | 0.277 | 0.045 |
| Zechstein | P08-06 | 0.228 | 0.226 | 0.042 |
| Zechstein | Q11-03 | 0.226 | 0.251 | 0.079 |
| Up. Rotliegend* | L05-06 | 0.184 | 0.182 | 0.045 |
| Up. Rotliegend | P08-06 | 0.218 | 0.212 | 0.036 |
| Up. Rotliegend | Q11-03 | 0.160 | 0.159 | 0.039 |

**Table I2**: Mean, median and standard deviation for the dynamic Young's modulus for a number of wells from *NLOG*. The geological division is on a group basis. *Values are for the Slochteren Formation.

| Unit | Well | Mean $E_{dyn}$ [-] | Median $E_{dyn}$ [-] | Std. $E_{dyn}$ [-] |
|---|---|---|---|---|
| Up. North Sea | A15-02 | 3.23 | 3.12 | 0.77 |
| Up. North Sea | B13-14 | 2.88 | 2.64 | 1.18 |
| Up. North Sea | B16-01 | 3.25 | 2.93 | 1.44 |
| Chalk | BIR-13 | 26.54 | 26.24 | 9.52 |
| Chalk | P15-14 | 22.76 | 19.52 | 6.10 |
| Rijnland | P15-14 | 27.02 | 25.51 | 5.02 |
| Rijnland | PRW-01 | 27.32 | 26.45 | 5.34 |
| Schieland | F02-07 | 20.68 | 17.30 | 8.46 |
| Schieland | PRW-01 | 30.76 | 30.79 | 6.22 |
| Scruff | F02-07 | 14.42 | 14.37 | 1.07 |
| Altena | P15-14 | 25.84 | 25.26 | 5.19 |
| Up. Germanic Triassic | CAP-01 | 49.01 | 49.92 | 12.31 |
| Up. Germanic Triassic | L03-02 | 37.91 | 35.24 | 9.34 |
| Lo. Germanic Triassic | CAP-01 | 46.24 | 44.73 | 7.25 |
| Lo. Germanic Triassic | L03-02 | 43.02 | 38.50 | 10.04 |
| Lo. Germanic Triassic | L06-01 | 37.33 | 35.47 | 6.43 |
| Lo. Germanic Triassic | Q11-03 | 41.82 | 39.43 | 7.05 |
| Zechstein | GRL-01 | 54.19 | 61.36 | 23.29 |
| Zechstein | J06-04 | 56.20 | 51.53 | 21.81 |
| Zechstein | P08-06 | 55.01 | 54.36 | 10.81 |
| Zechstein | Q11-03 | 53.54 | 52.20 | 10.62 |
| Up. Rotliegend* | L05-06 | 46.62 | 44.42 | 8.67 |
| Up. Rotliegend | P08-06 | 45.61 | 46.16 | 13.45 |
| Up. Rotliegend | Q11-03 | 40.42 | 39.95 | 3.60 |

**Table I3**: Mean, median and standard deviation for the converted static Young's modulus (McCann and Entwissle, 1992) for a number of wells from *NLOG*. The geological unit division is on a group basis. *Values are for the Slochteren Formation.

| Unit | Well | Mean $E_{stat}$ [-] | Median $E_{stat}$ [-] | Std. $E_{stat}$ [-] |
|---|---|---|---|---|
| Up. North Sea | A15-02 | 1.74 | 1.67 | 0.49 |
| Up. North Sea | B13-14 | 1.52 | 1.37 | 0.76 |
| Up. North Sea | B16-01 | 1.76 | 1.55 | 0.92 |
| Chalk | BIR-13 | 16.67 | 16.48 | 6.09 |
| Chalk | P15-14 | 14.24 | 12.17 | 3.90 |
| Rijnland | P15-14 | 16.97 | 16.01 | 3.22 |
| Rijnland | PRW-01 | 17.16 | 16.61 | 3.42 |
| Schieland | F02-07 | 12.91 | 10.75 | 5.42 |
| Schieland | PRW-01 | 19.37 | 19.39 | 3.98 |
| Scruff | F02-07 | 8.91 | 8.88 | 0.69 |
| Altena | P15-14 | 16.22 | 15.84 | 3.32 |
| Up. Germanic Triassic | CAP-01 | 31.04 | 31.63 | 7.88 |
| Up. Germanic Triassic | L03-02 | 23.94 | 22.17 | 5.98 |
| Lo. Germanic Triassic | CAP-01 | 29.28 | 28.31 | 4.64 |
| Lo. Germanic Triassic | L03-02 | 27.21 | 24.32 | 6.42 |
| Lo. Germanic Triassic | L06-01 | 23.57 | 22.38 | 4.11 |
| Lo. Germanic Triassic | Q11-03 | 26.45 | 24.91 | 4.51 |
| Zechstein | GRL-01 | 34.36 | 38.95 | 14.90 |
| Zechstein | J06-04 | 35.65 | 32.66 | 13.96 |
| Zechstein | P08-06 | 34.89 | 34.47 | 6.92 |
| Zechstein | Q11-03 | 33.94 | 33.09 | 6.79 |
| Up. Rotliegend* | L05-06 | 29.51 | 28.11 | 5.55 |
| Up. Rotliegend | P08-06 | 28.87 | 29.22 | 8.61 |
| Up. Rotliegend | Q11-03 | 25.55 | 25.25 | 2.31 |

**Table I4**: Mean, median and standard deviation for the converted static Young's modulus (Barree et al., 1992) for a number of wells from *NLOG*. The geological unit division is on a group basis. *Values are for the Slochteren Formation.

| Unit | Well | Mean $E_{stat}$ [-] | Median $E_{stat}$ [-] | Std. $E_{stat}$ [-] |
|---|---|---|---|---|
| Up. North Sea | A15-02 | 1.94 | 1.88 | 0.48 |
| Up. North Sea | B13-14 | 1.68 | 1.56 | 0.60 |
| Up. North Sea | B16-01 | 1.92 | 1.71 | 0.89 |
| Chalk | BIR-13 | 18.44 | 18.65 | 7.43 |
| Chalk | P15-14 | 12.11 | 10.43 | 3.89 |
| Rijnland | P15-14 | 19.37 | 18.29 | 4.11 |
| Rijnland | PRW-01 | 19.24 | 18.26 | 4.38 |
| Schieland | F02-07 | 14.10 | 11.49 | 6.71 |
| Schieland | PRW-01 | 22.11 | 22.07 | 4.82 |
| Scruff | F02-07 | 9.35 | 9.30 | 0.92 |
| Altena | P15-14 | 18.32 | 18.42 | 4.23 |
| Up. Germanic Triassic | CAP-01 | 37.02 | 38.20 | 10.42 |
| Up. Germanic Triassic | L03-02 | 25.13 | 24.54 | 7.83 |
| Lo. Germanic Triassic | CAP-01 | 34.42 | 33.49 | 5.73 |
| Lo. Germanic Triassic | L03-02 | 31.86 | 28.72 | 7.35 |
| Lo. Germanic Triassic | L06-01 | 27.24 | 26.06 | 4.93 |
| Lo. Germanic Triassic | Q11-03 | 30.00 | 28.51 | 4.78 |
| Zechstein | GRL-01 | 40.33 | 45.67 | 22.34 |
| Zechstein | J06-04 | 39.91 | 32.32 | 21.90 |
| Zechstein | P08-06 | 41.41 | 40.36 | 8.40 |
| Zechstein | Q11-03 | 37.83 | 36.34 | 7.90 |
| Up. Rotliegend* | L05-06 | 33.40 | 31.34 | 7.66 |
| Up. Rotliegend | P08-06 | 32.17 | 32.28 | 10.70 |
| Up. Rotliegend | Q11-03 | 27.42 | 27.03 | 2.61 |

# Appendix J

Model pore pressure

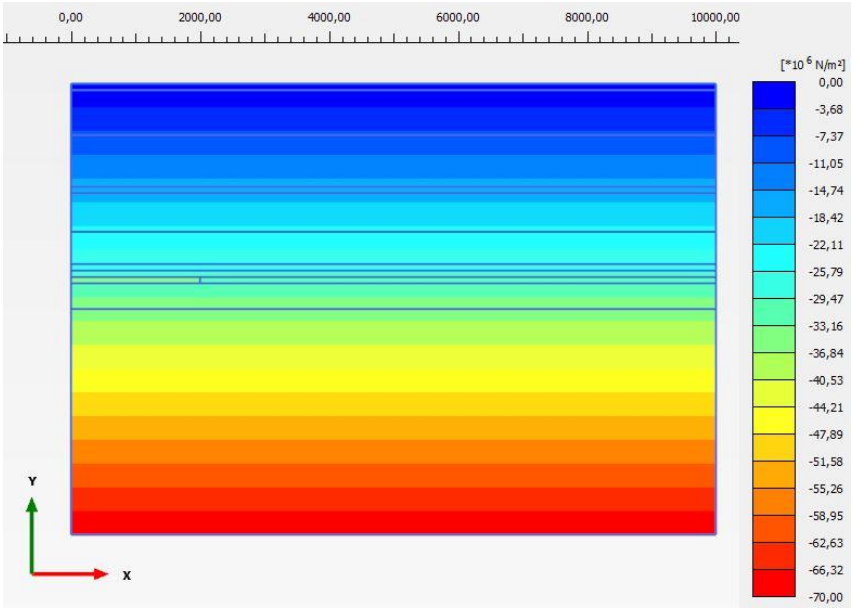


**Figure J1**: Model showing the pore pressure prior to reservoir depletion. As can be seen the reservoir has a higher pore pressure than the surrounding rock. Note that the pore pressure is defined as negative.

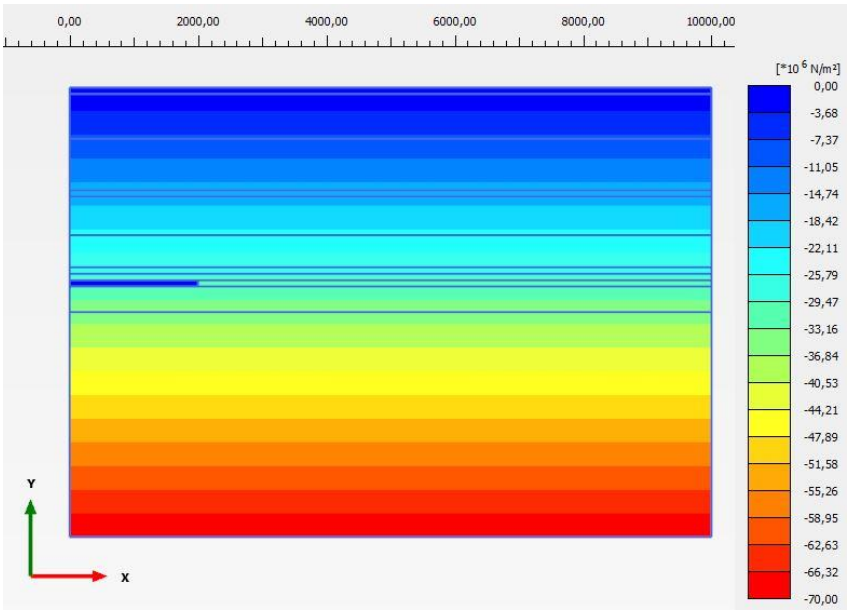


**Figure J2**: Model showing the pore pressure at the end of depletion. As can be seen the reservoir has a much lower pore pressure than the surrounding rock and is easily distinguished. Note that the pore pressure is defined as negative.

# Appendix K

Examples of Vertical and Horizontal Displacement in *Plaxis*

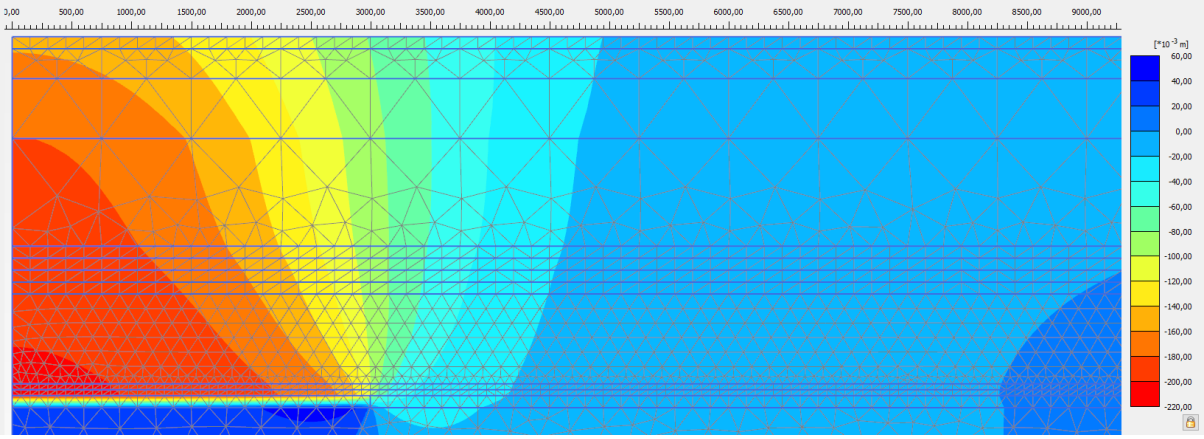


**Figure K1**: Vertical displacement in *Plaxis*. The vertical displacement is greatest above the reservoir edge. Note the lack of a vertical scale, but the reservoir depth is 3000 m and is at the same level as the area with the greatest amount of displacement.

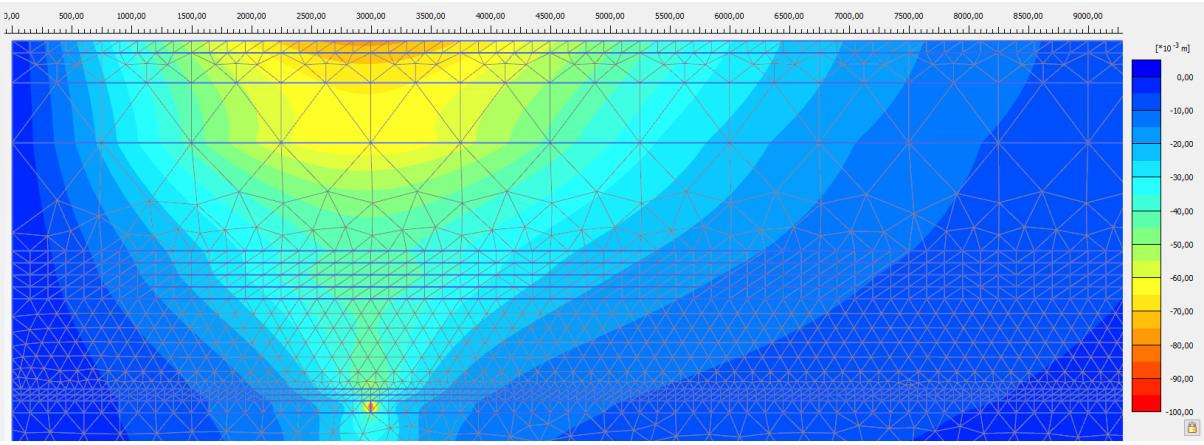


**Figure K2**: Horizontal displacement in *Plaxis*. The horizontal displacement is greatest above the reservoir edge. Note the lack of a vertical scale, but the reservoir depth is 3000 m and is at the same level as the area with the greatest amount of displacement.

# Appendix L

Horizontal Effective Stress and Vertical Strain h = 100 m D = 2900 m

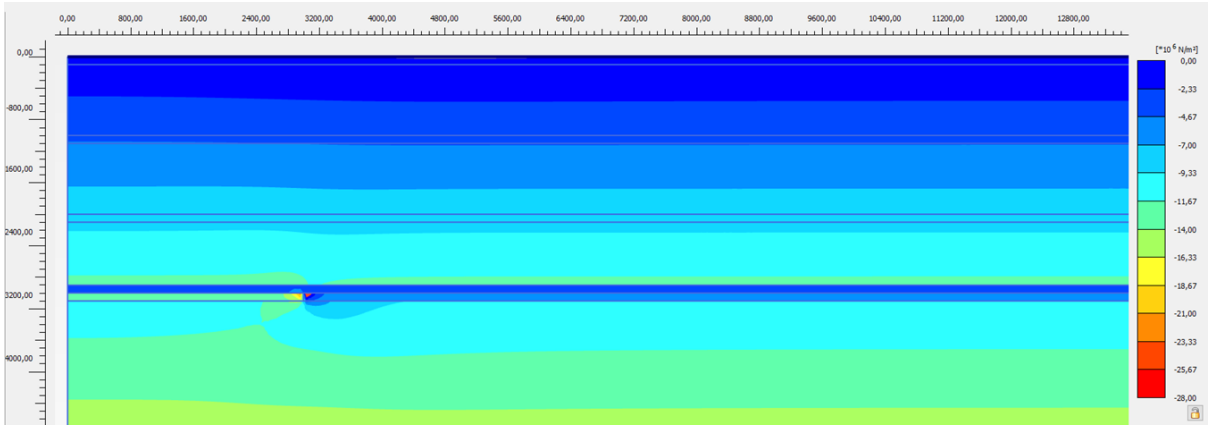

**Figure L1**: Horizontal effective stress for a model with E = 2.5 GPa and v = 0.10, 100 m thick and at a depth of 2900 m. Note that the horizontal effective stress in the layer above the reservoir (= layer with butterfly shape) is very low (blue).

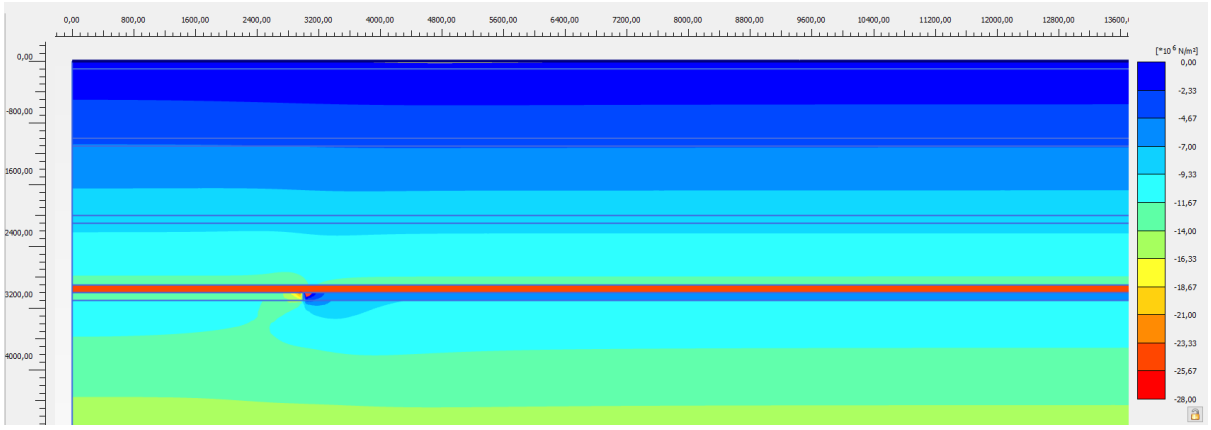

**Figure L2**: Horizontal effective stress for a model with E = 2.5 GPa and v = 0.40, 100 m thick and at a depth of 2900 m. Note that the horizontal effective stress in the layer above the reservoir (= layer with butterfly shape) is very high (red).

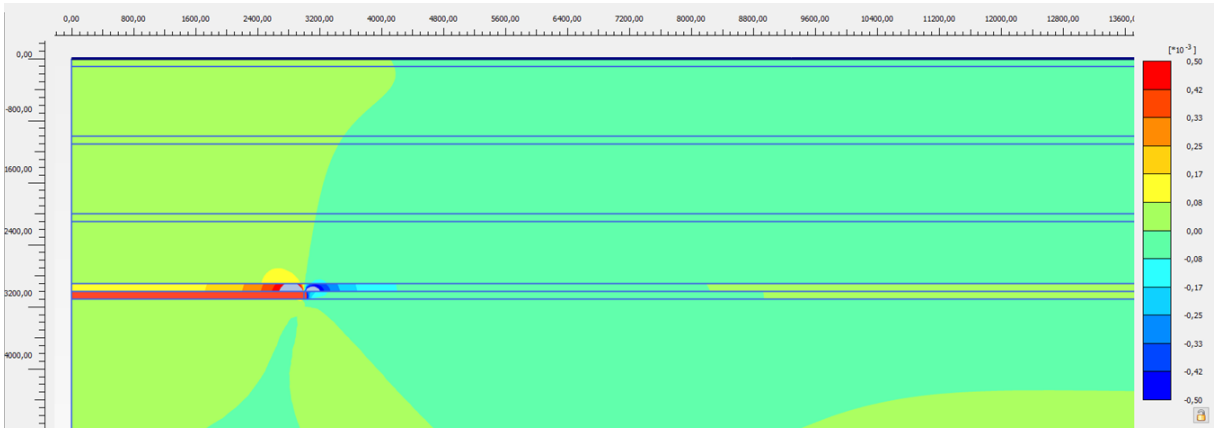

**Figure L3**: Vertical strain for a model with E = 2.5 GPa and v = 0.10, 100 m thick and at a depth of 2900 m. Note that there clearly is vertical elongation (red/yellow) in the layer above the reservoir (red rectangle).

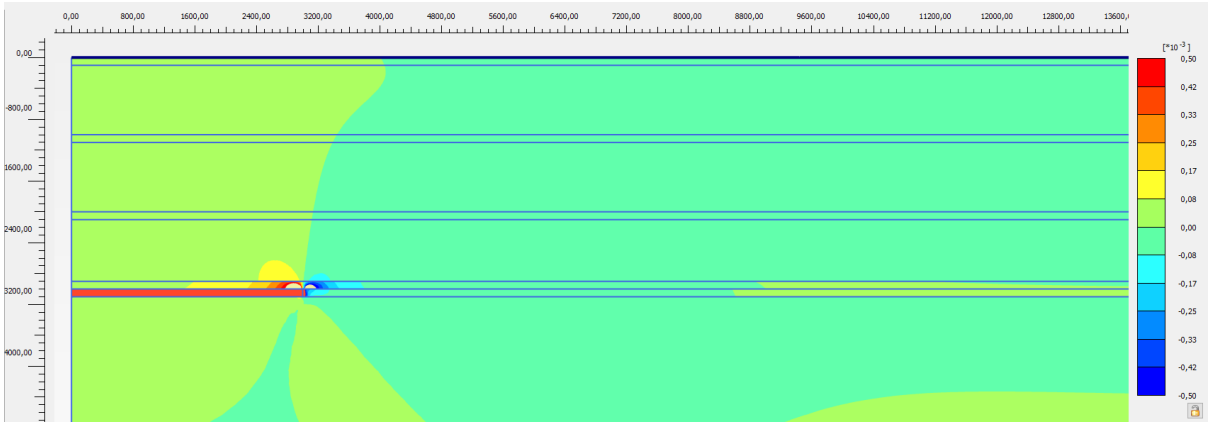

**Figure L4**: Vertical strain for a model with E = 2.5 GPa and v = 0.40, 100 m thick and at a depth of 2900 m. Note that there is less vertical elongation (red/yellow) in the layer above the reservoir (red rectangle) than when the Poisson's ratio equals 0.10 (Figure L3).

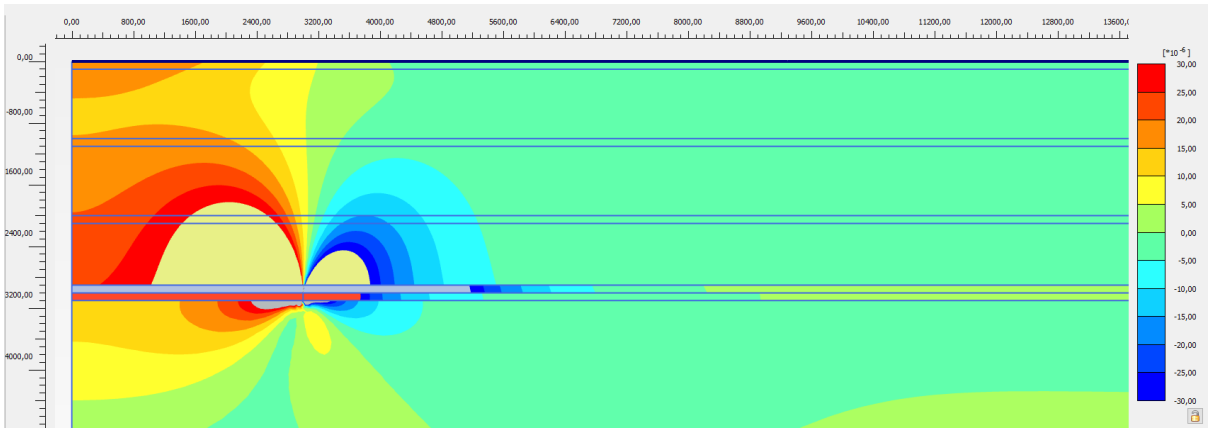

**Figure L5**: Vertical strain in a narrower range for a model with E = 2.5 GPa and v = 0.10, 100 m thick and at a depth of 2900 m. Note that there clearly is vertical elongation (red/yellow) in the zone above the reservoir (red rectangle), which can be seen in more detail than in Figure L3.

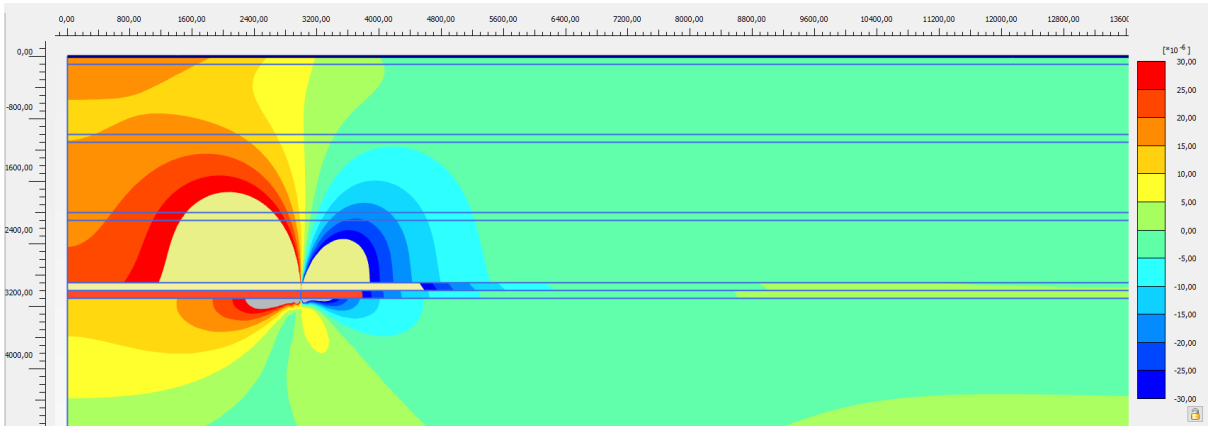

**Figure L6**: Vertical strain in a narrower range for a model with E = 2.5 GPa and v = 0.40, 100 m thick and at a depth of 2900 m. Note that there clearly is vertical elongation (red/yellow) in the zone above the reservoir (red rectangle), which can be seen in more detail than in Figure L4. The vertical elongation is less than when the Poisson's ratio equals 0.10 (Figure L5).

# Appendix M

Vertical Strain h = 100 m D = 1000 m

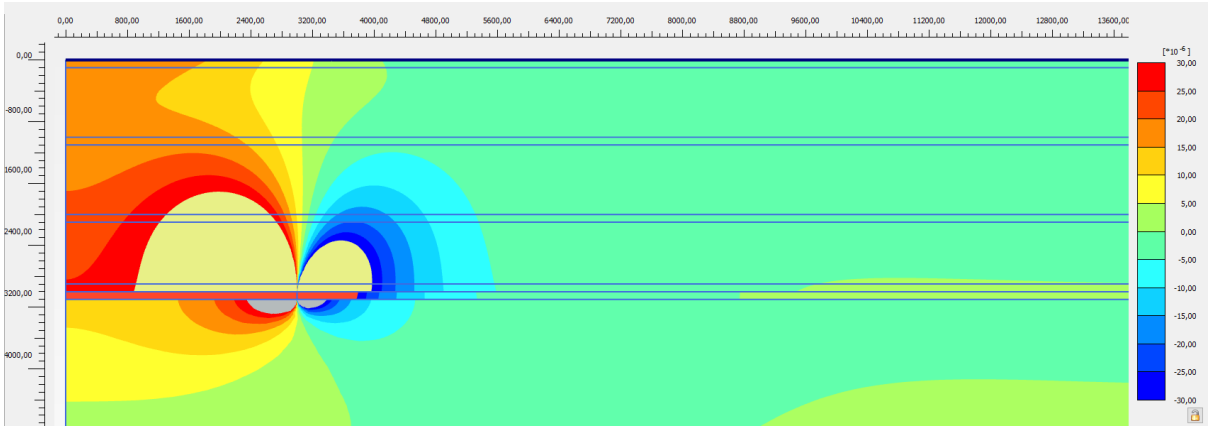


**Figure M1**: Vertical strain in a narrower range for a model with E = 10 GPa and v = 0.25, 100 m thick and at a depth of 1000 m. Note that there clearly is vertical elongation (red/yellow) in the zone above the reservoir (red rectangle).

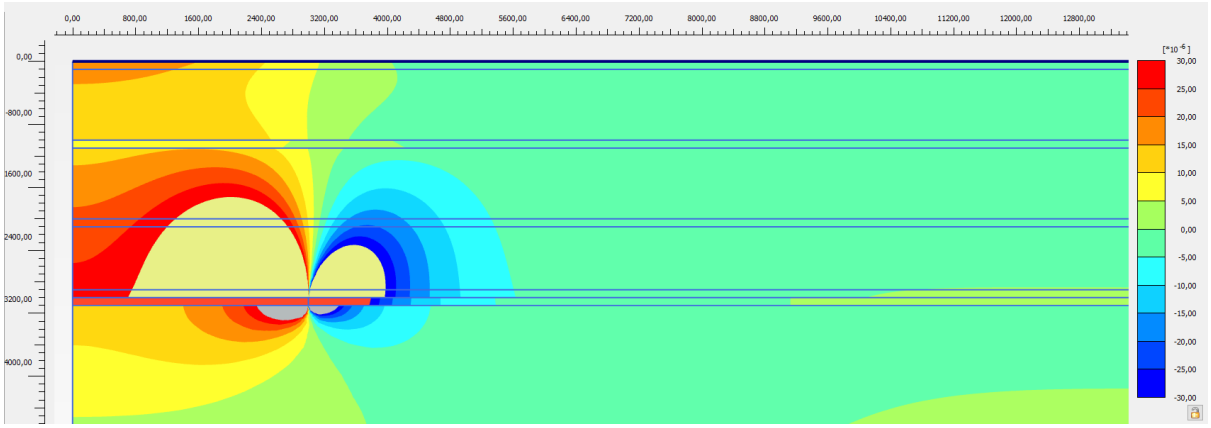


**Figure L2**: Vertical strain in a narrower range for a model with E = 80 GPa and v = 0.25, 100 m thick and at a depth of 1000 m. Note that there clearly is vertical elongation (red/yellow) in the zone above the reservoir (red rectangle), but in the rigid layer at D = 1000 m there is less elongation than for a less rigid layer (Figure M1). This seems to cause the overlying overburden to undergo less elongation as well. There is a bit more vertical elongation close above the reservoir.

# Appendix N

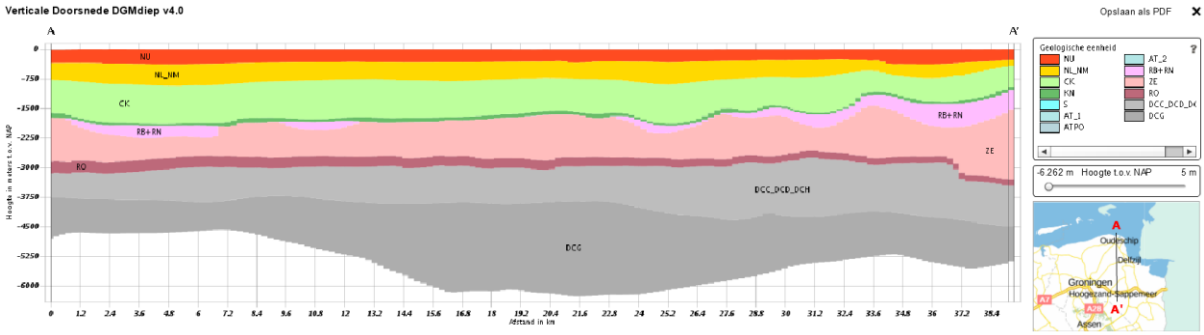


**Figure N1**: North-south cross section of the Groningen field used to determine the *Plaxis* model.

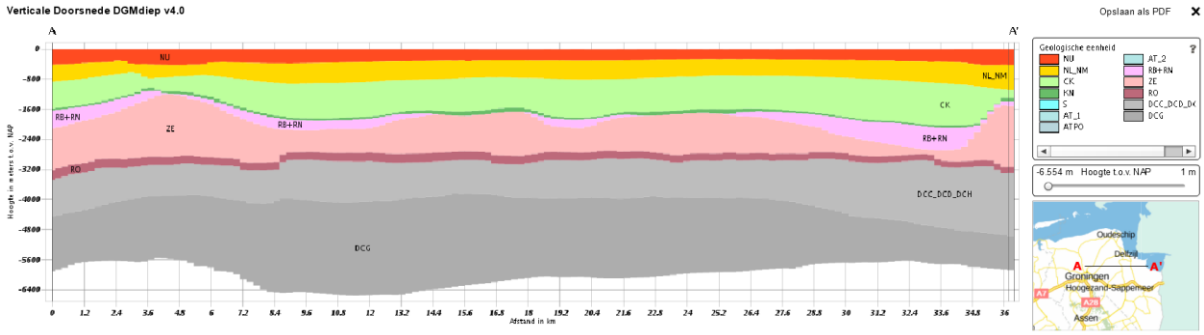


**Figure N2**: West-east cross section of the Groningen field used to determine the *Plaxis* model.

# References


Barree, R.D., Gilbert, J.V., Conway, M.W., (2009). Stress and Rock Property Profiling for Unconventional Reservoir Stimulation. SPE 118703.

Burkitov, U., van Oeveren, H., Valvatne, P., (2016). Groningen field review 2015 subsurface dynamic modelling report. NAM (Nederlandse Aardolie Maatschappij).

Cuisiat, F.D.E., Grande, L., Jostad, H.P., (2010). The importance of clay behaviour for geomechanical modelling of gas production in unconsolidated reservoir sands. 72nd EAGE Conference & Exhibition incorporating SPE EUROPEC 2010. Barcelona, Spain, 14-17 June 2010.

Doornhof, D., Kristiansen, T.G., Nagel, N.B., Pattilo, P.D., Sayers, C., (2006). Compaction and subsidence. Oilfield review.

Eason, G., Noble, B., Sneddon, I.N., On certain integrals of Lipschitz-Hankel type involving products of Bessel functions. *Philosophical Transactions of the Royal Society of London*. Series A, Mathematical and Physical Sciences, 247, 529-551.

Fjaer, E., Holt, R.M., Horsrud, P., Raaen, A.M., Risnes, R., (2008). *Petroleum related rock mechanics*. Amsterdam: Elsevier.

Fossen, H., (2010). *Structural geology*. 1st ed. Cambridge: Cambridge University Press.

Gambolati, G., Ferronato, M., Teatini, P., (2006). Reservoir compaction and land subsidence. Department of Mathematical Models and Methods for Scientific Applications. University of Padova, Padova, Italy.

Gambolati, G., Ricceri, G., Bertoni, W., Brighenti G., Vuillermin, E., (1991). Mathematical Simulation of the Subsidence of Ravenna. *Water Resources Research*, 27, 2899-2918.

Geertsma, J., (1973). A basic theory of subsidence due to reservoir compaction: the homogeneous case. *Verhandelingen Kon. Ned. Geol. Mijnbouwk*, 28, 43-62.

Geertsma, J., van Opstal, G., (1973). A numerical technique for predicting subsidence above compacting reservoirs, based on the nucleus of strain concept. *Verhandelingen Kon. Ned. Geol. Mijnbouwk*, 28, 63-78.

Keszthelyi, D., Dysthe, D.K., Jamtveit, B., (2016). Compaction of North-Sea Chalk by pore-failure and pressure solution in a producing reservoir. *Frontiers in Physics*, 4.

Kroon, I.C., Nguyen, B.-L., Fokker, P.A., Muntendam-Bos, A.G., de Lange, G., (2009). Disentangling shallow and deep processes causing surface movement. *Mathematical Geosciences*, 41, 571-584.

Kruiver, P.P., van Dedem, E., Romijn, R., de Lange, G., Korff, M., Stafleu, J., Gunnink, J.L., Rodrigeuz-Marek, A., Bommer, J.J., van Elk, J., Doornhof, D., (2017). An integrated shear-wave velocity model for the Groningen gas field, The Netherlands. *Bullitin Earthquake Engineering*, 15, 3555-3580.

Lawless, J., Okada, W., Terzaghi, S., White, P., Gilbert, C., (2003). Two dimensional subsidence modelling at Wairakei-Tauhara, New Zealand. International Geothermal Conference, Reykjavik, Sept. 2003.

Lele, S.P., Garzon, J.L., Hsu, S-Y., DeDontney, N.L., Searles, K.H., Sanz, P.F., (2015). Groningen 2015 Geomechanical Analysis. NAM (Nederlandse Aardolie Maatschappij).

Markov, G., Mukerji, T., Dvorkin, J., (1998). The rock physics handbook. 1st ed. Cambridge: Cambridge University Press.

McCann, D.M., Entwisle, D.C., (1992). Determination of Young's modulus of the rock mass from geophysical well logs.

Mehrabian, A., Abousleiman, Y.N., (2015). Geertsma's subsidence solution extended to layered stratigraphy. *Journal of Petroleum Science and Engineering*, 130, 68-76.

Morales, R.H., Marcinew, R.P., (1993). Fracturing of High-Permeability Formation: Mechanical Properties Correlations. SPE 26561.

Nagel, N.B., (2001). Compaction and subsidence issues within the petroleum industry: from Wilmington to Ekofisk and beyond. *Phys. Chem. Earth (A)*, 26, 3-14.

NAM (Nederlandse Aardolie Maatschappij), (2013). Technical Addendum to the Winningsplan 2013.

NAM (Nederlandse Aardolie Maatschappij), (2016). Technical Addendum to the Winningsplan 2016.

Orlic, B., (2016). Geomechanical effects of $CO_2$ storage in depleted gas reservoirs in the Netherlands: inferences from feasibility studies and comparison with aquifer storage. *Journal of Rock Mechanics and Geotechnical Engineering*, 8, 846-859.

Plaxis, 2017. Plaxis 2D Reference Manual.

Plaxis, 2017. Plaxis 2D Material Manual.

Tempone, P., Fjaer, E., Landrø, M., (2010). Improved solution of displacement due to a compacting reservoir over a rigid basement. *Applied Mathematical Modelling*, 34, 3352-3362.

Van Eijs, R.M.H.E., Mulders, F.M.M., Nepveu, M., Kenter, C.J., Scheffers, B.C., (2006). Correlation between hydrocarbon reservoir properties and induced seismicity in the Netherlands.

Van Opstal, G., (1974). The effect of base rock rigidity on subsidence due to compaction. In: Proceedings of the Third Congress of the International Society of Rock Mechanics, vol. 2. Denver, Colorado, No. part B.

Wang, F., Li, X., Couples, G., Shi, J., Zhang, J., Tepinhi, Y., Wu, L., (2015). Stress arching effect on stress sensitivity of permeability and gas well production in Sulige gas field. *Journal of Petroleum Science and Engineering*, 125, 234-246.

Wong, T., Batjes, D.A.J., de Jager, J., (2007). *Geology of the Netherlands*. Amsterdam: Royal Netherlands Academy of Arts and Sciences.

(www-1). Long Beach Gas and Oil. Subsidence.
http://www.longbeach.gov/LBGO/About-Us/Oil/Subsidence/
Retrieved: 12-12-2017

(www-2). FluxEnergie.nl, (2017). NOS: 'In heel Nederland groeit verzet tegen gaswinning
https://www.fluxenergie.nl/nos-heel-nederland-groeit-verzet-gaswinning/
Retrieved: 12-12-2017

(www-3). Kouwenhoven, A., (2017). Minder gaswinning om bevingen te verminderen.

https://www.nrc.nl/nieuws/2017/04/19/minder-gaswinning-om-bevingen-te-verminderen-8285124-a1555058
Retrieved: 12-12-2017

(www-4). NAM. Gas- en oliewinning.
https://www.nam.nl/feiten-en-cijfers/gaswinning.html#iframe=L2VtYmVkL2NvbXBvbmVudC8/aWQ9Z2Fzd2lubmluZw==
Retrieved: 12-12-2017

(www-5). Nationaal Coördinator Groningen. Onderzoek oorzaak schade.
https://www.nationaalcoordinatorgroningen.nl/themas/t/tu-delft-schadeoorzaken
Retrieved: 12-12-2017

(www-6). Wikipedia. Shear modulus.
https://en.wikipedia.org/wiki/Shear_modulus
Retrieved: 28-09-2017

(www-7). umdberg. Bulk modulus – solids (2013).
http://umdberg.pbworks.com/w/page/68393228/Bulk%20modulus%20--%20solids%20(2013)
Retrieved: 28-09-2017

(www-8). DINOloket. Home page.
https://www.dinoloket.nl/
Retrieved: 12-12-2017

(www-9). NLOG. Home page
http://nlog.nl/
Retrieved: 12-12-2017

(www-10) DINOloket. Table
https://www.dinoloket.nl/table
Retrieved 15-12-2017

(www-11). DINOloket. Digitaal Geologisch Model: DGM
https://www.dinoloket.nl/digitaal-geologisch-model-dgm
Retrieved: 12-12-2017

(www-12). DINOloket. Detaillering van de bovenste lagen met GeoTOP
https://www.dinoloket.nl/detaillering-van-de-bovenste-lagen-met-geotop
Retrieved: 12-12-2017

(www-13). DINOloket. Digitaal Geologisch Model: DGM-diep
https://www.dinoloket.nl/digitaal-geologisch-model-dgm-diep
Retrieved: 17-12-2017